

**A STUDY OF LARGE-SCALE STRUCTURES IN THE  
SOLAR CORONA AT LONG WAVELENGTHS**

A THESIS  
SUBMITTED FOR THE DEGREE OF  
DOCTOR OF PHILOSOPHY

IN  
DEPARTMENT OF PHYSICS  
MANGALORE UNIVERSITY

by

**C.KATHIRAVAN**



**INDIAN INSTITUTE OF ASTROPHYSICS  
BANGALORE - 560034, INDIA  
November 2005**

## DECLARATION

I hereby declare that the matter embodied in this thesis is the result of the work carried out by me in the Indian Institute of Astrophysics, Bangalore. I further declare that no part of this work has been submitted for the award of any other degree, diploma, membership, associateship or similar title of any university or institution.

C. Kathiravan  
(Ph.D. Candidate)

## CERTIFICATE

This is to certify that the thesis entitled 'The study of large-scale structures in the solar corona at long wavelengths' submitted to the Mangalore University by C. Kathiravan for the award of the degree of Doctor of Philosophy in the Department of Physics, is based on the results of the investigation carried out by him under my general supervision and guidance, at the Indian Institute of Astrophysics. This thesis has not been submitted for the award of any degree, diploma, associateship, fellowship, etc., of any university or institution.

K. R. Subramanian  
(Thesis supervisor)

# ABSTRACT

## A STUDY OF LARGE-SCALE STRUCTURES IN THE SOLAR CORONA AT LONG WAVELENGTHS

C. Kathiravan

Mangalore University, 2005

Thesis supervisor: Prof. K. R. Subramanian

The characteristic properties of coronal mass ejections, the most energetic large-scale structure in the solar atmosphere are introduced briefly to begin with. The kinematics of coronal mass ejection (CME) propagation in the outer corona, the interplanetary medium, and the strength of the geomagnetic disturbances in the near-Earth environment depend on the initial speed and acceleration of CMEs close to the Sun. The above parameters are calculated mainly through a back-projection using values obtained at distances  $> 2.5 R_{\odot}$  (from the center of the Sun) using white-light coronagraph images. Since the occulter in a coronagraph generally covers up to distance of  $\approx 2 R_{\odot}$  from the center of the Sun, non-coronagraphic observations are very essential to study the kinematics of CMEs close to the Sun. Radio observations particularly in the frequency range 30-110 MHz play an important role, since they are free from occulters. Also, one can simultaneously image the corona both above the disk as well off the limb. In this regard, we describe the array characteristics and imaging capabilities of the Gauribidanur Radioheliograph (GRH), since it is the only instrument available for solar observations at the above mentioned frequency after the decommissioning of the Clark Lake Radioheliograph (CLRH). In order to understand the inner coronal kinematics, the thermal radio counterpart of the white-light 'halo' CME of November 24, 2000 is discussed with the time sequence images observed with the GRH. The locations of the radio enhancement associated with the CME is obtained as a function of time from the radio images and its average velocity in the plane of the sky is derived. The observations indicate that the radio data can be used to successfully derive the parameters of a CME in the low corona ( $\leq 3 R_{\odot}$ ). For a complete understanding of CME associated phenomena, we need to determine the parameters of a CME in a 3-D space. A three-dimensional ray-tracing technique is developed to determine the optical depth accumulated by the radio waves (and hence to reproduce the observed brightness temperature) when they propagate through the

corona from the inner to the outer layers. In order to incorporate the density and temperature structures associated with the large-scale structures (during periods of activity), a Gaussian model in three-dimensions with the distribution for the electron density and temperature suggested by Newkirk (1961) as the ‘background’ corona is introduced in the technique. Then the technique is applied to study the properties of the corona observed with the GRH prior to the giant prominence eruption associated with the CME of June 2, 1998. The average density of the radio structure at the location of the above CME and its three-dimensional size are determined without any assumptions (excluding the models for density and temperature) through simulations. The same technique is used to obtain the positional information of a CME front in 3-D space as a function of time from the GRH radio images obtained on January 21, 1998. From the position vectors of the center of mass of the CME and its eruption location the speed of the CME in 3-D space is determined. Thus the ray-tracing analysis is an useful tool to study the characteristics of CMEs in the low corona. The low frequency radio observations (obtained with the GRH on June 2, 1997) of the angular broadening of the Crab nebula at a distance of  $\approx 41 R_{\odot}$  from the center of the Sun due to the occultation of the former by a coronal mass ejection in the foreground is described. Assuming a radial expansion of  $5 R_{\odot} \text{ day}^{-1}$  for the CME, the depth along the line of sight equal to its radial width, a scale length of 1000 km for the scattering inhomogeneities, the mass of the CME is calculated from the enlarged size of the Crab nebula. Observations of this type might be useful in understanding the properties of CMEs at large distances from the Sun.

## ACKNOWLEDGMENTS

I thank all the staff members of Indian Institute of Astrophysics (IIA), Bangalore for their kind help throughout my PhD tenure. My heart felt thanks goes to all people at the Radio Astronomy Field Station, Gauribidanur, for their hard effort in the construction and maintenance of various antenna and receiver systems. I avoid mentioning the names of individuals since it would definitely require ample number of pages and moreover I do not want to miss anyone of them. I would like to convey my sincere thanks to my thesis supervisor Prof. K. R. Subramanian, who allowed me to work according to my interest. I specially thank Dr. R. Ramesh, who was with me all the time and taught the basics of Radio astronomy and Solar Physics; I am really grateful to him. I thank the SOHO team for providing us with the LASCO coronagraph images. The SOHO data are produced by the consortium of the Naval Research Laboratory (US), Max-Planck-institut fuer Aeronomie (Germany), Laboratoire d' Astronomie (France), and the University of Birmingham (UK); SOHO is a project of international cooperation between ESA and NASA. The NASA CME catalogue (generated and maintained by the Center for Solar Physics and Space Weather at the Catholic University of America in cooperation with the Naval Research Laboratory and NASA) is extensively used in the thesis; I express my thanks to the above team members. The staff of the Mangalore university are thanked for their timely help and co-operation in carrying out the official procedures from the time of registration till submission. Finally, I thank my parents, colleagues, friends and relatives for their blessings and moral support.

# TABLE OF CONTENTS

	Page
List of Tables . . . . .	x
List of Figures . . . . .	xx
CHAPTERS	
1 Coronal Large-scale Structures . . . . .	1
1.1 Introduction . . . . .	1
1.1.1 Coronal Mass Ejections . . . . .	1
1.2 Coronagraphic Observations . . . . .	3
1.2.1 Evolution of a CME . . . . .	5
1.2.2 Characteristics of CMEs . . . . .	7
1.3 Non-Coronagraphic Observations . . . . .	13
1.3.1 Radio Observations . . . . .	15
2 The Gauribidanur Radioheliograph . . . . .	18
2.1 Introduction . . . . .	18
2.1.1 Array geometry . . . . .	21
2.1.2 Element grouping and signal transmission . . . . .	21
2.1.3 Grating lobes . . . . .	22
2.2 Receiver system . . . . .	22
2.2.1 Front end analog receiver . . . . .	22
2.2.2 Back end digital receiver . . . . .	27
2.2.3 Data acquisition . . . . .	27
2.3 Calibration and Imaging . . . . .	27
2.3.1 Calibration scheme used in the GRH . . . . .	31
2.3.2 Map formation . . . . .	32
3 The evolution of a ‘Halo’ coronal mass ejection close to the Sun . . . . .	37
3.1 Introduction . . . . .	37
3.2 Observations . . . . .	38
3.3 Analysis . . . . .	39
3.3.1 The speed of the CME in the plane of the sky . . . . .	39
3.3.2 The electron density of the CME . . . . .	49
3.3.3 The mass associated with the CME . . . . .	52
3.4 Conclusion . . . . .	52
4 The Ray-Tracing technique in three-dimensions . . . . .	55
4.1 The equation of Radiation Transfer . . . . .	55
4.2 Radio wave propagation in the solar Corona . . . . .	56
4.2.1 The optical depth ( $\tau$ ) . . . . .	56
4.2.2 The attenuation constant ( $\alpha$ ) . . . . .	58
4.3 The Theory of Ray-Tracing . . . . .	58
4.3.1 The Ray Equation . . . . .	59
4.3.2 Electron density model for the background corona . . . . .	62

4.4	Computing the Ray Path . . . . .	63
4.4.1	The Unrefracted Central Ray . . . . .	63
4.4.2	The Brewster's angle and the reflection of a Central Ray . . .	67
4.4.3	The Refraction of a Non-Central Ray . . . . .	70
4.5	Determination of the optical depth . . . . .	70
4.6	The Reversibility Property . . . . .	73
4.7	The radio brightness temperature distribution in two dimensions . .	75
4.7.1	The 'undisturbed' solar corona . . . . .	75
4.7.2	The ray plane . . . . .	75
4.7.3	The active solar corona - Density and Temperature models . .	79
4.7.4	The non-coplanar property . . . . .	84
5	Meter wavelength observations and ray-tracing analysis of the pre-event phase of a coronal mass ejection . . . . .	86
5.1	Introduction . . . . .	86
5.2	Observations . . . . .	88
5.3	Analysis . . . . .	88
5.3.1	Reproduction of the observed radio brightness distribution . .	88
5.3.2	Quality of the reproduced data . . . . .	92
5.3.3	Error in the fitted parameters (corresponding to the radio structures associated with the pre-eruption feature of June 2, 1998-CME) . . . . .	105
5.3.4	Results . . . . .	107
5.4	Conclusion . . . . .	110
6	Estimation of the three-dimensional space speed of a coronal mass ejection using meter wavelength radio data . . . . .	111
6.1	Introduction . . . . .	111
6.2	observations . . . . .	112
6.3	Analysis . . . . .	116
6.3.1	The density of the radio CME . . . . .	123
6.3.2	The volume of the CME . . . . .	124
6.3.3	The mass of the CME . . . . .	125
6.3.4	The motion of a system of particles in a 3-D space . . . . .	126
6.3.5	The center of mass of the CME ( $\vec{\mathbf{R}}_{\text{CME}}$ ) . . . . .	127
6.3.6	The location of eruption of the CME . . . . .	128
6.3.7	The space-speed of the CME . . . . .	129
6.4	Conclusion . . . . .	130
7	Decameter wavelength observations of the Crab nebula and its angular broadening due to a coronal mass ejection . . . . .	132
7.1	Introduction . . . . .	132
7.2	Observations . . . . .	135
7.3	Analysis . . . . .	140
7.3.1	The scattering angle and the electron density associated with the CME . . . . .	140



7.3.2	The approximate volume and mass of the CME at a distance of $41 R_{\odot}$ from the center of the Sun . . . . .	143
7.4	Conclusion . . . . .	143
8	Conclusions . . . . .	145
BIBLIOGRAPHY . . . . .		147
APPENDIX		
A	The Ray-Tracing Program . . . . .	161
VITA . . . . .		171

# LIST OF TABLES

Page

## CHAPTERS

1	Coronal Large-scale Structures . . . . .	1
2	The Gauribidanur Radioheliograph . . . . .	18
1	Antenna parameters . . . . .	20
2	Array parameters of the GRH . . . . .	24
3	The evolution of a ‘Halo’ coronal mass ejection close to the Sun . . . . .	37
4	The Ray-Tracing technique in three-dimensions . . . . .	55
5	Meter wavelength observations and ray-tracing analysis of the pre-event phase of a coronal mass ejection . . . . .	86
1	Parameters of discrete sources used in the ray-tracing calculations for the event observed with the GRH on June 2, 1998 at 07:30 UT . . . . .	95
6	Estimation of the three-dimensional space speed of a coronal mass ejection using meter wavelength radio data . . . . .	111
1	Parameters of the discrete sources used in the ray-tracing calculations to reproduce the radioheliogram obtained with the GRH on January 21, 1998 at 06:01 UT. . . . .	119
7	Decameter wavelength observations of the Crab nebula and its angular broadening due to a coronal mass ejection . . . . .	132
8	Conclusions . . . . .	145

## APPENDIX

A	The Ray-Tracing Program . . . . .	161
---	-----------------------------------	-----

# LIST OF FIGURES

Page

## CHAPTERS

1	Coronal Large-scale Structures . . . . .	1
1	A typical CME observed with the LASCO C2 coronagraph on January 18, 2000. The black circular region is the occulter of the coronagraph and the white inner circle represents the solar limb (photosphere). North is straight up and east is to the left. The frontal structure, cavity and the bright core (corresponding to the underlying prominence), are clearly visible above the occulting disk in the western hemisphere. The other bright structures in the image are stable and long lived coronal helmet streamers. . . . .	4
2	Images showing the different stages of evolution of the Coronal Mass Ejection observed on January 18, 2000 with the LASCO C2 Coronagraph. The images (a) and (b) in the top row show the pre-eruption swelling of the coronal helmet streamer before the onset of CME. Those in second row [(c) and (d)] describe the motion of the frontal structure, expanded cavity and the core. The post-ejection phase of the CME (i.e. the stage after the complete lift-off of the frontal structure) is shown in image (e) and (f) [bottom row]. . . . .	6
3	Cartoon showing the evolution of a typical CME. The circular disk (radius $\approx 1 R_{\odot}$ ) represents the photosphere. The dotted arc (Radius $\approx 2.2 R_{\odot}$ ) in all the panels represents the location of the LASCO C2 occulter. The conical structures above the solar limb in the Eastern hemisphere are stable coronal streamers. (a) The pre-eruption coronal helmet streamer (white outer structure) and the underlying prominence (slightly darker inner loop). The darker region between the above mentioned structures is the cavity. (b) The formation of a typical three-part ( <i>i.e.</i> , <i>frontal structure</i> , <i>underlying dark cavity</i> and <i>the prominence core</i> ) CME from the coronal helmet streamer. (c) During propagation the CME transports both the coronal material and frozen-in magnetic field into the interplanetary medium. (d) The formation of neutral current sheet in the aftermath of the CME eruption [Ko (2003)]. . . . .	8
4	The width (B) and position angle (P.A.) of a CME. The former is the angular extent between the foot-points $F_1$ and $F_2$ . The P.A. is the angular distance of the line OC from the solar north (the reference axis) measured through the East. The line OC joins the center of the Sun (O) and the mid point of the frontal structure/leading edge of the CME (C). Both ‘B’ and ‘P.A.’ are measured in degrees. . . . .	9

5	Height-time plot of the CME observed on January 18, 2000 with the LASCO C2 coronagraph. Each point in the graph represents the location of the CME front (height in units of solar radius from the center of the Sun) at different epoch. The initial and final measurements were made close to 2 and 21 $R_{\odot}$ , respectively. The first order fit to the above set of points gives a value of $\approx 643 \text{ km s}^{-1}$ for the velocity of the CME. The $y$ -intercept of the fitted line at 1 $R_{\odot}$ is the onset time of the CME and is 09:30:43 UT in the present case. . . . .	11
6	The graph on the top shows the second order fit for the same set of points in Figure 5. The graph at the bottom shows the velocity of the CME front as a function of radial distance from the center of the Sun. It is evident that the CME has decelerated at a rate of $\approx 11 \text{ m s}^{-2}$ . . . . .	12
2	The Gauribidanur Radioheliograph . . . . .	18
1	Structure of the log periodic dipole (LPD) used in the GRH array. . . . .	19
2	The layout of the GRH array. The E-W arm consists of 128 LPDs and the spacing between adjacent elements is 10m except for LPDs EW64 and EW65, which are separated by 20 m. The elements in the E-W arm are divided into 16 groups containing 8 each. The South arm has 64 LPDs with an inter-element spacing of 7 m. It is also divided into 16 groups containing 4 elements each. . . . .	23
3	Schematic of the E-W group. The gain of the pre-amplifier is $\approx 28 \text{ dB}$ and the insertion loss is about 3 dB. The loss in the interconnecting cables between adjacent LPD and the delay shifters is about 50 dB. The gain of the group amplifier is $\approx 34 \text{ dB}$ . The delay shifters are for tilting the E-W beam of the corresponding LPDs/group of LPDs in the E-W direction. Since the N-S beam of each E-W group is about $90^{\circ}$ (3 dB width), tilting in that direction is not required. . . . .	25
4	Schematic of the South group. The delay shifters in this arm tilt the N-S beam of the corresponding LPDs/group of LPDs in the N-S direction at different declinations. The 3 dB width of the E-W beam of the north-south group is $60^{\circ}$ . Therefore, no tilting is required in the E-W direction. . . . .	26
5	Front end analog receiver . . . . .	28
6	Back end digital receiver - The 1024 channel correlator . . . . .	29
7	Composite image of the LASCO-EIT difference image (05:30 UT) and the Gauribidanur radioheliogram (05:25 UT) obtained on November 24, 2000. The last contour in the N-W quadrant of the GRH image is at a distance of $\sim 4.0 R_{\odot}$ from the center. . . . .	34
8	The synthesized beam pattern of the GRH at 109 MHz. The contour levels are 0.005, 0.01, 0.1, 0.5, 0.8 of the peak value ( $\approx 1.0$ ). The 'X' mark [at (24' W, 52' N)] indicates the location of the outermost contour in Figure 7. The maximum amplitude at that location is $\approx 0.005$ . . . . .	36
3	The evolution of a 'Halo' coronal mass ejection close to the Sun . . . . .	37

1	A composite of the LASCO-EIT running difference image of the CME obtained on November 24, 2000 at 05:30 UT and the radio image observed with the GRH at 05:25 UT. The inner circle indicates the solar limb, and the outer circle is the occulting disk of the coronagraph. It extends up to $2.2 R_{\odot}$ from the center of the Sun. Solar north is straight up, and east is to the left. A comparison of the radio and white light enhancements in the northwest quadrant indicates that the former is the radio counterpart of the latter. Refer text for explanation of 'I'. . . . .	40
2	The second order fit (constant acceleration) to the LASCO height-time measurements of the CME observed on November 24, 2000. The estimated acceleration is $\approx 72 \text{ m s}^{-2}$ . The linear fit (constant speed) for the same set of points gives an average speed of $\approx 994 \text{ km s}^{-1}$ for the leading edge of the CME. The extrapolated onset time of the CME was 04:55:52 UT. Note that the white light measurements were made at a mean position angle of $353^{\circ}$ . . . . .	41
3	Radioheliogram obtained with the GRH on November 24, 2000 around 04:55 UT. The peak $T_b$ is $\approx 4.18 \times 10^6 \text{ K}$ and it corresponds to the source near the east limb. The open circle at the center is the solar limb. The outer circle corresponds approximately to the occulter size ( $2.2 R_{\odot}$ ) of the white-light coronagraph. The filled contour near the bottom right corner is the GRH beam at 109 MHz. . . . .	42
4	Same as Figure 3 but obtained at 05:05 UT. The peak $T_b$ is $\approx 6.08 \times 10^6 \text{ K}$ and it corresponds to the same source as in Figure 3. . . . .	43
5	Same as Figures 3 & 4, but the time of observation is 05:15 UT. The peak $T_b$ is $\approx 6.1 \times 10^6 \text{ K}$ . Again it corresponds to the source near the east limb as in Figure 3 and 4. . . . .	44
6	Same as Figures 3, 4 and 5, but observed at 05:25 UT. The peak $T_b$ is $\approx 5.6 \times 10^6 \text{ K}$ . It corresponds to the source near the disk center. Note that there is a shift in the centroid of the source near the east limb between Figures 3, 4, 5, 6. This is probably due to a localized activity there. The difference in their peak $T_b$ at that location also indicates the same. The bulged contours above the limb in the northwest quadrant in this as well as in the earlier Figures 3, 4 and 5 correspond to the white light CME (Figure 1). . . . .	45
7	Radio difference image obtained by subtracting the image shown in Figure 3 from Figure 4. In order to clearly identify the radio enhancement associated with the white light CME, we have plotted only the positive difference values up to half-maximum level. The '+' mark indicates the centroid of the radio CME. Its position coordinate in the image plane is ( $3'.5 \text{ N}$ , $17' \text{ W}$ ) and the average brightness temperature is $5.3 \times 10^5 \text{ K}$ . . . . .	46

8	Same as in Figure 7, but obtained by subtracting Figure 4 from Figure 5. The position coordinate of the centroid of radio enhancement associated with the CME is (17'.5 N,24' W). Its average brightness temperature is $5.5 \times 10^5$ K. . . . .	47
9	Radio difference image obtained by subtracting Figure 5 from Figure 6. The position coordinate of the centroid of the radio enhancement associated with the CME and the average brightness temperature are (32'.5 N,29' W) and $6.4 \times 10^5$ K respectively. The presence/absence of contours at locations other than the northwest limb in Figure 7, 8 and 9 indicate the transient activity going on there. . . . .	48
10	A composite of the radio difference images in Figure 7, 8 and 9 and the LASCO-EIT running difference image obtained at 05:30 UT. The half-power contour correspond to the structure of the radio CME at 05:05, 05:15 and 05:25 UT are shown with dash, dash-dot-dash and thick lines for clarity. The '+' mark indicates the centroid of the radio CME as earlier. . . . .	54
4	The Ray-Tracing technique in three-dimensions . . . . .	55
1	The schematic diagram explaining the concept of ray path in a medium of variable refractive index (varying from $\mu_1$ to $\mu_2$ ). $P_1$ and $P_2$ are slices of the cross-section of two spherical layers of the corona. The radius of them are $R$ and $R - dR$ ( $dR = 0.01 R_\odot$ here) respectively from the center of the Sun. $\mu_1$ is the refractive index to the right of the spherical layer $P_1$ and $\mu_2$ for the region between the layers $P_1$ and $P_2$ . $T_1$ and $T_2$ are two tangent planes to the above layers. The point of contact of $T_1$ and $T_2$ with $P_1$ and $P_2$ are $I_1$ and $I_2$ respectively. The normal vector $\vec{L}$ is calculated using the electron density gradient. As we know the coronal density distribution follows a spherical symmetry and falls off radially, the gradient will be radially inward and therefore $\vec{L}$ will be pointing outward in accordance with the definition. The trajectory/path of the ray is traced by sending $\vec{S}_1$ from $Q_1(x_1, y_1, z_1)$ towards $I_1$ where it gets refracted (as $\vec{S}_2$ ) and reaches $Q_2(x_2, y_2, z_2)$ by following the Snell's law. . . . .	61
2	The above diagram shows the trajectory of an unrefracted ray ( $\vec{S}_1 = \vec{S}_2$ ) at the point $I_1(4.0 R_\odot, 0.0 R_\odot, 0.0 R_\odot)$ . The ray travels unrefracted because the values of refractive index to the right and to the left of it are approximately equal ( <i>i.e.</i> , $\mu_1 \approx \mu_2 = 1.0$ ). The 'dashed' line with an arrow head represents the normal vector ( $\vec{L}$ ). The incident ray ( $\vec{S}_1$ ) starts at $Q_1$ and the refracted ray ( $\vec{S}_2$ ) ends at $Q_2$ . This is a typical example for normal incidence since $\vec{S}_1$ is anti-parallel to $\vec{L}$ (the angle between them are $180^\circ$ ). The ray of normal incidence is also called as the central ray (also it is the only ray that can reach the corresponding plasma layer). Refer Figure 1 for a more generalized situation of ray propagation. . . . .	64

- 3 The reflection of the ray near the layer where the refractive index is zero is explained in the above figure. The inner circle ( $R_1 = 1.0 R_\odot$ ) represents the photosphere and the outer dashed circle corresponds to the 109 MHz plasma layer. According to the density model of Newkirk (1961) the latter is at a height of  $1.22 R_\odot$  ( $R_2$ ) in the ‘undisturbed’ corona. The refractive index is  $\mu_1 (> 0.0)/\mu_2 (< 0.0)$  to the right/left of  $Q_n$  respectively. The dashed line with an arrow head is the normal vector  $\vec{L}$ . The thick line with a double sided arrow represent both the incident and the reflected ray ( $\vec{S}_1$  and  $\vec{S}_2$ ). The latter is drawn slightly away from the former for clarity. The magnitude of the emergent/reflected ray is equal to that of the incident ray but the direction is opposite, i.e. ( $\vec{S}_2 = -\vec{S}_1$ ). . . . . 68
- 4 The above figure explains the oblique incidence of a non-central ray. The inner thick circle represents the photosphere and the outer dashed circle corresponds to the plasma layer where the attenuation for the 109 MHz radiation will be maximum. The non-central ray is drawn ‘ $a R_\odot$ ’ (value of the impact parameter) away from the central ray (considered as reference) near the observer’s location ( $\approx 4 R_\odot$ ).  $\vec{S}_1$  is the incident ray vector and  $\vec{S}_2$  is the reflected ray vector. The normal vector ( $\vec{L}$ ) at any point on a spherically symmetric distribution will point outward in the radial direction. It is to be noted that the central ray has reached up to the plasma level whereas the non-central ray has not because the latter has undergone regular refraction and hence the reflection took place well above its corresponding plasma level near  $R_t$  (the turning point). The coordinates of the turning point for the ray which starts at  $Q_a(4.0 R_\odot, 0.5 R_\odot, 0.5 R_\odot)$  was obtained as  $R_t(1.045 R_\odot, 0.617 R_\odot, 0.612 R_\odot)$ . . . . . 71
- 5 The procedure that the computer program follows in estimating the accumulated optical depth along the complete ray path is shown in the above figure. The inner thick circle represents the photosphere and the outer dashed circle represents the 109 MHz plasma layer. The non-central ray is divided into 13 small segments with the vertical lines. The length of each segment ( $l_i$ ) is assumed as  $0.01 R_\odot$  (and is not according to the scale). The attenuation constant at the center of each segment ( $\alpha_i$ ) is calculated and multiplied with  $l_i$  to obtain the infinitesimal optical depth corresponding to that ray segment. The procedure is repeated for all the segments and total optical depth ( $\tau_{tot}$ ) is obtained by summing all  $\tau_i$ . . . . . 72

- 6 The top panel (a) shows the ray trajectories that reach different points on the image plane. The thick circle ( $R = 1 R_{\odot}$ ) represents the photosphere. A similar cross section of the 109 MHz plasma layer ( $R = 1.2 R_{\odot}$ ) is represented with the dashed circle. The north pole goes through the point 'O' and is perpendicular to the plane of the paper. East is to the left and west is to the right. The impact parameter 'a' is varied from  $-3.75 R_{\odot}$  to  $3.75 R_{\odot}$  along the east-west direction in steps of  $0.075 R_{\odot}$  (the spatial separation between adjacent points in GRH radio images). The thick circular arc ( $C_1C_2$ ) represents the locus of turning points of rays of different impact parameter. The bottom panel (b) shows a theoretically generated one dimensional brightness temperature distribution as a function of the impact parameter. The coordinates can be converted from linear to angular scale using the relation:  $1 R_{\odot}$  to  $16'$  (see Figure 7). . . . . 74
- 7 The contour map represents the simulated two dimensional brightness temperature distribution of the background corona at 109 MHz. The background density and temperature are assumed to be equal to  $(4.2 \times 10^4) \times 10^{4.32/r} \text{ cm}^{-3}$  and  $1.0 \times 10^6 \text{ K}$  respectively. The peak brightness temperature is  $\approx 1.0 \times 10^6 \text{ K}$  and the difference in temperature between successive contours is  $\sim 1.0 \times 10^5 \text{ K}$ . The region between any two successive/adjacent contours represent the region of equal intensity in the image plane (and hence in the sky plane). The north pole of the Sun is marked as 'N'. The direction west ('W') is to the right and East is to the left. The filled contour at the right bottom is the beam size of the GRH at 109 MHz. . . . . 76
- 8 The above figure explains the planar property of a central/non-central ray in the 'undisturbed' corona. The equatorial plane is marked as 'A' while the ray plane is marked as 'B'. The angle ( $\theta_p$ ) between the above two planes is  $\approx 135^\circ$ , which means that the set of points on the ray trajectory whose starting point is at  $Q_1(4.0 R_{\odot}, 0.5 R_{\odot}, 0.5 R_{\odot})$  will lie in plane 'B'. Therefore the planes of the rays with different starting points in the image plane will have different tilt angles with respect to the equatorial (or reference) plane. But, it has to be kept in mind that the trajectory will not lie in a plane if the density gradient of the background corona is altered by the enhancement/decrement of density due to coronal activity; The ray will deviate from the plane at the point where it encounters a density enhancement/decrement. . . . 78



9	The outer most contour (closed envelope) of the radio image observed with the GRH on November 24, 2000 is shown (refer Figure 6 in chapter 3). The eight long dashed contours inside the outer envelope of the observed brightness temperature represent the angular extents (both east-west and north-south) of the discrete radio structures. Their approximate centroids are marked from 1 to 8. The approximate centroids and the angular extents of the above discrete radio sources obtained by a visual inspection of the observed radioheliograms are used as the initial parameters in the ray-tracing program to reproduce the observed brightness temperature distribution. . . . .	80
10	Iso-density contours explaining the difference between the conical and Gaussian model (conical and Gaussian) for the density enhancement/decrement. In both panels [(a) and (b)] the center of the Sun is at ‘O’ and the solid line with an arrow head is pointing towards the location of the observer. The direction west is straight up and the north pole is perpendicular to the plane of the paper. Only the equatorial cross sections are shown here and the contours represent constant density/temperature (D/T) regions. (a) The D/T enhancement in Newkirk model assumes a conical/cylindrical distribution (in 3-D) whose axis (dashed line with an arrow head) makes an angle $\theta_0$ with respect to observer’s line of sight. (b) The Gaussian model is localized at $Q_i(x_i, y_i, z_i)$ and its size in all three directions are finite (resembles a sphere/ellipsoid in 3-D) and independent. The centroid of this closed structure from ‘O’ is at a distance of $R_i \left( = \sqrt{x_i^2 + y_i^2 + z_i^2} \right)$ .	83
11	Ray trajectory of a non-central ray in the presence of a density enhancement (marked as ‘E’). The inner thick circle represents the photosphere and the outer dashed circle corresponds to the background plasma layer at 109 MHz. The non-central ray is drawn ‘ $a R_\odot$ ’ away from the central ray that starts at a location $\approx 4 R_\odot$ (taken as reference) from the center of the Sun. $\vec{S}_1$ is the incident ray vector and $\vec{S}_2$ represents the emergent ray vector. $R_t$ is its turning point. Note that the ray trajectory before $R_t$ lies in the plane of the paper whereas the emergent ray is not (shown without an arrow head). . . . .	85
5	Meter wavelength observations and ray-tracing analysis of the pre-event phase of a coronal mass ejection . . . . .	86
1	White light image of the CME observed with the LASCO C2 coronagraph on June 2, 1998 at around 10:29 UT. Arrows labeled 1, 2 and 3 indicate the three-part structure (frontal structure, cavity and prominence respectively) of the CME. The open circle at the center is the solar limb. The outer circle is the occulter of C2 coronagraph. It extends approximately up to $2.2 R_\odot$ from the center of the Sun. . . .	87

2	Radio image of the solar corona obtained with the GRH around 07:30 UT on June 2, 1998. The peak brightness temperature is $\approx 1.4 \times 10^6$ K. The contours are in intervals of $1.4 \times 10^5$ K. The inner thick circle corresponds to the photosphere. The outer thick circle represents the approximate size of the C2 coronagraph occulter. Refer text for arc 'AB'. . . . .	89
3	LASCO-EIT running difference image [08:08-07:35 UT] showing two different CME associated activities ('W' and 'E') observed on June 2, 1998. The CME close to the west limb (W) is the event under study. . . . .	90
4	The reproduced brightness temperature distribution of the observed radioheliogram (Figure 2) using ray-tracing technique. The approximate locations where the density enhancements/decrements were introduced to fit the observation are marked with S1,...,S14. The parameters of the fitted radio structures are given in Table 1. . . . .	93
5	The absolute normalized difference ( $T_D$ ) between the observed brightness distribution (Figure 2) and its reproduction (Figure 4). The magnitude of difference at any particular location is obtained by multiplying the contour value there with the corresponding $T_{obs}(y, z)$ . . . . .	96
6	The average $T_D$ due to error in the $x$ -coordinate of density enhancement. The $z$ -coordinate is assumed to be $0.0 R_\odot$ for all $y$ . The solid and dashed line represent average $T_D$ for $\Delta x = \pm 0.1$ and $\pm 0.2 R_\odot$ , respectively. . . . .	98
7	Same as Figure 6. The solid and dashed lines represent average $T_D$ for $\Delta y = \pm 0.1$ and $0.2 R_\odot$ , respectively. . . . .	99
8	Same as Figure 6 and 7. The solid and dashed line represent average $T_D$ for $\Delta \sigma_x = \pm 0.1$ and $0.2 R_\odot$ , respectively. . . . .	101
9	Same as Figure 6, 7 and 8. The solid and dashed line represent $T_D$ for $\Delta \sigma_y = \pm 0.1$ and $0.2 R_\odot$ , respectively. This distribution also holds good for the change in $z$ -width ( $\Delta \sigma_z$ ). . . . .	102
10	Same as Figure 6 - 9. The solid and dashed line represent the average $T_D$ for $\Delta C_n = \pm 2.0$ and $\pm 4.0$ , respectively. . . . .	103
11	Same as Figure 6 - 10. The solid and dashed line represent average $T_D$ for $\Delta G_n = \pm 0.1$ and $\pm 0.2$ , respectively. . . . .	104
6	Estimation of the three-dimensional space speed of a coronal mass ejection using meter wavelength radio data . . . . .	111
1	Radioheliogram obtained with the GRH at 109 MHz on January 21, 1998 at 05:01 UT. The peak brightness temperature is $\sim 1.10 \times 10^6$ K and the contour interval is $1.1 \times 10^5$ K. The inner circle represents the solar limb and the outer circle corresponds approximately to the size of the occulter of the LASCO C2 coronagraph ( $\approx 2.2 R_\odot$ ). The filled contour near the bottom right corner is the GRH instrument beam at 109 MHz. . . . .	113
2	Same as Figure 1, but obtained at 06:01 UT. The peak brightness temperature is $\sim 1.20 \times 10^6$ K and the contour interval is $1.2 \times 10^5$ K. . . . .	114

3	Difference image obtained by subtracting the radioheliogram in Figure 1 (05:01 UT) from that in Figure 2 (06:01 UT). Only contours whose levels greater than 50% of the peak value are shown here. The brightness temperature of the enhanced emission above the limb in the southern hemisphere is $5.3 \times 10^5$ K. . . . .	115
4	Difference image (07:32-06:06 UT) of the ‘halo’ CME event observed with the LASCO C2 coronagraph on January 21, 1998. The inner open circle represents the solar limb. The outer filled circle is the occulting disk of the coronagraph. It extends approximately up to $2.2 R_{\odot}$ from the center of the Sun. Solar north is straight up and east is to the left. The CME under study can be noticed as a faint ring (indicated by the arrow marks) above the occulter of the coronagraph in the southern quadrant. . . . .	117
5	Radio brightness distribution of the Sun obtained through ray-tracing calculations of the GRH data obtained at 06:01 UT (Figure 2). The numbers S1-S16 indicate the location of the centroid of the discrete sources used to reproduce this image. Refer Table 1 for the values of different parameters used in the simulation. . . . .	118
6	Reproduced brightness temperature distribution corresponding to the radio sources S8 to S13 alone in Table 1. The brightness temperature of the CME is about $5.4 \times 10^5$ K. . . . .	120
7	Contours showing the normalized absolute difference obtained by subtracting Figure 6 from Figure 3. The maximum residual is about 9%. Some portion of the contours appear darker because the successive contours there are closely spaced. . . . .	121
7	Decameter wavelength observations of the Crab nebula and its angular broadening due to a coronal mass ejection . . . . .	132
1	Schematic showing the scattering of an electro-magnetic wave (traveling from $z < 0$ ) by density inhomogeneities (or scattering blobs) present in a thin slab (of thickness $\delta z$ ) located at $z = 0$ . The observer is at a distance L from the slab and receives the scattered radiation at an angle $\phi$ (scattering angle) w.r.t the incident direction. The $(x, y)$ -plane is perpendicular to the plane of the paper. . . . .	133
2	Radio map of the Crab nebula obtained with the GRH on June 3, 1997 at 50 MHz, when it was at a distance of $\approx 45 R_{\odot}$ from the center of the Sun (indicated by the arrow mark) The peak flux is $2287 \pm 200$ Jy, and the contour levels are 0.05, 0.15, 0.25, 0.35, 0.45, 0.55, 0.65, 0.75, and 0.85 times the peak flux. North is straight up, and east is to the left. The GRH beam at 50 MHz is shown in the bottom right-hand corner. . . . .	136

3	Same as Figure 2 but obtained on June 4, 1997 with the CME in the foreground at $41 R_{\odot}$ from the Sun. The peak flux is $1852 \pm 200$ Jy, and the contour levels are 0.1, 0.2, 0.3, 0.4, 0.5, 0.6, 0.7, 0.8, and 0.9 times the peak flux. One can see a noticeable broadening in the angular size of the Crab nebula both in radial and tangential directions. . . . .	137
4	Same as Figures 2 and 3 but obtained on June 5, 1997, when Crab nebula was at a distance of $\approx 37 R_{\odot}$ from the center of the Sun. The peak flux is $2287 \pm 200$ Jy, and the contour levels are 0.05, 0.15, 0.25, 0.35, 0.45, 0.55, 0.65, 0.75, and 0.85 times the peak flux. . . . .	138
5	LASCO C2-EIT running difference image of the CME observed on June 2, 1997. The occulting disk is at a distance of $2.2 R_{\odot}$ from the center of the Sun. The location of the CME (near the southeast limb) is indicated by the open rectangular box. North is straight up and east is to the left. The direction of the Crab ( $\sim 41 R_{\odot}$ from the center of the Sun) is indicated by the arrow mark. . . . .	139
8	Conclusions . . . . .	145

## APPENDIX

A	The Ray-Tracing Program . . . . .	161
---	-----------------------------------	-----

# CHAPTER 1

## CORONAL LARGE-SCALE STRUCTURES

### 1.1 INTRODUCTION

The large-scale structures in the solar corona are those whose typical sizes are comparable to or larger than the radius of the Sun [ $\approx 6.96 \times 10^5$  km = 1  $R_{\odot}$ ]. The coronal streamers, polar coronal holes and coronal mass ejections (CMEs) are some of them. The CMEs are the most widely studied among the above because of their importance in the context of *space weather* that deals with conditions on the Sun and in the near-Earth environment. Adverse conditions in the latter can lead to disruption of satellite operations, communications, navigation and electric power distribution grids, leading to a variety of socioeconomic losses [Lanzerotti (2004) and the references therein].

#### 1.1.1 Coronal Mass Ejections

The CMEs are large-scale transient explosions that occur in the outer atmosphere of the Sun. They contain huge mass ( $\sim 10^{15}$  g) of magnetically confined coronal material [Vourlidas et al. (2000)], which eventually get detached from the solar surface and enter the interplanetary space. The CMEs propagate outward through the ambient corona at speeds ranging from  $\sim 100$  to 2500 km/s [Manoharan et al. (2004)]. This implies that they can give rise to magneto-hydrodynamic (MHD) shocks in the corona. The typical Alfvén speed ( $V_A$ ) at the coronal base for magnetic field strength of 1 G and a density of  $\approx 5 \times 10^8$  cm $^{-3}$  is  $\sim 175$  km/s. The sound speed is about 110 km/s. However,  $V_A$  in active regions is much higher in the low corona. For a 100 G field (typical of flaring regions) and a density  $\sim 10^9$  cm $^{-3}$ , the  $V_A \approx 4000$  km/s [Gopalswamy et al. (2001a); Warmuth and Mann (2005)]. The CMEs that propagate faster than the Alfvén speed lead to fast and intermediate MHD shocks. The slower ones (faster than the sound speed but slower than the Alfvén speed) generate slow MHD shocks [Bougeret (1985); Steinolfson (1985); Mann (1995); Gopalswamy (2000c)]. The leading edge of the fast CMEs usually have outward speeds considerably greater than that associated with normal solar wind expansion (300-700 km/s) [Foukal (1990)]. The associated shock (ahead of the CME) accelerates coronal and solar wind particles (electrons, protons and ions) in the interplanetary medium to

very high energies [Roussev (2004)]. According to Gosling (1993), the major energetic particles observed in the near Earth space environment are produced by such CME driven interplanetary shocks. The two primary geo-space consequences of CMEs are the solar energetic particles [SEPs; refer Reames (1999) and Tylka (2001)] and geomagnetic storms (GMS). The former depends on the energy budget of CMEs and the latter on their structure. The first effect of CMEs in the geo-space is the arrival of SEPs within a few minutes after the eruption, followed by the arrival of MHD shocks and the CME that drives it [Gosling (1993)]. This is because fast CMEs drive MHD shocks, which in turn accelerates the particles. SEPs pose a severe radiation hazard in the geo-space. They can penetrate space suits of astronauts, destroy living cells and potentially cause cancer. They also pose a major problem to spacecraft microelectronics and solar panels [Luhmann (1997); Lanzerotti (2004)]. When the aforementioned energetic particles enter into the Earth's magnetosphere, they induce ionospheric and ground currents. The latter are collectively called 'geomagnetic storms'. Their effects are rather harmful. GMS occur when the CME associated interplanetary magnetic field (IPMF) impinges upon the Earth's magnetosphere and reconnect [Dungey (1961)]. Since the geomagnetic field is directed northward, the IPMF needs to have a southward component for reconnection and subsequent injection of CME driven energetic particles into the Earth's atmosphere.

The discovery as well as most of our present understanding of CMEs are mainly from observations with white-light coronagraphs, instruments that are specially designed for imaging the solar corona using the scattered photospheric light. Its essential component is the occulter, a circular disk whose diameter subtends an angle slightly larger than that subtended by the equatorial diameter of the photosphere at the location of the observer. It produces an artificial eclipse by occulting both photosphere as well as chromosphere and allows us to study the white light emission from the corona. The CME discovery came in 1971 from images obtained with the coronagraph in OSO-7, orbiting our planet then [Tousey (1973)]. CMEs got immediate attention of many solar physicists because of their conspicuous bright appearance against the dark background, large spatial extent, highly transient nature, rapid expansion and their eventual disappearance. Many proposals demanding large coronagraphic databases led to the launch of new space-borne instruments soon after the discovery. *Skylab* was the immediate one launched in 1974 [MacQueen (1974)] and it gave a preliminary report on CME properties [Gosling et al. (1974)]. Observations

from *Solwind* [Michels (1980)], *Solar Maximum Mission* [SMM; MacQueen (1980)] and the most recent *Large Angle Spectrometric COronagraph* [LASCO; Brueckner et al. (1995)] on board the *Solar and Heliospheric Observatory* [SOHO; Fleck et al. (1995)] have enriched our knowledge of CMEs. Since the coronagraph in each mission has its own scientific objective and instrumental design, the characteristics of the occulter vary from one mission to another to meet the desired requirements. For example, the coronagraph in SMM imaged the corona from  $1.6 - 6.0 R_{\odot}$  with a resolution of  $10''$ , and the LASCO that is presently in operation has three different coronagraphs C1, C2 and C3. Their respective field of view are 1.1-3.0, 1.7-6.0, and 3.7-32.0  $R_{\odot}$ . and they image different regions of the corona simultaneously.

## 1.2 CORONAGRAPHIC OBSERVATIONS

Though one can witness many shapes or external appearances of ejections in white-light coronagraphic images [Sheeley et al. (1982); Munro & Sime (1984); Howard et al. (1985)], a typical CME is the one which has a bulb or balloon-like structure during its initial stages before eruption. Figure 1 shows one such CME observed with the LASCO C2 coronagraph on January 18, 2000. The bright ring like structure at a distance of  $\approx 5 R_{\odot}$  from the center of the Sun is the frontal structure or leading edge. It is presumed to contain a large fraction of the CME mass and is at coronal temperature  $\sim 10^5$  K [Gopalswamy and Kundu (1992); Ramesh et al. (2003)]. The two ends of the ring (or the foot points) hidden in the shadow region of the occulter, are anchored to the photosphere. The moderately thick inner bright feature at the center of the foot points is the prominence core. It contains cool chromospheric material of temperature  $\sim 10^4$  K and can be observed in microwave [Gopalswamy et al. (1997); Gopalswamy and Hanaoka (1998)] and ultra-violet [Akmal et al. (2001)] wavelength range. The relatively darker region between the frontal loop and the underlying prominence core is the cavity. The above are the three familiar parts of a typical CME. While most of the CMEs appear in the above form [Hundhausen (1988)], there are exceptions. According to Gopalswamy (2000b) and Michalek (2003), the difference arises mainly because of their position/orientation relative to the observer's line of sight or in other words it is an effect of projection. However, in a few cases it could either be due to the complex configuration of the magnetic field present in the vicinity of the eruption location or the nature of drivers triggering such eruptions. The other bright radial features off the occulter in Figure 1 are the relatively stable and long lived coronal

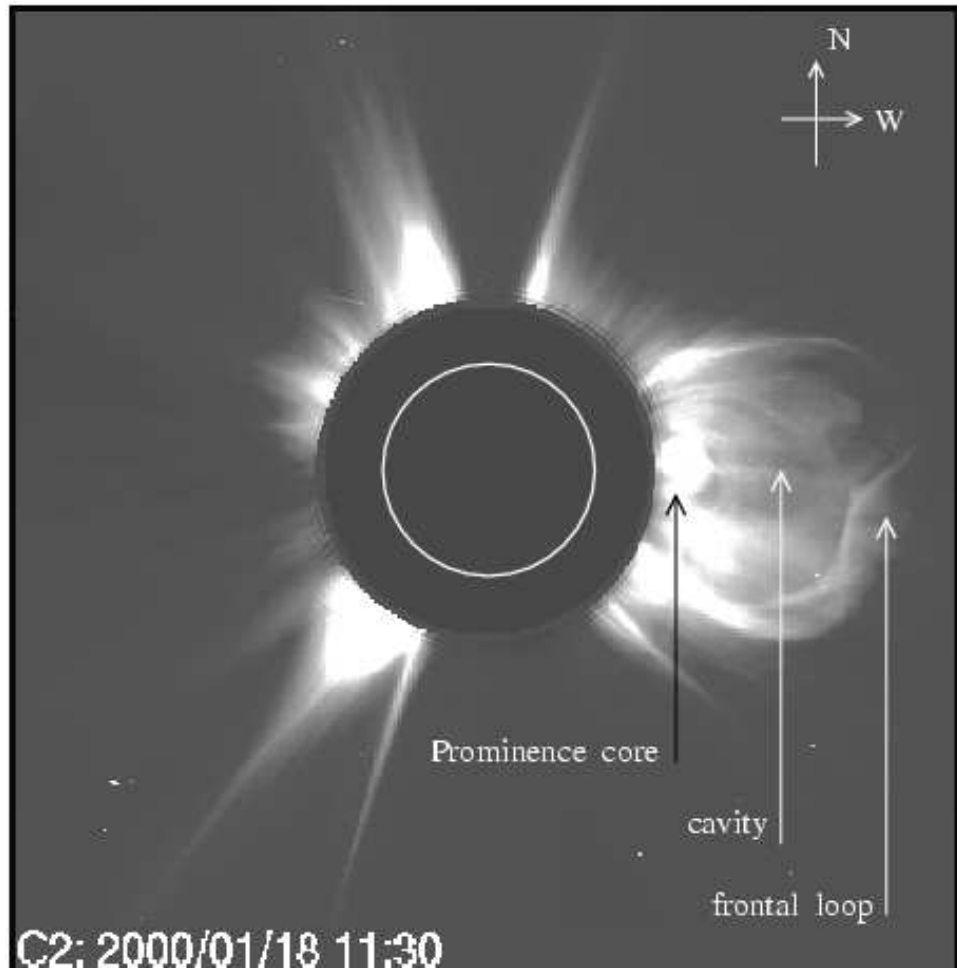


FIG. 1: A typical CME observed with the LASCO C2 coronagraph on January 18, 2000. The black circular region is the occulter of the coronagraph and the white inner circle represents the solar limb (photosphere). North is straight up and east is to the left. The frontal structure, cavity and the bright core (corresponding to the underlying prominence), are clearly visible above the occulting disk in the western hemisphere. The other bright structures in the image are stable and long lived coronal helmet streamers.



streamers.

### 1.2.1 Evolution of a CME

A typical CME in white-light reveal three phases of evolution. They are,

#### (a) The pre-ejection phase

Figure 2(a) shows the pre-ejection state of a typical CME observed with the LASCO C2 coronagraph on board SOHO. The image was obtained at 10:30 UT on January 18, 2000. The top of the helmet streamer is located at a radial distance of  $\approx 3.0 R_{\odot}$ . By 10:54 UT, the structure has considerably expanded and also moved to a distance of  $\approx 3.8 R_{\odot}$  [Figure 2(b)]. This phase is called the ‘pre-ejection swelling of the coronal helmet streamer’. The swelling time scale is event dependent and in many cases it lies in the range of a few days [Hundhausen (1997)]. CMEs that swell before ejection have the well known three-part structure [Hundhausen (1988)], and it is evident in the present example also [Figure 2(b)].

#### (b) The propagation phase

The images (c) and (d) of Figure 2 shows the evolution of the helmet streamer as well as the prominence, after the pre-ejection phase. Note that the top of the streamer is now at a height of approximately  $5 R_{\odot}$  from the center. This image was obtained at 11:30 UT on the same day. The streamer has enlarged both in the radial and lateral directions leading to a bulb-like appearance. The cavity beneath the frontal structure has also expanded with the latter. But the structural changes of the prominence core is at a slower rate as compared to the above two. This can be seen from the image taken at 11:54 UT [Figure 2(d)]. The foot points of the leading edge rooted to the solar surface constrains the coronal plasma from expanding into the heliosphere [Gosling et al. (1974); Munro (1979)]. But the stress built up eventually breaks or opens up the frontal structure/top portion of the streamer and the confined mass is expelled into the interplanetary space with considerable momentum.

#### (c) The post-ejection phase

This is the stage during which the mass confined by the frontal structure of the CME gets almost fully detached from the solar surface. Though it is difficult to detect such a disconnection after the mass ejection, theories claim that it is inevitable to maintain

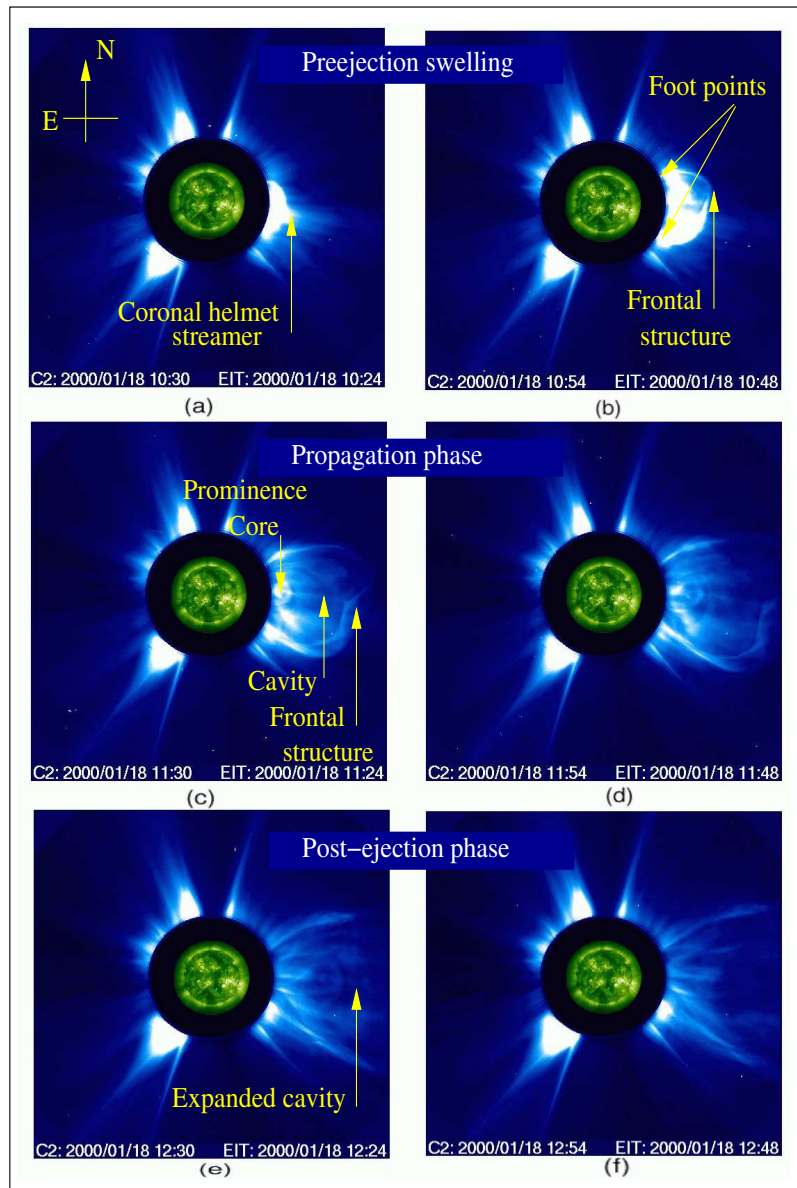


FIG. 2: Images showing the different stages of evolution of the Coronal Mass Ejection observed on January 18, 2000 with the LASCO C2 Coronagraph. The images (a) and (b) in the top row show the pre-eruption swelling of the coronal helmet streamer before the onset of CME. Those in second row [(c) and (d)] describe the motion of the frontal structure, expanded cavity and the core. The post-ejection phase of the CME (i.e. the stage after the complete lift-off of the frontal structure) is shown in image (e) and (f) [bottom row].

the magnetic flux balance far from the Sun [Gosling et al. (1975)]. Note that one can see only the faint foot points of the frontal structure in the images at the bottom row [Figure 2 (e) and (f)]. The bright core or the prominence is also not visible since the CME structures have crossed the LASCO field of view. The intensity at the location of CME features in the plane of the sky has reduced and become almost equal to that of the background. New magnetic loops are supposed to form at the location of the CME during the post-ejection phase. The long duration flares observed in soft X-rays are an indication of the above [Sheeley et al. (1975); Webb et al. (1976); Kahler (1977)]. Figure 3 shows a cartoon of the various stages in the evolution of a typical white light CME.

### 1.2.2 Characteristics of CMEs

#### (a) Mass

The CME material is mostly of coronal origin [Hildner et al. (1975)]. However, Gilbert et al. (2000) report that some of the CMEs contain the associated eruptive prominence material also. The white-light observations show that the mass of a typical CME lie in the range  $\approx 10^{14} - 10^{16}$  g [Gosling et al. (1974); Hildner (1977); Howard et al. (1984); Hundhausen (1988); Vourlidas et al. (2000); Burkepile et al. (2004)]. Images obtained with the soft X-ray telescope on board Yohkoh [Tsuneta et al. (1991)] frequently show ‘dimming’ at the location of CME eruption on the disk [Hudson et al. (1998)]. In one case study, Sterling and Hudson (1997) showed that the mass depletion ( $\approx 2 \times 10^{14}$  g) associated with a X-ray dimming near the foot of a preflare S-shaped active region structure is of the same order as the mass of the CME observed in white light coronagraphic images. Gopalswamy and Kundu (1992), Ramesh et al. (2003) report mass values  $\sim 10^{15} - 10^{16}$  g through meter wavelength radio observations of white light CMEs.

#### (b) Position Angle and Angular Width

The CMEs are identified by their position angle (P.A.) and projected size in the plane of the sky, determined from the white-light coronagraphic images. The P.A. of a CME is the angular distance between the reference axis (a hypothetical line that join the north pole and the center of the Sun) and the mid point between the foot points of its frontal structure. The width of a CME is the angular extent between its foot points. Both P.A. and width are measured in degrees (refer Figure 4 for details). In the past, the projected latitudes of CMEs were used to determine the true values. The error in

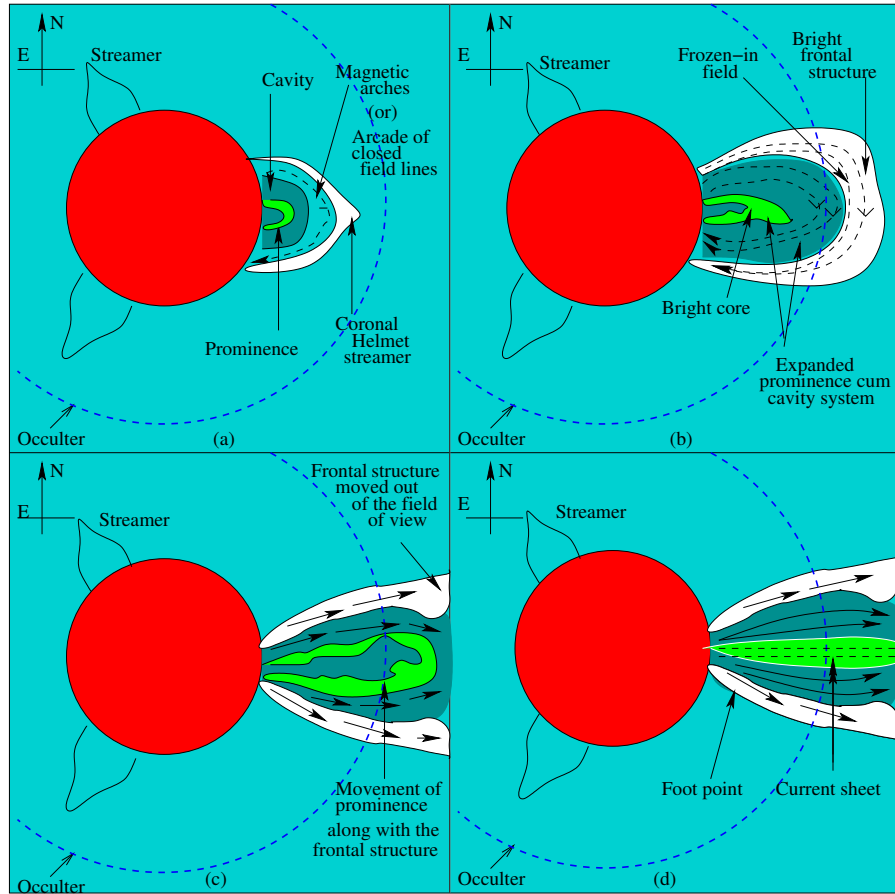


FIG. 3: Cartoon showing the evolution of a typical CME. The circular disk (radius  $\approx 1 R_{\odot}$ ) represents the photosphere. The dotted arc (Radius  $\approx 2.2 R_{\odot}$ ) in all the panels represents the location of the LASCOC2 occulter. The conical structures above the solar limb in the Eastern hemisphere are stable coronal streamers. (a) The pre-eruption coronal helmet streamer (white outer structure) and the underlying prominence (slightly darker inner loop). The darker region between the above mentioned structures is the cavity. (b) The formation of a typical three-part (*i.e.*, *frontal structure*, *underlying dark cavity* and *the prominence core*) CME from the coronal helmet streamer. (c) During propagation the CME transports both the coronal material and frozen-in magnetic field into the interplanetary medium. (d) The formation of neutral current sheet in the aftermath of the CME eruption [Ko (2003)].

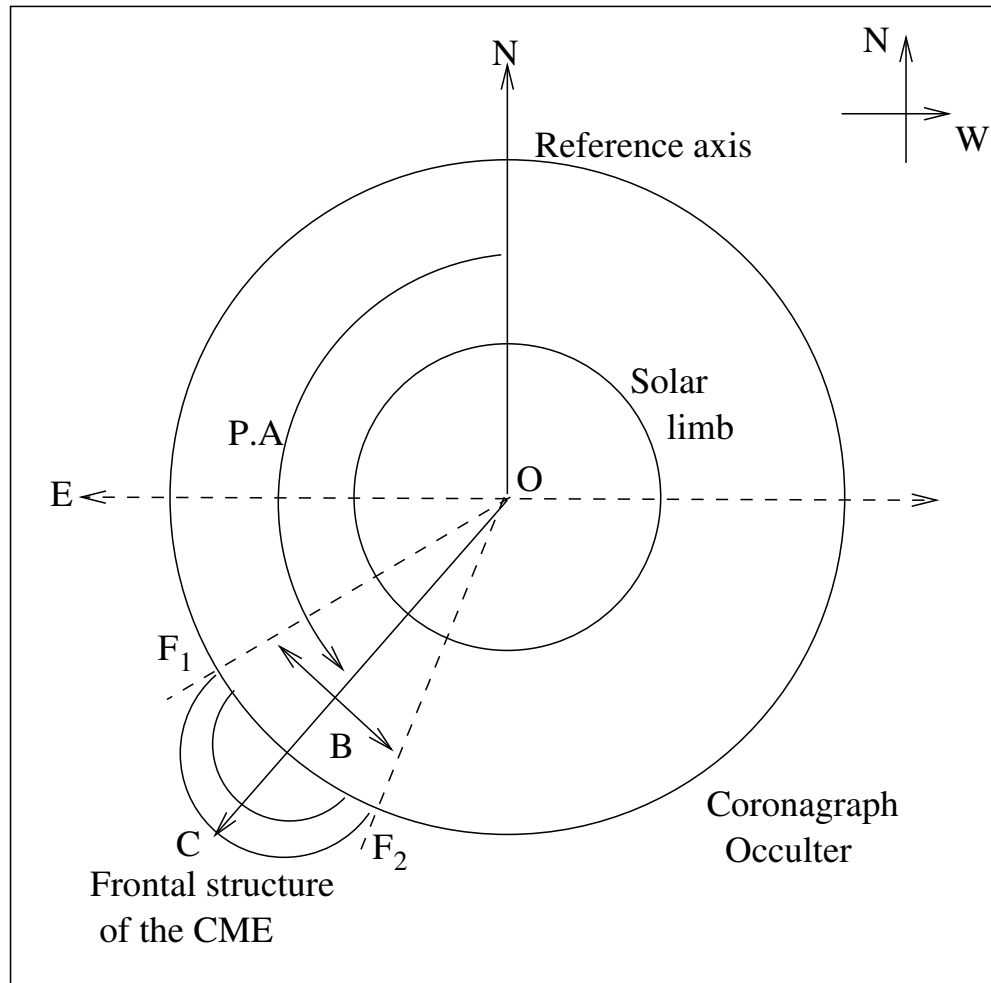


FIG. 4: The width (B) and position angle (P.A.) of a CME. The former is the angular extent between the foot-points  $F_1$  and  $F_2$ . The P.A. is the angular distance of the line OC from the solar north (the reference axis) measured through the East. The line OC joins the center of the Sun (O) and the mid point of the frontal structure/leading edge of the CME (C). Both 'B' and 'P.A.' are measured in degrees.

such measurements depend on latitude of ejection. Hundhausen (1993) pointed out that the error due to the aforementioned effects are smaller for eruptions near the equator and larger for those greater than  $\sim 60^\circ$ . Again, assigning P.A. to CMEs that originate from near the disk center will be difficult. Therefore the above position angle discussion is generally valid only for events close to the limb. Hundhausen (1993) found an average value of  $\approx 55^\circ$  for the angular width of the frontal structure of CMEs observed with Skylab and SMM coronagraphs. The average width of all the other mass ejection features (cavity and the core) was lesser than that of the former and was  $\sim 47^\circ$ . McAllister et al. (1996) demonstrated that CMEs often have substantial longitudinal extents, covering as much as  $180^\circ$  in longitude, or more, on occasions. A statistical study of all SOHO-LASCO CMEs (both halo as well as non-halo CMEs) carried out by St. Cyr et al. (2000) for the events observed between January 1996 and June 1998 indicate a comparatively large width ( $\sim 72^\circ$ ). The authors attribute the latter to the detection of comparatively large number of partial and full ‘halo’ CMEs. But if one considers only the non-halo LASCO CMEs, then the average width is  $\approx 58^\circ$  [Gopalswamy et al. (2001c)].

### (c) Kinematics of a CME

The kinematics of CME features above the coronagraph occulter are usually inferred from time sequence images. The velocity and acceleration of a CME at any instant can be determined from the height-time plot generated using a set of images observed over a specific interval of time. Figure 5 shows the height-time plot of the CME front observed on January 18, 2000 (set of images in Figure 2). The first order fit gives an average speed of  $\approx 642 \text{ km s}^{-1}$ , in the range 3-30  $R_\odot$ . However, a second order fit to the same set of measurements indicate that the velocity of the CME has considerably reduced over a period of time [Figure 6(a) and (b)]. The estimated deceleration is  $11 \text{ m s}^{-2}$ . The preliminary results of Skylab [Gosling et al. (1976)], Solwind [Howard et al. (1986)] and SMM [Burkepile and St. Cyr (1993); Burkepile et al. (2004)] observations showed that the apparent speed of CMEs range from 80 to  $1050 \text{ km s}^{-1}$  and the average speed is around  $450 \text{ km s}^{-1}$ . But the individual annual speed distributions were found to differ drastically from the over all distribution. St. Cyr et al. (2000) determined the average speed of all the CMEs (inclusive of both halo and non-halo CMEs) observed with the SOHO-LASCO during 1996-1998 and the average value was  $\approx 424 \text{ km s}^{-1}$ . This is in good agreement with the value

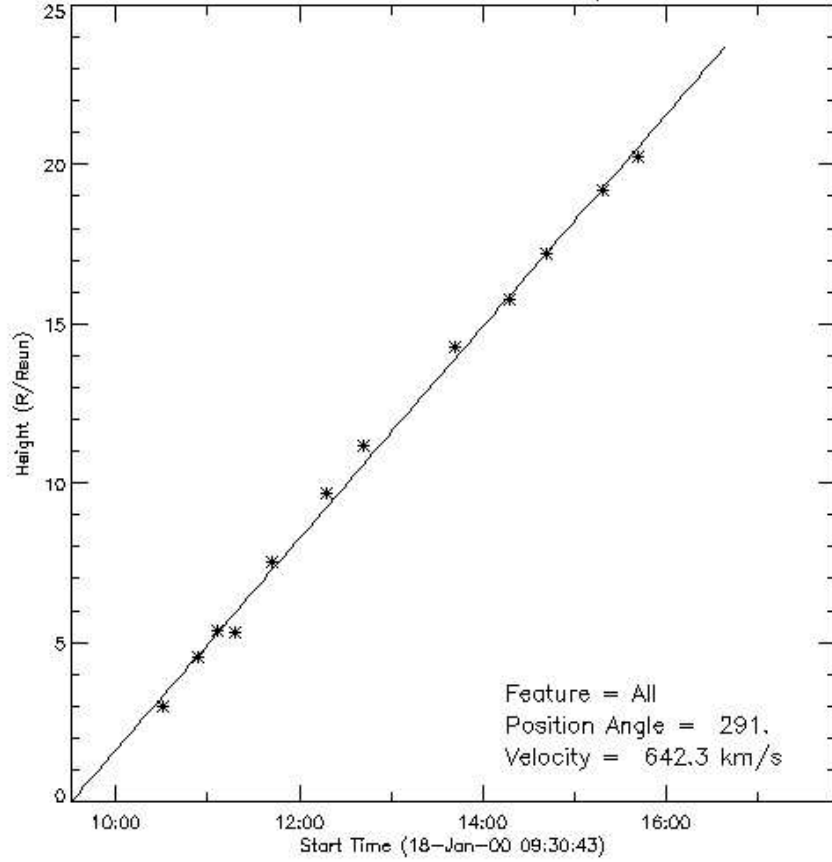


FIG. 5: Height-time plot of the CME observed on January 18, 2000 with the LASCO C2 coronagraph. Each point in the graph represents the location of the CME front (height in units of solar radius from the center of the Sun) at different epoch. The initial and final height measurements were made close to 2 and 21  $R_{\odot}$ , respectively. The first order fit to the above set of points gives a value of  $\approx 643 \text{ km s}^{-1}$  for the velocity of the CME. The  $y$ -intercept of the fitted line at 1  $R_{\odot}$  is the onset time of the CME and is 09:30:43 UT in the present case.

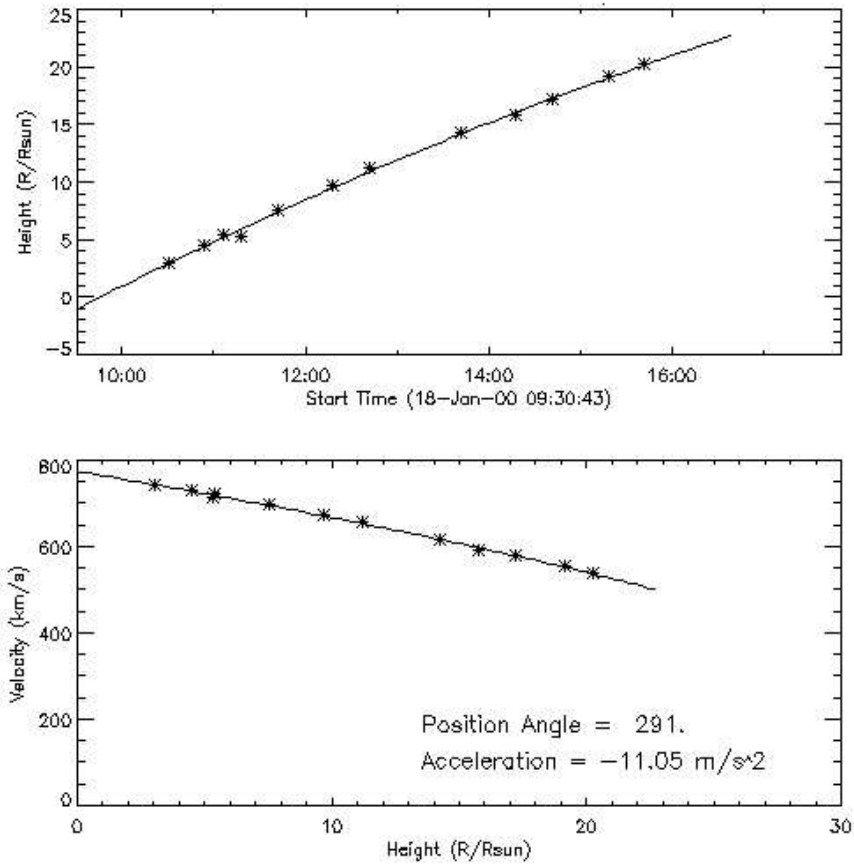


FIG. 6: The graph on the top shows the second order fit for the same set of points in Figure 5. The graph at the bottom shows the velocity of the CME front as a function of radial distance from the center of the Sun. It is evident that the CME has decelerated at a rate of  $\approx 11 \text{ m s}^{-2}$ .



reported using coronagraphs on board Skylab and SMM mission. A similar work was carried out by Gopalswamy et al. (2001b) for the SOHO-LASCO CMEs during the period 1996-2000 and that were associated with type-II radio bursts observed with the WIND-WAVES [Bougeret et al. (1995)] instrument in the decameter-hectometer wavelength range. The minimum and maximum speed were 241 and 2519 km/s. The average value was 961 km/s. For the limb CMEs, the range was 356-2221 km/s and the average was 1144 km/s. Note that the latter have minimal projection effect and hence a comparatively larger value.

### 1.3 NON-CORONAGRAPHIC OBSERVATIONS

It is difficult to determine the properties of a CME in the low corona ( $\leq 2 R_{\odot}$ ) from white light observations because of the occulting disk in the coronagraph. Hence observing instruments free from such limitation play an important role particularly in the study of CMEs. Also, since the corona is realized as a black body at a temperature of  $\sim 10^6$  K, thermal emission following Planck's distribution is expected. This implies that the corona as well as CMEs can be observed in other wavelengths also.  $H\alpha$  pictures were the primary source of information on CMEs in the past [Fisher et al. (1981); Low et al. (1982)].  $H\alpha$  flares and filament/prominence eruptions are the two types of events that are often observed in association with CMEs. Eruptive prominences were later identified as the innermost substructures of CMEs [Illing and Hundhausen (1985)]. The frontal structure of a CME contains material which is mostly coronal in origin [Wagner (1984)], and hence cannot be observed using  $H\alpha$  filtergrams. Soft X-ray images obtained with the Skylab mission revealed new details of the early phase of CMEs in the form of transient coronal holes [Rust (1983)], and post-eruption arcades [Kahler (1977)]. The Yohkoh mission [Tsuneta et al. (1991)] confirmed all the results of Skylab mission and provided additional clarity. The giant arches reported by Svestka et al. (1995) provide possible evidence for large scale restructuring associated with CMEs. The X-ray dimmings [Hudson et al. (1998)] gave a new insight into the origin of CMEs in the low corona. The X-ray observations also sometimes show faint large scale global brightenings [Gopalswamy (1999)]. After the advent of SOHO's *Extreme-Ultraviolet Imaging Telescope* [EIT; Delaboudinière et al. (1995)], a closer link between CMEs and early near surface activities has been established [Gopalswamy (1999); Hudson (1999); Thompson et al. (1999); Gopalswamy and Thompson (2000a)]. One of the most interesting phenomenon discovered in the last

decade is the coronal EIT waves. These events originate in volumes comparable to that of the associated flare or active region. This suggests a flare origin, but the EIT waves also appear to be highly associated with CMEs [Thompson et al. (1998, 1999)].

The radio observations also play a useful role in the study of CMEs since the solar corona above the disk as well as off the limb can be imaged simultaneously. Therefore, one can observe the initiation of the ejection close to the solar surface. An added advantage is that we do not have to worry about sky conditions. Again, radio observations of thermal plasma are sensitive to a broad range of temperature, from chromosphere to corona, because of the  $T^{-1/2}$  dependence of radio emissivity. Also, observations at radio wavelengths are sensitive to non-thermal electrons [Bastian and Gary (1997)]. White light coronagraphs detect the photospheric light scattered by the CMEs and hence provide information on the density distribution of thermal electrons contained in a CME. These thermal electrons also emit detectable bremsstrahlung radiation at meter-decameter radio wavelengths [Sheridan et al. (1978); Gopalswamy and Kundu (1992)]. Since emission from the undisturbed Sun in the above wavelength range is due to thermal bremsstrahlung from the hot coronal plasma, a change in thermal emission describe changes taking place in the macroscopic parameters of the plasma. Therefore, the enhanced bremsstrahlung emission can be attributed to the density enhancement corresponding to the CME. Again, the radio brightness (due to thermal bremsstrahlung) in optically thin regions above the limb is directly proportional to the electron density and path length according to  $\int N_e^2 ds$ . The white light radiance is directly proportional to  $\int N_e ds$ . Thus an excess radio brightness indicates density enhancement in the corona. However, thermal emission is usually masked by a wide variety of non-thermal radio bursts that accompany the CME.

Hildner et al. (1987) provided a summary of early work on moving Type-IV burst continuum, and the shock associated Type-II radio burst. Aurass (1997) reviewed common aspects of coronal shocks and CMEs, as well as non-thermal radio signatures of CMEs. Kerdraon et al. (1983) found that solar radio storms spatially correlate with the appearance of CME associated additional mass in the corona. In a recent statistical study, Ramesh and Sundaram (2001b) pointed out possible temporal correlation between noise storms and CMEs. Ramesh and Ebenezer (2001c) reported a transient intensity reduction/absorption burst at decameter wavelength in close temporal association with the onset of a halo CME. The size of the absorption region was estimated to be 28,000 km. In this connection we would like to point Dere et

al. (1997) observed a CME that originated in a compact ( $< 10^5$  km) source. But, note that one needs fast radio imaging capabilities to understand the coronal changes resulting from activities associated with the onset of a CME [Pick (1998a); Pick et al. (1998b); Maia et al. (1998); Aurass et al. (1999); Pohjolainen et al. (2001)]. For flare-CME events, the evolution is extremely fast of the order of a few minutes. One needs to identify the successive sequences in the evolution of coronal restructuring leading to the full development of the CME as shown by Maia et al. (1998), Pick (1998a). A study of these radio bursts and their emission mechanism(s) provide information on the non-thermal particles, the magnetic field strength and sometimes the structure of the magnetic field involved. Bastian et al. (2000) report the imaging of a CME at decimeter and meter wavelengths and in white light using the NRH and the LASCO experiment respectively. The authors show that the CME expanding arches are illuminated by  $\sim 0.5$ -5 MeV electrons emitting synchrotron radiation in a  $\sim 0.2$  G magnetic field, and that these particles could have been produced during the associated flare. Such observations provide independent diagnostics of the CME magnetic field as well as of the ambient electron density. The *Nobeyama Radioheliograph* [NoRH; Nakajima (1994)] has turned out to be a very useful instrument to study the early life of CMEs. Several interesting results on the association between eruptive prominences and CMEs have been reported in the literature [Gopalswamy et al. (1997); Gopalswamy and Hanaoka (1998)]. The proposed *Frequency Agile Solar Radiotelescope* (FASR) array is expected to provide new information on eruptive solar activities [Bastian (2003); Gary (2003); Bastian (2004)]. This instrument will consist of about 100 antennas, and will detect solar radiation in the 0.3-3.0 GHz frequency range, with high angular, temporal and spectral resolution. FASR will essentially address solar flare physics and active region magnetic structure questions. Combined with other existing radio facilities like the *Nancay Radioheliograph* [NRH; Kerdraon and Delouis (1997)] and the *Gauribidanur Radioheliograph* [GRH; Ramesh et al. (1998)], FASR will be very suitable to study the initiation and other aspects of CMEs at low frequencies.

### 1.3.1 Radio Observations

This thesis describes low frequency observations of CMEs particularly in the low corona ( $\leq 3 R_{\odot}$ ) with the GRH (30-110 MHz). An examination of the brightness distribution of the Sun in the above range reveals different kinds of emission features

which vary very widely in time scales. One can broadly classify them into two main streams, namely (1) the transient non-thermal events and (2) the thermal emission from the disturbed and undisturbed Sun.

**(a) The transient events**

The transient events are sudden enhancements in the observed brightness temperature and they last approximately for a few seconds to minutes. Their emission mechanism is non-thermal in nature and the observed  $T_b$  often exceeds  $10^7$  K. They are due to the rapid release of different forms of energy into the solar corona from the layers beneath it. These events are called radio bursts and are classified as Type II, III, V, U and so on, depending on their drift-rates and durations. One can clearly make out these different types using radiospectrograms, which contain information on the intensity as a function of time and frequency (generally over a large bandwidth). The signatures of the radio bursts cover a certain bandwidth ( $\Delta f$  Hz) over a specific period of time ( $\Delta t$  s). The ratio  $\Delta f/\Delta t$  distinguishes different types of bursts [Wild et al. (1963, 1972); Dulk (1985); Bastian et al. (1998)].

**(b) The ‘undisturbed’ Sun**

The concept of quiet Sun at radio frequencies came into existence, after Pawsey and Yabsley (1949) studied the radio flux over a wide frequency range to understand the radiation characteristics of the Sun. They indicated the existence of a relatively constant component whose intensity pattern resembled Martyn’s model for thermal radiation [Martyn (1946, 1948)]. By definition, the Sun is said to be ‘undisturbed’ at radio frequencies when there are no contributions from the transient events and slowly varying components to the observed brightness distribution. The brightness distribution of the ‘undisturbed’ Sun was computed theoretically from centimeter to meter wavelengths for the first time by Smerd (1950). During the ‘undisturbed’ period, the latter is generally symmetric and resembles a Gaussian, especially at meter wavelengths. Smerd assumed a spherically symmetric corona to derive the solution for the radiative transfer equation for an ionized medium by numerical integration.

### (c) The ‘disturbed’ Sun

The existence of density enhancements overlying sunspot regions, active filaments make the corona asymmetric and one has to take recourse in a more involved ray-tracing technique to derive the brightness distribution. Such calculations were carried out by Newkirk (1961) and he derived the brightness profiles at  $\lambda = 21$  cm. Sastry et al. (1981; 1983) used a ray-tracing technique similar to that of the latter to explain the one-dimensional brightness distribution observed by them in the decameter wavelength range. Recently, the above scheme was extended to the analysis of an observed two-dimensional thermal radio brightness distribution during the pre-event stage of a CME [Kathiravan et al. (2002)]. In this respect, imaging observations particularly at frequencies  $\leq 110$  MHz play a useful role since CMEs can be noticed with comparatively better contrast, particularly near the limb. The observed brightness temperature of the background corona there is usually less compared to the coronal electron temperature [refer Ramesh (2004) for a review on the topic]. Apart from features above the solar limb, one can also observe activity on the disk similar to X-ray and EUV wavelengths [Ramesh (2000b)]. The density depletions observed in the white light coronagraph images (in the aftermath of the CME lift-off) sometimes give rise to short lived coronal hole ( $\sim 1$  day) in the low frequency radio images [Ramesh and Sastry (2000a)]. In addition to direct imaging, ray-tracing analysis of the thermal radio counterpart of a CME also play a vital role since the position of the associated density enhancement and its speed in a three-dimensional space can be derived [Kathiravan and Ramesh (2004, 2005)]. One can also use imaging observations of the apparent angular broadening of a distant cosmic source when the radio waves from it undergo scattering while happen to pass through a CME, to infer the characteristics of the latter at large distances from the Sun [Ramesh et al. (2001a)].

## CHAPTER 2

### THE GAURIBIDANUR RADIOHELIOGRAPH

#### 2.1 INTRODUCTION

The principal objective behind the construction of the Gauribidanur Radioheliograph is to make two dimensional images of the solar corona simultaneously at many frequencies in the 30-150 MHz range [GRH; Ramesh et al. (1998); Ramesh (1998b)]. After the closing down of the Clark Lake Radioheliograph [CLRH; Kundu et al. (1983)] and the Culgoora Radioheliograph [CRH; Wild et al. (1967)], there are no other instruments in operation for imaging the solar corona in the above frequency range. The GRH is a T-shaped interferometer array with the long arm (1280 m) in the E-W direction and the short arm (441 m) in the South direction. The Latitude and Longitude of the mid-point of the array are  $13^{\circ}36'12''$  and  $77^{\circ}27'07''$  respectively. The Log periodic dipole (LPD) was chosen as the basic receiving element because of its wide frequency coverage [Isbell (1960)]. Figure 1 shows the structural design of the LPD used in the GRH. It is a collection of several dipoles made of aluminium tubes of different length attached to a common rod (the main 'boom'). The stacking of dipoles is such that the ratio of length( $l$ ) of adjacent elements as well as that of their spacing ( $d$ ) is a constant, i.e.

$$\frac{l_{i+1}}{l_i} = \frac{d_{i+1}}{d_i} = k \quad . \quad (1)$$

This leads to the electrical characteristics of the antenna vary logarithmically as a function of frequency and hence the name LPD [Kraus (1988)]. The collecting area ( $A_e$ ) of the LPD in the GRH is  $0.5 \lambda^2$  and it responds to frequencies in the range 30-150 MHz. The lengths of individual dipoles and spacing between adjacent elements are given in Table 1. The voltage developed due to the RF signal incident on each LPD is tapped from its top using a coaxial cable. The characteristic impedance ( $Z_0$ ) of the antenna is  $50 \Omega$  and the voltage standing wave ratio (VSWR) is  $< 2$  in the above frequency range. The directional gain of each LPD is  $\approx 8$  dB. The observed beam pattern along the E-plane<sup>1</sup> and H-plane of the LPD used in the GRH array

---

<sup>1</sup>E-plane is along the arms of the LPD and H-plane is perpendicular to it.

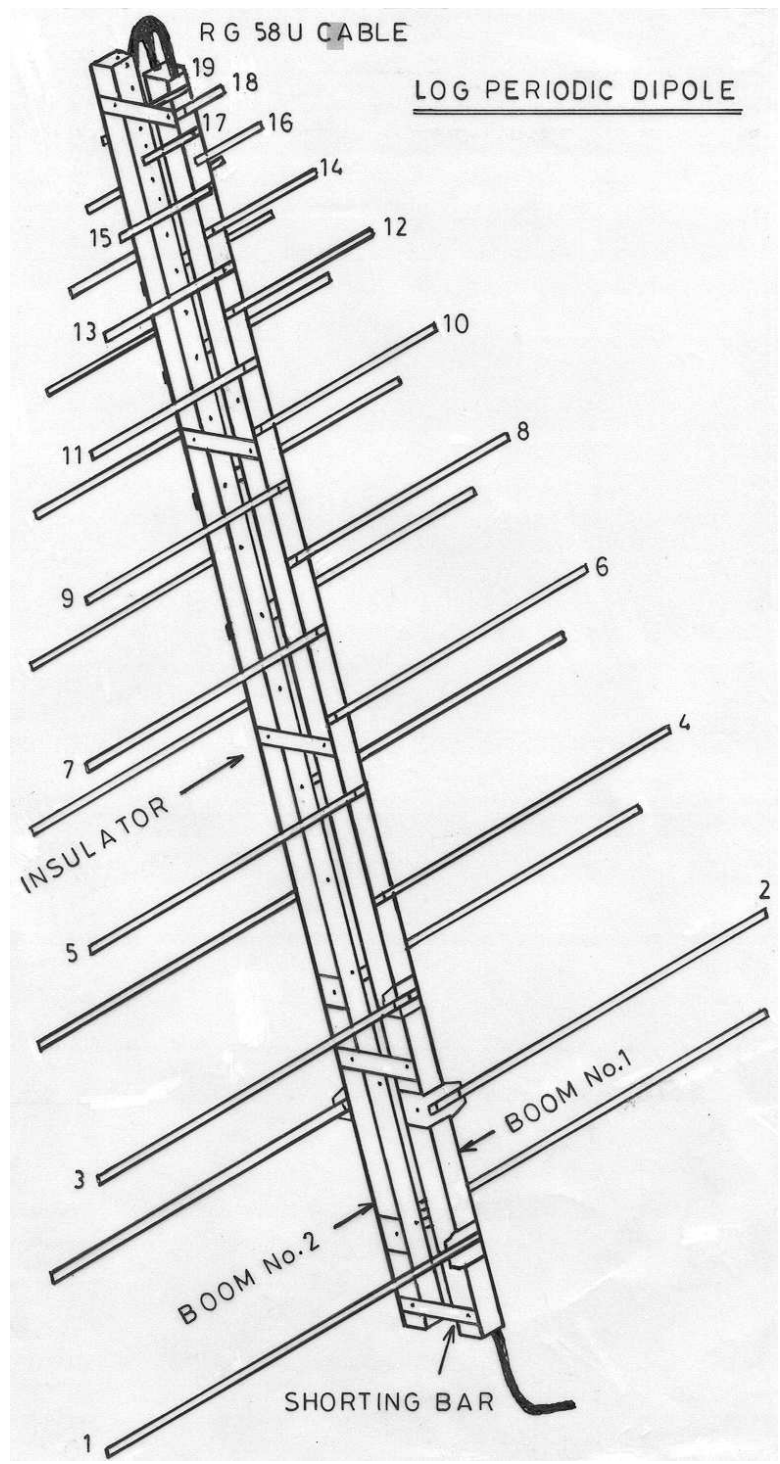


FIG. 1: Structure of the log periodic dipole (LPD) used in the GRH array.

TABLE 1: Antenna parameters

Dipole number	Length (in cm)	Dipole numbers	Spacing (in cm)
1	275	1 & 2	54.8
2	245	2 & 3	48.7
3	218.5	3 & 4	43.4
4	194.5	4 & 5	38.6
5	173	5 & 6	34.4
6	154.5	6 & 7	30.6
7	137.5	7 & 8	27.2
8	122.5	8 & 9	24.2
9	109	9 & 10	21.6
10	97	10 & 11	19.2
11	87	11 & 12	17.1
12	77	12 & 13	15.2
13	68.5	13 & 14	13.8
14	62	14 & 15	12
15	55	15 & 16	10.7
16	49	16 & 17	9.5
17	44	17 & 18	8.5
18	39	18 & 19	7.6
19	35	19 & top	6.7



are approximately  $60^\circ$  and  $100^\circ$  respectively. Therefore, one can observe the Sun for longer duration with good declination coverage [Refer Ramesh (1998b) for details of the LPD used in the GRH].

### 2.1.1 Array geometry

Figure 2 shows the layout of the GRH array. The E-W arm consists of 128 LPDs and the adjacent antennas are separated by 10 m except for the elements EW64 and EW65 which are separated by 20 m. The South arm has 64 elements and the first element is placed at the center of the E-W arm. The spacing between the adjacent antennas in the South arm is 7 m because of limitation of space in that direction. The arms of the LPDs in both arms are oriented in the E-W direction and therefore they receive linear polarization in that direction. The various array parameters are listed in Table 2.

### 2.1.2 Element grouping and signal transmission

The E-W arm has 16 groups ( $G_1 - G_{16}$ ) and the spacing between adjacent groups is 80 m except for the group G8 and G9 which are separated by 90 m. Each group contains 8 antennas (Figure 3). The South arm also has 16 groups ( $G_{17} - G_{32}$ ), but with 4 antennas each. The intergroup spacing is 28 m (Figure 4). The signal from individual antenna in the group are combined in a branched feeder system using delay shifters, power combiners and RG8U cables. The delay shifters (computer controlled analog devices) in the E-W arm tilt the beam (response pattern) of the associated group to different directions along the Right Ascension (R.A.). This way a radio source can be tracked continuously for a longer period. Similarly, the delay shifters in the South arm enable tilting of beam of each group to different directions along the declination. Note that no tilting of N-S beam of each E-W group and E-W beam of South group is required. They are wide  $\sim 90^\circ$  and  $60^\circ$ , respectively. The group signal is then passed through a high pass filter ( $f_h = 50$  MHz) to remove the spurious inter-modulation products due to large interfering signals present occasionally at frequencies  $< 40$  MHz. The signal after filtering is amplified by a 28 dB wide band amplifier (0.5 - 500 MHz). The system noise is dominated by the sky background and is  $\approx 10^4$  K in our frequency range. The output from each group is amplified approximately by 34 dB using a wide band amplifier and passed through an electronic switch which periodically inverts the phase of the input signal between  $0^\circ$  and  $180^\circ$

with the help of a switching signal. This process is called Walsh switching and is required to minimize the possible coupling between signal flowing through adjacent cables.

### 2.1.3 Grating lobes

Because of the spacing between individual antennas within each group in the GRH being greater than the wavelength of observation, there are grating responses. The angular distance of the grating lobes from the primary beam is [Kraus (1966)]

$$\phi_g = \sin^{-1}\left(\frac{n \lambda}{d}\right). \quad (2)$$

Here  $\lambda$  is the wavelength of observation,  $d$  is the spacing between adjacent elements or groups and  $n$  is the grating lobe number. In the case of the GRH  $\phi_g$  at 150 MHz is  $12^\circ$  in the E-W direction and  $17^\circ$  in the South direction for the first grating lobe. Since the size of the Sun is  $\approx 0.6^\circ$  the possibility of both the primary and grating responses receiving radiation at the same time is eliminated. Even if some other radio source happen to contribute through one of the grating lobes, its effect will be very minimal since we are correlating the output of each group in the E-W arm with the South arm.

## 2.2 RECEIVER SYSTEM

### 2.2.1 Front end analog receiver

The R.F. signal from each group goes through two frequency conversions. It is first up-converted to an intermediate frequency (I.F.) of 170 MHz by mixing with a local oscillator (1<sup>st</sup> L.O.) signal. This conversion places all the image frequencies well above the frequency range (30-150 MHz) of observation. By changing the 1<sup>st</sup> L.O. to different frequencies in the range of 200 to 320 MHz one can perform multi-frequency operation. The I.F. signal is then sent through a bandpass filter with a center frequency ( $f_c$ ) of 170 MHz and a bandwidth ( $\Delta f$ ) of 6 MHz. This suppresses the image frequencies and possible inter-modulation products. After further amplification, the signal is down-converted to a 2<sup>nd</sup> I.F of 10.7 MHz by mixing with a 2<sup>nd</sup> L.O. of 180.7 MHz (refer Figure 5). The output is again amplified and passed through a band pass filter with a  $f_c$  of 10.7 MHz and a  $\Delta f$  of 1 MHz. The narrow bandwidth helps in carrying out interference free observations. The I.F. signals from each of the 32

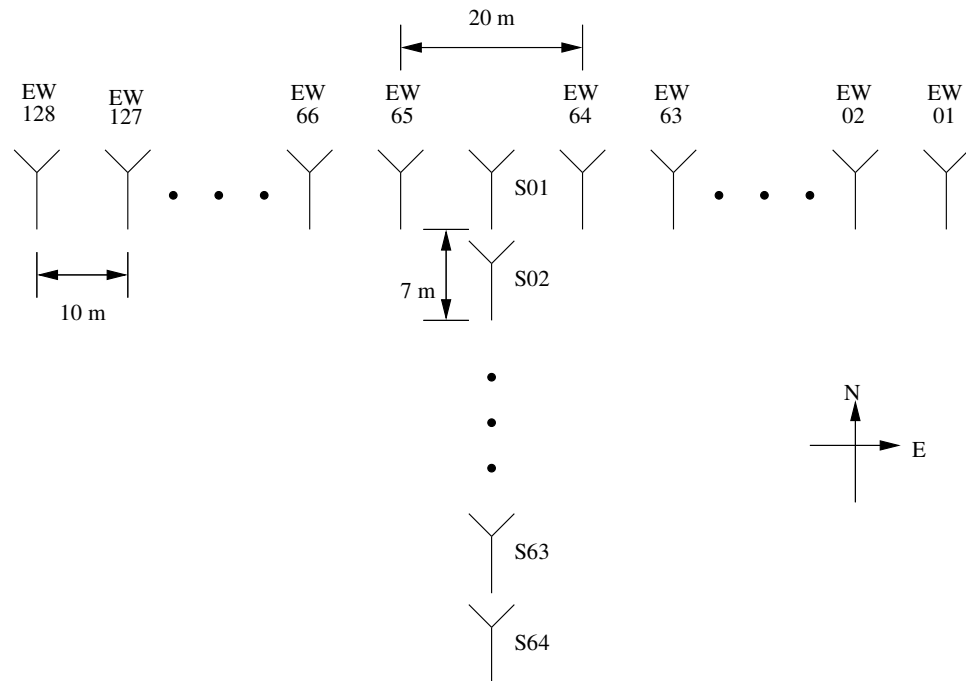


FIG. 2: The layout of the GRH array. The E-W arm consists of 128 LPDs and the spacing between adjacent elements is 10m except for LPDs EW64 and EW65, which are separated by 20 m. The elements in the E-W arm are divided into 16 groups containing 8 each. The South arm has 64 LPDs with an inter-element spacing of 7 m. It is also divided into 16 groups containing 4 elements each.

TABLE 2: Array parameters of the GRH

Parameter	Value
Basic element	Log periodic dipole
Frequency of operation	30-150 MHz
Declination coverage	$-31^\circ$ S to $+59^\circ$ N
Number of antenna groups	32 (16 E-W and 16 S)
Back end receiver	Digital correlator - 1024 channels (1 bit - 2 level)
Effective collecting area	$96 \lambda^2$
Field of view	$3^\circ \times 4^\circ$ at 150 MHz
Angular resolution	$5' \times 8'$ (R.A. $\times$ Dec.) at 150 MHz
I.F. Bandwidth	1 MHz
Sampling Rate	2.04 MHz
Observing period	$\pm 4$ hours around local meridian
sensitivity ( $5 \sigma$ )	$\approx 2 \times 10^{-2}$ sfu at 150 MHz (for 10 sec integration time)

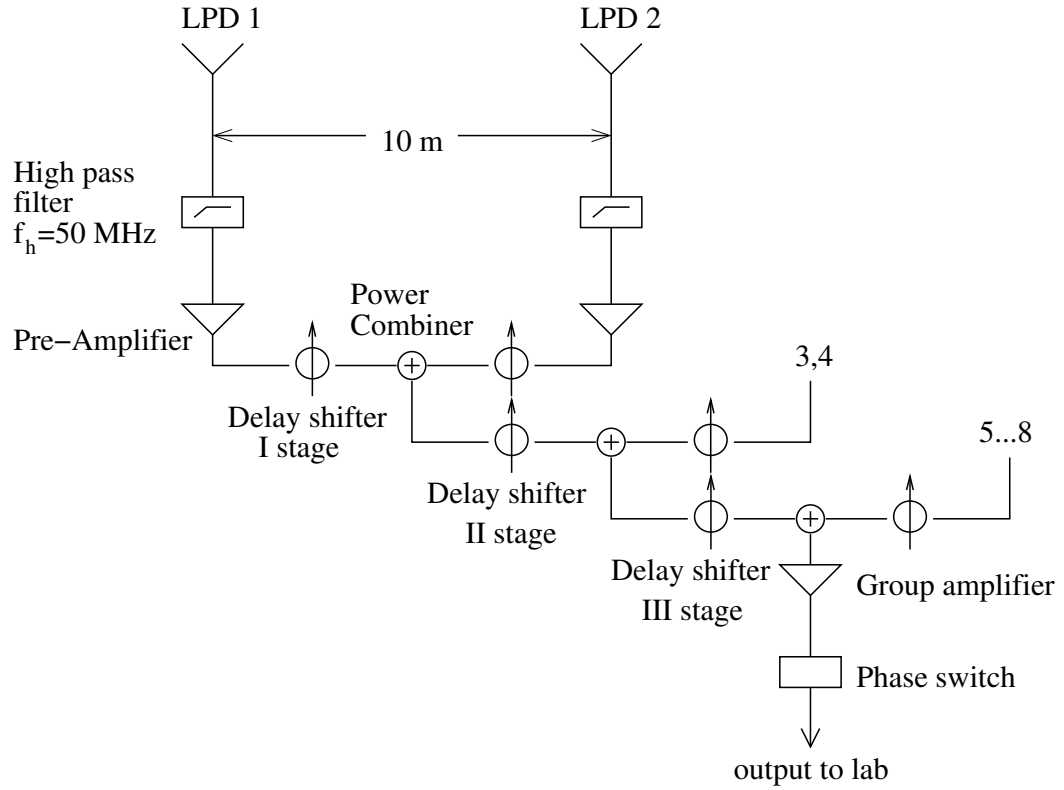


FIG. 3: Schematic of the E-W group. The gain of the pre-amplifier is  $\approx 28$  dB and the insertion loss is about 3 dB. The loss in the interconnecting cables between adjacent LPD and the delay shifters is about 50 dB. The gain of the group amplifier is  $\approx 34$  dB. The delay shifters are for tilting the E-W beam of the corresponding LPDs/group of LPDs in the E-W direction. Since the N-S beam of each E-W group is about  $90^\circ$  (3 dB width), tilting in that direction is not required.

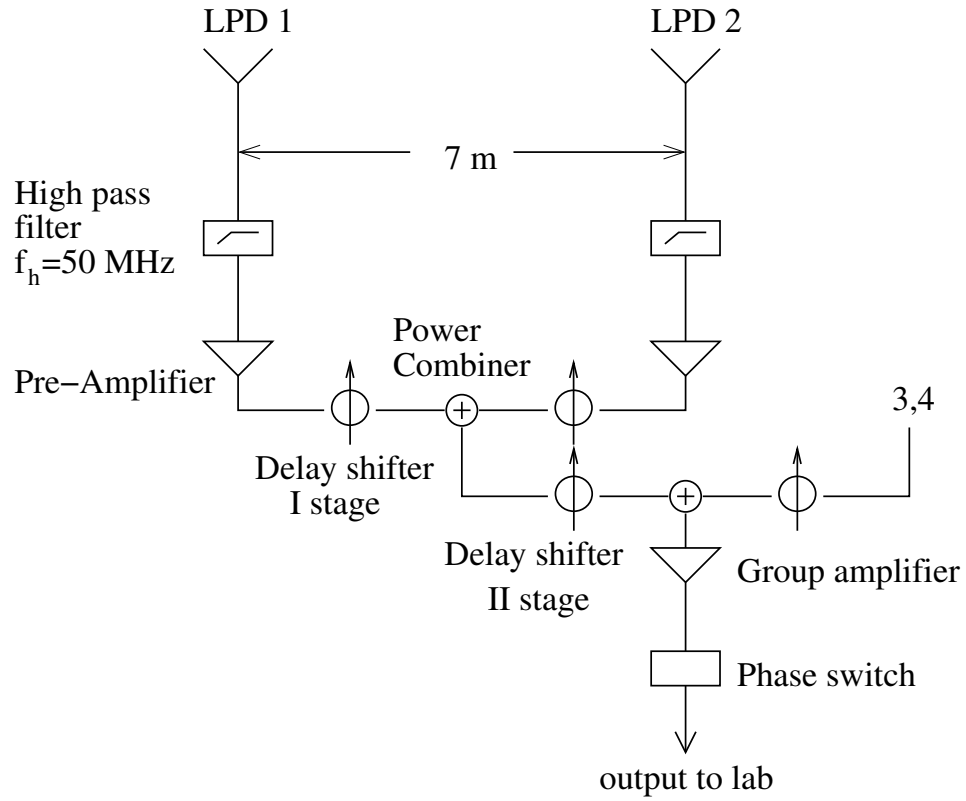


FIG. 4: Schematic of the South group. The delay shifters in this arm tilt the N-S beam of the corresponding LPDs/group of LPDs in the N-S direction at different declinations. The 3 dB width of the E-W beam of the north-south group is  $60^\circ$ . Therefore, no tilting is required in the E-W direction.

antenna groups are split into in-phase (cosine) and quadrature (sine) components by sending them through analog quadrature hybrids and then fed to the digital back end receiver.

### 2.2.2 Back end digital receiver

In the GRH, correlations are measured for all the interferometer pairs formed by 32 antenna groups. In order to obtain all possible multiplications, i.e.  $\frac{n(n-1)}{2} = 512$  complex correlations, a 1024 channel correlator is used. The measurements are made using a one-bit two-level correlator. The signals from the I.F. amplifiers are quantized to two levels using a zero cross detector and sampled at a rate of 2.04 GHz. This ensures that the 5<sup>th</sup> harmonic (10.2 MHz) of the sampling clock falls exactly at the edge of the I.F band (10.2-11.2 MHz) and there will not be any signal to noise degradation due to aliasing [Ramesh et al. (2005)]. The sampled signals are then delayed (using shift register) in order to preserve the coherence for signals arriving from larger zenith angle. Since the digital delay is applied only in discrete steps, the maximum delay error corresponding to above sampling rate is about 245 nsec. The corresponding coherence loss is  $\approx 10\%$  for 1 MHz bandwidth

### 2.2.3 Data acquisition

The correlator system has 8 boards and each board has 16 correlator chips. Each one of them correlates signals corresponding to  $8 \times 8$  antenna pairs, giving 128 correlations. The correlated data from all the chips are read and written into a memory unit after the end of each integration period (about 256 msec). This process goes on for 256 integration cycles. During this time, the data acquired in the previous 256 integration cycles (stored in a similar memory unit) are read into the computer. The role of the memory units are reversed at the end of 256 integration cycles [Ramesh et al. (2005)].

## 2.3 CALIBRATION AND IMAGING

A two-element correlation interferometer measures the spatial coherence of a distant radiation field at a given location as a function of the baseline separation between antennas, measured in wavelengths. Therefore an array of antennas measure the above spatial coherence at many discrete locations. The output of a correlation

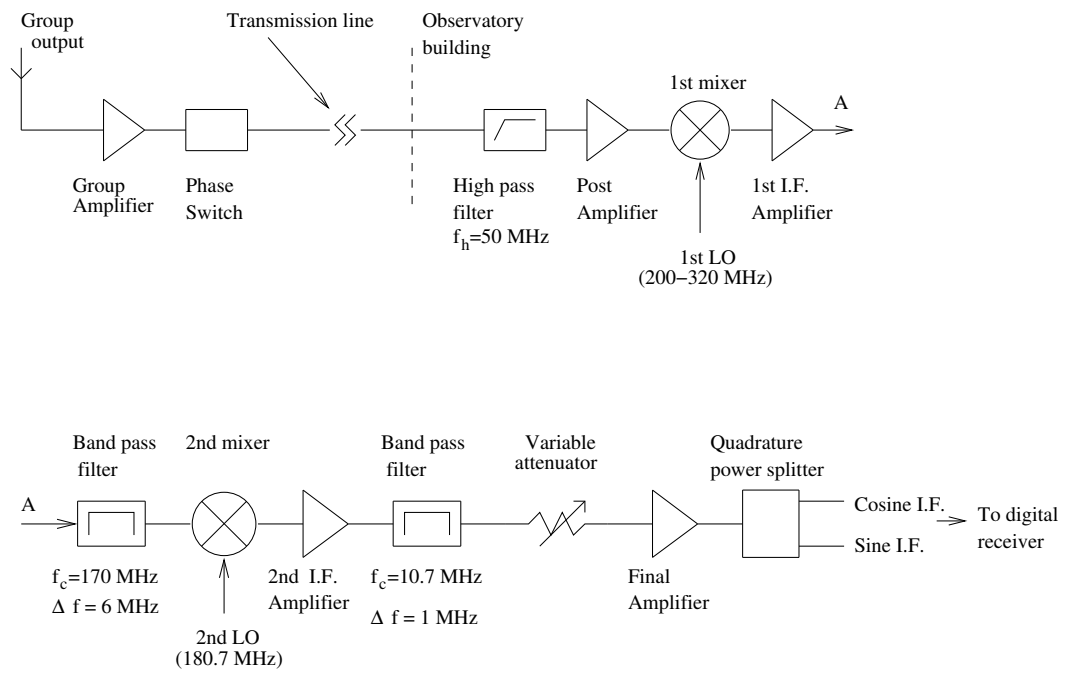


FIG. 5: Front end analog receiver



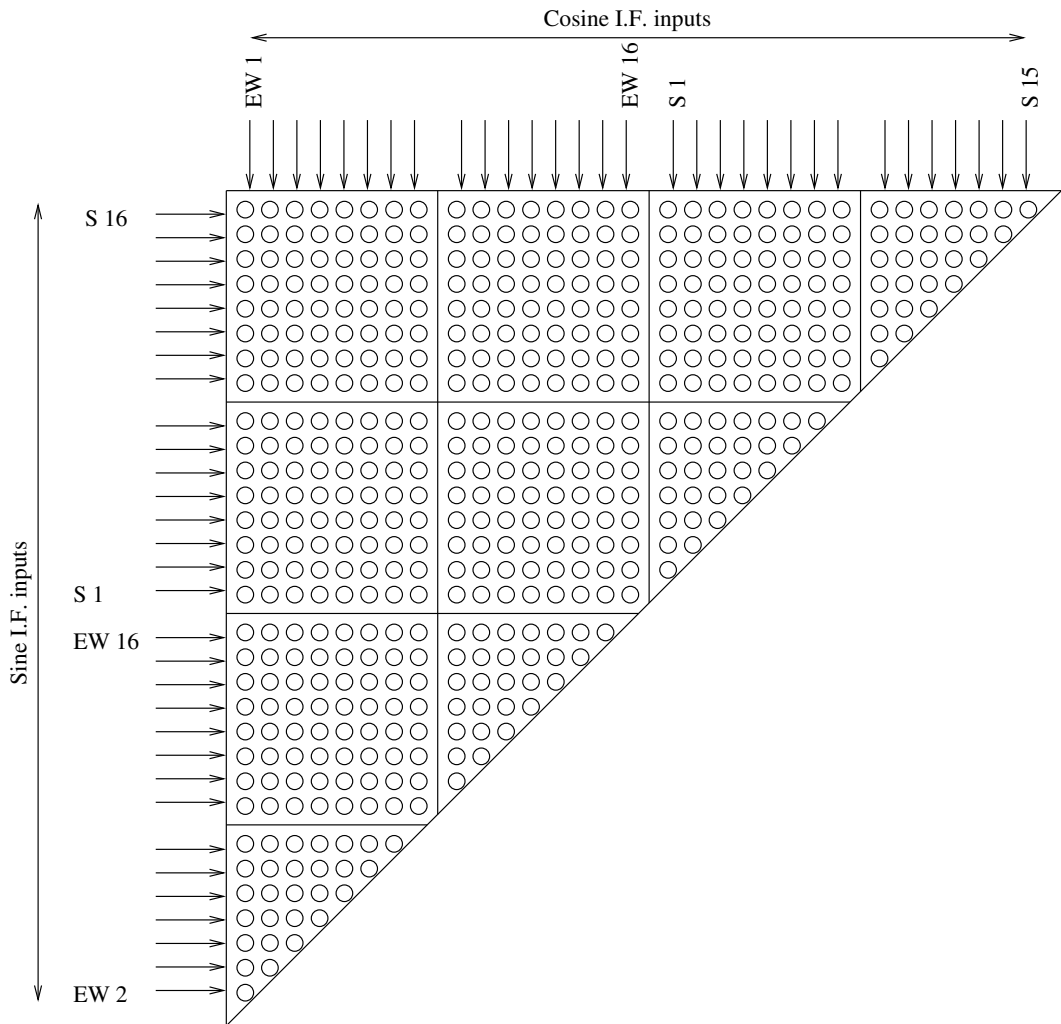


FIG. 6: Back end digital receiver - The 1024 channel correlator

interferometer is called the visibility function. The process of recovering true visibilities from the observed quantities (often contaminated with errors) is known as calibration. The errors may either be related to receiver parameters such as delay errors, band pass mismatches etc., or other factors like interference, cross-talk, atmospheric/ionospheric turbulence etc. The process of correcting the observed visibilities vary from case to case. If the instrumental parameters and atmosphere conditions are stable, then simultaneous observations of nearby calibration sources of known flux and position can be used to minimize the errors involved in the observed visibilities from the target source. This is called external calibration. In the case of the GRH, shifting of the beam to different directions in the sky (for example between the calibrator and target) is carried out by the introduction of appropriate delay gradients across the individual LPDs/groups of LPDs in the array as mentioned earlier. This makes it difficult to maintain the antenna parameters constant. Therefore, a direct application of the external calibration procedure to the GRH is difficult. On the other hand, if the time rate of change of brightness over a small region of the source is negligible as compared to the rest, then visibility correction can be achieved using the target source itself. This is called internal calibration and it has two variants: (i) self-calibration and (ii) redundancy calibration. The first method uses a source model (with visibility function  $V^{mod}$ ) to obtain error ( $g^s$ ) in the observed visibilities by minimizing the quantity

$$\sum_{1 \leq i < j \leq n} |V_{ij}^{obs} - g_i g_j^* V_{ij}^{mod}|^2 \quad (3)$$

At the end of each iteration a new model is generated using the corrected data. The process is continued until the residuals reach a minimum. Though the characteristics of the final image depends on the initial model distribution, images with high dynamic range can be obtained with this technique [Perley (1989); Shevgaonkar (1984)]. But, if the source is highly dynamic and extended, the self calibration scheme may not yield desirable results [Cornwell and Fomalont (1989)]. The redundancy method is useful if the configuration of the interferometer array is such that it has many identical baselines (at the cost of reduced uv coverage). Since the true visibilities on identical baselines are equal, the complex gain of each antenna (with respect to a common reference) can be derived from the measured visibilities themselves. The errors can be obtained using the least square technique and is independent of any models [Wieringa (1991)]. The redundancy calibration also produces images of high

dynamic range [Noordam and de Bruyn (1982)] and it can be applied with a good degree of success to time varying sources like the Sun [Koshishi et al. (1994)].

### 2.3.1 Calibration scheme used in the GRH

Though multiplication among all the 32 antenna groups is carried out in the GRH, it is only the cross-multiplications (i.e. between antennas in the East-West and the South arm) are used for obtaining the 2-D brightness distribution of the source. This involves tilting of the antenna beam using analog delay units (Figure 3 and 4), and hence a direct application of the calibration schemes mentioned in the previous section is not possible [Ramesh et al. (1999)]. In view of the above mentioned difficulties with the existing phase calibration schemes, a combination of the closure phase method [Jennison (1958); Rogers et al. (1974)] and the availability of redundant baselines is effectively used to correct the phase errors in the observed complex visibilities. Apart from the 256 E-W  $\times$  S baselines, the fundamental baselines formed by the multiplications ( $G_1 \times G_2$ ), ( $G_2 \times G_3$ )...(  $G_{15} \times G_{16}$ ) in the E-W arm are also utilized.

The phase of the observed complex visibility on the baseline formed by the antenna groups  $G_i$  and  $G_j$  is

$$\phi_{ij}^{obs} = \phi_{ij}^{true} + \phi_i^{err} - \phi_j^{err} + \phi_{ij}^g \quad (4)$$

The geometric phase term  $\phi_{ij}^g$  is eliminated from equation (4) by calculating the time of transit of the optical Sun over the local meridian at Gauribidanur using the following relation:

$$\begin{aligned} \phi^g &= 2\pi\nu\tau_g \\ &= [u\cos(\delta) \sin(H) + v(\cos(\delta) \cos(H) \sin(\phi) - \sin(\delta) \cos(\phi)) \\ &\quad + w(\cos(\delta) \cos(H) \cos(\phi) + \sin(\delta) \sin(\phi))] \end{aligned}$$

where

- $u, v, w$  – X, Y, Z components of the baseline
- $\tau_g$  – delay between the arrival time of the wavefronts
- $\delta$  – declination of the source
- $\phi$  – latitude of the observer
- $H$  – hour angle of the source

Therefore, equation (4) becomes

$$\phi_{ij}^{obs} = \phi_{ij}^{true} + \phi_i^{err} - \phi_j^{err} \quad (5)$$

The antenna based errors ( $\phi_i^{err}$ ) can be eliminated from this equation by forming a closure relation [Jennison (1958)] between the antenna groups  $G_i$ ,  $G_j$  and  $G_k$  as shown below.

$$\theta_{ijk} = \phi_{ij}^{obs} + \phi_{jk}^{obs} - \phi_{ik}^{obs} \quad (6)$$

$$\Rightarrow \theta_{ijk} = \phi_{ij}^{true} + \phi_{jk}^{true} - \phi_{ik}^{true} \quad (7)$$

By forming a complete set of equations for an interferometer of 'N' elements, one can arrive at a matrix equation of the following form:

$$Ax = b \quad (8)$$

where

$A$  – coefficient matrix

$x$  – column matrix containing true visibilities ( $\phi^{true}$ )

$y$  – column matrix containing closure phases ( $\theta$ )

By matrix inversion one can solve for the true visibility phase ( $\phi^{true}$ ) of any baseline. The phases can then be combined with the observed visibility amplitudes on the corresponding baseline to form the true complex visibilities pertaining to the source. It is to be noted that it is not required to remove the geometrical phase term in equation (4) since it will get canceled automatically while summing the observed phases on the baselines between any three interferometers as shown in equation (7).

### 2.3.2 Map formation

Consider a three dimensional Cartesian coordinate system X, Y and Z pointing towards West, South and zenith respectively. If  $u$ ,  $v$ ,  $w$  represent their corresponding component of interferometer baseline (fraction of wavelength expressed in radians), then the observed complex visibility on any baseline is,

$$V(u, v, w) = \int \int A(l, m) B(l, m) e^{-j(lu+mv+nw)} \frac{dl dm}{n} \quad (9)$$

In the above equation,  $B(l, m)$  is the sky brightness distribution,  $A(l, m)$  is the antenna response,  $j = \sqrt{-1}$  and  $l, m, n$  are the direction cosines with respect to X, Y

and Z axis respectively. Rewriting equation (9), one can solve for the sky brightness distribution. That is

$$\frac{A(l, m) B(l, m)}{n} = \int \int \int V(u, v, w) e^{j(lu+mv+nw)} du dv dw \quad (10)$$

For a certain range of  $l$  and  $m$ ,  $V(u, v, w)$  is almost independent of  $w$  and therefore,

$$\frac{A(l, m) B(l, m)}{n} = \int \int V(u, v) e^{j(lu+mv)} du dv \quad (11)$$

The above expression at the time of transit ( $l = 0$ ) becomes,

$$\frac{A(0, m) B(0, m)}{\sqrt{1 - m^2}} = \int V(u, v) e^{j(mv)} dv \quad (12)$$

The L.H.S of equation (12) is the raw map and one can obtain this for every integration time at transit. The one dimensional Fourier transformation gives the sky brightness distribution. Before doing that, the errors in the observed visibilities have to be corrected for amplitude and phase errors. For each observed complex visibility one can calculate the amplitude and phase as,

$$G = \sqrt{A_c^2 + A_s^2} \quad (13)$$

$$\phi = \tan^{-1} \left( \frac{A_s \sin\theta}{A_c \cos\theta} \right) \quad (14)$$

respectively.  $A_c$  and  $A_s$  in the above set of relationship are the deflections in the cosine and sine channel. The observed complex visibility in terms of above deflections at any instant can be written as  $A_c \cos\theta + j A_s \sin\theta$ . Since in the GRH, the amplitude errors are comparatively smaller than the phase errors, we use external calibration procedures for correcting amplitude errors. The amplitude correction for the Sun in terms of the calibrator is given as,

$$\left( G_{ij}^{true} \right)_{Sun} = \left( G_{ij}^{obs} \right)_{Sun} \left( \frac{G_{ij}}{G_{max}} \right)_{cal} \quad (15)$$

The corrected amplitudes along with the corresponding phases (calibrated as described in the previous section) are then Fourier transformed to get the map. In practice, only the Discrete Fourier transformation is carried out to obtain the source brightness distribution. Therefore

$$B(0, m) \propto \sum_{j=1}^{16} V(u, v) e^{-i2\pi \frac{v_j}{\lambda} m} \quad (16)$$

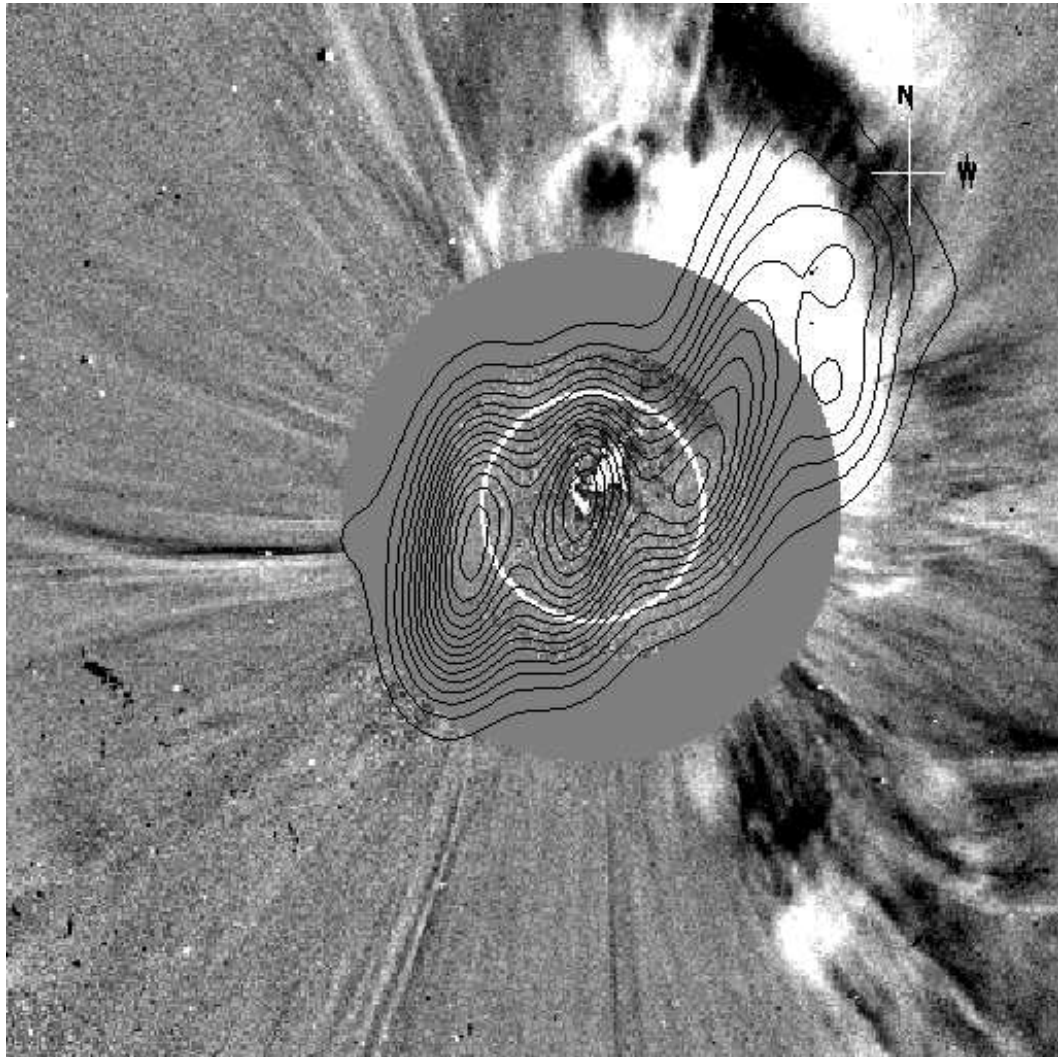


FIG. 7: Composite image of the LASCO-EIT difference image (05:30 UT) and the Gauribidanur radioheliogram (05:25 UT) obtained on November 24, 2000. The last contour in the N-W quadrant of the GRH image is at a distance of  $\sim 4.0 R_{\odot}$  from the center.

Figure 7 shows the composite image of LASCO/white light and EIT difference image (05:30 UT) and the Gauribidanur radioheliogram (05:25 UT) observed on November 24, 2000. There is a good correspondence between the structures (both off the limb as well as on the disk) in the radio and optical images. This indicates that the GRH can image large scale structures of the solar corona up to  $\approx 4.0 R_{\odot}$  from the center of the Sun. In other words, we were able to correct the amplitude and phase errors in the array such that its response as far as about  $1^{\circ}$  away from the center of the field of view (that is mapped) is reliably known. Figure 8 shows the synthesized beam of the GRH array at 109 MHz. The 'X' mark [at (24' W, 52' N)] in that indicates the location of the outermost contour in Figure 7. From Figure 8 one can see that the maximum amplitude at (24' W, 52' N) is about 0.005. Note that the peak value of the map is 1.0 and is at (0,0). This implies that the dynamic range of the radioheliogram is  $\geq 20$  dB. The various GRH images presented in this thesis were obtained using the aforementioned calibration scheme.

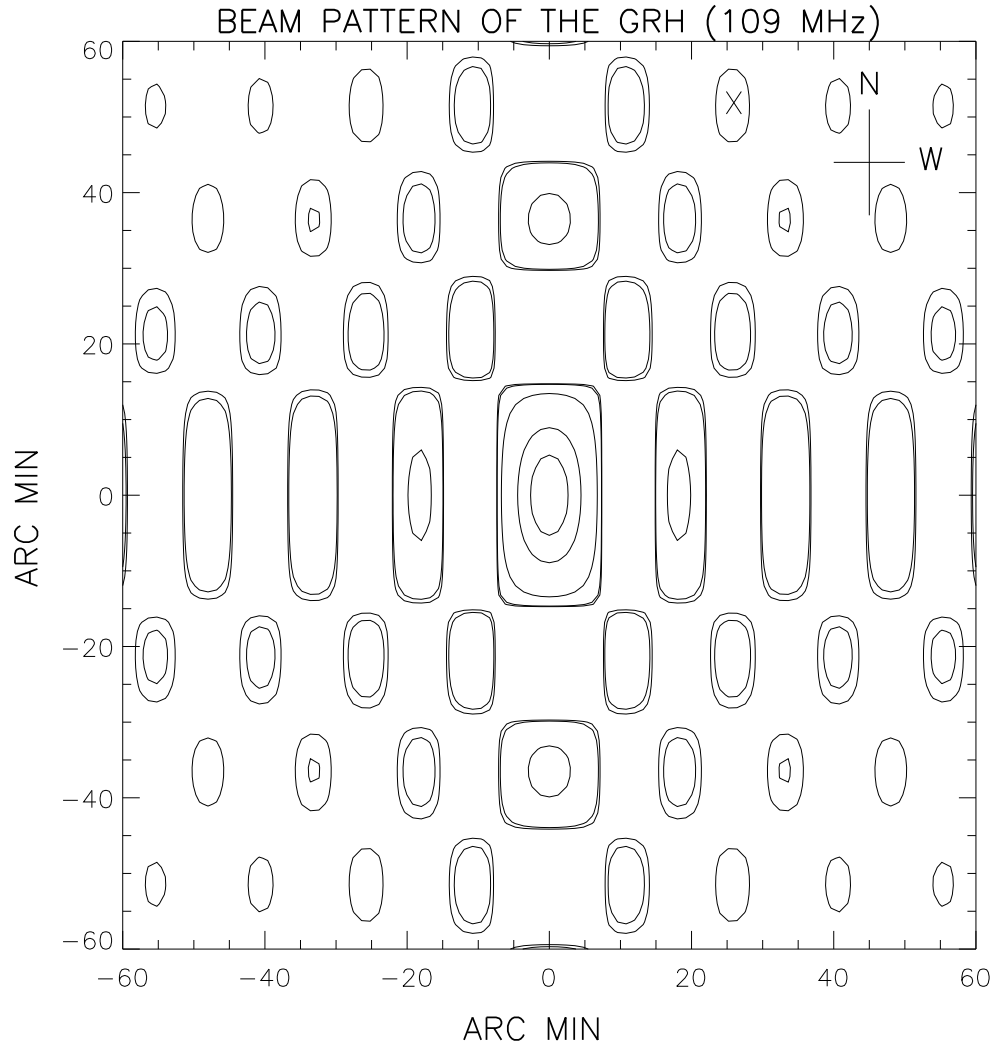


FIG. 8: The synthesized beam pattern of the GRH at 109 MHz. The contour levels are 0.005, 0.01, 0.1, 0.5, 0.8 of the peak value ( $\approx 1.0$ ). The 'X' mark [at (24' W, 52' N)] indicates the location of the outermost contour in Figure 7. The maximum amplitude at that location is  $\approx 0.005$ .



## CHAPTER 3

# THE EVOLUTION OF A ‘HALO’ CORONAL MASS EJECTION CLOSE TO THE SUN

### 3.1 INTRODUCTION

The white-light coronagraphs provide us with the majority of information on CMEs and the observations from instruments such as LASCO on board SOHO have now revolutionized our perception and understanding of them. But, to obtain information on the early evolution of CMEs, in particular for those directed along the Sun-Earth axis that occur far from the plane of the sky, non-coronagraphic observations are required. This is because the occulter in a coronagraph generally covers both the solar disk as well as the low corona from at least 1.2 to a few solar radii above the limb depending on the instrument design. The Earth-directed (geo-effective) events originate on the visible hemisphere of the Sun and appear as a ‘halo’ of expanding circular brightening that completely surrounds or spans a large angle outside the occulting disk of a coronagraph [Howard et al. (1982)]. The ‘halo’ CMEs are geophysically important, in the context of space-weather related phenomena such as geomagnetic storms [Gosling et al. (1991)]. Measurements of the properties of a CME in the low corona are significant for several reasons. CMEs may be accelerating, moving with constant speed or decelerating during their early phase in the low corona. Therefore, the assumption that CMEs have a constant speed behind the occulting disk of the coronagraph may be invalid [Michalek (2003)]. In other words, the kinematics and energetics of a CME close to the Sun are largely not observed [Vourlidas et al. (2000)] except the few observations reported by St. Cyr et al. (1999), Zhang et al. (2001) and Gallagher et al. (2003). This sets a major limitation on the understanding of the relationship between CME and other surface phenomena like flares and filament eruptions ([Lin (2004)] and the references therein). The kinematic evolution of a CME can be described in a three-phase scenario: the initiation phase, impulsive acceleration phase, and propagation phase. Among these, the first two phases take place primarily in the low corona [Zhang et al. (2001)]. These suggest that a more complete description of the motion of a CME in the low corona is crucial for better prediction of its characteristics at large distances from the Sun. Radio imaging observations, particularly at meter wavelengths play an important role in this connection,

since they do not have the limitation of an occulting disk and the CMEs can be detected early in their development both on the disk as well as off the limb. In addition, radio observations offer unique diagnostic capabilities, including constraints on the CME magnetic field [Bastian and Gary (1997)]. Radio signatures of CMEs, particularly meter and longer wavelengths, correspond in principle to both thermal and non-thermal emissions ([Pick (1998a, 2004); Vourlidas (2004)] and the references therein). Several interesting results on the triggering and development of CMEs have been reported in the last few years particularly using combined radio imaging data obtained with the Nancay radioheliograph [NRH; Kerdraon and Delouis (1997)] and the white light coronagraphs on board the SOHO. For example, it was shown that observations of non-thermal radio bursts provide signatures of CME lift-off [Maia et al. (1998); Pick et al. (1998b); Pohjolainen et al. (2001)] and angular spread [Maia et al. (1999)] in the corona. Evidence for existence of Type-II like weak radio bursts closely associated with the leading edge of CMEs was presented by Maia et al. (2000). For events related to flaring regions located behind the limb, radio imaging data have revealed synchrotron emission from CMEs. The corresponding discrete radio sources are seen as an expanding ensemble of loops which closely resemble the white light CME [Bastian et al. (2001)]. White light coronagraphs detect the photospheric light scattered by the CMEs and hence provide information on the density distribution of thermal electrons contained in a CME. It is also possible to observe the latter via bremsstrahlung radiation at meter and longer wavelengths, particularly from the excess electrons (above the ambient) in its frontal structure [Sheridan et al. (1978); Gopalswamy and Kundu (1992); Bastian and Gary (1997)]. However, it is to be noted that without polarization or spectral observations, a precise distinction between thermal and weak non-thermal emissions may be ambiguous. Radio imaging data obtained simultaneously at more than one frequency will be also useful since one can derive the spectral index of the observed emission. In this situation, we report radio imaging observations of the propagation of a diffuse enhancement associated with a ‘Halo’ CME, and estimate its kinematics in the low corona.

## 3.2 OBSERVATIONS

According to the CME list<sup>1</sup> for the year 2000, the LASCO C2 coronagraph observed a full ‘halo’ CME on November 24, 2000 around 05:30 UT, the time at which it

---

<sup>1</sup>[http://cdaw.gsfc.nasa.gov/CME\\_list/UNIVERSAL/2000\\_11/univ2000\\_11.html](http://cdaw.gsfc.nasa.gov/CME_list/UNIVERSAL/2000_11/univ2000_11.html)

was first noticed in its field of view. Figure 1 shows the composite of the LASCO-EIT running difference image obtained at 05:30 UT and the radioheliogram obtained with the GRH at around 05:25 UT. The CME can be clearly noticed as a bright feature above the northwest quadrant of the occulting disk of the coronagraph. The extrapolated lift-off time of the CME was 04:55:52 UT. The reported linear speed of the event was  $994 \text{ km s}^{-1}$ . The second order fit gives an acceleration of  $72 \text{ m s}^{-2}$  and a velocity of  $\sim 465 \text{ km s}^{-1}$ . The latter is at  $5.71 R_{\odot}$ , the radial distance corresponding to the first height time measurement using LASCO data (Figure 2). Figure 3, 4, 5, and 6 show the radioheliogram obtained with the GRH at 109 MHz around 04:55, 05:05, 05:15, and 05:25 UT respectively on that day.

In addition to the discrete sources on the disk, one can clearly observe enhanced radio emission above the limb. The approximate structural similarity between the white light and radio images (in the northwest quadrant), their positional proximity indicate that the enhanced radio emission off the northwest limb in Figure 4, 5 and 6 could possibly represent a portion of the radio counterpart of the white light ‘halo’ CME in Figure 1. However, we would like to point out that the radio counterpart is not exactly co-spatial with the white-light CME. Though the radio and the white light images were obtained at different times, the possible reason for the above is that the radio emission at a particular observing frequency emanates only from the specific region of the frontal structure of a CME where the density is equal to the plasma density corresponding to the observing frequency.

### 3.3 ANALYSIS

#### 3.3.1 The speed of the CME in the plane of the sky

An inspection of the radioheliogram in Figure 3, 4, 5, and 6 indicate that the radio enhancement off the limb in the northwest quadrant evolves as a function of time. Hence, we adopted the strategy of the running difference technique (generally used with the SOHO LASCO and EIT images) to understand the characteristics of the radio CME. Figure 7, 8, and 9 show the radio difference images obtained using the above method. In order to clearly identify the centroid of the radio CME (indicated by ‘+’ in the images), we have plotted only the positive contours up to the half-maximum level. It can be seen that there are other discrete sources of emission both near the disk center as well as close to the limb in the southeast quadrant. These

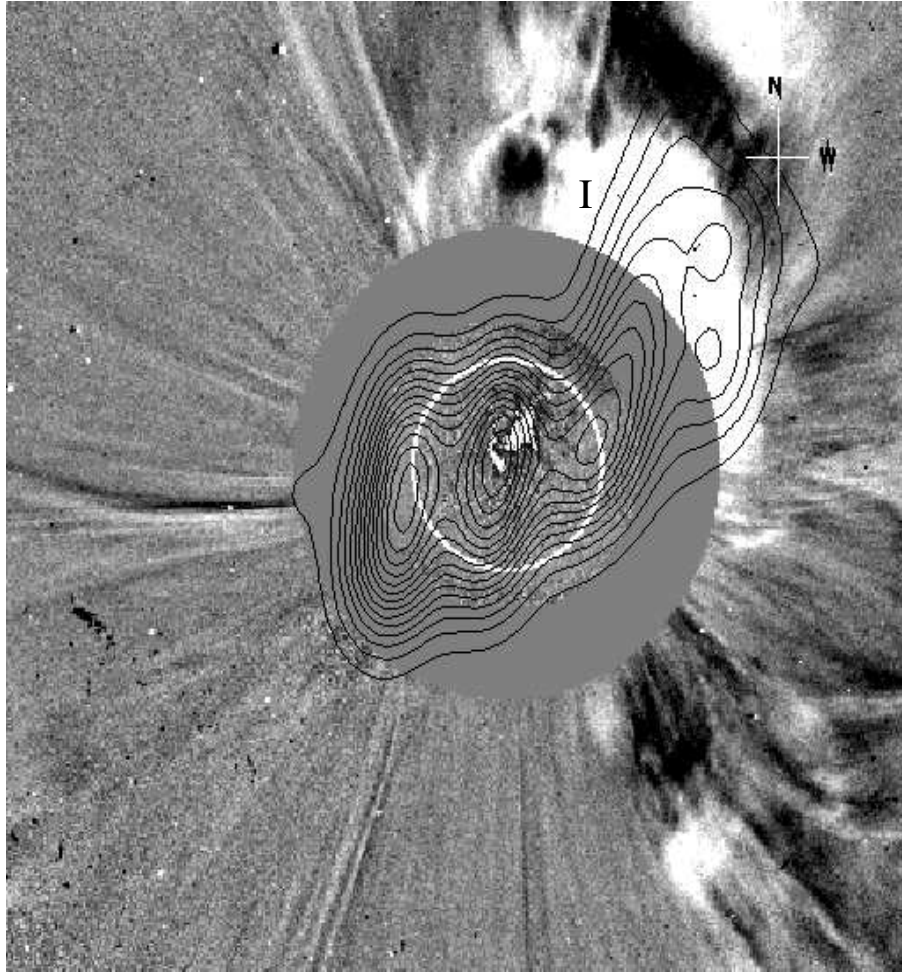


FIG. 1: A composite of the LASCO-EIT running difference image of the CME obtained on November 24, 2000 at 05:30 UT and the radio image observed with the GRH at 05:25 UT. The inner circle indicates the solar limb, and the outer circle is the occulting disk of the coronagraph. It extends up to  $2.2 R_{\odot}$  from the center of the Sun. Solar north is straight up, and east is to the left. A comparison of the radio and white light enhancements in the northwest quadrant indicates that the former is the radio counterpart of the latter. Refer text for explanation of ‘I’.

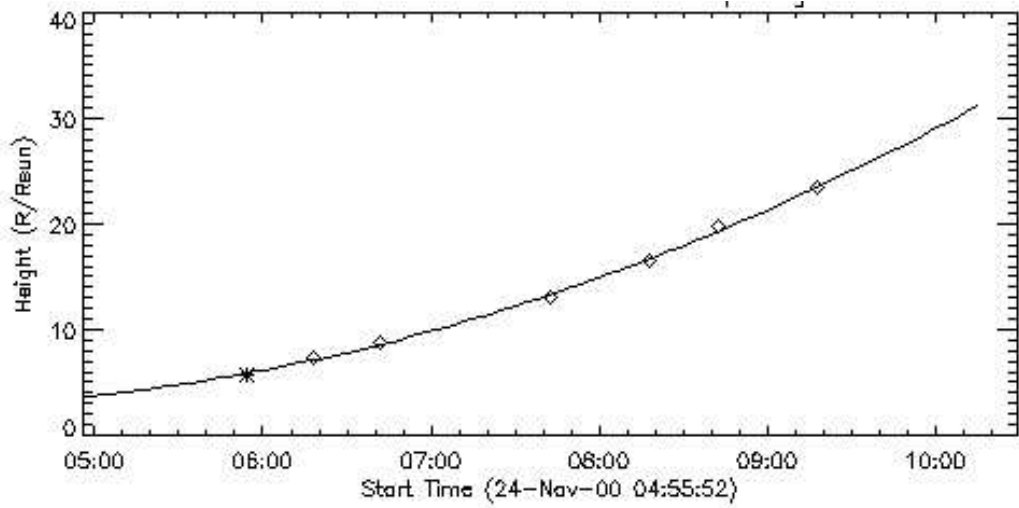


FIG. 2: The second order fit (constant acceleration) to the LASCO height-time measurements of the CME observed on November 24, 2000. The estimated acceleration is  $\approx 72 \text{ m s}^{-2}$ . The linear fit (constant speed) for the same set of points gives an average speed of  $\approx 994 \text{ km s}^{-1}$  for the leading edge of the CME. The extrapolated onset time of the CME was 04:55:52 UT. Note that the white light measurements were made at a mean position angle of  $353^\circ$ .

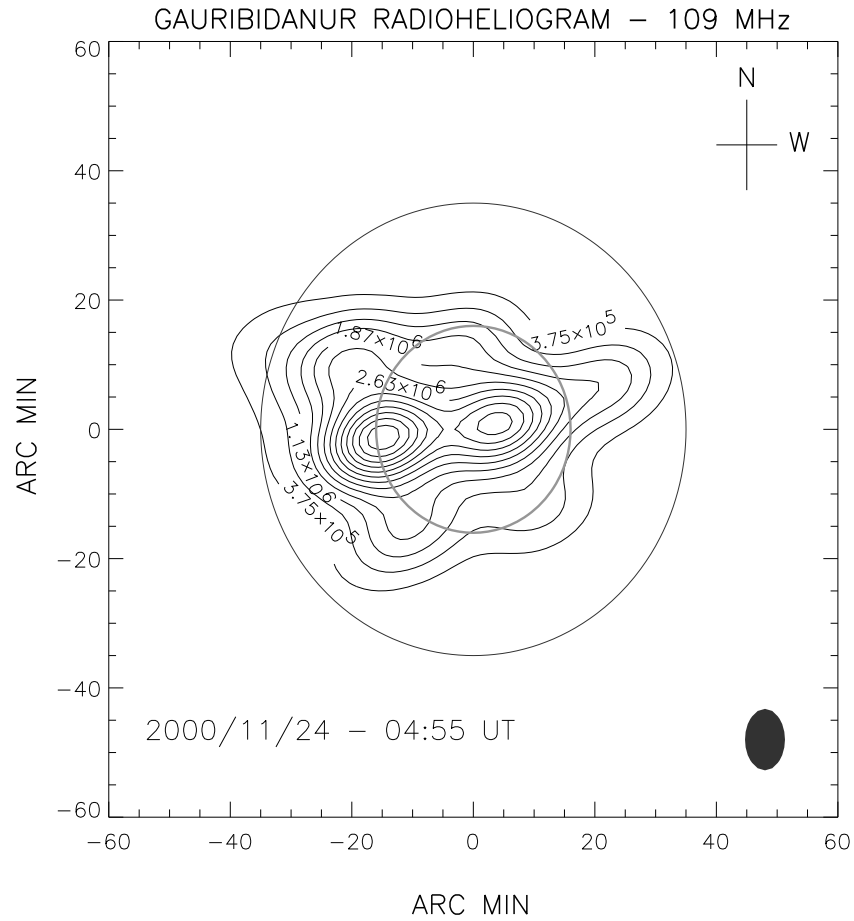


FIG. 3: Radioheliogram obtained with the GRH on November 24, 2000 around 04:55 UT. The peak  $T_b$  is  $\approx 4.18 \times 10^6$  K and it corresponds to the source near the east limb. The open circle at the center is the solar limb. The outer circle corresponds approximately to the occulter size ( $2.2 R_\odot$ ) of the white-light coronagraph. The filled contour near the bottom right corner is the GRH beam at 109 MHz.

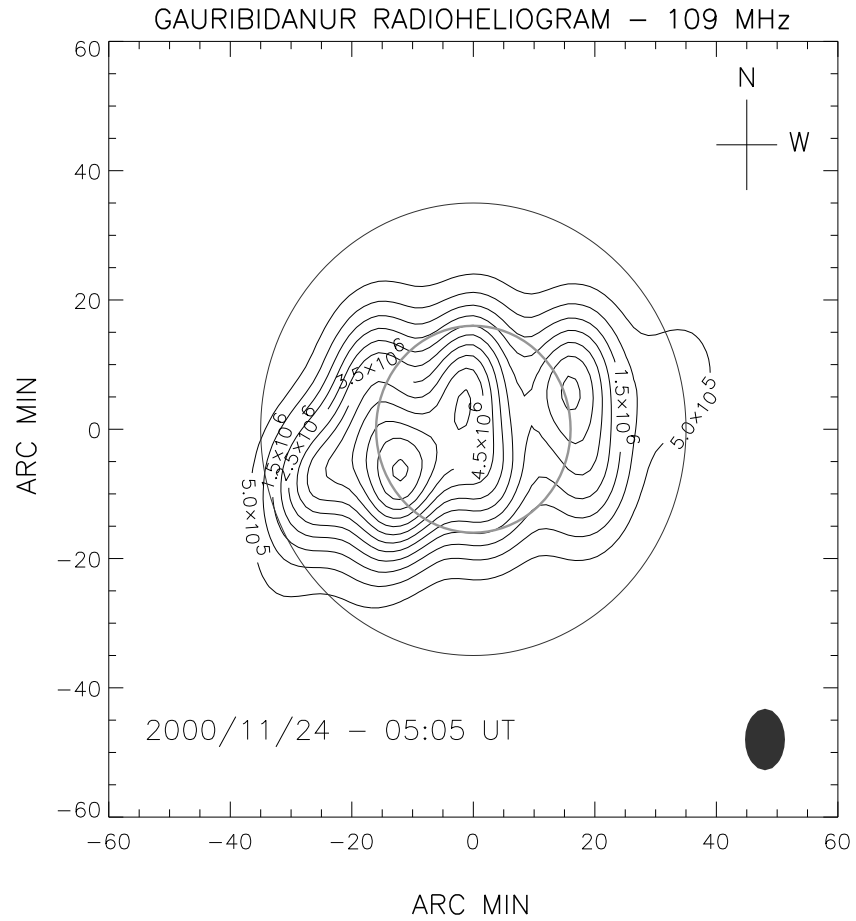


FIG. 4: Same as Figure 3 but obtained at 05:05 UT. The peak  $T_b$  is  $\approx 6.08 \times 10^6$  K and it corresponds to the same source as in Figure 3.

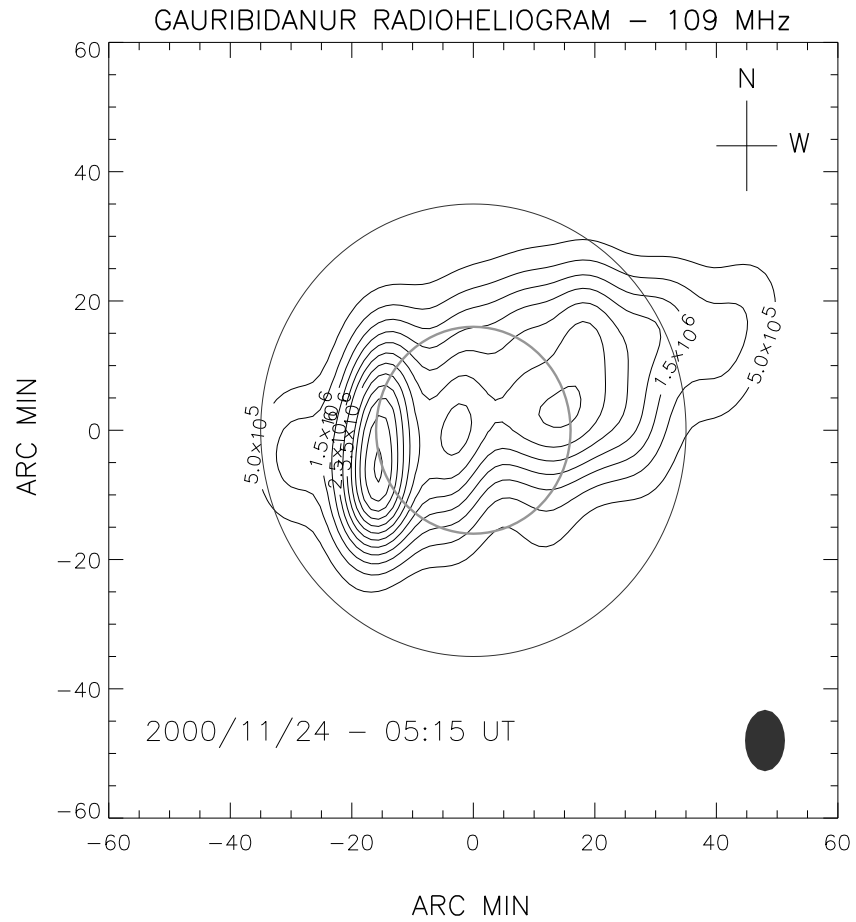


FIG. 5: Same as Figures 3 & 4, but the time of observation is 05:15 UT. The peak  $T_b$  is  $\approx 6.1 \times 10^6$  K. Again it corresponds to the source near the east limb as in Figure 3 and 4.



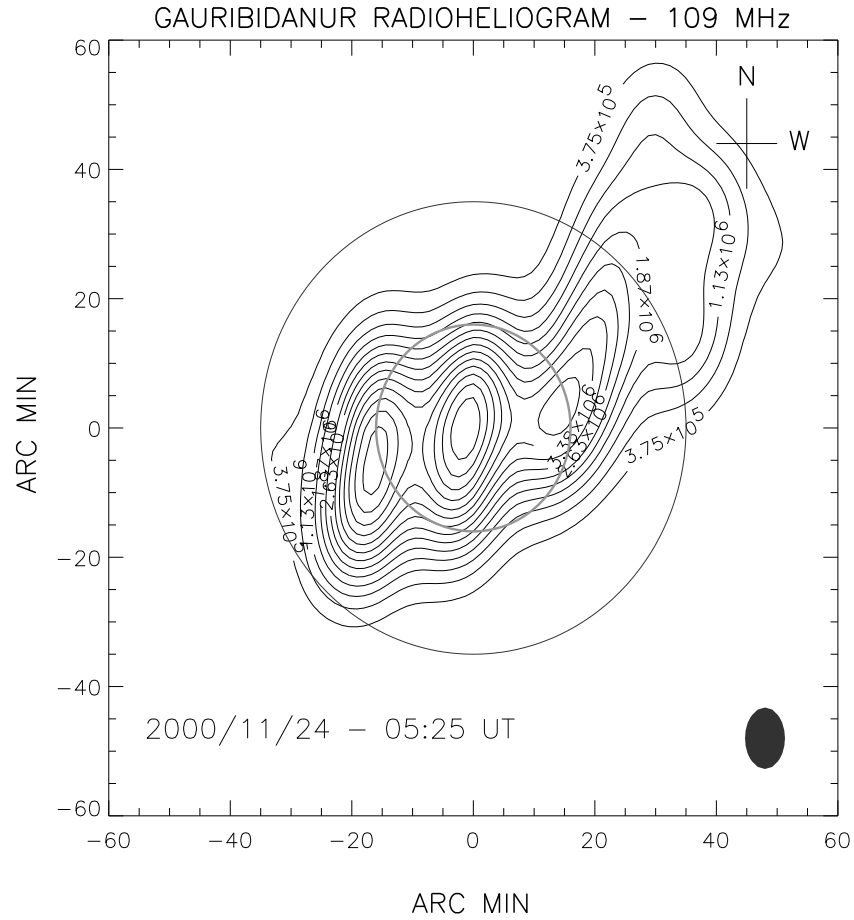


FIG. 6: Same as Figures 3, 4 and 5, but observed at 05:25 UT. The peak  $T_b$  is  $\approx 5.6 \times 10^6$  K. It corresponds to the source near the disk center. Note that there is a shift in the centroid of the source near the east limb between Figures 3, 4, 5, 6. This is probably due to a localized activity there. The difference in their peak  $T_b$  at that location also indicates the same. The bulged contours above the limb in the northwest quadrant in this as well as in the earlier Figures 3, 4 and 5 correspond to the white light CME (Figure 1).

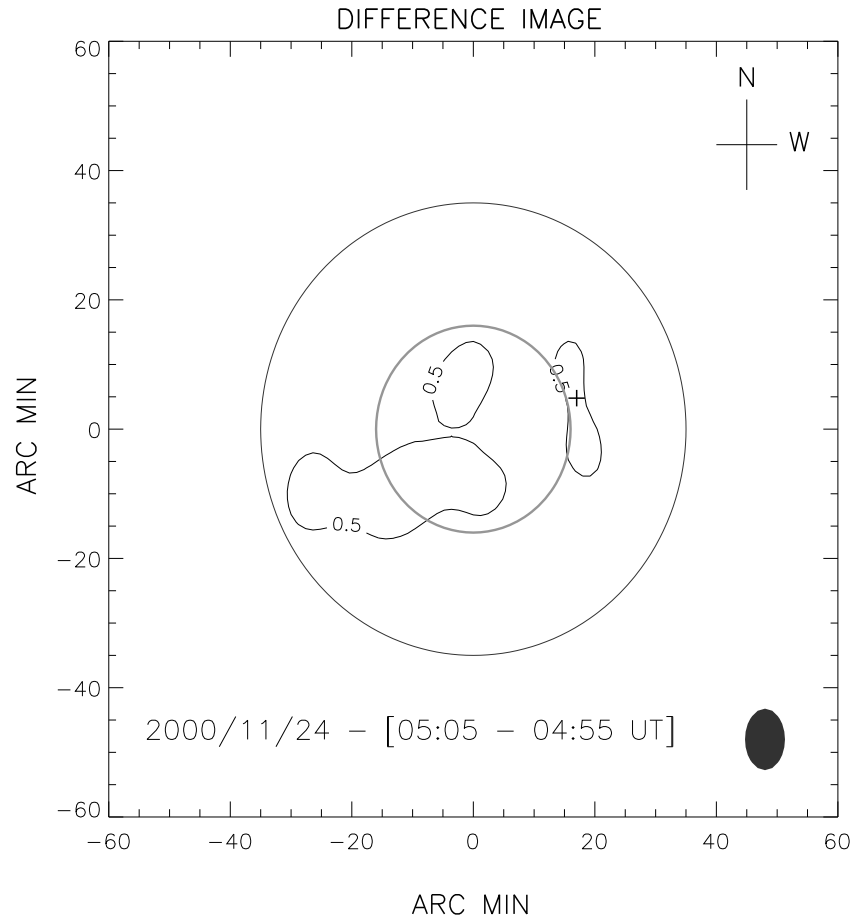


FIG. 7: Radio difference image obtained by subtracting the image shown in Figure 3 from Figure 4. In order to clearly identify the radio enhancement associated with the white light CME, we have plotted only the positive difference values up to half-maximum level. The '+' mark indicates the centroid of the radio CME. Its position coordinate in the image plane is (3'.5 N, 17' W) and the average brightness temperature is  $5.3 \times 10^5$  K.

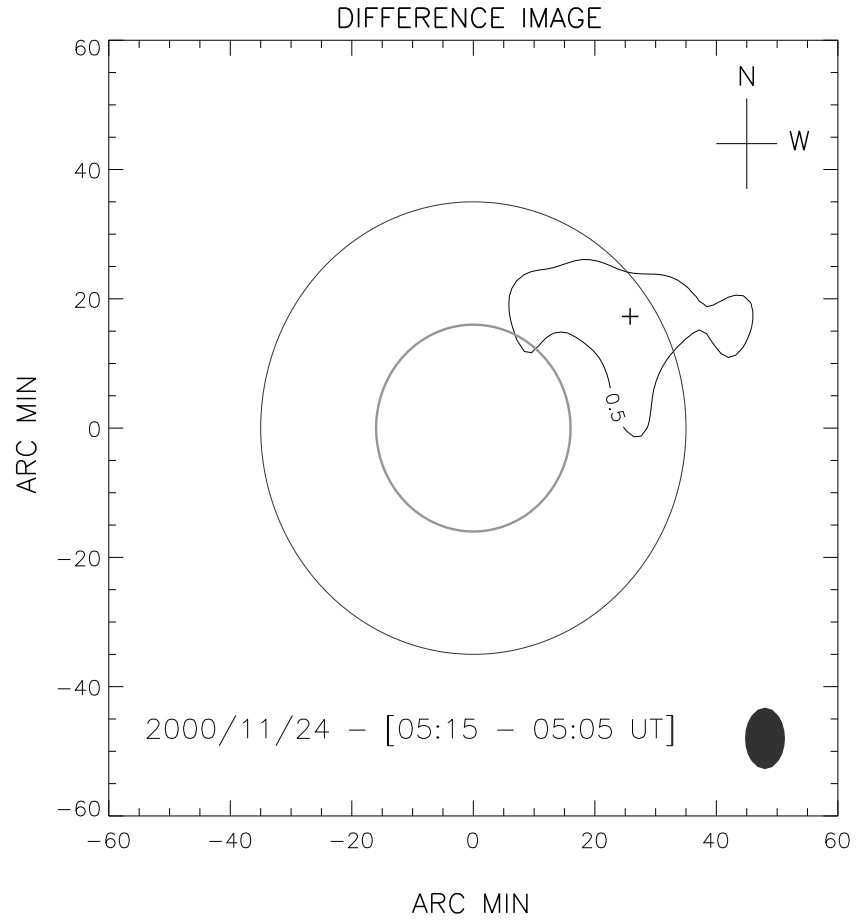


FIG. 8: Same as in Figure 7, but obtained by subtracting Figure 4 from Figure 5. The position coordinate of the centroid of radio enhancement associated with the CME is (17'.5 N, 24' W). Its average brightness temperature is  $5.5 \times 10^5$  K.

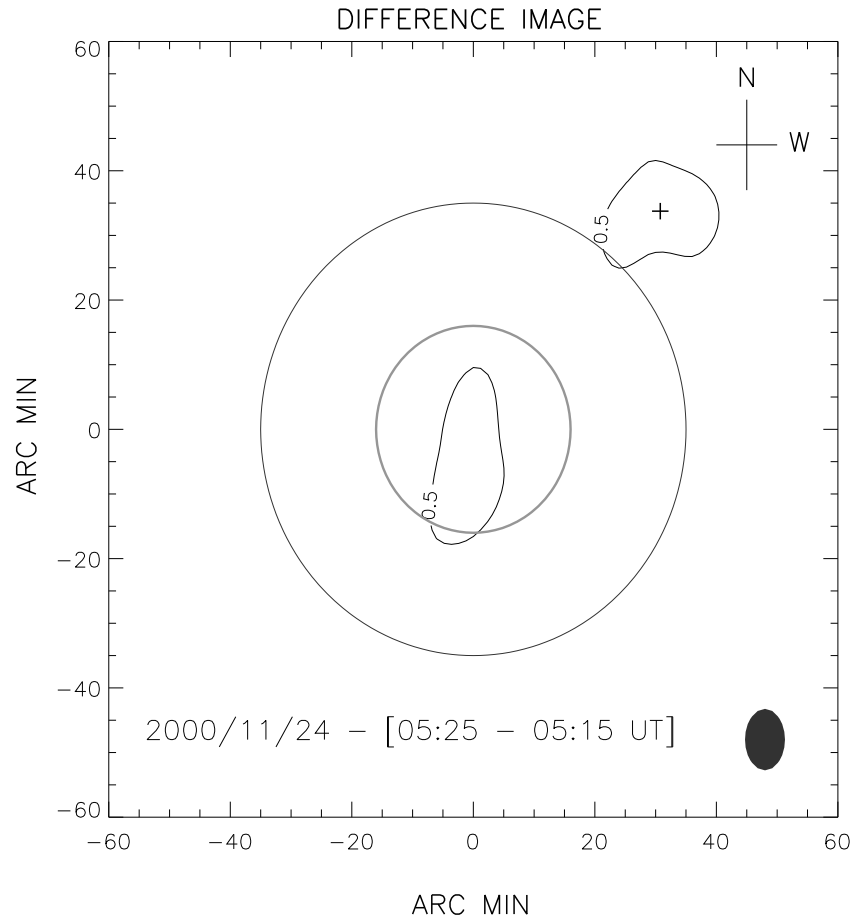


FIG. 9: Radio difference image obtained by subtracting Figure 5 from Figure 6. The position coordinate of the centroid of the radio enhancement associated with the CME and the average brightness temperature are  $(32'.5 \text{ N}, 29' \text{ W})$  and  $6.4 \times 10^5 \text{ K}$  respectively. The presence/absence of contours at locations other than the northwest limb in Figure 7, 8 and 9 indicate the transient activity going on there.

sources might be due to localized activity taking place there. Since our interest is mainly on the radio enhancement in the northwest quadrant, we do not consider the above sources for further study. We followed the movement of the radio CME as a function of time and the location of its centroid at different epoch are,

<u>Time</u>	<u>North – South</u>	<u>East – West</u>
05 : 05 UT	→ 03'.5 (= 0.22 R <sub>⊙</sub> ) N,	17' (= 1.06 R <sub>⊙</sub> ) W
05 : 15 UT	→ 17'.5 (= 1.09 R <sub>⊙</sub> ) N,	24' (= 1.50 R <sub>⊙</sub> ) W
05 : 25 UT	→ 32'.5 (= 2.03 R <sub>⊙</sub> ) N,	29' (= 1.81 R <sub>⊙</sub> ) W

From this we derive the displacement of the CME during above successive time interval as,

$$\begin{aligned}\Delta R_1 &= \left[ (1.09 - 0.22)^2 + (1.50 - 1.06)^2 \right]^{0.5} R_{\odot} \\ &\approx 6.78 \times 10^5 \text{ km, and} \\ \Delta R_2 &= \left[ (2.03 - 1.09)^2 + (1.81 - 1.50)^2 \right]^{0.5} R_{\odot} \\ &\approx 6.90 \times 10^5 \text{ km}\end{aligned}$$

respectively. Therefore, the corresponding velocities are

$$\begin{aligned}u_1 &= \frac{\Delta R_1}{\Delta T_1} = \frac{6.78 \times 10^5 \text{ km}}{600 \text{ s}} \approx 1130 \text{ km s}^{-1} \text{ and} \\ u_2 &= \frac{\Delta R_2}{\Delta T_2} = \frac{6.90 \times 10^5 \text{ km}}{600 \text{ s}} \approx 1150 \text{ km s}^{-1}\end{aligned}$$

respectively.

### 3.3.2 The electron density of the CME

From Figures 7, 8 and 9 it can be seen that the radio CME is an extended structure with respect to the GRH beam at 109 MHz. So we calculated its average brightness temperature in the following manner. That is,  $T_{avg} = \frac{\text{Total flux of the source}}{\text{Source area}}$  [Kraus (1966)]. The source area and the corresponding total flux density at different epoch was calculated from the running difference radioheliogram and the values are,

<u>Time</u>	<u>East – West</u>	<u>North – South</u>	<u>Total Flux (Jy)</u>
05 : 05 UT →	$8' = 0.5 R_{\odot}$ ( <sup>2</sup> Rw)	$21' = 1.3 R_{\odot}$ ( <sup>3</sup> Lw)	2173
05 : 15 UT →	$40' = 2.5 R_{\odot}$ (Lw)	$13' = 0.8 R_{\odot}$ (Rw)	8806
05 : 25 UT →	$20' = 1.25 R_{\odot}$ (Lw)	$20' = 1.25 R_{\odot}$ (Rw)	8042

respectively. Therefore, the average value of the brightness temperature of the CME at 05:05, 05:15 and 05:25 UT is 5.3, 5.5,  $6.4 \times 10^5$  K respectively. Note that single frequency observations of CME-associated discrete radio sources traveling outward to large heights ( $\sim 2 - 3 R_{\odot}$ ) in the solar corona are generally attributed to non-thermal continuum emission from moving type IV radio bursts, since the observed  $T_b$  is usually higher ( $\geq 10^7$  K) than that of the emission from the background ‘quiet’ Sun ( $\sim 10^6$  K), which is purely thermal in nature. But in the present case, the average  $T_b$  of the enhanced radio emission corresponding to the white-light CME is less than the electron temperature ( $T_e \approx 1 \times 10^6$  K) of the solar corona. Also, no type IV emission was reported during our observing period [04:55-05:25 UT] on November 24, 2000 [Sol.-Geophys. Data, January (2001)]. Bastian et al. (2001) recently showed that optically thin synchrotron emission from the non-thermal electrons entrained in the magnetic field of the CME could also give rise to low values of  $T_b$  ( $\sim 10^4 - 10^5$  K). But the above could not be verified (through spectral index estimation) in the present case, since the radio imaging data is available at only one frequency. However, it is to be noted that the CME event described here was not accompanied by any non-thermal continuum emission in the metre wavelength range, unlike the event reported by Bastian et al. (refer [Sol.-Geophys. Data (1998b)] for the associated spectral information of the latter). Therefore it is possible that the CME-associated enhanced radio emission in the present case is thermal in nature and the excess emission observed off the limb in the northwest quadrant of the GRH images is due to thermal bremsstrahlung from the extra electrons in the frontal structure of the ‘halo’ CME. Therefore, we can make an order-of-magnitude estimate of the density of the latter using the approximation given by Sheridan et al. (1978), and Gopalswamy & Kundu (1992): The brightness temperature of the quiet Sun is given by,

$$T_Q = T_e (1 - e^{-\tau}) \quad (1)$$

---

<sup>2</sup>Radial width

<sup>3</sup>Lateral width

where  $\tau$  is the optical depth of the corona. For cases where the optical depth of the medium is less than 1, the above relation can be rewritten as follows:

$$\begin{aligned} T_Q &\approx T_e [1 - (1 - \tau)] \\ &= T_e \tau \end{aligned} \quad (2)$$

where,

$$\tau = 0.2 T_e^{-3/2} \nu^{-2} \int_0^\infty [n_e(l)]^2 dl \quad (3)$$

Here,  $\nu$  is the observing frequency,  $n_e$  is the electron density and  $dl$  is the elemental length of integration (along the line of sight). We find that the peak  $T_b$  of the radio Sun in Figure 3, 4, 5, and 6 did not change significantly before or during the occurrence of the CME. Also when the CME was brightest ( $6.4 \times 10^5$  K at 05:25 UT), the peak  $T_b$  of the radio Sun continued to be on the disk. This suggests that the optical depth of the radio CME is comparatively smaller. The total brightness temperature of the corona (the CME plus the background) is,

$$\begin{aligned} T_t &= 0.2 T_e^{-1/2} \nu^{-2} \int_0^\infty (n_e + n_{CME})^2 dl \\ &\approx 0.2 T_e^{-1/2} \nu^{-2} \left[ \int_0^\infty n_e^2 dl + \int_0^\infty n_{CME}^2 dl + \int_0^\infty n_e n_{CME} dl \right] \end{aligned} \quad (4)$$

The last term in the above equation can be neglected since its contribution to the total brightness ( $T_t$ ) will be lesser compared to the first two terms. Therefore, by rearranging equation (4) for  $T_{CME}$ , we get

$$T_{CME} = T_t - T_{bg} = 0.2 T_e^{-1/2} \nu^{-2} \int_0^\infty n_{CME}^2 dl , \quad (5)$$

where  $T_{bg} (= 0.2 T_e^{-1/2} \nu^{-2} \int_0^\infty n_e^2 dl)$  corresponds to the background. If we define the average value of density at the location of the CME is  $\langle n_{CME} \rangle$  and the depth along the line of sight is  $L$ , then the above expression can be written as

$$T_{CME} = 0.2 T_e^{-1/2} \nu^{-2} \langle n_{CME} \rangle^2 L . \quad (6)$$

Therefore,

$$\langle n_{CME} \rangle = \left[ \frac{5 T_e^{1/2} \nu^2 T_{CME}}{L} \right]^{1/2} . \quad (7)$$

Assuming the depth along the line of sight ( $L$ ) of the CME is equal to its radial width, the density of the CME at the aforementioned epoch are determined. The values are 3.0, 2.4 and  $2.0 \times 10^7 \text{ cm}^{-3}$  respectively.

### 3.3.3 The mass associated with the CME

The coronal plasma is a fully ionized gas of normal solar composition (90% hydrogen and 10% helium by number), and each electron is associated with approximately  $2 \times 10^{-24}$  g of material, and therefore the mass ( $M$ ) is given by,

$$M = 2 \times 10^{-24} \langle n_{CME} \rangle V \text{ g} , \quad (8)$$

The volume ( $V$ ) of the region of the enhanced emission was determined by multiplying its radial and lateral width with the depth along the line of sight. Their values at different epoch are  $\approx 1.10$ ,  $5.40$ , and  $6.60 \times 10^{32}$  cm<sup>3</sup>, respectively. Substituting the above values and the respective electron densities in equation (8), we get the mass of the CME as  $6.6 \times 10^{15}$ ,  $2.6 \times 10^{16}$ , and  $2.6 \times 10^{16}$  g respectively.

### 3.4 CONCLUSION

We studied the characteristics of the radio enhancement associated with the white light CME observed on November 24, 2000 around 05:30 UT. The electron density of the radio CME at the height of 1.08 (05:05 UT), 1.85 (05:15 UT) and 2.71  $R_{\odot}$  (05:25 UT) are 3.0, 2.4, and  $2.0 \times 10^7$  cm<sup>-3</sup>, respectively. Compared to this, Sheridan et al. (1978) and Gopalswamy & Kundu (1992) reported an electron density of  $1.2 \times 10^7$  cm<sup>-3</sup> and  $9.5 \times 10^6$  cm<sup>-3</sup> for the radio CME observed by them at a similar height ( $\sim 2 R_{\odot}$ ) in the low corona. Also, these values are close to that adopted by Bastian and Gary (1997) in their CME model calculations ( $3 \times 10^7$  cm<sup>-3</sup>). We also calculated the mass of the radio CME at different epoch mentioned above and the values are  $6.6 \times 10^{15}$ ,  $2.6 \times 10^{16}$ , and  $2.6 \times 10^{16}$  g, respectively. The corresponding value reported by Gopalswamy & Kundu (1992) is  $2.7 \times 10^{15}$  g. Though our mass estimate is larger, we also found a change in CME mass with height as shown by Vourlidas et al. (2000). The speed of the CME in the low corona was estimated from the observed displacement of the associated radio enhancement, and the average value is  $\approx 1140$  km s<sup>-1</sup>. This is higher compared to the white light value of 994 km/s (linear speed) mentioned earlier. The discrepancy is most likely due to the difference in position angle of white light and radio measurements. The former were obtained between P.A. = 348° and 358°. The latter were at P.A. = 282°, 306°, 318° at 05:05, 05:15 and 05:25 UT respectively. It is also possible that the radio measurements may correspond to feature close to the occulter (marked 'I') in Figure 1. The white light measurements correspond to



the leading edge. Also, note that the angular resolution of GRH ( $7' \times 11'$  at 109 MHz) does not allow us to precisely identify the location of the centroid of the radio CME. The estimated uncertainty in the position measurement is about  $\pm 0.4 R_{\odot}$ . The corresponding error in the measurement of velocity is  $\pm 475 \text{ km s}^{-1}$ . Data with better spatio-temporal resolution is required to determine the velocity and acceleration more accurately. However, a comparison of the LASCO and GRH images shows that the radio enhancement moved approximately in the same direction as the white-light CME (Figure 10). This indicates further radio observations of this type in the future with better sensitivity and angular resolution might provide useful information on the characteristics and kinematics of the CME close to its onset in the low corona. This is important since the major acceleration of a CME seems to take place in the inner corona [St. Cyr et al. (1999); Zhang et al. (2001); Gallagher et al. (2003)]. The epoch from which the CME starts accelerating and its duration are crucial since the final velocity of a CME depends on them as demonstrated recently by Zhang et al. (2004). Again, the spatial and temporal development of a CME will provide useful information in determining whether there are two physically distinct classes of CMEs as proposed by Sheeley et al. (1999).

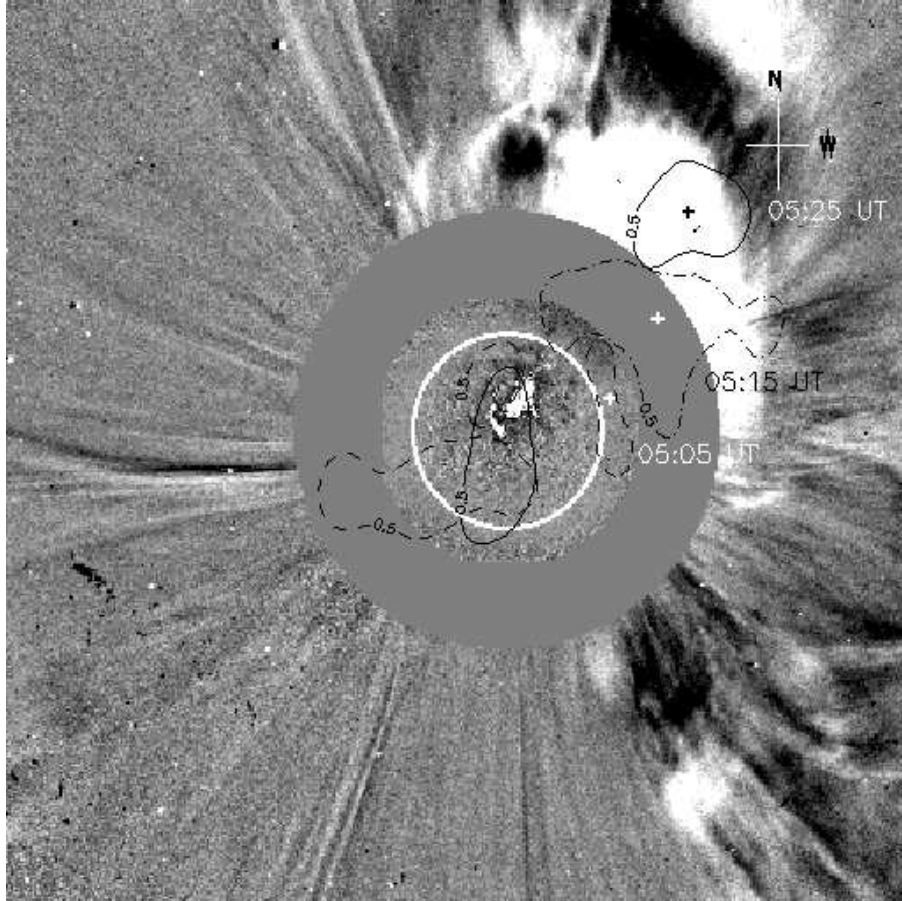


FIG. 10: A composite of the radio difference images in Figure 7, 8 and 9 and the LASCO-EIT running difference image obtained at 05:30 UT. The half-power contour correspond to the structure of the radio CME at 05:05, 05:15 and 05:25 UT are shown with dash, dash-dot-dash and thick lines for clarity. The '+' mark indicates the centroid of the radio CME as earlier.

## CHAPTER 4

### THE RAY-TRACING TECHNIQUE IN THREE-DIMENSIONS

#### 4.1 THE EQUATION OF RADIATION TRANSFER

Spectral observations of the Sun prove that the radiation energy density from the ‘undisturbed’ solar corona follows the Planck’s distribution for the black body, whose maximum emission peaks at  $\sim 10^6$  K. Since the black body is a perfect emitter and absorber at all wavelengths, the propagation of radiation inside the solar corona depends on its absorption and emission properties.

The radiation transfer can be understood if we approximate the situation to a case where a radiating source of brightness<sup>1</sup>  $B_s$  is viewed through a self-emitting and absorbing cloud of temperature  $T_c$ . The change in brightness  $dB$  of the source after its radiation travels a distance  $dr$  through the cloud can be written as [Kraus (1966)]

$$\frac{dB}{dr} = \frac{j\rho}{4\pi} - \kappa\rho B. \quad (1)$$

Here,  $\rho$  (in  $\text{kg m}^{-3}$ ) is the density of the cloud,  $j$  (in  $\text{watts kg}^{-1} \text{ Hz}^{-1}$ ) and  $\kappa$  (in  $\text{m}^2 \text{ kg}^{-1}$ ) are its emission and absorption coefficients respectively. The first term on the right hand side represents the gain in brightness due to internal emission (of the cloud) and the second term gives the loss due to absorption in the cloud. The solution for the above transfer equation can be written as,

$$B = B_{obs} = B_s e^{-\int_0^{r_c} \kappa\rho dr} + \frac{j}{4\pi\kappa} (1 - e^{-\int_0^{r_c} \kappa\rho dr}). \quad (2)$$

This implies that the observed/apparent brightness  $B$  (or  $B_{obs}$ ) is a sum of modified source intrinsic brightness (by the cloud of thickness  $r_c$ ) and the cloud intrinsic brightness. The integration has to be performed over the entire path traversed by the radiation inside the cloud. This can be easily understood by rewriting equation (2) in the following form,

$$B_{obs} = B_s e^{-\tau_c} + B_i (1 - e^{-\tau_c}). \quad (3)$$

---

<sup>1</sup>The power received from the source per unit area per unit solid angle per unit bandwidth (unit:  $\text{watts m}^{-2} \text{ rad}^{-2} \text{ Hz}^{-1}$ )

The term

$$B_i = \frac{j}{4\pi\kappa}, \quad (4)$$

in equation (3) is the intrinsic brightness of the cloud and is equal to the ratio of the emission and absorption coefficient.

$$\tau_c = \int_0^{r_c} \kappa\rho \, dr = \int_0^{r_c} \alpha \, dr \quad (5)$$

is the optical depth, an indirect measure of absorption. The element of integration  $dr$  is the infinitesimal path length which the radiation follows inside the medium. The term  $\alpha$  ( $= \kappa\rho$ ) in equation (5) is the attenuation constant. At radio wavelengths one can equate the source brightness to a blackbody temperature using Rayleigh-Jeans law, i.e

$$B = \frac{2k_B T}{\lambda^2} \quad (6)$$

where  $k_B$  ( $= 1.38 \times 10^{-23}$  joule  $K^{-1}$ ) is the Boltzmann's constant,  $\lambda$  (in meters) is the wavelength of observation and  $T$  is the equivalent black body temperature. Therefore, equation (3) becomes,

$$T_{obs} = T_s e^{-\tau_c} + T_c (1 - e^{-\tau_c}). \quad (7)$$

Here,  $T_{obs}$  is the observed brightness temperature,  $T_s$  and  $T_c$  are the source and cloud brightness temperature respectively.

## 4.2 RADIO WAVE PROPAGATION IN THE SOLAR CORONA

### 4.2.1 The optical depth ( $\tau$ )

The coronal plasma can be considered as the cloud described in the previous section and the layers such as the chromosphere and the transition region (TR) are the source beneath the former. Now, in the case of radio wave propagation through the solar corona, equation (7) is modified as follows;

$$T_{obs} = T_e (1 - e^{-\tau}) + T_{ch} e^{-\tau}. \quad (8)$$

Here,  $T_e$  is the electron temperature of the corona and  $T_{ch}$  is the chromospheric temperature. Since the value of chromospheric temperature ( $\sim 10^4$  K) is much less compared to the electron temperature of the corona ( $\sim 10^6$  K) from where most of the meter wavelength radiation originates, the contribution of the second

term in equation (8) to the observed brightness temperature at meter wavelengths is negligible. So, the second term will be ignored hereinafter.

Our main objective is to understand the physical parameters associated with the discrete large scale thermal radio structures of the solar corona in the observed radio images at meter wavelength range. So, we wanted to develop a technique that can reproduce the observed radio brightness distribution. According to equation (8) the value of optical depth ( $\tau$ ) should be known in order to obtain  $T_{obs}$  from the intrinsic temperature  $T_e$  of the corona. Therefore, the reproduction of a two dimensional image requires the values of  $\tau$  at all points in the image plane. For any generalized two dimensional brightness temperature distribution in the absence of non-thermal emission, equation (8) can be written as,

$$T_{obs}(y, z) = T_e \left[ 1 - e^{-\tau(y,z)} \right]. \quad (9)$$

The variables  $y$  and  $z$  represent the east-west (Longitude) and north-south (Latitude) direction respectively on the image plane. The total optical depth  $\tau_{tot}$  is a sum of infinitesimal optical depths  $\tau_i$  obtained at all points over the entire path traversed by radiation through the medium, i.e,

$$\tau_{tot} = \sum_{i=1}^n \tau_i. \quad (10)$$

We would like to point out here that the variation of  $T_e$  as a function of height [McMullin (1977); Fludra et al. (1999); Subramanian and Sastry (1988)] should also be accounted for in equation (9) while calculating  $T_{obs}$ . But since this is our first attempt to reproduce an observed two dimensional radio brightness distribution, we wanted to minimize the number of free parameters and hence assumed a constant temperature in our calculations. The effect of this assumption is unknown at this stage. Also, the temperature ( $T_h$ ) at an arbitrary height  $h$  inside the corona should be calculated using the optical depth. That is,

$$T_h = T_{h-\delta h} (1 - e^{-\tau_1}), \quad (11)$$

where  $T_{h-\delta h}$  is the temperature at the height of  $h - \delta h$  and  $\tau_1$  is the optical depth corresponding to the infinitesimal layer of thickness  $\delta h$  at  $h$ .

Therefore the problem simplifies to a stage where the estimation of optical depth at all points in the image plane [i.e.,  $\tau(y, z)$ ] is sufficient to reproduce the observed brightness temperature distribution.

### 4.2.2 The attenuation constant ( $\alpha$ )

From equation (5), one can notice that the optical depth involves the attenuation constant of the medium. For the solar corona in the absence of magnetic field and with less number of collisions per unit time [Smerd and Westfold (1949)] compared to the observing frequency, it is given as

$$\alpha = \frac{10^{-11} N_e^2}{\nu^2 \mu T_e^{1.5}} . \quad (12)$$

where,  $N_e$  (in  $\text{m}^{-3}$ ) is the electron density,  $\nu$  (in Hz) is the observing frequency,  $\mu$  is the refractive index, and  $T_e$  (in K) is the electron temperature, of the corona. The refractive index in the absence of magnetic field is a function of the plasma frequency ( $f_p$ ) of the medium, and is given by the formula,

$$\mu = \sqrt{1 - \frac{f_p^2}{\nu^2}} . \quad (13)$$

The plasma frequency is expressed as,

$$f_p = \frac{e}{2\pi} \sqrt{\frac{N_e}{\epsilon_0 m}} , \quad (14)$$

where  $e$  ( $=1.6 \times 10^{-19}$  C) is the charge of the electron and  $\epsilon_0$  ( $=8.85 \times 10^{-12}$  F  $\text{m}^{-1}$ ) is the permittivity of free space. Eclipse observations show that the electron density gradually decreases from the inner layers to the outer layers of the solar atmosphere. This implies that the plasma frequency also behaves in the same manner. Substituting equations (13) and (14) in equation (12), we get

$$\alpha = \frac{10^{-11} N_e^2}{T_e^{1.5} \left( \nu^4 - \frac{e^2 \nu^2 N_e}{4\pi^2 m \epsilon_0} \right)^{0.5}} . \quad (15)$$

Since we have assumed  $T_e$  ( $\approx 1.0 \times 10^6$  K) to be uniform throughout the corona, for any observing frequency  $\nu$  the attenuation constant is only a function of  $N_e$  (because rest of the terms in equation (15) are constants).

This suggests that the observed brightness temperature at any desired wavelength of observation depends mainly on the electron density distribution of the corona in our case.

## 4.3 THE THEORY OF RAY-TRACING

The brightness distribution of the ‘undisturbed’ Sun was computed from centimeter to meter wavelengths for the first time by Smerd (1950). He assumed a spherically

symmetric corona to derive the solution of the radiative transfer equation for an ionized medium by numerical integration. A more involved ray-tracing technique to reproduce the observed brightness distribution of the active corona at centimeter wavelengths was developed by Newkirk (1961). Sastry et al. (1981; 1983) used a ray-tracing technique similar to that of the latter to explain the one-dimensional brightness distribution observed by them in the decameter wavelength range. We now extend this scheme to the analysis of an observed two-dimensional thermal radio brightness distribution in the following sections.

### 4.3.1 The Ray Equation

It is evident from the solution of the transfer equation [(1) and (2)] that the propagation of an electromagnetic radiation through the medium depends on the absorption and emission coefficients of the latter. Since the above coefficients are not constant throughout the medium, the exact direction of propagation of the wave (or the ray trajectory/path) is required to calculate the accumulated/total optical depth. The trajectory of the ray can be traced using the ray equation for skew rays (rays which are not coplanar with the optic axis of the system) and the basic principles of geometrical optics [Born & Wolf (1970)]. The equation of a ray which travels in a medium of varying refractive index can be obtained from the fundamental equation, i.e,

$$\text{curl}(\mu\vec{\mathbf{S}}) = 0 . \quad (16)$$

Here,  $\mu$  is a function describing the refractive index variation in the medium and  $\vec{\mathbf{S}} = \left(\frac{d\vec{\mathbf{r}}}{ds}\right)$ , is the ray vector [ $\vec{\mathbf{r}}$  is the position vector of an arbitrary point on the ray path ( $s$ )]. Applying Stokes theorem over a small area through which the ray passes, equation (16) can be rewritten as,

$$\int \mu\vec{\mathbf{S}} \cdot d\vec{\mathbf{r}} = \int_{c1} \mu_1\vec{\mathbf{S}}_1 \cdot d\vec{\mathbf{r}} + \int_{c2} \mu_2\vec{\mathbf{S}}_2 \cdot d\vec{\mathbf{r}} + \int_{c3} (\mu_2\vec{\mathbf{S}}_2 - \mu_1\vec{\mathbf{S}}_1) \cdot d\vec{\mathbf{r}} = 0 . \quad (17)$$

Here  $c1$ ,  $c2$ , and  $c3$  are the closed contours (surface integral to line integral using Stokes theorem) over which the integration has to be performed. The vector  $\vec{\mathbf{S}}_1/\vec{\mathbf{S}}_2$  points towards/away from the interface. Contours  $c1$ ,  $c2$  are within the regions of refractive index  $\mu_1$  and  $\mu_2$  respectively, and  $c3$  is along the interface between  $c1$  and  $c2$ . By rearranging the terms in the above equation, we get the following equation for the ray in a homogeneous medium of varying refractive index.

$$\left(\frac{\mu_1}{\mu_2}\right)\vec{\mathbf{S}}_1 - \vec{\mathbf{S}}_2 = k\vec{\mathbf{L}} , \quad (18)$$

The vectors  $\vec{\mathbf{S}}_1$  and  $\vec{\mathbf{S}}_2$  represent the incident and the emergent ray.  $\vec{\mathbf{L}}$  represents the normal vector.

The general procedure of tracing a small segment of the ray path is explained in Figure 1. The incident ray is marked as  $\vec{\mathbf{S}}_1$  [which starts at  $Q_1(x_1, y_1, z_1)$ ] and the emergent ray is marked as  $\vec{\mathbf{S}}_2$  [which reaches  $Q_2(x_2, y_2, z_2)$  after getting refracted at the interface ( $I_1$ ) where the refractive index  $\mu_1$  changes to  $\mu_2$ ]. Equation (13) implies that the values of refractive index  $\mu_1$  (at  $Q_1$ ) and  $\mu_2$  (at  $Q_2$ ) depend on  $N_e$  at the respective location. Therefore, the refractive indices specifically at  $Q_1$  and  $Q_2$  would become,

$$\mu_1 = \left[ 1 - \left( \frac{f_p(x + \delta x, y + \delta y, z + \delta z)}{\nu} \right)^2 \right]^{\frac{1}{2}} \quad (19)$$

$$\mu_2 = \left[ 1 - \left( \frac{f_p(x - \delta x, y - \delta y, z - \delta z)}{\nu} \right)^2 \right]^{\frac{1}{2}} \quad (20)$$

The ray vector  $\vec{\mathbf{S}}_1$  in equation (18) is derived from the line joining the points  $Q_1$  and  $I_1$ . Similarly  $\vec{\mathbf{S}}_2$  is from the line  $I_1Q_2$ . It is well known that a straight line in three dimensional space can be represented by its direction cosines (dc<sup>s</sup>). For example, the incident and emergent rays are written using their dc<sup>s</sup> as,

$$\vec{\mathbf{S}}_1 = a_1\hat{\mathbf{x}} + b_1\hat{\mathbf{y}} + c_1\hat{\mathbf{z}}, \quad (21)$$

$$\vec{\mathbf{S}}_2 = a_2\hat{\mathbf{x}} + b_2\hat{\mathbf{y}} + c_2\hat{\mathbf{z}} \quad (22)$$

respectively. The coefficients  $a_1, b_1, c_1$  in equation (21) are the dc<sup>s</sup> of the incident ray, whereas  $a_2, b_2, c_2$  in equation (22) are for the emergent ray.  $\hat{\mathbf{x}}, \hat{\mathbf{y}}, \hat{\mathbf{z}}$  are the unit vectors along the  $x, y,$  and  $z$  axis respectively, in the three-dimensional Cartesian coordinate system. The value of  $k$  in equation (18) is calculated from the following expression.

$$k = \frac{\mu_1}{\mu_2} (\vec{\mathbf{S}}_1 \cdot \vec{\mathbf{L}}) + \sqrt{\left( \frac{\mu_1}{\mu_2} \right)^2 (\vec{\mathbf{S}}_1 \cdot \vec{\mathbf{L}})^2 - \left( \frac{\mu_1}{\mu_2} \right)^2 + 1} \quad (23)$$

The normal vector  $\vec{\mathbf{L}}$  can be written as

$$\vec{\mathbf{L}} = a_L \hat{\mathbf{x}} + b_L \hat{\mathbf{y}} + c_L \hat{\mathbf{z}}, \quad (24)$$

where  $a_L, b_L,$  and  $c_L$  are its dc<sup>s</sup>, and are calculated using the following set of equations.

$$a_L = -\frac{\Delta N_x}{\Delta N} \frac{D}{|D|} \quad (25)$$



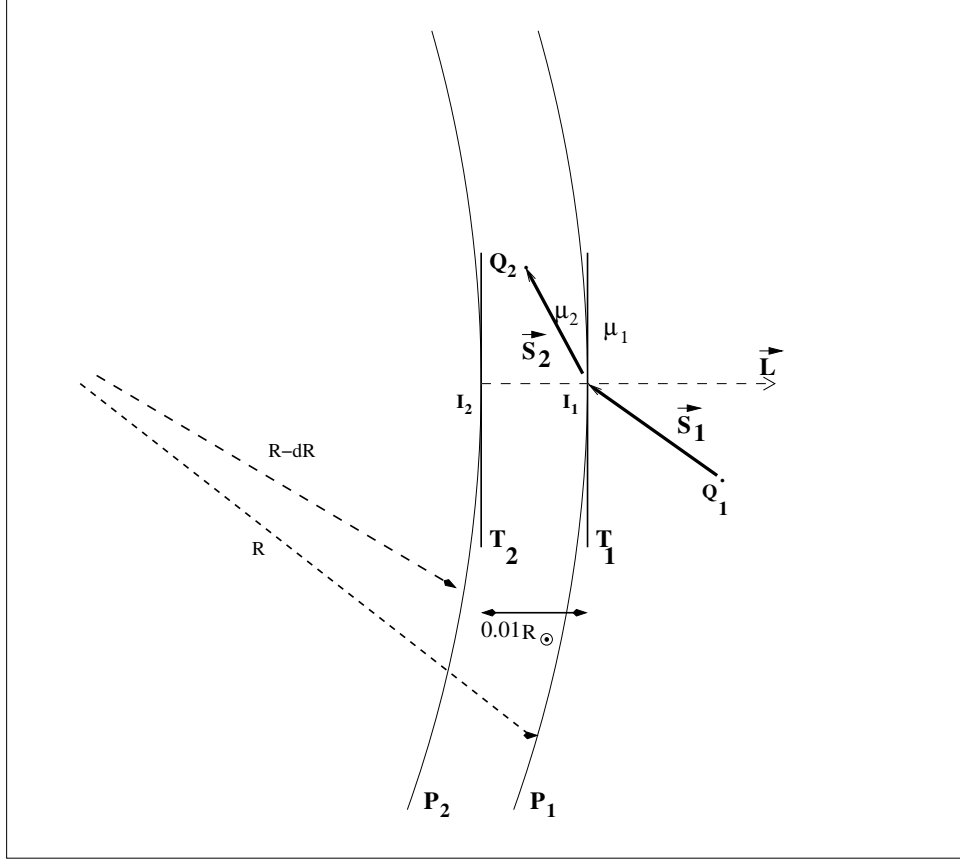


FIG. 1: The schematic diagram explaining the concept of ray path in a medium of variable refractive index (varying from  $\mu_1$  to  $\mu_2$ ).  $P_1$  and  $P_2$  are slices of the cross-section of two spherical layers of the corona. The radius of them are  $R$  and  $R - dR$  ( $dR = 0.01 R_\odot$  here) respectively from the center of the Sun.  $\mu_1$  is the refractive index to the right of the spherical layer  $P_1$  and  $\mu_2$  for the region between the layers  $P_1$  and  $P_2$ .  $T_1$  and  $T_2$  are two tangent planes to the above layers. The point of contact of  $T_1$  and  $T_2$  with  $P_1$  and  $P_2$  are  $I_1$  and  $I_2$  respectively. The normal vector  $\vec{L}$  is calculated using the electron density gradient. As we know the coronal density distribution follows a spherical symmetry and falls off radially, the gradient will be radially inward and therefore  $\vec{L}$  will be pointing outward in accordance with the definition. The trajectory/path of the ray is traced by sending  $\vec{S}_1$  from  $Q_1(x_1, y_1, z_1)$  towards  $I_1$  where it gets refracted (as  $\vec{S}_2$ ) and reaches  $Q_2(x_2, y_2, z_2)$  by following the Snell's law.

$$b_L = -\frac{\Delta N_y}{\Delta N} \frac{D}{|D|} \quad (26)$$

$$c_L = -\frac{\Delta N_z}{\Delta N} \frac{D}{|D|}, \quad (27)$$

where

$$\Delta N_x = N_e(x - \delta x, y, z) - N_e(x + \delta x, y, z) \quad (28)$$

$$\Delta N_y = N_e(x, y - \delta y, z) - N_e(x, y + \delta y, z) \quad (29)$$

$$\Delta N_z = N_e(x, y, z - \delta z) - N_e(x, y, z + \delta z), \quad (30)$$

are the change in the electron density (components of the density gradient along  $x$ ,  $y$ , and  $z$  axis respectively) which the ray experiences as it propagates through the medium. The quantities  $\Delta N$  and  $D$  are given as

$$(\Delta N)^2 = (\Delta N_x)^2 + (\Delta N_y)^2 + (\Delta N_z)^2 \quad (31)$$

$$D = (\Delta N_x) a_1 + (\Delta N_y) b_1 + (\Delta N_z) c_1 \quad (32)$$

Equations (25)-(27), imply that the tracing of ray path in the solar corona, depends on the electron density.

Hence, the reproduction of the observed brightness temperature  $T_{obs}$  through simulation requires a model for the coronal electron density distribution.

#### 4.3.2 Electron density model for the background corona

The electron density ( $N_e$ ) at any given point in the ‘background’<sup>2</sup> solar corona is generally determined from density models obtained using eclipse observations at visible wavelengths. Baumbach (1937) produced the first model which was later revised by Allen (1947). According to them,

$$N_e(r) = 1.55 \times 10^{14} r^{-6} + 2.99 \times 10^{14} r^{-16} \text{ m}^{-3}, \quad (33)$$

in the height range of 1-3  $R_\odot$  above the solar limb. ‘ $r$ ’ is the radial distance from the center of the Sun. The white light coronagraph data of Skylab were used by Saito (1977), Poland et al. (1977) to determine the density from 2.5-5.5  $R_\odot$ , i.e.

$$N_e(r) = 1.36 \times 10^{12} r^{-2.14} + 1.68 \times 10^{14} r^{-6.13} \text{ m}^{-3}. \quad (34)$$

---

<sup>2</sup>The corona free of sunspots, active regions and active filaments/prominences, etc.

Schmahl et al. (1994) had earlier used the density model of Allen (1947) and Saito (1977) to reproduce the one dimensional slices of coronal streamers observed with the Clark Lake Radioheliograph [CLRH; Kundu et al. (1983)]. They concluded that the reproduction of the observed brightness of a visible streamer in the latitude range 30-60° with reasonable density enhancement factors was not possible. Again, the streamer brightness temperature approaches and even exceeds the central brightness temperature for density enhancement factor above 10. In view of the above, we followed the density model given by Newkirk (1961) for our work. According to the latter the background electron density is,

$$N_q(r) = (4.2 \times 10^{10}) 10^{(4.32/r)} \text{ m}^{-3} \quad (35)$$

The subscript  $q$  means that the given electron density is for the ‘quiet’ corona.

#### 4.4 COMPUTING THE RAY PATH

The following subsections (4.4.1, 4.4.2, 4.4.3) explain how to trace a ray through the solar corona using the above model for electron density [equation (35)] under different circumstances. A program written in FORTRAN to achieve the above is given in Appendix-A with explanation.

##### 4.4.1 The Unrefracted Central Ray

The incident ray which makes an angle of 180° with respect to the normal is defined as the ‘central’ ray. The propagation path of a central ray through the solar corona is treated in this section (an example of normal incidence). Consider an arbitrary point  $I_1(x = 4.0 R_\odot, y = 0.0 R_\odot, z = 0.0 R_\odot)$  in the solar corona (see Figure 2). Let  $\vec{S}_1$  be an incident ray (of frequency <sup>3</sup>109 MHz) traveling in the negative  $x$  direction and therefore its dc<sup>s</sup> are  $a_1 = -1$ ,  $b_1 = 0$ , and  $c_1 = 0$ . The vectorial representation of the above incident ray is,

$$\vec{S}_1 = -1 \hat{x} + 0 \hat{y} + 0 \hat{z} . \quad (36)$$

Deducing the emergent ray vector  $\vec{S}_2$  from the incident ray constitutes the basic step of ray-tracing. Using equation (18),

$$\vec{S}_2 = \left( \frac{\mu_1}{\mu_2} \right) \vec{S}_1 - k \vec{L} , \quad (37)$$

---

<sup>3</sup>The frequency 109 MHz is specifically chosen because most of the GRH observations reported in this thesis were carried out at that frequency.

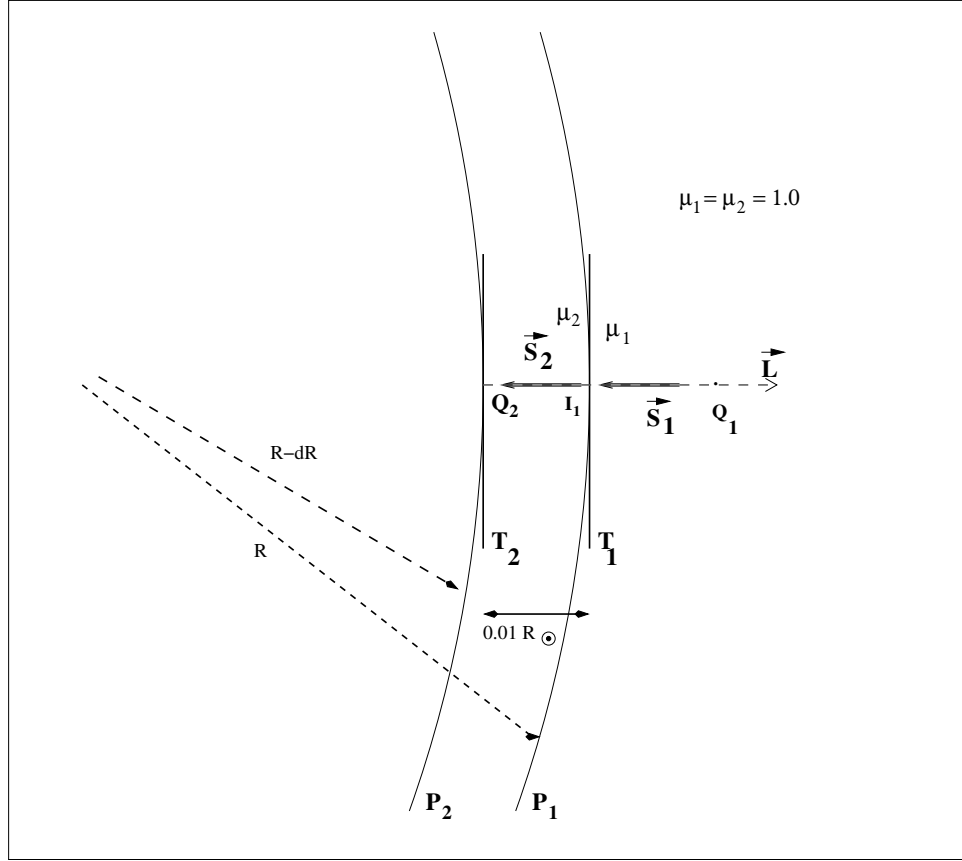


FIG. 2: The above diagram shows the trajectory of an unrefracted ray ( $\vec{S}_1 = \vec{S}_2$ ) at the point  $I_1(4.0 R_\odot, 0.0 R_\odot, 0.0 R_\odot)$ . The ray travels unrefracted because the values of refractive index to the right and to the left of it are approximately equal (*i.e.*,  $\mu_1 \approx \mu_2 = 1.0$ ). The ‘dashed’ line with an arrow head represents the normal vector ( $\vec{L}$ ). The incident ray ( $\vec{S}_1$ ) starts at  $Q_1$  and the refracted ray ( $\vec{S}_2$ ) ends at  $Q_2$ . This is a typical example for normal incidence since  $\vec{S}_1$  is anti-parallel to  $\vec{L}$  (the angle between them are  $180^\circ$ ). The ray of normal incidence is also called as the central ray (also it is the only ray that can reach the corresponding plasma layer). Refer Figure 1 for a more generalized situation of ray propagation.

and its components can be written as,

$$a_2 = \left( \frac{\mu_1}{\mu_2} \right) a_1 - k a_L \quad (38)$$

$$b_2 = \left( \frac{\mu_1}{\mu_2} \right) b_1 - k b_L \quad (39)$$

$$c_2 = \left( \frac{\mu_1}{\mu_2} \right) c_1 - k c_L \quad (40)$$

The value of  $\mu_1$  and  $\mu_2$  in the above 3 equations should be calculated using equations (19) and (20) at  $Q_1(x + \delta x, y + \delta y, z + \delta z)$  and  $Q_2(x - \delta x, y - \delta y, z - \delta z)$  respectively. Let us assume that  $\delta x = \delta y = \delta z = 0.01 R_\odot$  in our calculations. Therefore,

$$\mu_1 = \mu(4.01 R_\odot, +0.01 R_\odot, +0.01 R_\odot) \text{ and} \quad (41)$$

$$\mu_2 = \mu(3.99 R_\odot, -0.01 R_\odot, -0.01 R_\odot) . \quad (42)$$

The explicit expressions of refractive indices become

$$\mu_1 = \left[ 1 - \left( \frac{e^2}{4\pi^2 \epsilon_0 m} \times \frac{N_e(4.01 R_\odot, +0.01 R_\odot, +0.01 R_\odot)}{\nu^2} \right) \right]^{\frac{1}{2}} \text{ and} \quad (43)$$

$$\mu_2 = \left[ 1 - \left( \frac{e^2}{4\pi^2 \epsilon_0 m} \times \frac{N_e(3.99 R_\odot, -0.01 R_\odot, -0.01 R_\odot)}{\nu^2} \right) \right]^{\frac{1}{2}} . \quad (44)$$

Substituting for all the physical constants, we get a value of 80.6 for  $\frac{e^2}{4\pi^2 \epsilon_0 m}$ , and the values  $5.01 \times 10^{11}$  and  $5.08 \times 10^{11}$  per  $\text{m}^3$  for  $N_e$  at  $Q_1$  and  $Q_2$  respectively. For the 109 MHz ray, the values of respective refractive index would become

$$\mu_1 = \left[ 1 - (80.6) \frac{5.01 \times 10^{11}}{1.18 \times 10^{16}} \right]^{\frac{1}{2}} \approx 0.99 \text{ and} \quad (45)$$

$$\mu_2 = \left[ 1 - (80.6) \frac{5.08 \times 10^{11}}{1.18 \times 10^{16}} \right]^{\frac{1}{2}} \approx 0.99. \quad (46)$$

One can notice that the magnitudes of  $\mu_1$  and  $\mu_2$  are almost equal and close to unity. Therefore  $\mu_1/\mu_2$  will be 1.0 in equations (38)-(40). We also know the values of  $a_1, b_1, c_1$  from equation (36). The remaining unknown values in equations (38)-(40) are  $k, a_L, b_L$  and  $c_L$ . Equations (25)-(27) show that the above unknowns require the electron density gradient at the point  $I_1$ . Therefore,

$$\Delta N_x = N_e(3.99 R_\odot, 0.00 R_\odot, 0.00 R_\odot) - N_e(4.01 R_\odot, 0.00 R_\odot, 0.00 R_\odot) , \quad (47)$$

$$\Delta N_y = N_e(4.00 R_\odot, -0.01 R_\odot, 0.00 R_\odot) - N_e(4.00 R_\odot, 0.01 R_\odot, 0.00 R_\odot), \quad (48)$$

and

$$\Delta N_z = N_e(4.00 R_\odot, 0.00 R_\odot, -0.01 R_\odot) - N_e(4.00 R_\odot, 0.00 R_\odot, 0.01 R_\odot), \quad (49)$$

are evaluated and their values are  $6.278 \times 10^9$ ,  $0.0$  and  $0.0 \text{ m}^{-3}$  respectively. Substituting the above three values in equation (31), we get  $\Delta N = 6.278 \times 10^9 \text{ m}^{-3}$ . From equation (32),

$$D = (6.278 \times 10^9) (-1) + (0.0) (0.0) + (0.0) (0.0) = -6.278 \times 10^9 \text{ m}^{-3}, \quad (50)$$

and  $|D| = 6.278 \times 10^9$  per  $\text{m}^3$ . With the help of equations (25)-(27), and the ratio of  $D$  and  $|D|$  (which is equal to  $1.0$  here), we get  $a_L = 1.0$ ,  $b_L = 0.0$ , and  $c_L = 0.0$ . Therefore, the normal vector  $\vec{L} = 1.0 \hat{x} + 0.0 \hat{y} + 0.0 \hat{z}$ . The expression of  $k$  involves the projection of the incident vector on the normal vector through the dot product  $\vec{S}_1 \cdot \vec{L}$ , which is equal to  $-1.0$  in the present case. Inserting the numerical values for the above dot product and the ratio  $(\mu_1/\mu_2)$  in equation (23), we get  $k = 0.0$ . By substituting all known values in equations (38)-(40), the components of the emergent ray vector can be obtained as  $a_2 = -1.0$ ,  $b_2 = 0.0$  and  $c_2 = 0.0$ . Therefore

$$\vec{S}_2 = -1 \hat{x} + 0 \hat{y} + 0 \hat{z} . \quad (51)$$

From equations (36) and (51) it is clear that the incident and emergent ray vectors are identical, which implies that the incident ray is not refracted by the variation in refractive index at  $I_1(4.0 R_\odot, 0.0 R_\odot, 0.0 R_\odot)$ . Hence the ray which starts at  $Q_1$  will be directed to  $Q_2$ , according to the transfer characteristics of the medium (by following all the steps as explained before). The coordinates of  $Q_2(x_2, y_2, z_2)$  are obtained from  $Q_1(x_1, y_1, z_1)$  using the next set of equations.

$$x_2 = x_1 + (\Delta s) a_2 \quad (52)$$

$$y_2 = y_1 + (\Delta s) b_2 \quad (53)$$

$$z_2 = z_1 + (\Delta s) c_2 \quad (54)$$

The value of  $\Delta s$  should be chosen such that the ray should be accommodated well within the region of validity of the obtained refractive index. It is equal to  $0.005 R_\odot$  for our present example. Therefore, the ray which started at  $Q_1(4.0 R_\odot, 0.0 R_\odot, 0.0 R_\odot)$  will reach  $Q_2(3.995 R_\odot, 0.0 R_\odot, 0.0 R_\odot)$  after following equation (18), the Snell's law in vector form.

#### 4.4.2 The Brewster's angle and the reflection of a Central Ray

As the ray travels further into the inner layers of the corona, its intensity gets reduced due to absorption of the medium. The reduction is maximum where the refractive index is close to zero (for those rays whose frequency is close to the local plasma frequency). The nature of the ray trajectory near the plasma layer of zero refractive index is as follows.

Consider a ray of frequency 109 MHz sent from  $Q_1(4.0 R_\odot, 0.0 R_\odot, 0.0 R_\odot)$  which did not undergo refraction and reached a point  $Q_n(1.23 R_\odot, 0.0 R_\odot, 0.0 R_\odot)$  as shown in Figure 3. Note that the value of plasma frequency at  $Q_n$  is close to 109 MHz. The values of

$$\mu_1 = \mu(1.24 R_\odot, +0.01 R_\odot, +0.01 R_\odot) \quad (55)$$

and

$$\mu_2 = \mu(1.22 R_\odot, -0.01 R_\odot, -0.01 R_\odot) \quad (56)$$

are 0.26 and  $0.24i$  (an imaginary number) respectively. The law of wave propagation states that rays will not propagate inside a medium of imaginary refractive index and hence suffer total internal reflection (therefore only evanescent waves can exist over very small distances inside the medium). The above condition of reflection is verified with the following expression. That is, if

$$\left[ 1 - \left( \frac{f_p}{\nu} \right)^2 \right] \leq 0.0 \quad (57)$$

then equation (18) can not be applied directly as we saw in the previous example [refer section 4.4.1]. Special cases of this kind are treated under the category that deals with rays whose angle of incidence exceed the Brewster's angle. The latter can be confirmed from the value of the expression within the square root of equation (23). That is, if

$$\left( \frac{\mu_1}{\mu_2} \right)^2 (\vec{\mathbf{S}}_1 \cdot \vec{\mathbf{L}})^2 - \left( \frac{\mu_1}{\mu_2} \right) + 1 \leq 0.0, \quad (58)$$

then we get the following condition (a more comprehensible form that can be obtained by rearranging the terms in the above equation) which can be used to verify the reflection phenomenon.

$$(\vec{\mathbf{S}}_1 \cdot \vec{\mathbf{L}})^2 \leq 1 - \left( \frac{\mu_2}{\mu_1} \right)^2 \quad (59)$$

Once the square of the dot product of the ray vector with the normal satisfies the above inequality,  $\left( \frac{\mu_2}{\mu_1} \right)$  will be forced to 1, and  $k$  in equation (37) will be equal to

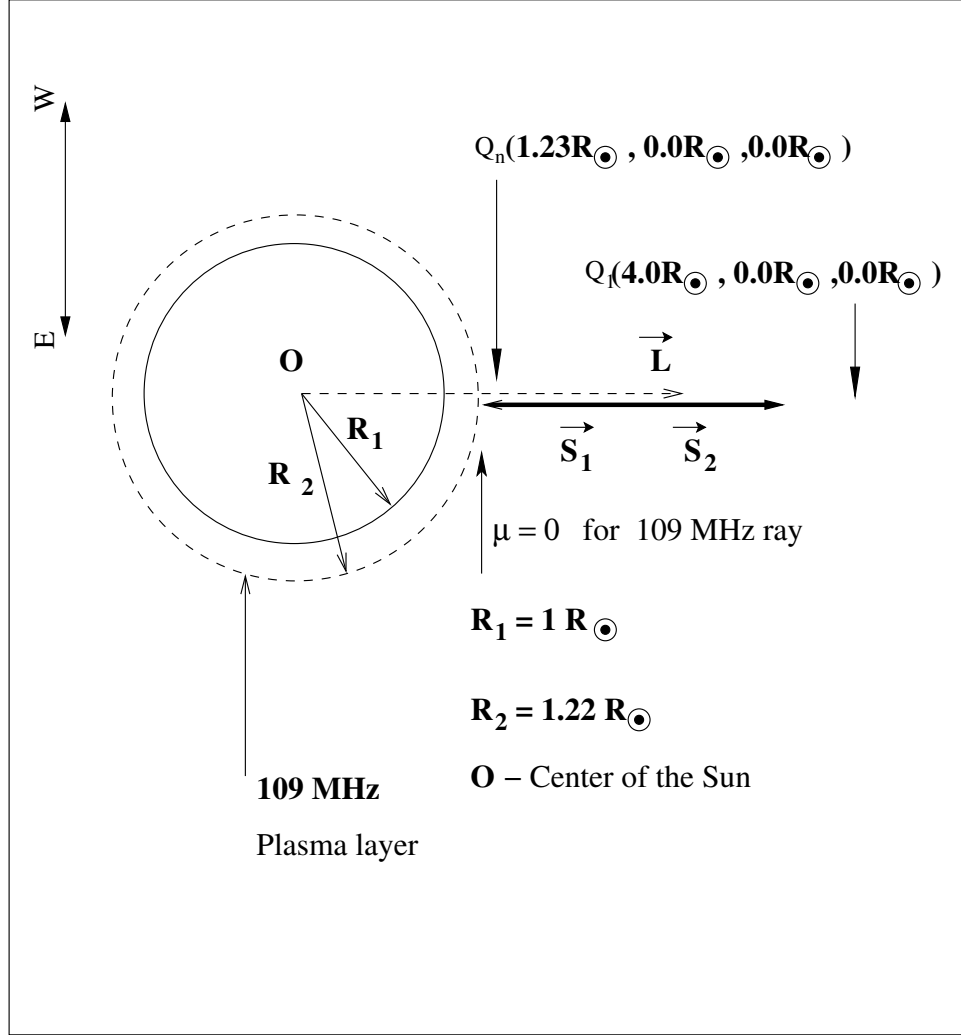


FIG. 3: The reflection of the ray near the layer where the refractive index is zero is explained in the above figure. The inner circle ( $R_1 = 1.0 R_\odot$ ) represents the photosphere and the outer dashed circle corresponds to the 109 MHz plasma layer. According to the density model of Newkirk (1961) the latter is at a height of  $1.22 R_\odot$  ( $R_2$ ) in the ‘undisturbed’ corona. The refractive index is  $\mu_1 (> 0.0)/\mu_2 (< 0.0)$  to the right/left of  $Q_n$  respectively. The dashed line with an arrow head is the normal vector  $\vec{L}$ . The thick line with a double sided arrow represent both the incident and the reflected ray ( $\vec{S}_1$  and  $\vec{S}_2$ ). The latter is drawn slightly away from the former for clarity. The magnitude of the emergent/reflected ray is equal to that of the incident ray but the direction is opposite, i.e. ( $\vec{S}_2 = -\vec{S}_1$ ).



two times  $\vec{S}_1 \cdot \vec{L}$ . Substituting the above values for  $(\mu_2/\mu_1)$  and  $k$  in equation (37), we get

$$\vec{S}_2 = \vec{S}_1 - 2(\vec{S}_1 \cdot \vec{L})\vec{L} \quad (60)$$

Taking dot product on both sides of equation (60) with  $\vec{L}$  leads to

$$\vec{S}_2 \cdot \vec{L} = \vec{S}_1 \cdot \vec{L} - 2(\vec{S}_1 \cdot \vec{L})(\vec{L} \cdot \vec{L}) \quad (61)$$

Since the sum of the squares of direction cosines ( $a_L, b_L, c_L$ ) of the normal is equal to unity, the term  $\vec{L} \cdot \vec{L}$  on the right hand side of equation (61) can be replaced with 1.0. Therefore equation (61) becomes,

$$\vec{S}_2 \cdot \vec{L} = -\vec{S}_1 \cdot \vec{L} \quad . \quad (62)$$

This leads to an emergent ray  $\vec{S}_2$  equal to  $-\vec{S}_1$  signifying the reflection of the latter by the plasma layer where the frequency of the incident ray is nearly equal to the local plasma frequency ( $f_p/\nu \approx 1.0$ ). Therefore

$$\vec{S}_2 = -\vec{S}_1 = -(-1\hat{x} + 0\hat{y} + 0\hat{z}) = 1\hat{x} + 0\hat{y} + 0\hat{z} \quad . \quad (63)$$

It should not be forgotten that the condition given in equation (59) has to be checked throughout the ray path to make sure that the ray is guided properly while undergoing refraction and reflection. The reflection that takes place for a ray whose angle of incidence is equal to  $180^\circ$  near the coronal medium of zero refractive index is shown in the same diagram (refer Figure 3). The location of the observer is approximately  $4 R_\odot$  from the center of the Sun.

Unwanted computational complications may occur at times when the emergent ray happens to enter into the region of imaginary refractive index. This problem for a ray arises when its coordinates of the destination are calculated from its previous point [which lies close to the layer of zero refractive index for that particular ray]. To overcome this, the value of the increment  $\Delta s$  [in equations (52)-(54)] has to be reduced such that the incident ray gets reflected exactly at the interface of zero refractive index (in other words it can be stated that the emergent ray has to be brought back into the region of real refractive index from the complex domain). The latter is achieved by equating  $\Delta s$  to its original value minus half of it (*for example, if the original value is  $0.01 R_\odot$  then the new value would be  $0.005 R_\odot$* ) until the above condition is achieved.

### 4.4.3 The Refraction of a Non-Central Ray

Consider a more general case in which the incident ray makes an angle different from  $180^\circ$  with the normal shown in Figure 4 (an example of oblique incidence). It should be noted that, apart from the central ray a non-central is drawn at a horizontal distance of ‘ $a$ ’ along the west direction. The latter is called as the impact parameter and in the present case it is equal to  $0.5 R_\odot$ ; The central ray is at  $a = 0.0 R_\odot$ . The attenuation for the non-central ray is maximum near the turning point (marked as ‘ $R_t$ ’) where the value of the absorption coefficient is relatively larger along the ray path. No extra steps are required to obtain ‘ $R_t$ ’, since the usual computational procedure handles easily this type of assignment too. For example, the turning point for the ray sent from the point  $Q_a(x = 4.0 R_\odot, y = 0.5 R_\odot, z = 0.5 R_\odot)$  was obtained as  $R_t(x = 1.045 R_\odot, y = 0.617 R_\odot, z = 0.612 R_\odot)$ . The dc<sup>s</sup> of the incident ray before getting refracted near  $R_t$  are  $a_1 = -0.06$ ,  $b_1 = 0.43$ , and  $c_1 = 0.43$  and  $a_2 = 0.004$ ,  $b_2 = 0.44$ , and  $c_2 = 0.44$ , respectively. As we saw in the case of reflection, the sign of the direction cosine got changed from a negative ( $a_1 = -0.06$ ) to a positive ( $a_2 = 0.004$ ) value (due to refraction) in the present case. Also, it implies that the ray did not get reflected exactly in the opposite direction like that of the central ray; but got refracted (from  $\vec{S}_1$ ) and followed the trajectory described by  $\vec{S}_2$ . It has to be highlighted here that rays which start at  $Q_a(x = 4.0 R_\odot, |y| \text{ and } |z| > 1.0 R_\odot)$  will undergo normal refraction (and it will not be a partial reflection as discussed here).

Apart from the basic requirements, the above necessary and sufficient conditions have to be met with in any simulation program related to ray-tracing.

## 4.5 DETERMINATION OF THE OPTICAL DEPTH

The ray path thus traced is divided into small segments of predefined length ( $l_i = 0.01 R_\odot$ ). The average value of the attenuation constant  $\alpha_i$  is evaluated at the mid point of every segment. The infinitesimal optical depth  $\tau_i$  is estimated by multiplying  $\alpha_i$  with its corresponding length segment  $l_i$  (refer Figure 5). Therefore, the total optical depth accumulated over the entire ray path is

$$\tau_{tot} = \int_0^{r_c} \alpha dr = \sum_{i=1}^n \alpha_i l_i , \quad (64)$$

where ‘ $n$ ’ is the number of segments that constitute the complete ray trajectory. The ray is stopped at  $10 R_\odot$ , after getting reflected or refracted due to the variation of

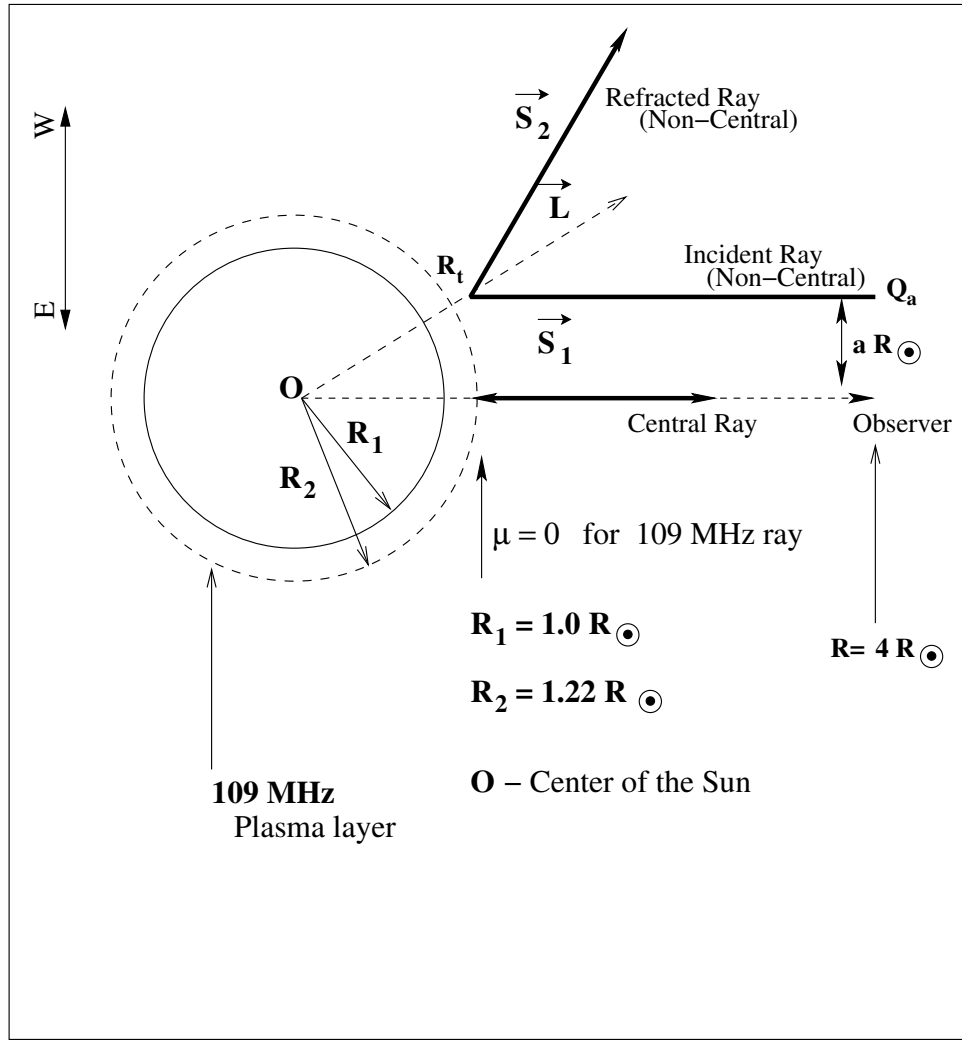


FIG. 4: The above figure explains the oblique incidence of a non-central ray. The inner thick circle represents the photosphere and the outer dashed circle corresponds to the plasma layer where the attenuation for the 109 MHz radiation will be maximum. The non-central ray is drawn ' $a R_\odot$ ' (value of the impact parameter) away from the central ray (considered as reference) near the observer's location ( $\approx 4 R_\odot$ ).  $\vec{S}_1$  is the incident ray vector and  $\vec{S}_2$  is the reflected ray vector. The normal vector ( $\vec{L}$ ) at any point on a spherically symmetric distribution will point outward in the radial direction. It is to be noted that the central ray has reached up to the plasma level whereas the non-central ray has not because the latter has undergone regular refraction and hence the reflection took place well above its corresponding plasma level near  $R_t$  (the turning point). The coordinates of the turning point for the ray which starts at  $Q_a(4.0 R_\odot, 0.5 R_\odot, 0.5 R_\odot)$  was obtained as  $R_t(1.045 R_\odot, 0.617 R_\odot, 0.612 R_\odot)$ .

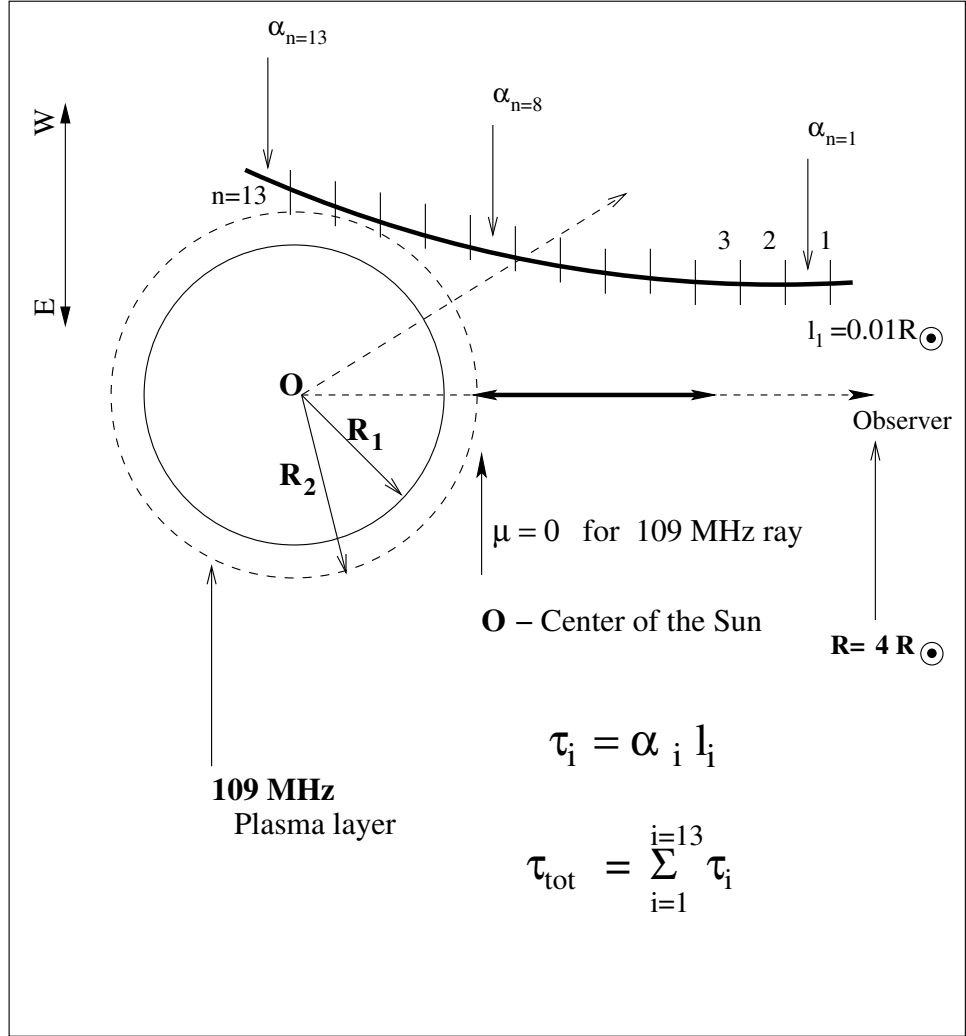


FIG. 5: The procedure that the computer program follows in estimating the accumulated optical depth along the complete ray path is shown in the above figure. The inner thick circle represents the photosphere and the outer dashed circle represents the 109 MHz plasma layer. The non-central ray is divided into 13 small segments with the vertical lines. The length of each segment ( $l_i$ ) is assumed as  $0.01 R_{\odot}$  (and is not according to the scale). The attenuation constant at the center of each segment ( $\alpha_i$ ) is calculated and multiplied with  $l_i$  to obtain the infinitesimal optical depth corresponding to that ray segment. The procedure is repeated for all the segments and total optical depth ( $\tau_{tot}$ ) is obtained by summing all  $\tau_i$ .

the electron density gradient in the medium, since the incremental optical depths obtained at larger distances away from the turning point will not contribute much to the total optical depth. The final value of  $\tau_{tot}$  has to be divided by 2 since the traced path has a length twice as that of the required path length. The next section will clarify this point.

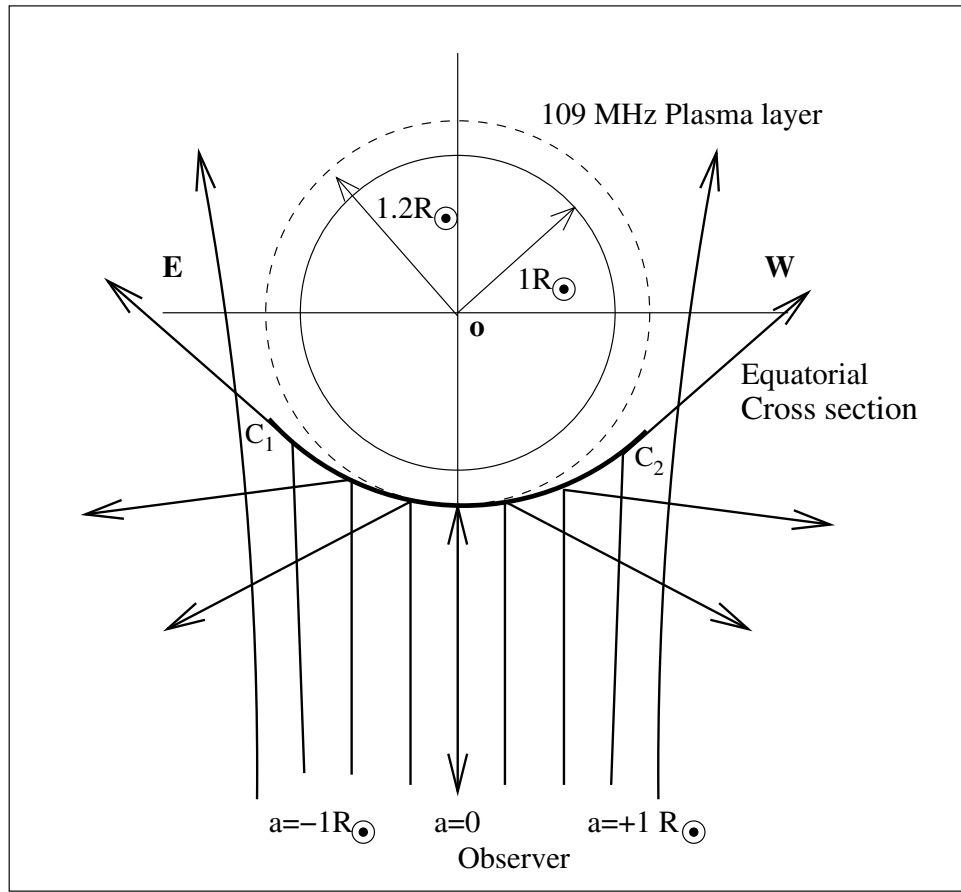
#### 4.6 THE REVERSIBILITY PROPERTY

The calculation of the total optical depth described in the previous section took the complete ray path into account. But actually  $\tau_{tot}$  has to be calculated from the point of generation of the ray to the location of the observer. From the computational point of view, tracing a ray from its exact point of origin in the inner layers of the corona to its outer layers is difficult. So, the ray paths are traced by sending rays parallel<sup>4</sup> to the direction of the observer's line of sight. Starting at a distance of  $\approx 10 R_{\odot}$  away from the front side of the Sun (the assumed apparent location of the observer or the image plane) each ray is first traced through the solar atmosphere (in the direction of the Sun) up to the plasma layer from where it gets reflected/refracted, and then continued for a similar distance (away from the Sun) either in the backward or a different direction depending on the case. Hence the technique uses the basic reversibility property of a ray [Born & Wolf (1970)].

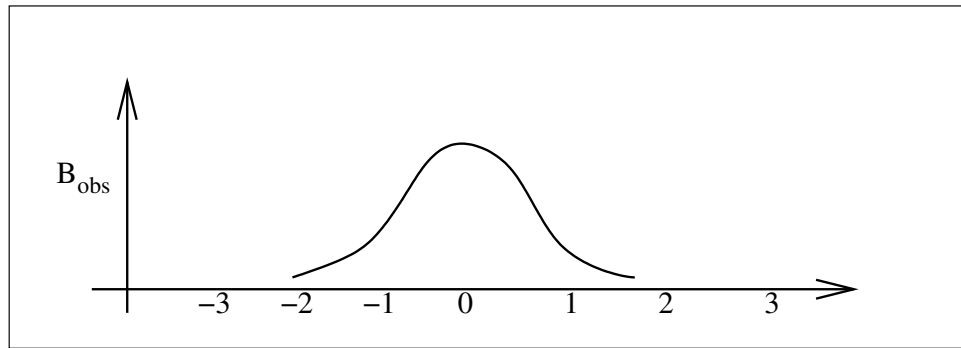
Making use of the above property, rays with different values of  $a$  are sent towards the Sun such that a spatial extent of  $7.5 R_{\odot}$  (the field of view of the GRH at 109 MHz), ranging from  $-3.75 R_{\odot}$  to  $3.75 R_{\odot}$ , is covered in steps of  $0.075 R_{\odot}$  both in the longitudinal (*east-west*) and latitudinal (*north-south*) directions in the image plane. This will give the values of optical depth at all points  $[\tau(y, z)]$  in the image plane. The ray trajectories for different values of  $a$  are shown in Figure 6 (a). It is clear that as the value of  $a$  increases the deviation of rays with respect to the incident direction (along the line of sight) reduces near their respective turning points ( $R_t$ ). Also, the turning points of rays of a particular frequency lie far away from the plasma layer as  $a$  increases. Hence, the accumulated optical depth will be very much less for higher values of the impact parameter and vice versa. Therefore, if we plot the brightness temperature as a function of impact parameter along the east-west direction, then the former has larger values close to small values of the latter and vice versa [Figure

---

<sup>4</sup>The plane wave fronts from a source will be parallel if the distance ' $d$ ' between the observer and the source of radiation is larger compared to its wavelength ' $\lambda$ '.



(a) Ray trajectories



(b) Brightness temperature distribution

FIG. 6: The top panel (a) shows the ray trajectories that reach different points on the image plane. The thick circle ( $R = 1 R_{\odot}$ ) represents the photosphere. A similar cross section of the 109 MHz plasma layer ( $R = 1.2 R_{\odot}$ ) is represented with the dashed circle. The north pole goes through the point 'O' and is perpendicular to the plane of the paper. East is to the left and west is to the right. The impact parameter ' $a$ ' is varied from  $-3.75 R_{\odot}$  to  $3.75 R_{\odot}$  along the east-west direction in steps of  $0.075 R_{\odot}$  (the spatial separation between adjacent points in GRH radio images). The thick circular arc ( $C_1C_2$ ) represents the locus of turning points of rays of different impact parameter. The bottom panel (b) shows a theoretically generated one dimensional brightness temperature distribution as a function of the impact parameter. The coordinates can be converted from linear to angular scale using the relation:  $1 R_{\odot}$  to  $16'$  (see Figure 7).

6 (b)]. A similar distribution for the brightness temperature can be drawn along the north-south direction also. The temperature along the different longitudinal and latitudinal directions on the Sun can be filled up in a similar fashion and the radio brightness temperature distribution in two-dimensions [ $T_o(y, z)$ ] in the image plane can be obtained.

## 4.7 THE RADIO BRIGHTNESS TEMPERATURE DISTRIBUTION IN TWO DIMENSIONS

### 4.7.1 The ‘undisturbed’ solar corona

Figure 7 shows the contour map of a two dimensional brightness temperature distribution of the ‘undisturbed’ Sun at 109 MHz obtained using the ray-tracing method. The background density is assumed to be equal to the Newkirk density [given in equation (35)], and the background temperature is taken as  $1.0 \times 10^6$  K. The variable  $y$  along the equatorial direction and  $z$  along the polar direction are allowed to vary from  $-3.75 R_\odot$  to  $3.75 R_\odot$  in steps of  $0.075 R_\odot$ . The ray trajectories are traced for all possible combinations of  $y$  and  $z$  and the respective total optical depth  $\tau_{tot}(y, z)$  accumulated by each ray is calculated. Finally the brightness temperature is obtained using equation (9). The region between any two successive contours in the simulated radio map represent area of iso-brightness temperature. The peak brightness temperature of the theoretically generated distribution in the aforementioned image is  $\approx 1.0 \times 10^6$  K, and the temperature difference is of the order of  $1.0 \times 10^5$  K, between any two adjacent/successive contours.

### 4.7.2 The ray plane

As it is expected all points on the ray trajectory in an ‘undisturbed’ solar corona lie in a plane (will be referred to as ‘ray plane’ hereafter) according to the principle of congruence [Born & Wolf (1970)] of rays in a homogeneous medium. We know that the general equation of a plane is written as

$$A_1 x + A_2 y + A_3 z + A_4 = 0 , \quad (65)$$

where  $A_1, A_2, A_3$  are  $x, y, z$  coefficients of the plane respectively and  $A_4$  is a constant. Also, if any three points [say,  $H_1(x_1, y_1, z_1)$ ,  $H_2(x_2, y_2, z_2)$ , and  $H_3(x_3, y_3, z_3)$ ] that lie in a plane are known, then the equation of the latter in terms of the former

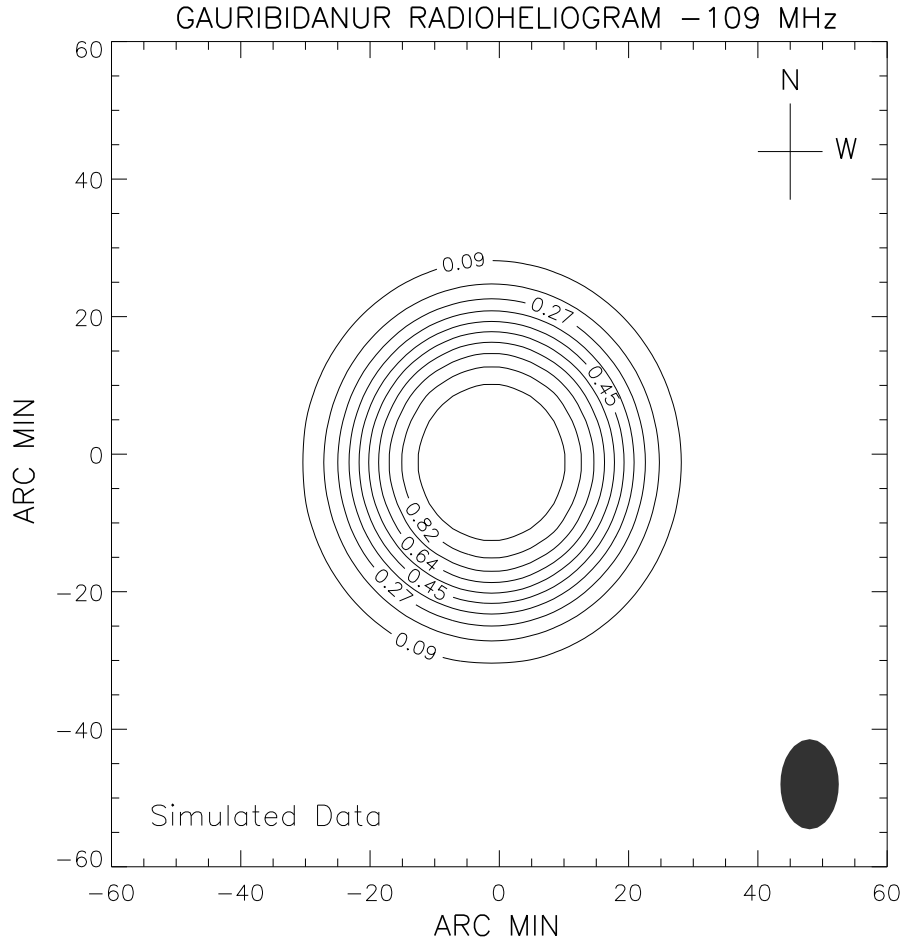


FIG. 7: The contour map represents the simulated two dimensional brightness temperature distribution of the background corona at 109 MHz. The background density and temperature are assumed to be equal to  $(4.2 \times 10^4) \times 10^{4.32/r} \text{ cm}^{-3}$  and  $1.0 \times 10^6 \text{ K}$  respectively. The peak brightness temperature is  $\approx 1.0 \times 10^6 \text{ K}$  and the difference in temperature between successive contours is  $\sim 1.0 \times 10^5 \text{ K}$ . The region between any two successive/adjacent contours represent the region of equal intensity in the image plane (and hence in the sky plane). The north pole of the Sun is marked as ‘N’. The direction west (‘W’) is to the right and East is to the left. The filled contour at the right bottom is the beam size of the GRH at 109 MHz.



can be written using a determinant in the following form, i.e.,

$$\begin{vmatrix} x & y & z & 1 \\ x_1 & y_1 & z_1 & 1 \\ x_2 & y_2 & z_2 & 1 \\ x_3 & y_3 & z_3 & 1 \end{vmatrix} = 0 . \quad (66)$$

For example, the following 3 points (a subset) were arbitrarily selected from a set of points (generated by the FORTRAN code given in Appendix-A) on the ray trajectory whose starting point was at  $Q_1(4.0 R_\odot, 0.5 R_\odot, 0.5 R_\odot)$ . They were,

$$H_1 = (1.91, 0.50, 0.50), \quad (67)$$

$$H_2 = (1.04, 0.62, 0.62), \quad (68)$$

$$H_3 = (2.88, 3.05, 3.05). \quad (69)$$

Substituting the above points (all in units of  $R_\odot$ ) in the determinant expression the equation of the ray plane becomes,

$$y - z = 0 . \quad (70)$$

The co-planarity of any other point on the plane can be demonstrated with equation (65). The angle ( $\theta_p$ ) between the above ray plane and any other reference plane can be calculated from the following formula.

$$\theta_p = \cos^{-1} \left( \pm \frac{A_1 B_1 + A_2 B_2 + A_3 B_3}{\sqrt{(A_1^2 + A_2^2 + A_3^2)} \sqrt{(B_1^2 + B_2^2 + B_3^2)}} \right) , \quad (71)$$

where the set of coefficients ( $B_1$ ,  $B_2$ ,  $B_3$ , and  $B_4$ ) represent the reference plane. Therefore, ' $\theta_p$ ' between the above ray plane ( $y - z = 0$ ) and the equatorial plane ( $z=0$ ) is estimated to be  $135^\circ$  (see Figure 8). The angle  $\theta_p$  may vary from  $0 - 180^\circ$  depending upon the starting point of the ray in the image plane. Hence, it is obvious that the whole  $360^\circ$  angular span can be covered with the complete set of rays that form the image plane.

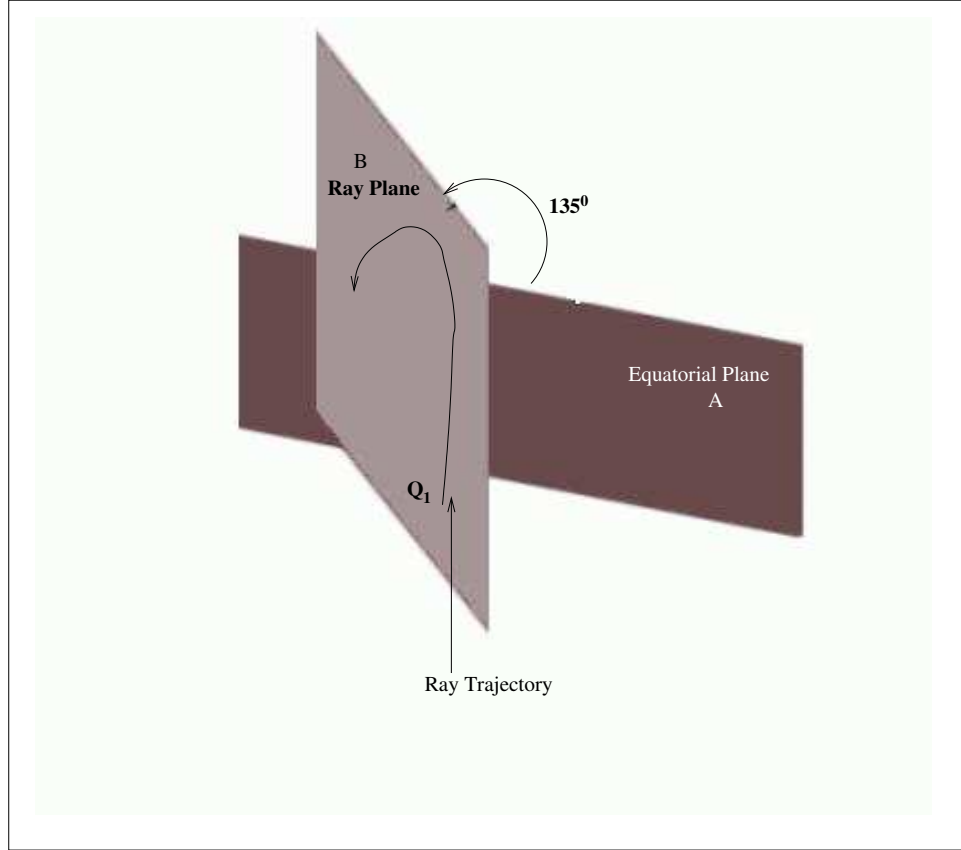


FIG. 8: The above figure explains the planar property of a central/non-central ray in the ‘undisturbed’ corona. The equatorial plane is marked as ‘A’ while the ray plane is marked as ‘B’. The angle ( $\theta_p$ ) between the above two planes is  $\approx 135^\circ$ , which means that the set of points on the ray trajectory whose starting point is at  $Q_1(4.0 R_\odot, 0.5 R_\odot, 0.5 R_\odot)$  will lie in plane ‘B’. Therefore the planes of the rays with different starting points in the image plane will have different tilt angles with respect to the equatorial (or reference) plane. But, it has to be kept in mind that the trajectory will not lie in a plane if the density gradient of the background corona is altered by the enhancement/decrement of density due to coronal activity; The ray will deviate from the plane at the point where it encounters a density enhancement/decrement.

### 4.7.3 The active solar corona - Density and Temperature models

#### (a) The Newkirk's model

Usually the observed brightness distribution of the solar corona will not be symmetric, particularly in the meter-decameter wavelength range. Figure 9 shows the outer most contour of the observed brightness distribution of the solar corona obtained with the GRH on November 24, 2000 at 05:25 UT.

Obviously, models which represent only the background electron density and temperature of the solar corona will not be sufficient to reproduce an asymmetric brightness distribution. One has to introduce density and temperature enhancement/decrement in the ray-tracing calculations. Newkirk (1959) had developed a conical model for the density distribution within coronal condensations that form above active regions. The total electron density within the region of the cone is  $N_e(r) = N_q(r) + N_{\mathcal{A}}(r)$ . The subscript  $\mathcal{A}$  is given for the electrons present within the active region. One can write the above equation explicitly in the following form, i.e.,

$$N_e(r) = (4.2 \times 10^{10}) 10^{4.32/r} \left[ 1 + \sum_{i=1}^n C_i e^{-(\beta_i^2/2\sigma_i^2)} \right] \quad (72)$$

where  $C_i$  is the enhancement/decrement factor and  $\sigma_i$  is its corresponding size.  $\beta_i$  can be obtained from the following expression.

$$\beta_i^2 = (x - R\cos\theta_i)^2 + (y - R\sin\theta_i)^2 + z^2 \quad , \quad (73)$$

where  $\theta_i$  is the orientation of the axis of the active region with respect to the observer's line of sight and  $R$  is the radial distance from the center of the Sun. Initially the same model given by Newkirk (1961) for the density enhancement pertinent to coronal structures was used. But only a few structures present on the solar disk could be reproduced with the above model, with the enhancement factor in the range 5-10. Also it was found that a faithful reproduction was not at all possible for the structures which were completely off the limb (for example the extended structure off the north west limb in Figure 9) even for large values of the enhancement factor.

The difficulties experienced with the above model for the density enhancement/decrement are the following.

- Consider the radio source at location '8' (will be specified as  $S_8$  hereafter) in Figure 9. In the image plane its linear distance from the center of the Sun is

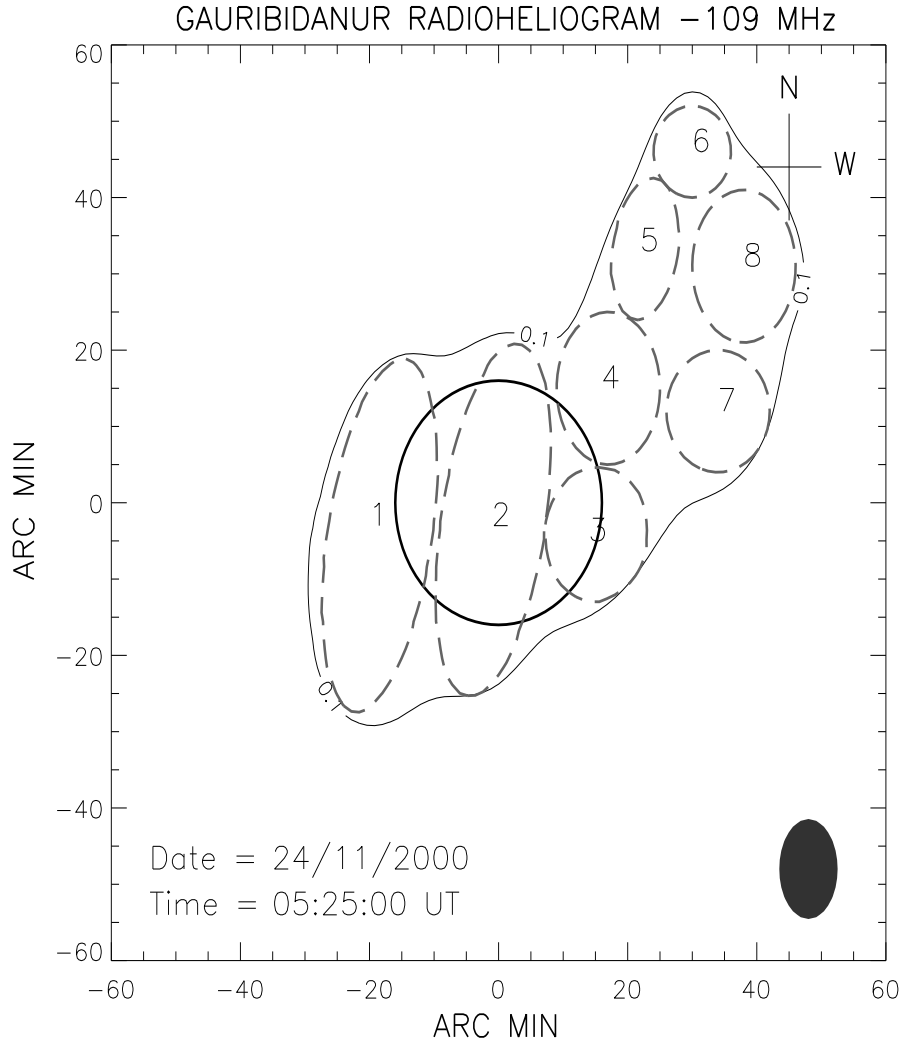


FIG. 9: The outer most contour (closed envelope) of the radio image observed with the GRH on November 24, 2000 is shown (refer Figure 6 in chapter 3). The eight long dashed contours inside the outer envelope of the observed brightness temperature represent the angular extents (both east-west and north-south) of the discrete radio structures. Their approximate centroids are marked from 1 to 8. The approximate centroids and the angular extents of the above discrete radio sources obtained by a visual inspection of the observed radioheliograms are used as the initial parameters in the ray-tracing program to reproduce the observed brightness temperature distribution.

approximately  $3 R_{\odot}$ . With Newkirk's density model for the quiet corona,  $N_e$  should be approximately  $1.1 \times 10^{12} \text{ m}^{-3}$  at  $S_8$ . This corresponds to a plasma frequency of 10 kHz. But, on the other hand the observed radio emission at 109 MHz in the present case indicates that the electron density at  $3 R_{\odot}$  was  $\approx 1.5 \times 10^{14} \text{ m}^{-3}$ . This implies that the local electron density has been enhanced nearly 100 times. Though the density was enhanced by a factor of 50 (taking into consideration the refraction effects) and above at  $S_8$  the observed radio enhancement in the map could not be reproduced successfully using Newkirk's conical model for density enhancement.

Hence, it is clear that the density can not be enhanced/decreased at large distances from the limb with the present model.

- The size of a radio structure in any specified direction is its 'Full Width at Half Maximum' (FWHM). For example the FWHM of  $S_8$  in Figure 9 is about  $30'$  in the east-west direction (y-size) and  $40'$  in the north-south direction (z-size). It should be noted that the size along the observer's line of sight (along x-axis) can not be determined from the image since it is projected onto the plane of the sky. An estimation of the size along the line of sight using ray-tracing calculations with Newkirk's model was not possible, since it does not have the provision for the inclusion of the size of a structure along its line of sight. Also, the size along different directions (in 3-Dimension) were assumed to be the same.

Therefore, the new model for the density enhancement/decrement should have independent parameters to include the size of a radio structure along three orthogonal directions ( $x$ ,  $y$ , and  $z$  axis respectively).

- Also from the observed images it is clear that the structures of different sizes are located at different positions in the 3-Dimensional space. In other words it can be stated that centroids of different structures have to be localized at their respective places such that the radio emission of a particular frequency emanate from them should produce the expected/observed radio flux density. The latter demands that the new model should have suitable means to supply the parameters related to the coordinates of source centroids.

Schmahl et al. (1994) reached a similar conclusion while trying to reproduce CLRH observations of coronal streamer using (i) fan/cone model in which the density falls

off as a Gaussian function from the axis and (ii) cylinder model in which the density falls off as a function of distance perpendicular to the axis.

### (b) The Gaussian Model

The above points led us to follow a Gaussian model (in 3-Dimension) for incorporating the density enhancement/decrement associated with coronal structures. Again, the expression for the resultant electron density resemble Newkirk's model [equation (72)], and is given as,

$$N_e(r) = (4.2 \times 10^4) 10^{(4.32/r)} \left[ 1 + \sum_{i=1}^n C_i e^{-\beta_i^2} \right] \quad (74)$$

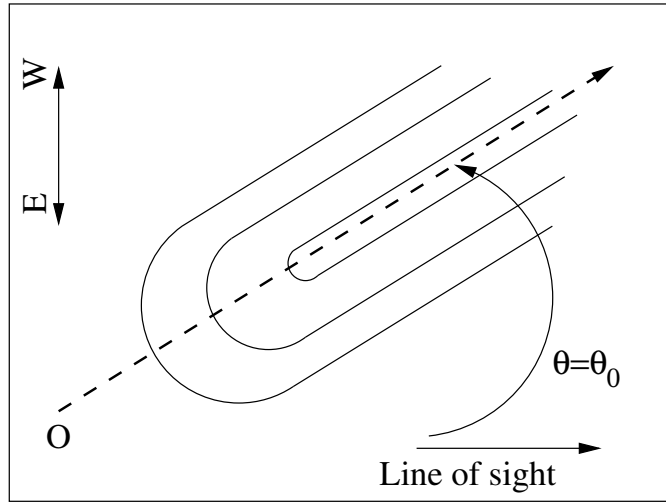
But the definition of  $\beta$  differs from his idea, and is written as

$$\beta_i^2 = \left[ \frac{x - x_i}{2(\sigma_x)_i} \right]^2 + \left[ \frac{y - y_i}{2(\sigma_y)_i} \right]^2 + \left[ \frac{z - z_i}{2(\sigma_z)_i} \right]^2 \quad (75)$$

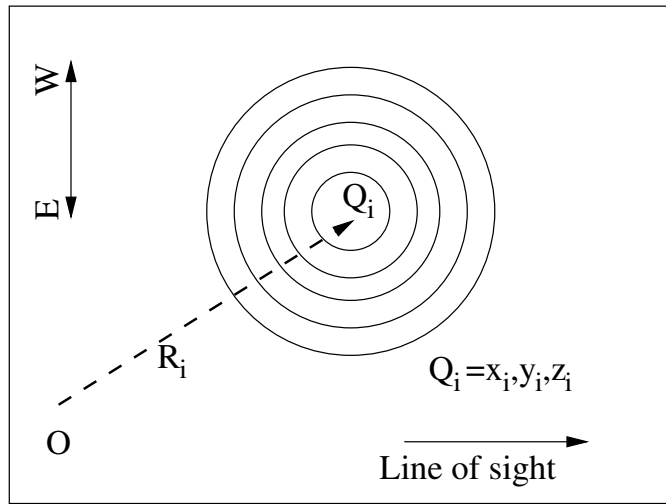
where  $(x_i, y_i, z_i)$  is the centroid of the 'i' th radio structure and  $(\sigma_x)_i$ ,  $(\sigma_y)_i$  and  $(\sigma_z)_i$  are its size along the  $x$ ,  $y$ , and  $z$  axis respectively. Therefore a radio structure in three dimensional space can be localized at a particular location  $(x_i, y_i, z_i)$  with specified dimensions  $[(\sigma_x)_i, (\sigma_y)_i, (\sigma_z)_i]$  on three different axes. Also, a similar distribution for the temperature was developed to study the effects of temperature variation inside radio structures. Thus it becomes,

$$T = T_e \left[ 1 + \sum_{i=1}^n G_i e^{-\gamma_i^2} \right], \quad (76)$$

Where  $G_i$  denotes the temperature enhancement/decrement, of 'i' th radio structure with respect to the quiet background and  $\gamma_i$  (like  $\beta_i$ ) details its location and sizes along different axes. By fitting structures of different sizes at different locations using the above model the observed brightness temperature can be reproduced. Figure 10 (a) and (b) explain the difference between the above two models. Newkirk model for the density enhancement follows conical/cylindrical symmetry; But the Gaussian model assumes nearly spherical symmetry. The latter is localized and has a finite size along the three orthogonal axes of a 3-D Cartesian coordinate system. The localization property is used to enhance the density even at large distances from the limb and the sizes can be used to enlarge/reduce the structures so that the reproduced image nicely fits with the observed radio maps of the Sun. Also, it can be shown that the conical model is a subset of the Gaussian model, i.e., the former can be simulated with the latter.



(a) Newkirk model



(b) Gaussian model

FIG. 10: Iso-density contours explaining the difference between the conical and Gaussian model (conical and Gaussian) for the density enhancement/decrement. In both panels [(a) and (b)] the center of the Sun is at ‘O’ and the solid line with an arrow head is pointing towards the location of the observer. The direction west is straight up and the north pole is perpendicular to the plane of the paper. Only the equatorial cross sections are shown here and the contours represent constant density/temperature (D/T) regions. (a) The D/T enhancement in Newkirk model assumes a conical/cylindrical distribution (in 3-D) whose axis (dashed line with an arrow head) makes an angle  $\theta_0$  with respect to observer’s line of sight. (b) The Gaussian model is localized at  $Q_i(x_i, y_i, z_i)$  and its size in all three directions are finite (resembles a sphere/ellipsoid in 3-D) and independent. The centroid of this closed structure from ‘O’ is at a distance of  $R_i \left( = \sqrt{x_i^2 + y_i^2 + z_i^2} \right)$ .

#### 4.7.4 The non-coplanar property

From the condition of co-planarity (refer section 4.7.2) it can be proved that the ray trajectory before and after it encounters the enhancement/decrement will not lie in the same plane. Let us consider, a density enhancement (10 times as that of the background) at location  $Q_{en}(1.0 R_{\odot}, 0.5 R_{\odot}, 0.5 R_{\odot})$  and compute the ray path from  $Q_1(4.0 R_{\odot}, 0.5 R_{\odot}, 0.5 R_{\odot})$  with the help of the ray-tracing program. The suffix 'en' represents the enhancement of density at the point  $Q_{en}$ . It was found that the ray went through the following point  $Q_{404}(1.36 R_{\odot}, 1.12 R_{\odot}, 1.20 R_{\odot})$ , when it encountered the density enhancement at  $Q_{en}$ . The suffix '404' implies that the point  $Q_{404}$  is on the 404<sup>th</sup> ray segment in the ray path. We already know that the equation of the ray plane in the 'undisturbed' corona for the ray which starts at  $Q_1$  in the image plane is  $y - z = 0$  [equation (66)]. Therefore, if  $Q_{404}$  has to lie on the above plane, it has to satisfy the above equation. By substituting  $Q_{404}$ , it can be shown that the right hand side of equation (66) is a non-zero value ( $-0.07 R_{\odot}$ ) and hence it will not lie on the above ray plane. Therefore, it is clear that the ray after encounter will travel in a different plane from that it traveled before (refer Figure 11).



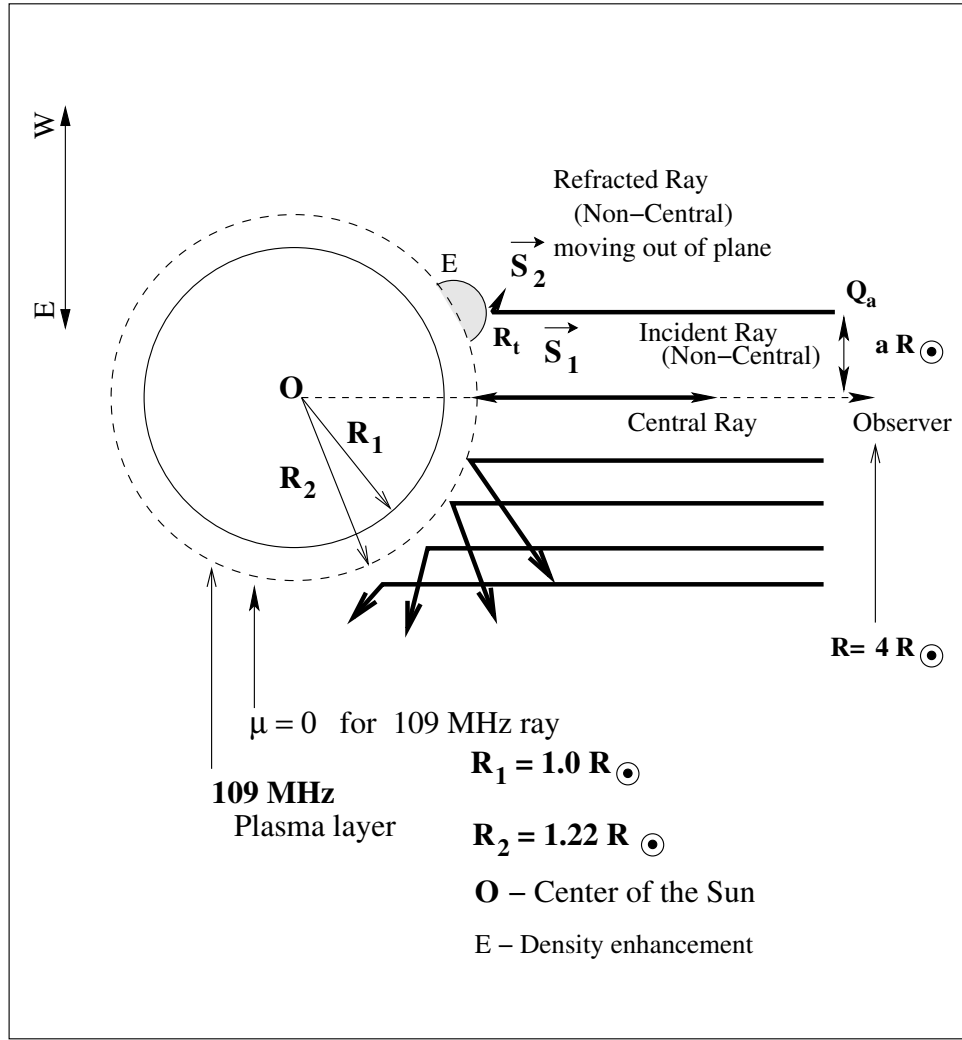


FIG. 11: Ray trajectory of a non-central ray in the presence of a density enhancement (marked as 'E'). The inner thick circle represents the photosphere and the outer dashed circle corresponds to the background plasma layer at 109 MHz. The non-central ray is drawn ' $a R_{\odot}$ ' away from the central ray that starts at a location  $\approx 4 R_{\odot}$  (taken as reference) from the center of the Sun.  $\vec{S}_1$  is the incident ray vector and  $\vec{S}_2$  represents the emergent ray vector.  $R_t$  is its turning point. Note that the ray trajectory before  $R_t$  lies in the plane of the paper whereas the emergent ray is not (shown without an arrow head).

## CHAPTER 5

# METER WAVELENGTH OBSERVATIONS AND RAY-TRACING ANALYSIS OF THE PRE-EVENT PHASE OF A CORONAL MASS EJECTION

### 5.1 INTRODUCTION

The pre-event evolution of coronal structures (both on the disk as well as off the limb) is an integral part of a mass ejection phenomena from the solar atmosphere, and it is essential to study their characteristics.  $H\alpha$ , microwave, EUV and X-ray observations play a useful role in this connection since one can observe activity at any longitude on the solar surface. In a typical CME/flux rope scenario, a CME is described as a streamer arcade containing a flux rope (filament) overlying a single magnetic neutral line [Hirayama (1974); Kopp and Pneuman (1976); Low (1994); Lin and Forbes (2000)]. In one case study of a prominence associated CME, Illing and Hundhausen (1985) showed that the lift-off of the latter is closely associated with rise of the prominence and surrounding dark cavity through the low corona. The top of the helmet streamer is pushed outside and it swells/expands like a balloon. This phase is called as the ‘pre-ejection swelling of the existing coronal helmet streamer’. The swelling time scale is event dependent and in many cases it lies in the range of a few days [Hundhausen (1997)]. Observations of CMEs that are associated with pre-event swelling of helmet streamer indicate that its mass is almost equal to the mass of the frontal structure of the former [Illing and Hundhausen (1986)]. Since the CME frontal structure has a large optical depth at meter wavelengths [Bastian and Gary (1997); Gopalswamy (1999)], one should be able to observe the pre-event swelling of a helmet streamer in the above wavelength range. According to Hundhausen (1988), CMEs that exhibit 3-part structure are usually associated with the swelling of helmet streamer that existed at the same location, prior to its eruption. Given the situation, we present meter wavelength radio imaging observations of the prominence eruption associated CME of June 2, 1998 that showed a nice 3-part structure (Figure 1). We modeled the observed radio brightness distribution by reproducing it using ray-tracing technique. Note that the modeling of CMEs particularly in three dimensions is an active area of research, of late. Raymond (2004) suggested the possibility of

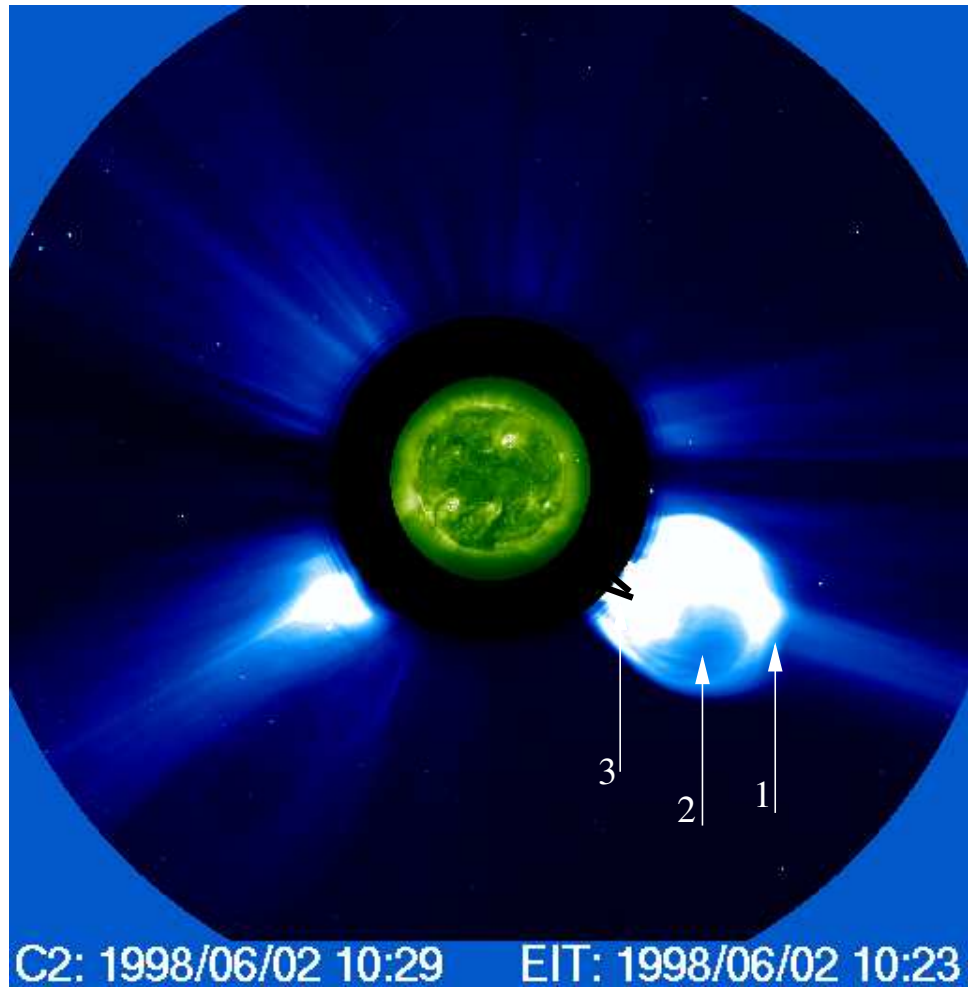


FIG. 1: White light image of the CME observed with the LASCO C2 coronagraph on June 2, 1998 at around 10:29 UT. Arrows labeled 1, 2 and 3 indicate the three-part structure (frontal structure, cavity and prominence respectively) of the CME. The open circle at the center is the solar limb. The outer circle is the occulter of C2 coronagraph. It extends approximately up to  $2.2 R_{\odot}$  from the center of the Sun.

using a series of LASCO CME images obtained at different time intervals and their corresponding velocity measurements along the line of sight to reconstruct the three dimensional structure of CMEs. Moran and Davila (2004), Dere et al. (2005) used the degree of polarization as a function of scattering angle to determine the three dimensional structure of CMEs.

## 5.2 OBSERVATIONS

Figure 2 shows the radioheliogram obtained with the GRH on June 2, 1998 at 109 MHz around 07:30 UT. The observed peak brightness temperature was  $1.4 \times 10^6$  K. No non-thermal emission were reported during our observing period [Sol.-Geophys. Data (1998b)]. According to the CME catalog<sup>1</sup> for the year 1998, the LASCO C2 coronagraph observed a CME close to the west limb on that day at around 08:08 UT (the time at which it was first noticed in C2 field of view). The event was accompanied by a prominence eruption from a location that was about  $15^\circ$  south of active regions NOAA AR8224 (S35E01) and AR8228 (S23W52) [Plunkett et al. (2000)]. Figure 3 shows the LASCO C2 running difference of the CME obtained at 08:08 UT on June 2, 1998. The central position angle of the CME was  $245^\circ$ , and its angular span was  $59^\circ$ . The estimated speed (from a second order fit) and acceleration of the CME in the plane of the sky were  $1278 \text{ km s}^{-1}$  and  $45.2 \text{ m s}^{-2}$ , respectively. The leading edge of the CME was observed at a projected height of  $2 R_\odot$  around 07:40 UT in the field of view of the LASCO C1 coronagraph [Plunkett et al. (2000)]. This suggests that the extended, faint radio emission at the corresponding location in Figure 2 could be related to the former.

## 5.3 ANALYSIS

### 5.3.1 Reproduction of the observed radio brightness distribution

The ‘background’ corona free of any active centers is generally assumed to be homogeneous and spherically symmetric in ray-tracing calculations [Thejappa and Kundu (1992)]. The various discrete structures seen in the observed radio images are due to localized density and temperature enhancements above the ‘background’. Therefore, in order to reproduce the observed radio brightness distribution in Figure 2, suitable values for the background temperature ( $T_{bg}$ ) and density ( $N_{bg}$ ) should

---

<sup>1</sup>[http://cdaw.gsfc.nasa.gov/CME\\_list/UNIVERSAL/1998\\_06/univ1998\\_06.html](http://cdaw.gsfc.nasa.gov/CME_list/UNIVERSAL/1998_06/univ1998_06.html)

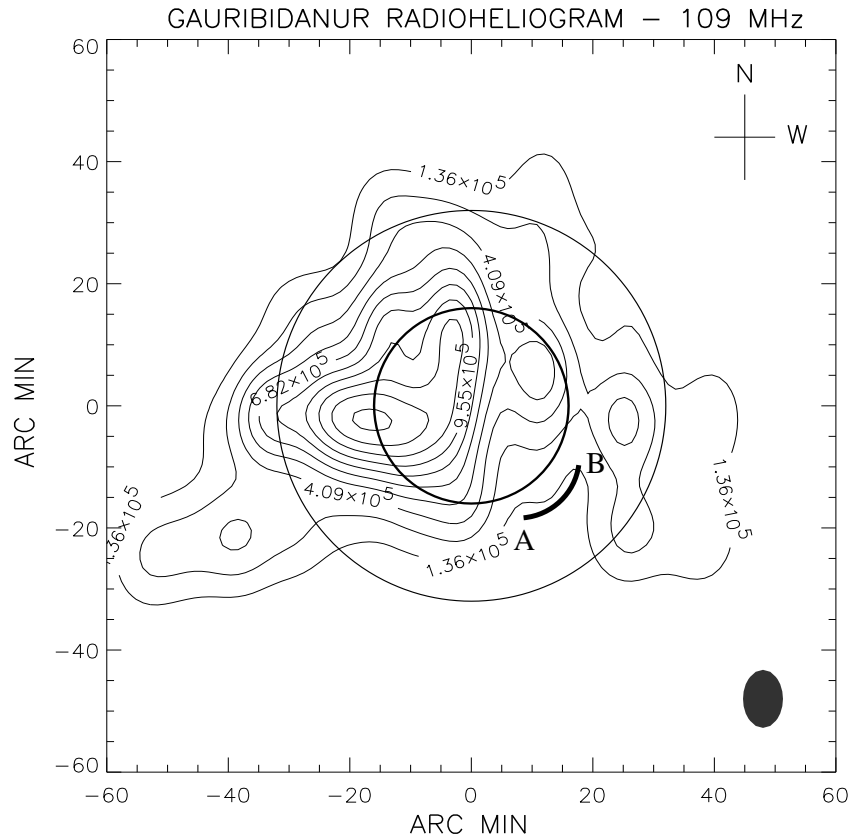


FIG. 2: Radio image of the solar corona obtained with the GRH around 07:30 UT on June 2, 1998. The peak brightness temperature is  $\approx 1.4 \times 10^6$  K. The contours are in intervals of  $1.4 \times 10^5$  K. The inner thick circle corresponds to the photosphere. The outer thick circle represents the approximate size of the C2 coronagraph occulter. Refer text for arc ‘AB’.

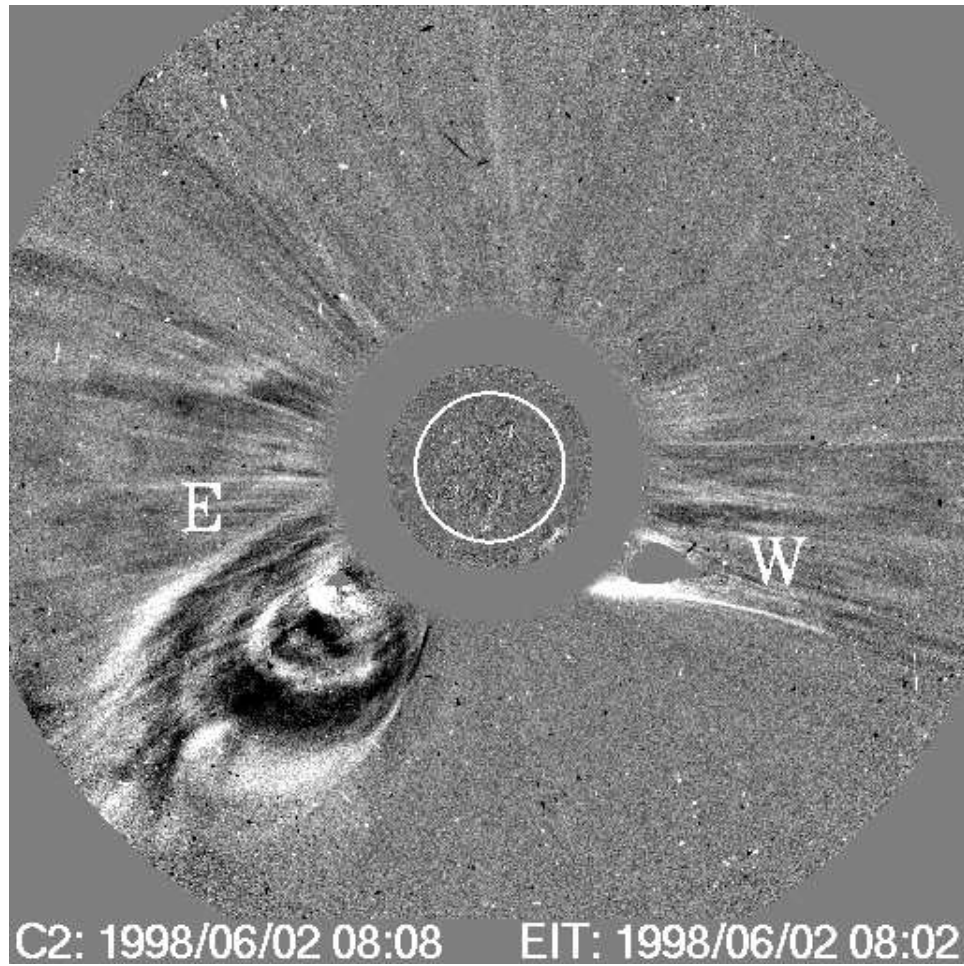


FIG. 3: LASCO-EIT running difference image [08:08-07:35 UT] showing two different CME associated activities ('W' and 'E') observed on June 2, 1998. The CME close to the west limb (W) is the event under study.

be fixed, to start with. Consider the different segments of the minimum brightness temperature contour (the outermost contour) in Figure 2. They are not equidistant from the disk center. The arc ‘AB’ represents the segment of the minimum brightness temperature contour which is at the least distance from the center of the Sun. We assumed it to be the location of the 109 MHz plasma level in the background corona and inferred the temperature and density of it from our ray-tracing calculations. The values are  $T_{bg} = 1 \times 10^6$  K and  $N_{bg} = 0.4 \times N_0$ . After establishing the background, the structures at different locations in the observed map were fitted one by one in a sequential manner by trial and error. For example, the structure near the east limb (hereinafter referred to as S1) was reproduced in the following manner.

**Step 1:** The approximate projected longitude<sup>2</sup> ( $y_0 = -18' = -1.12 R_\odot$ ) and latitude<sup>3</sup> ( $z_0 = -3' = -0.18 R_\odot$ ) of the structure S1 are determined from a visual inspection of Figure 2.

**Step 2:** The approximate projected width along the longitude and latitude are  $10'$  ( $\sigma_y = 0.6 R_\odot$ ) and  $8'$  ( $\sigma_z = 0.5 R_\odot$ ), respectively.

**Step 3:** The location of the centroid ( $x_0$ ) along the line of sight is determined from its longitude ( $y_0$ ), latitude ( $z_0$ ) and the radius ( $R_q$ ) of the background corona using the relation:

$$x_0 = \left( R_q^2 - y_0^2 - z_0^2 \right)^{1/2} \quad (1)$$

( $R_q = 18' = 1.12 R_\odot$ ). According to the assumed background density distribution ( $N_{bg} = 0.4 \times N_0$ ), the 109 MHz plasma level is at a height of  $\approx 1.12 R_\odot$ .

**Step 4:** The width/depth along the line of sight ( $\sigma_x$ ) is assigned to be equal to  $0.1 R_\odot$ , to start with.

**Step 5:** The density ( $C_1$ ) and temperature ( $G_1$ ) enhancement factors are assumed to be equal to +1.0 and 0.1 respectively.

Since a radio structure is typically characterized by its density, temperature, location of the centroid and width, the above values form the initial input parameters for our calculations. The reproduced brightness distribution [(the background) + S1] is superposed on the observed distribution and the error between them is minimized as follows:

---

<sup>2</sup> -/+ value of  $y$  implies that the source is in the Eastern/Western hemisphere of the Sun

<sup>3</sup> -/+ value of  $z$  implies that the source is in the Southern/Northern hemisphere of the Sun

**Exec-1** All the above parameters (mentioned in Step 1-5) except the location of S1 in the observer's line of sight  $x_0$  are kept as constants.  $x_0$  is varied from its initial value to a final value (initial value +  $3 R_\odot$ ) in steps of  $0.2 R_\odot$ . In each trial the simulated brightness distribution is compared with the observed brightness distribution to check the degree of agreement between them and is continued until a satisfactory fit (explained in section 5.3.2 of this chapter) is obtained.

**Exec-2** In the event of ourselves not obtaining good result in **Exec-1**,  $\sigma_x$  is then varied from  $0.1$  to  $0.2 R_\odot$  and the procedure in **Exec-1** is carried out again. If the fit is not satisfactory, then  $\sigma_x$  is changed to  $0.3 R_\odot$  and the entire sequence of operations is repeated.  $\sigma_x$  was varied in this manner up to a maximum of  $1 R_\odot$ , in steps of  $0.1 R_\odot$ .

**Exec-3** Even if **Exec-2** does not produce a satisfactory fit  $C_1$  will be changed to +3.0 unit (in steps of 2.0 unit from the initial value) from +1.0 unit and the procedures in **Exec-1** & **Exec-2** are repeated.

**Exec-4** As a final step, the temperature factor is enhanced by  $0.1 \times 10^6$  K if all the above steps fail to produce a good fit and all the aforementioned steps (from **Exec-1** to **Exec-3**) are repeated.

Following the above scheme, each one of the different visually identified discrete structures in the observed brightness distribution was reproduced. Figure 4 shows the image thus obtained. Table 1 shows the parameters of the various localized sources used in our calculations. The values are consistent with those used for modeling the discrete radio sources at meter-decameter wavelengths [Schmahl et al. (1994)].

### 5.3.2 Quality of the reproduced data

The degree of agreement between the observation and its reproduction can be calculated by taking their difference. Let us denote the observed two dimensional brightness temperature distribution of the corona and its fit as  $T_{obs}(y, z)$  and  $T_{fit}(y, z)$  respectively. The difference between them is

$$T_d(y, z) = T_{obs}(y, z) - T_{fit}(y, z) . \quad (2)$$



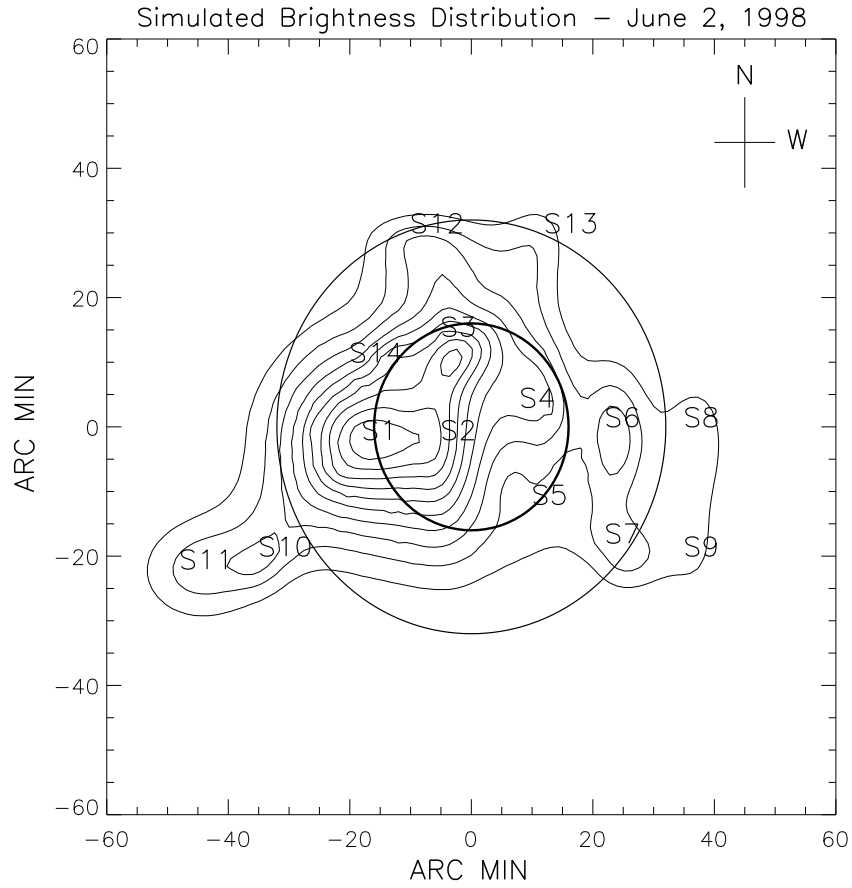


FIG. 4: The reproduced brightness temperature distribution of the observed radioheiligram (Figure 2) using ray-tracing technique. The approximate locations where the density enhancements/decrements were introduced to fit the observation are marked with S1,...,S14. The parameters of the fitted radio structures are given in Table 1.

One can obtain the normalized error and its absolute value [ $T_D(y, z)$ ] as follows:

$$\frac{T_d(y, z)}{T_{obs}(y, z)} = 1 - \frac{T_{fit}(y, z)}{T_{obs}(y, z)}, \quad (3)$$

$$T_D(y, z) = \left| \frac{T_d(y, z)}{T_{obs}(y, z)} \right| = \left| 1 - \frac{T_{fit}(y, z)}{T_{obs}(y, z)} \right| \quad (4)$$

If  $T_{fit}$  is equal to  $T_{obs}$  at all points, then the percentage error is 0.0 and  $T_{fit}$  will be the best fit to  $T_{obs}$ .

The difference between the observed and simulated data ( $T_D$ ) is shown in Figure 5. The deviation of the fit from the observations is as high as 15% of the ambient  $T_{obs}$  at some locations. This could be due to either an error in anyone or a combination of following parameters:

- (i) the location of density enhancement
- (ii) the width of a radio structure along different directions
- (iii) the density enhancement factor
- (iv) the temperature enhancement factor
- (v) the background density distribution
- (vi) the background temperature distribution

In order to estimate the error due to the above discrepancies in a quantitative manner, we carried out the following steps.

**Step 1 :** A model brightness temperature distribution with the parameters given below (and generated using the ray-tracing technique) was assumed to be the observed distribution ( $T_{obs}$ ):

- (a) background density  $N_{bg} = N_0 \times (4.2 \times 10^{4.32/r})$  (where  $N_0 = 4.2 \times 10^4 \text{ cm}^{-3}$ ),
- (b) background temperature  $T_{bg} = 1.0 \times 10^6 \text{ K}$ ,
- (c) a discrete source at  $(1.5 R_\odot, 0.0 R_\odot, 0.0 R_\odot)$  with
  - (c1) width 0.4, 0.4 and  $0.4 R_\odot$  along the  $x$ ,  $y$  and  $z$  axis respectively,
  - (c2) density enhancement of 5.0 more than the background and

TABLE 1: Parameters of discrete sources used in the ray-tracing calculations for the event observed with the GRH on June 2, 1998 at 07:30 UT

Source $n$	<sup>1</sup> Position ( $R_{\odot}$ ) $(x_n, y_n, z_n)$	<sup>2</sup> Distance ( $R_{\odot}$ )	<sup>3</sup> Size ( $R_{\odot}$ ) $[(\sigma_x)_n, (\sigma_y)_n, (\sigma_z)_n]$	<sup>4</sup> $C_n$	Density ( $cm^{-3}$ )
S1	1.40, -1.10, -0.06	1.78	0.70, 0.77, 0.67	20.0	$2.2 \times 10^8$
S2	1.40, -0.20, -0.04	1.41	0.70, 0.35, 0.71	8.0	$3.9 \times 10^8$
S3	1.40, -0.02, -0.04	1.40	0.77, 0.32, 0.32	10.0	$5.1 \times 10^8$
S4	1.60, 0.75, 0.40	1.81	0.32, 0.27, 0.45	10.0	$1.0 \times 10^8$
S5	1.23, 0.46, -0.46	1.39	0.39, 0.19, 0.32	-0.3	$5.4 \times 10^6$
S6	1.50, 1.70, -0.06	2.27	0.20, 0.22, 0.64	10.0	$3.4 \times 10^7$
S7	1.70, 1.72, -1.22	2.71	0.22, 0.29, 0.29	17.0	$2.8 \times 10^7$
S8	1.70, 2.48, -0.03	3.01	0.26, 0.29, 0.50	20.0	$2.3 \times 10^7$
S9	1.70, 2.44, -1.22	3.21	0.22, 0.29, 0.50	20.0	$1.9 \times 10^7$
S10	1.70, -2.10, -1.30	2.99	0.22, 0.22, 0.22	15.0	$1.8 \times 10^7$
S11	1.70, -2.86, -1.36	3.59	0.55, 0.53, 0.45	30.0	$2.0 \times 10^7$
S12	1.70, -0.46, 1.95	2.63	0.50, 0.50, 0.27	12.0	$2.2 \times 10^7$
S13	1.70, 0.80, 2.00	2.74	0.39, 0.32, 0.39	9.0	$1.4 \times 10^7$
S14	1.50, -0.80, 0.90	1.92	0.15, 0.08, 0.08	25.0	$1.9 \times 10^8$

- 1 The co-ordinates of the source centroid from the center of the Sun in units of  $R_{\odot}$ .
- 2 Radial distance of the source from the center of the Sun in units of  $R_{\odot}$ .
- 3 The  $x$ ,  $y$ , and  $z$  width of the source in units of  $R_{\odot}$ .
- 4 Density factor: Density higher/lower than the background. The assumed electron density and temperature for the background are  $(1.68 \times 10^4) 10^{4.32/r} cm^{-3}$  and  $1.0 \times 10^6$  K, respectively.

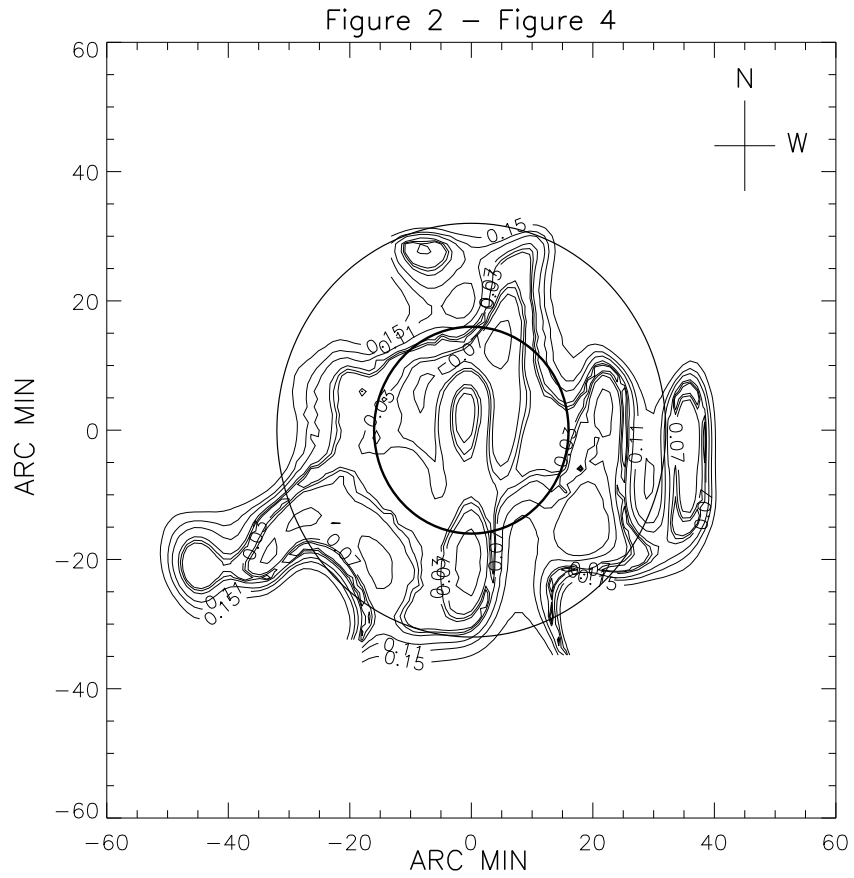


FIG. 5: The absolute normalized difference ( $T_D$ ) between the observed brightness distribution (Figure 2) and its reproduction (Figure 4). The magnitude of difference at any particular location is obtained by multiplying the contour value there with the corresponding  $T_{obs}(y, z)$ .

(c3) temperature enhancement of 0.5 more than the background.

**Step 2 :** We tried to reproduce the aforementioned  $T_{obs}$  through the ray-tracing method following the logic described in section 5.3. The only difference here is that we changed  $y$ ,  $\sigma_y$ ,  $T_{bg}$ , and  $N_{bg}$  also to get the fit.

**Step 3 :** The reproduced distributions ( $T_{fit}$ ) are subtracted from  $T_{obs}$  and the average of absolute normalized error ( $T_D$ ) was estimated using equation (4).

**Step 4 :** The source model is altered by changing the  $y$ -coordinate of the distribution to  $(1.5 R_\odot, 0.1 R_\odot, 0.0 R_\odot)$ .

**Step 5 :** Steps 2 and 3 were carried out again with the model in step 4 as the  $T_{obs}$ .

**Step 6 :** Steps 4 and 5 were repeated until the  $y$  coordinate of the model reaches  $2.5 R_\odot$ .

Though in principle one could carry out the calculations by changing the different input parameters of the model in addition to its  $y$ -coordinate (refer section 5.3), we stopped with the above since a visual inspection of the actual observed brightness distribution at different epoch (in the absence of non-thermal activity) indicate that they differ mostly in the location of the discrete sources along the latitudinal and longitudinal directions. Therefore, we changed only the  $y$ -coordinate (longitude) here. The results should be the same for  $z$ -coordinate (latitude) also.

**Case (i):**  $T_D$  due to discrepancy in  $x$ -coordinate of the density enhancement

In order to understand the effect of discrepancies in  $x$ -coordinate of density enhancement on  $T_D$ , the  $x$ -coordinate of density enhancement in the model  $T_{obs}$  was varied from  $1.3$  to  $1.7 R_\odot$  with an interval of  $0.1 R_\odot$ , and Steps 1-6 were followed for each one of them. Figure 6 shows the results of our calculations. It is clear that for a particular value of  $\Delta x$ , the average  $T_D$  increases gradually from the disk center up to a certain value of  $y$  and decreases rather slowly after that. The latter (i.e. turning point) is at  $\approx 1.3 R_\odot$  for  $\Delta x = \pm 0.1$  and  $1.5 R_\odot$  for  $\Delta x = \pm 0.2 R_\odot$ .

**Case (ii):**  $T_D$  due to discrepancy in  $y$ -coordinate of the density enhancement

Like the above case, the  $y$ -coordinate of the density enhancement in our ray-tracing calculations was shifted by  $\pm 0.1$  and  $\pm 0.2 R_\odot$  with respect to the reference in the model  $T_{obs}$ . Figure 7 shows the average  $T_D$  for different  $\Delta y$ . The results are the same

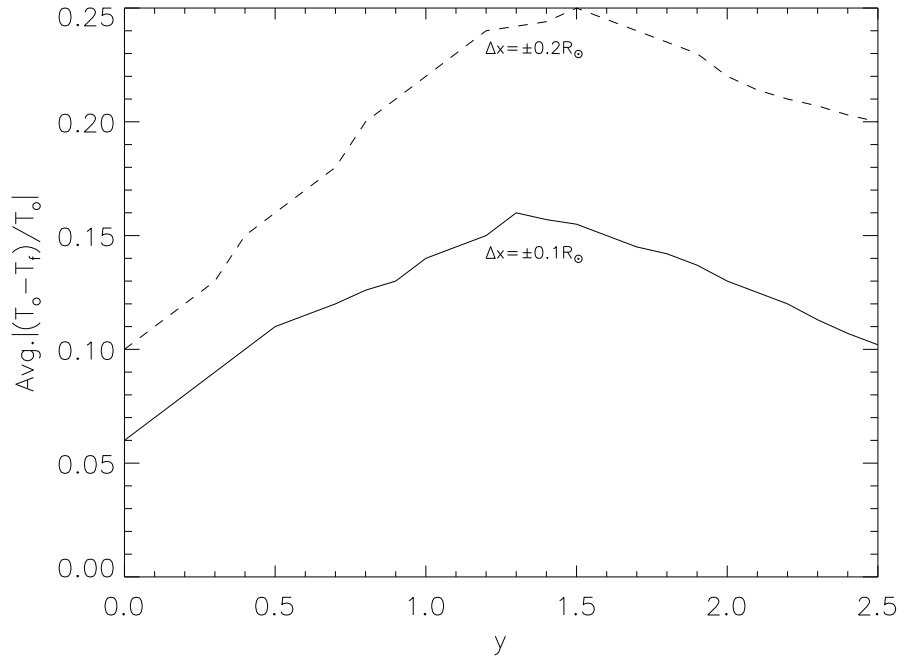


FIG. 6: The average  $T_D$  due to error in the  $x$ -coordinate of density enhancement. The  $z$ -coordinate is assumed to be  $0.0 R_\odot$  for all  $y$ . The solid and dashed line represent average  $T_D$  for  $\Delta x = \pm 0.1$  and  $\pm 0.2 R_\odot$ , respectively.

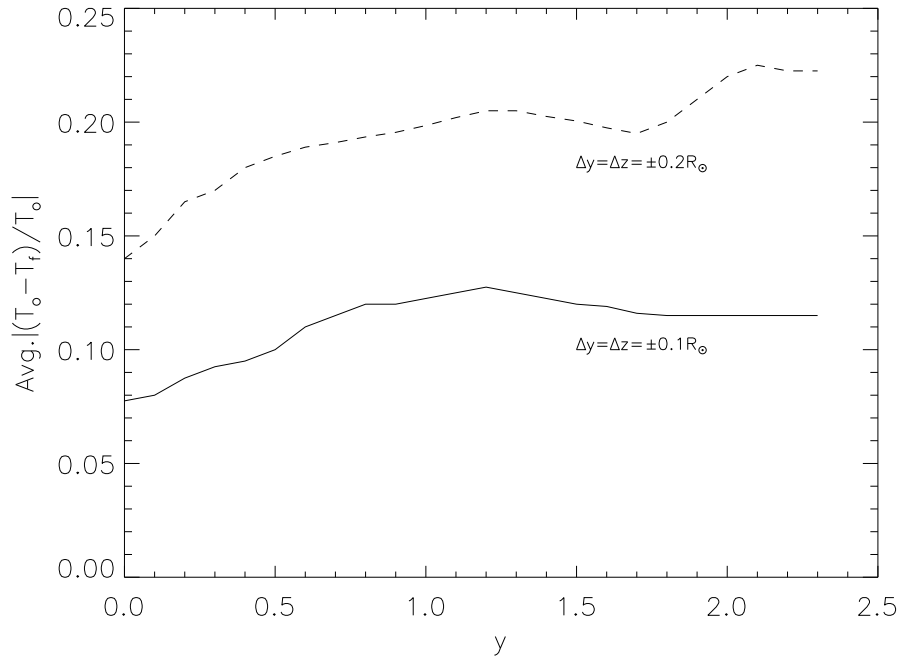


FIG. 7: Same as Figure 6. The solid and dashed lines represent average  $T_D$  for  $\Delta y = \pm 0.1$  and  $0.2 R_{\odot}$ , respectively.

for  $\Delta z$  also. It increases gradually up to  $y \simeq 1.2 R_{\odot}$  for all values of  $\Delta y$ . Thereafter it exhibits a different trend.

**Case (iii):  $T_D$  due to discrepancy in the  $x$ -width of density enhancement**

In order to study the influence of change in the width along the line of sight ( $\sigma_x$ ) on the brightness temperature,  $\sigma_x$  in the model  $T_{obs}$  was varied from 0.2 to 0.6  $R_{\odot}$  in steps of 0.1  $R_{\odot}$ . Figure 8 shows the average  $T_D$  for different values of  $\Delta\sigma_x$ . It remains approximately constant till about 1.1  $R_{\odot}$ . There after it increases sharply up to 1.6  $R_{\odot}$ . Beyond that, it again remains steady.

**Case (iv):  $T_D$  due to discrepancy in  $y$ -width of the density enhancement**

Like in the above case, the influence of change in  $y$ -width ( $\sigma_y$ ) of the density enhancement was studied by varying the latter from 0.2 to 0.6  $R_{\odot}$  in steps of 0.1  $R_{\odot}$ . The results are shown in Figure 9.  $T_D$  increases sharply between  $y = 0$  and  $y = 0.8 R_{\odot}$  for both  $\sigma_x = \pm 0.1$  and  $\pm 0.2 R_{\odot}$ . Beyond that it decreases gradually and become steady. The behavior would be the same for  $\sigma_z$  also.

**Case (v):  $T_D$  due to discrepancy in the density enhancement factor**

In order to comprehend the effect of density changes on  $T_D$ , the density enhancement factor ( $C_n$ ) was varied from 1.0 to 9.0 in steps of 2.0 units. The average  $T_D$  thus obtained for different values of  $C_n$  is shown in Figure 10. It is clear that  $T_D$  strongly depends on  $C_n$  for  $y$ -values greater than  $\approx 1.1 R_{\odot}$ .

**Case (vi):  $T_D$  due to discrepancy in the temperature enhancement factor**

The variation of average  $T_D$  for different temperature enhancements was studied by assigning  $\Delta G_n = \pm 0.1$  and  $\pm 0.2$  with respect to the reference. Figure 11 shows the distribution and it indicates that  $T_D$  sharply decreases up to about  $y \simeq 1.3 R_{\odot}$  and remains steady thereafter. This is in contrast to the variation of  $T_D$  with change in density.

**Case (vii):  $T_D$  due to discrepancy in background density and temperature**

It was found that a  $\pm 0.1$  and  $\pm 0.2$  variation in background density leads to an error of 11 and 18% in  $T_D$ . Likewise, a  $\pm 0.1$  and 0.2 variation in the background temperature gave an error of 7 and 13% in  $T_D$ .



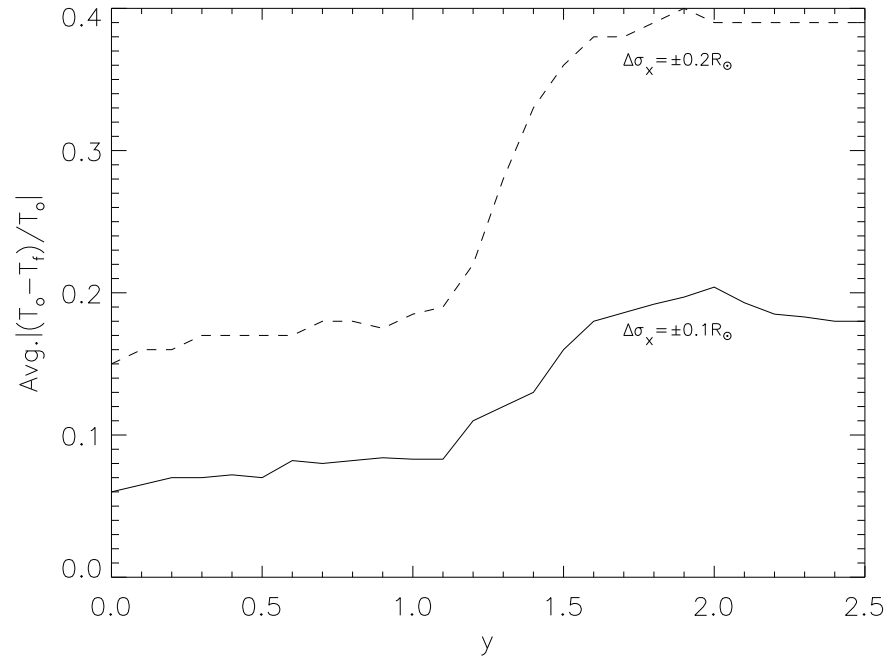


FIG. 8: Same as Figure 6 and 7. The solid and dashed line represent average  $T_D$  for  $\Delta\sigma_x = \pm 0.1$  and  $0.2 R_\odot$ , respectively.

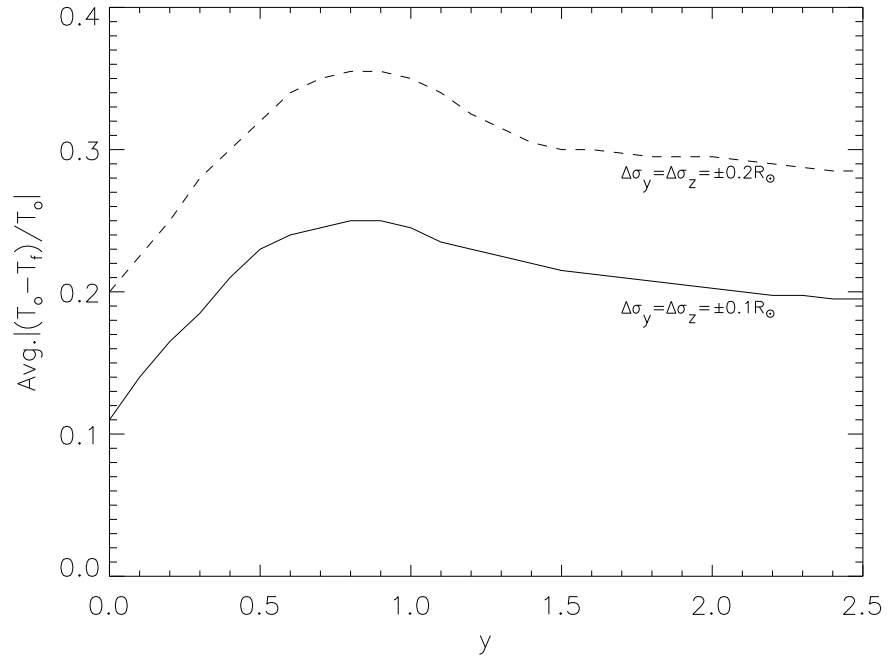


FIG. 9: Same as Figure 6, 7 and 8. The solid and dashed line represent  $T_D$  for  $\Delta\sigma_y = \pm 0.1$  and  $0.2 R_\odot$ , respectively. This distribution also holds good for the change in  $z$ -width ( $\Delta\sigma_z$ ).

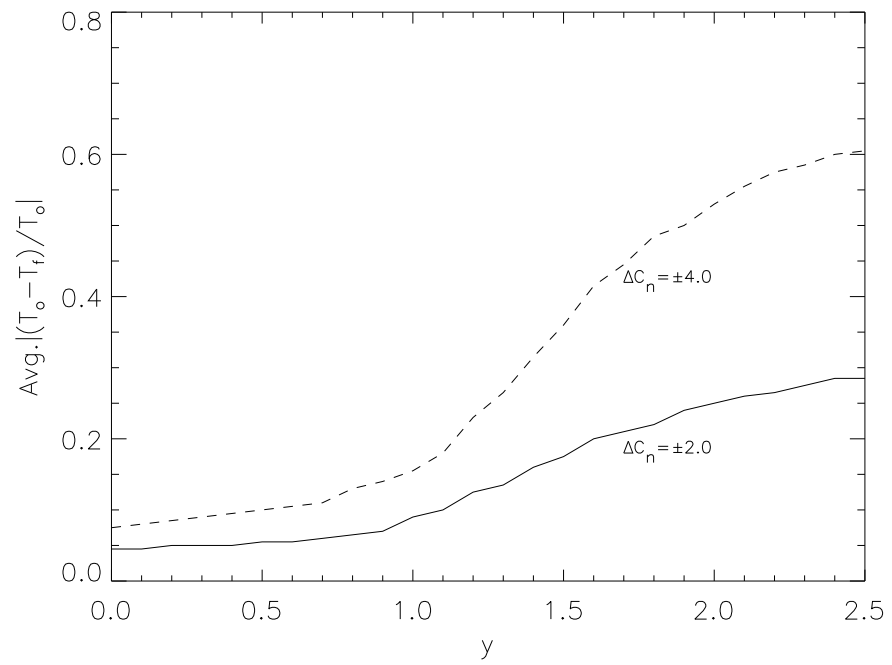


FIG. 10: Same as Figure 6 - 9. The solid and dashed line represent the average  $T_D$  for  $\Delta C_n = \pm 2.0$  and  $\pm 4.0$ , respectively.

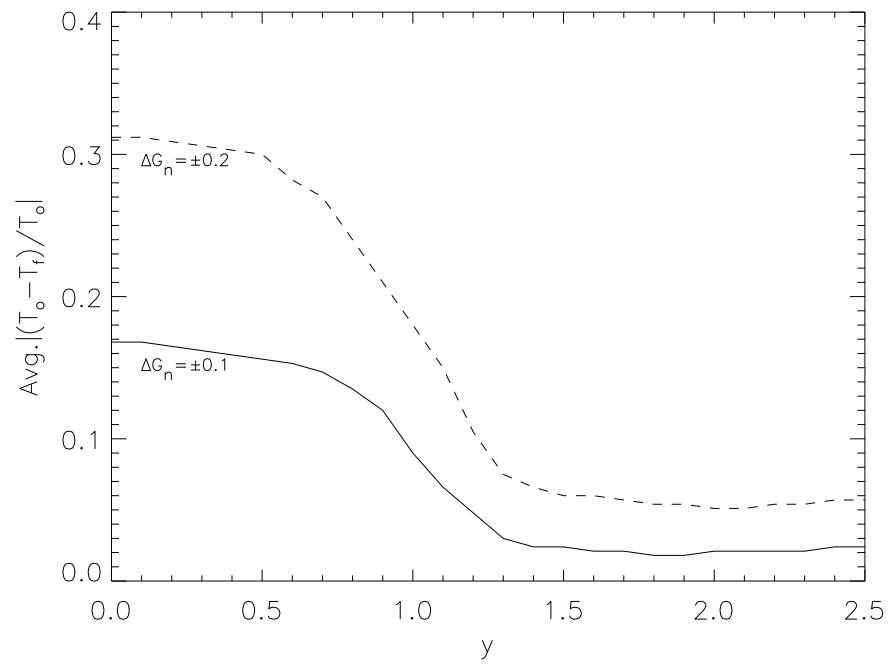


FIG. 11: Same as Figure 6 - 10. The solid and dashed line represent average  $T_D$  for  $\Delta G_n = \pm 0.1$  and  $\pm 0.2$ , respectively.

The reason for the above variation in the estimated error with  $y$  is not clear to us at this stage and we are working on it. However, we use the above quoted values to determine the error involved in various fitted parameters and hence the density, volume and mass estimate of the CME under study.

### 5.3.3 Error in the fitted parameters (corresponding to the radio structures associated with the pre-eruption feature of June 2, 1998-CME)

An inspection of Figure 2, 3, 4 and the results of Plunkett et al. (2000) indicate that the discrete sources S6-S9 in our ray-tracing calculations correspond most likely to the pre-eruption state of the white light CME in the southwest quadrant of Figure 3. The maximum error (refer Figure 5) between the observed and reproduced brightness distribution at their location is  $\approx 11\%$ . If we assume that  $T_D$  in the latter is due to:

- (a) Case (i) of section 5.3.1: Figure 6 indicates that the 11% difference at  $y = 1.7 R_\odot$  (will be referred to as  $E_1$  hereinafter) and 7% difference at  $y = 2.4 R_\odot$  (will be referred to as  $E_2$  hereinafter) could be accounted for  $\Delta x = \pm 0.1 R_\odot$ . Therefore, the position coordinates of the radio sources that correspond to the pre-eruption feature of the June 2, 1998 CME would become

<u>Source</u>	<u>Position (<math>x_n, y_n, z_n</math>)</u>
S6	$\rightarrow (1.50 \pm 0.1 R_\odot, 1.70 R_\odot, -0.06 R_\odot)$ ,
S7	$\rightarrow (1.70 \pm 0.1 R_\odot, 1.72 R_\odot, -1.22 R_\odot)$ ,
S8	$\rightarrow (1.70 \pm 0.1 R_\odot, 2.48 R_\odot, -0.03 R_\odot)$ ,
S9	$\rightarrow (1.70 \pm 0.1 R_\odot, 2.44 R_\odot, -1.22 R_\odot)$ .

- (b) Case (ii) of section 5.3.1: Simulations show that the difference  $E_1$  and  $E_2$  correspond to  $\Delta y = \pm 0.1$  and  $\pm 0.06 R_\odot$  respectively. Therefore, the position

coordinates of CME related radio enhancements in this case would become,

<u>Source</u>	<u>Position (<math>x_n, y_n, z_n</math>)</u>
S6	$\rightarrow (1.50 R_\odot, 1.70 \pm 0.10 R_\odot, -0.06 R_\odot)$ ,
S7	$\rightarrow (1.70 R_\odot, 1.72 \pm 0.10 R_\odot, -1.22 R_\odot)$ ,
S8	$\rightarrow (1.70 R_\odot, 2.48 \pm 0.06 R_\odot, -0.03 R_\odot)$ ,
S9	$\rightarrow (1.70 R_\odot, 2.44 \pm 0.06 R_\odot, -1.22 R_\odot)$ .

The error values are the same for discrepancies in  $z$ -coordinate also (i.e. interchanging  $y$  and  $z$  does not make any difference).

(c) Case (iii) of section 5.3.1: Both  $E_1$  and  $E_2$  correspond to a  $\Delta\sigma_x$  of  $\pm 0.05 R_\odot$ .

Therefore, the  $x$ -width of S6-S9 become,

<u>Source</u>	<u>Width (<math>\sigma_x, \sigma_y, \sigma_z</math>)</u>
S6	$\rightarrow 0.20 \pm 0.05 R_\odot, 0.22 R_\odot, 0.64 R_\odot$ ,
S7	$\rightarrow 0.22 \pm 0.05 R_\odot, 0.29 R_\odot, 0.29 R_\odot$ ,
S8	$\rightarrow 0.26 \pm 0.05 R_\odot, 0.29 R_\odot, 0.50 R_\odot$ ,
S9	$\rightarrow 0.22 \pm 0.05 R_\odot, 0.29 R_\odot, 0.50 R_\odot$ .

(d) Case (iv) of section 5.3.1: One can associate a  $\Delta\sigma_y$  of  $\pm 0.04 R_\odot$  to both  $E_1$  and  $E_2$ . Therefore,

<u>Source</u>	<u>Width (<math>\sigma_x, \sigma_y, \sigma_z</math>)</u>
S6	$\rightarrow 0.20 R_\odot, 0.22 \pm 0.04 R_\odot, 0.64 R_\odot$ ,
S7	$\rightarrow 0.22 R_\odot, 0.29 \pm 0.04 R_\odot, 0.29 R_\odot$ ,
S8	$\rightarrow 0.26 R_\odot, 0.29 \pm 0.04 R_\odot, 0.50 R_\odot$ ,
S9	$\rightarrow 0.22 R_\odot, 0.29 \pm 0.04 R_\odot, 0.50 R_\odot$ .

The error is the same for  $z$ -coordinate also.

- (e) Case (v) of section 5.3.1:  $E_1$  and  $E_2$  can be related to  $\Delta C_n$  of  $\pm 1.0$  and  $\pm 0.6$  respectively, for the density enhancement factor. Therefore,

<u>Source</u>	<u><math>C_n</math></u>
S6	$\rightarrow 10.0 \pm 1.0$ ,
S7	$\rightarrow 17.0 \pm 1.0$ ,
S8	$\rightarrow 20.0 \pm 0.6$ ,
S9	$\rightarrow 20.0 \pm 0.6$ .

- (f) Case (vi) of section 5.3.1: The error in the temperature enhancements ( $\Delta G_n$ ) corresponding to  $E_1$  and  $E_2$  are  $\pm 0.3$  and  $\pm 0.4$  respectively. We are interested in finding out the density, volume and mass of the radio structures. So the error in the position, width and density are mainly important for our further calculations.

### 5.3.4 Results

#### (a) The density

1. We know the locations of the radio sources S6-S9 from Table 1. The  $x$ ,  $y$  and  $z$  co-ordinates of the centroid of S6 are  $(1.5 R_\odot, 1.7 R_\odot, -0.06 R_\odot)$ . Therefore, the radial distance of S6 from the center of the Sun is  $R_6(\sqrt{x^2 + y^2 + z^2} = 2.27 R_\odot)$ . Similarly the distance of S7, S8, and S9 from the center of the Sun are  $R_7(= 2.71 R_\odot)$ ,  $R_8(= 3.00 R_\odot)$ , and  $R_9(= 3.21 R_\odot)$ , respectively.
2. The approximate density at the location of S6 is calculated by substituting its (i) radial distance from the center of the Sun ( $R_6$ ) and (ii) the corresponding density factor in the expression for electron density given by equation (74)-(75) in chapter 4. i.e.,

$$(N_e)_{S6} \times C_{S6} \simeq (4.2 \times 10^4) 10^{(4.32/2.27)} \text{ cm}^{-3} \times 10.0 = 3.36 \times 10^7 \text{ cm}^{-3}$$

Similarly,

$$(N_e)_{S7} \times C_{S7} \simeq (4.2 \times 10^4) 10^{(4.32/2.71)} \text{ cm}^{-3} \times 17.0 = 2.80 \times 10^7 \text{ cm}^{-3}$$

$$(N_e)_{S8} \times C_{S8} \simeq (4.2 \times 10^4) 10^{(4.32/3.00)} \text{ cm}^{-3} \times 20.0 = 2.28 \times 10^7 \text{ cm}^{-3}$$

$$(N_e)_{S9} \times C_{S9} \simeq (4.2 \times 10^4) 10^{(4.32/3.21)} \text{ cm}^{-3} \times 20.0 = 1.86 \times 10^7 \text{ cm}^{-3}$$

Therefore, the average density of the radio sources S6-S9 is  $\approx 2.58 \times 10^7 \text{ cm}^{-3}$ .

- 3** The average density can also be obtained in the following manner. According to **item (1)**, the mean distance of the centroid of the radio sources is  $2.8 R_{\odot}$  (average of the sum of  $R_6$ ,  $R_7$ ,  $R_8$  and  $R_9$ ). The ambient density at the above point is given by  $4.2 \times 10^4 [10^{(4.32/2.8)}] \approx 1.45 \times 10^6 \text{ cm}^{-3}$ . Multiplying the latter with the average density enhancement factor of the corresponding radio sources S6-S9 ( $\frac{10+17+20+20}{4} \approx 16.8$ ), we get the average density as  $2.44 \times 10^7 \text{ cm}^{-3}$ .
- 4** According to the errors discussed in **Case (i)**, **(ii)** and **(v)** of section 5.3.2, the radial distance of the source position/centroid from the center of the Sun can vary from  $2.7$  to  $2.9 R_{\odot}$  and the density enhancement can vary from  $16.0$  to  $17.6$ . This implies that the average density should be between  $2.1 - 2.9 \times 10^7 \text{ cm}^{-3}$ .

### (b) The volume

The total volume of the pre-eruption structure is obtained by summing the individual volume occupied by its associated radio sources, i.e,

$$V = V_{S6} + V_{S7} + V_{S8} + V_{S9} \quad (5)$$

where,

$$\begin{aligned} V_{S6} &= (\sigma_x) \times (\sigma_y) \times (\sigma_z) \\ &\simeq 0.2 R_{\odot} \times 0.22 R_{\odot} \times 0.64 R_{\odot} \\ &\simeq 0.03 R_{\odot}^3 \\ &\simeq 9.5 \times 10^{30} \text{ cm}^3 \end{aligned}$$

Similarly the volumes of other sources were calculated as,

$$\begin{aligned} V_{S7} &\simeq 6.2 \times 10^{30} \text{ cm}^3 \\ V_{S8} &\simeq 1.3 \times 10^{31} \text{ cm}^3 \\ V_{S9} &\simeq 1.1 \times 10^{31} \text{ cm}^3 \end{aligned}$$

Therefore, the total volume ( $V$ ) is  $\approx 3.97 \times 10^{31} \text{ cm}^3$ . If, we include the error in the width estimate discussed in **Case (iii)** and **(iv)** of section 5.3.2, then the volume of the radio structure should be about  $2.5 - 4.8 \times 10^{31} \text{ cm}^3$ .



### (c) The mass

Since the mass of the radio structures S6-S9 is distributed unequally at different locations (Figure 2 and Figure 4), its total mass is calculated by adding the mass associated with individual radio structures and is given by

$$M = (M)_{S6} + (M)_{S7} + (M)_{S8} + (M)_{S9} . \quad (6)$$

The mass associated with each radio source is calculated using the following formula:

$$M = 2 \times 10^{-24} N_e V \text{ g} , \quad (7)$$

where  $V$  is the volume of the observed enhancement and it is assumed that the coronal plasma is a fully ionized gas of normal solar composition (90% hydrogen and 10% helium by number); Therefore, each electron is associated with approximately  $2 \times 10^{-24}$  g of material. Calculating the mass of individual sources, we get

$$\begin{aligned} (M)_{S6} &= 2 \times 10^{-24} (N_e)_{S6} V_{S6} \text{ g} , \\ (M)_{S6} &= (3.36 \times 10^7 \text{ cm}^{-3}) \times (9.5 \times 10^{30} \text{ cm}^3) \times (2 \times 10^{-24} \text{ g}) \\ &= 6.38 \times 10^{14} \text{ g} , \\ (M)_{S7} &= 2 \times 10^{-24} (N_e)_{S7} V_{S7} \text{ g} , \\ (M)_{S7} &= (2.80 \times 10^7 \text{ cm}^{-3}) \times (6.2 \times 10^{30} \text{ cm}^3) \times (2 \times 10^{-24} \text{ g}) \\ &= 3.47 \times 10^{14} \text{ g} , \\ (M)_{S8} &= 2 \times 10^{-24} (N_e)_{S8} V_{S8} \text{ g} , \\ (M)_{S8} &= (2.28 \times 10^7 \text{ cm}^{-3}) \times (1.3 \times 10^{31} \text{ cm}^3) \times (2 \times 10^{-24} \text{ g}) \\ &= 5.92 \times 10^{14} \text{ g} , \\ (M)_{S9} &= 2 \times 10^{-24} (N_e)_{S9} V_{S9} \text{ g} , \\ (M)_{S9} &= (1.86 \times 10^7 \text{ cm}^{-3}) \times (1.1 \times 10^{31} \text{ cm}^3) \times (2 \times 10^{-24} \text{ g}) \\ &= 4.09 \times 10^{14} \text{ g} , \end{aligned}$$

Substituting the above values in equation (6), we get an estimate of  $\approx 2 \times 10^{15}$  g for the pre-eruption radio structure. If we include the error in density and volume, the mass will be in the range  $1.03 - 2.78 \times 10^{15}$  g.

## 5.4 CONCLUSION

The radio observations of the pre-event phase of the prominence eruption associated coronal mass ejection of June 2, 1998 was described. The observed brightness distribution ( $T_{obs}$ ) was reproduced using three dimensional ray-tracing technique. The degree of agreement between  $T_{obs}$  and its reproduction ( $T_{fit}$ ) was verified by taking their absolute normalized difference ( $T_D$ ), and the maximum deviation was found to be  $\approx 15\%$ . This is mostly due to error in the fitted parameters such as position, width, density factor etc. In order to understand the dependence of  $T_D$  on the aforementioned parameters, we simulated different source model and reproduced them with various parameter values close to that used to generate the former. The results obtained were then used to determine the error in our fitted parameters. We found that the density, volume and mass of the radio structures (S6-S9) associated with pre-eruption features of the CME, could be in the range  $2.1 - 2.9 \times 10^7 \text{ cm}^{-3}$ ,  $2.5 - 4.8 \times 10^{31} \text{ cm}^3$  and  $1.03 - 2.78 \times 10^{15} \text{ g}$ , respectively. These values are in reasonable agreement with that estimated by Gopalswamy and Kundu (1992) for the radio counterpart of the frontal loop of the white light CME observed with the coronagraph/polarimeter aboard Solar Maximum Mission [SMM; MacQueen (1980)] satellite. Vourlidas et al. (2000) had derived the mass of the corresponding white light CME using LASCO data and the value is  $\sim 10^{16} \text{ g}$ . A comparison of the latter with our mass estimate indicates that a major fraction of the CME mass was present in the pre-event radio structures associated with the swelled helmet streamer. This is consistent with the results of Illing and Hundhausen (1985), obtained using SMM observations. The present radio mass estimate is also lesser than the average value of white light CME mass reported earlier [Hildner (1977); Howard et al. (1984)]. We are in the process of estimating the mass of CMEs observed with the GRH and compare them with the corresponding white light observations. This will be useful since the observed radiation is of entirely different physical origin. Again, the brightness in radio and white light are proportional to  $\langle n_{CME}^2 \rangle$  and  $\langle n_{CME} \rangle$ , respectively. An accurate measurement of CME mass is necessary to estimate the mass flux contribution to the solar wind by CMEs. This will aid in determining the coronal mass flux near the Earth in a better manner. Note that a CME in general is a three dimensional structure and hence the sky-plane measurements under-estimate the mass of a CME [Howard et al. (1985); Vourlidas et al. (2000)].

## CHAPTER 6

# ESTIMATION OF THE THREE-DIMENSIONAL SPACE SPEED OF A CORONAL MASS EJECTION USING METER WAVELENGTH RADIO DATA

### 6.1 INTRODUCTION

What one measures usually from a time-lapse movie of the images of a CME obtained with a coronagraph is usually the speed at which the CME spreads in the plane of the sky. This is only a lower limit to the true speed especially in the case of Earth-directed ‘halo’ CMEs since they lie away from the plane of the sky. Attempts to obtain the true speed of a CME whose source region lies close to the center of the solar disk is one of the widely pursued areas of research in CME studies. This is very important since they are more likely to reach Earth’s environment [refer Moon et al. (2005) and the references therein]. Eselevich and Filippov (1991) showed that CMEs whose direction of propagation subtend a finite angle with the plane of the sky can be modeled either as a loop or shell, and the velocity of their leading edge, mass and kinetic energy in the height range  $2.5 R_{\odot} \leq R \leq 10 R_{\odot}$  can be determined. According to Plunkett et al. (1998), an estimate of the true frontal speed can be obtained by assuming a constant angular spread and sky-plane speed. Sheeley et al. (1999) developed a technique to track different features of CMEs up to  $30 R_{\odot}$  in order to estimate the velocity of CMEs both along the line of sight (which is comparable to the expansion rate of Halo CMEs) as well as in the plane of the sky. Contemporaneous observations of flares and coronal mass ejections can also be used to derive the radial velocity of CMEs [Leblanc et al. (2001)]. The cone model for the CME proposed by Zhao et al. (2002) effectively uses the idea of constant angular width and the central position angle as free parameters. By carefully matching the observed halo CMEs at different epoch with the model (at different radial distances), they calculated the radial velocity and acceleration of CMEs. Recently, Michalek et al. (2003) provided a technique to determine the crucial parameters such as width, location of eruption and space speed that decide the geo-effectiveness of CMEs. Their method is based on the measurements of sky-plane speeds and the moments of the first appearance of halo CMEs above opposite limbs of the coronagraph. It

was presumed that halo CMEs have constant velocities in their early phase, are symmetric (about the opposite limbs of the coronagraph occulter when they are first identified above latter), and propagate with constant angular widths. Using the drift rate of Type II radio emissions generated by the shocks driven by the white-light CMEs, Reiner et al. (2003) demonstrated that the space speed of CMEs are about 1.4 times greater than their sky-plane speed. Raymond (2004) suggested that the motion of a CME in three dimensional space can be determined by combining series of CME images in the plane of the sky and their corresponding line of sight velocity estimates obtained through Doppler shift measurements of spectral lines. The polarized brightness of a white light CME depends on its angle with respect to the sky plane. Making use of the above property, Moran and Davila (2004), Dere et al. (2005) determined the average distance of scattering plasma (confined by CME magnetic field) from the plane of the sky and calculated the velocity of CMEs in the three dimensional space. Given the situation, we now explore the possibility of utilizing meter wavelength radio observations to estimate the space speed of CMEs in the low corona (particularly close to their onset) through ray-tracing analysis.

## 6.2 OBSERVATIONS

The radio data considered for analysis in the present case were obtained with the GRH on January 21, 1998. The observing frequency was 109 MHz. Figures 1 and 2 show the radioheliogram observed with the GRH on that day around 05:01:06 and 06:01:06 UT, respectively. Due to the limitation in the observing capabilities of the GRH, we do not have data in between the above time interval in the present case. Figure 3 shows the difference of the above two images, i.e. 06:01:06 - 05:01:06 UT. One can notice enhanced radio emission above the limb in the southern hemisphere during the aforementioned period. Its average distance in the plane of the sky (from the center of the Sun) is  $1.7 R_{\odot}$ . The radio Sun was very ‘quiet’ and no non-thermal activity was reported, particularly during our observing period [Sol.-Geophys. Data (1998a)]. According to the LASCO CME catalog<sup>1</sup> for the year 1998, a full ‘halo’ event was observed on January 21, 1998 by the SOHO. The event was first observed above the southern quadrant of the occulting disk of the LASCO C2 coronagraph around 06:37:25 UT. Its estimated linear speed in the plane of the sky was  $361 \text{ km s}^{-1}$ . The extrapolated onset time of the event from the center of the Sun was 05:09:09

---

<sup>1</sup>[http://cdaw.gsfc.nasa.gov/CME\\_list/UNIVERSAL/1998\\_01/univ1998\\_01.html](http://cdaw.gsfc.nasa.gov/CME_list/UNIVERSAL/1998_01/univ1998_01.html)

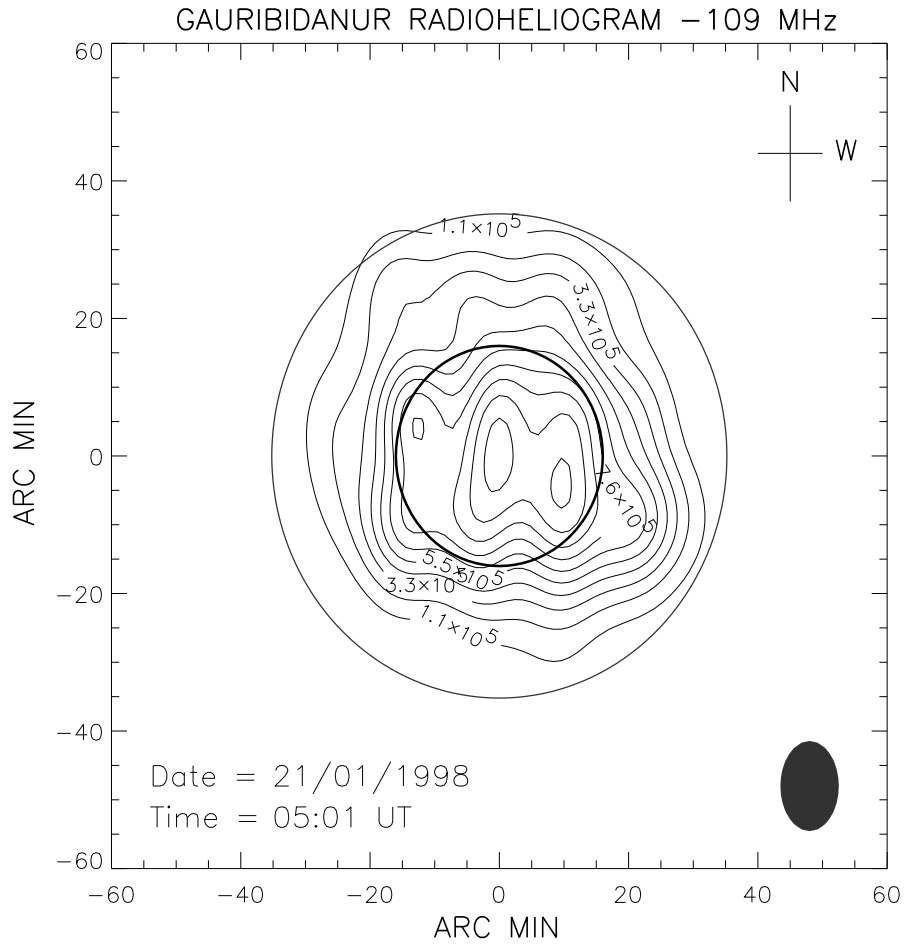


FIG. 1: Radioheliogram obtained with the GRH at 109 MHz on January 21, 1998 at 05:01 UT. The peak brightness temperature is  $\sim 1.10 \times 10^6$  K and the contour interval is  $1.1 \times 10^5$  K. The inner circle represents the solar limb and the outer circle corresponds approximately to the size of the occulter of the LASCO C2 coronagraph ( $\approx 2.2 R_{\odot}$ ). The filled contour near the bottom right corner is the GRH instrument beam at 109 MHz.

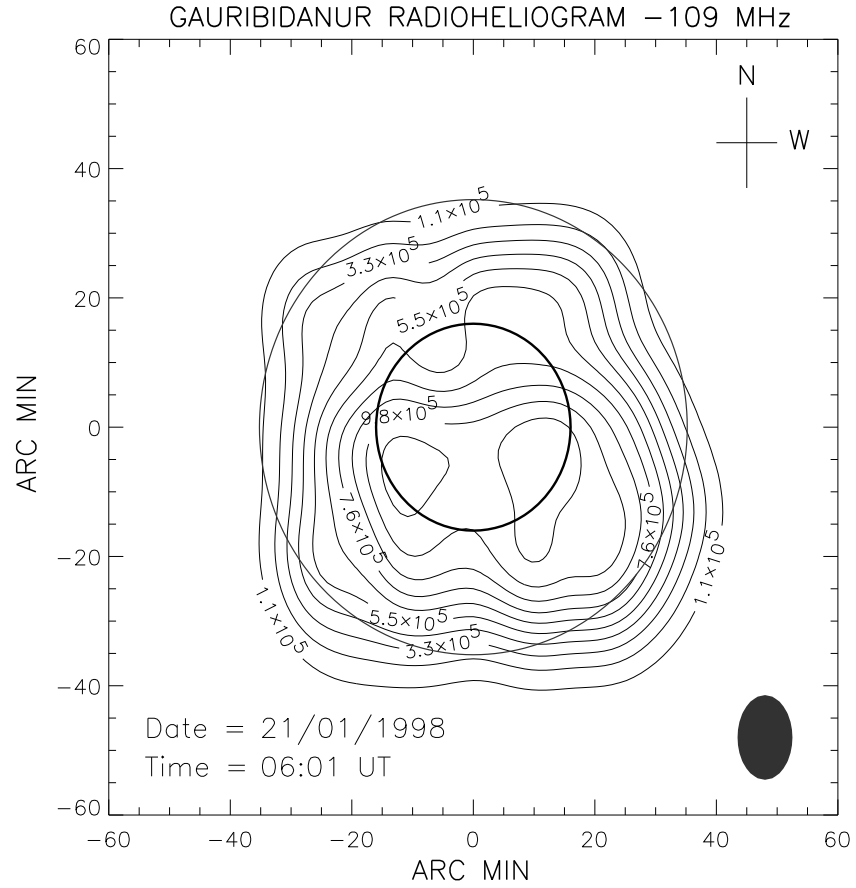


FIG. 2: Same as Figure 1, but obtained at 06:01 UT. The peak brightness temperature is  $\sim 1.20 \times 10^6$  K and the contour interval is  $1.2 \times 10^5$  K.

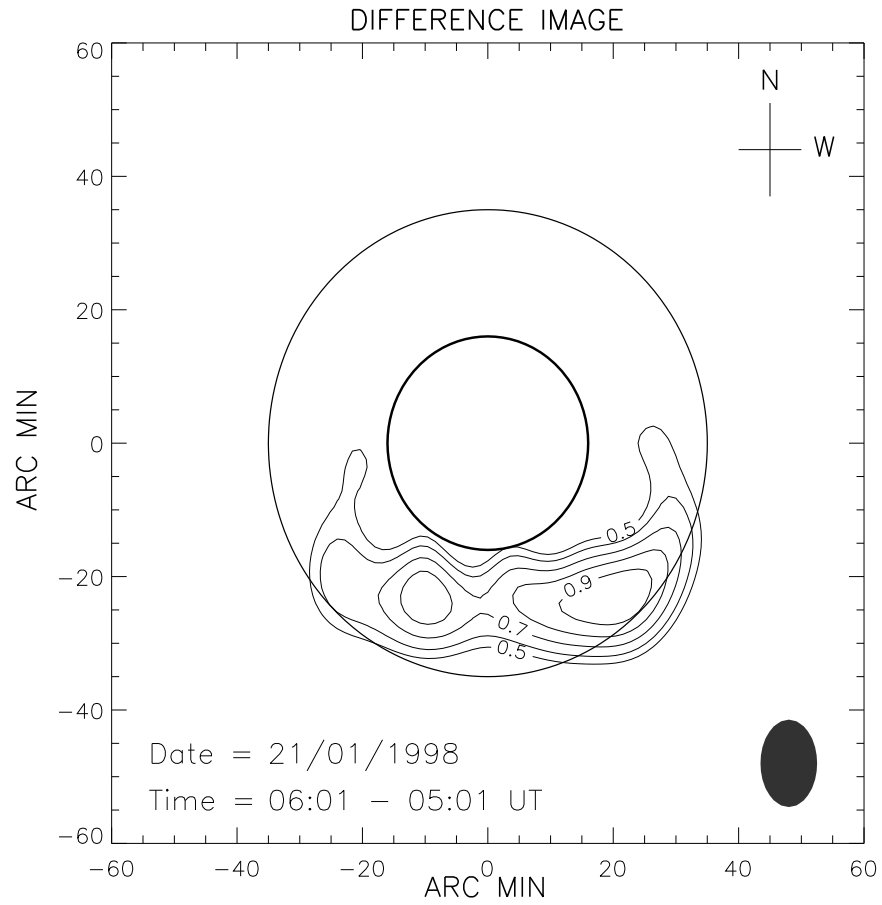


FIG. 3: Difference image obtained by subtracting the radioheliogram in Figure 1 (05:01 UT) from that in Figure 2 (06:01 UT). Only contours whose levels greater than 50% of the peak value are shown here. The brightness temperature of the enhanced emission above the limb in the southern hemisphere is  $5.3 \times 10^5$  K.

UT. It was associated with a H-alpha filament disappearance from location (S57 E19) on the solar disk between 04:00 - 06:03 UT on that day [Gopalswamy (2000b); Zhou et al. (2003)]. Figure 4 shows the LASCO difference image of the event obtained at 07:32 UT by subtracting a pre-event image obtained at 06:06 UT. One can notice the CME as a faint ring like feature in the southern hemisphere above the occulting disk. According to the LASCO height time measurements, the leading edge of the white light CME was located at a distance of  $2.75 R_{\odot}$  at 06:37:25 UT. This was the first epoch at which its position was observationally measured. Extrapolating the above value, we find that the leading edge of the white light CME should have been located at about  $1.7 R_{\odot}$  from the center of the Sun at 06:01:06 UT. This indicates that the radio enhancement seen in Figure 3 is most likely due to thermal bremsstrahlung from the excess electrons (above the ambient) in the frontal structure of the white-light CME, and is the radio counterpart of the latter.

### 6.3 ANALYSIS

Figure 5 shows the brightness distribution obtained using the ray-tracing technique for the observed radio map in Figure 2. As in the earlier case (refer section 5.3 of chapter 5), we selected the suitable background density ( $N_{bg}$ ) and temperature ( $T_{bg}$ ) to begin with. It was found that  $N_{bg}$  and  $T_{bg}$  should be equal to  $0.45 N_0$  (where  $N_0 = 4.2 \times 10^4 \text{ cm}^{-3}$ ) and  $1.0 \times 10^6 \text{ K}$  respectively, in the present case. The parameters of various localized sources used to reproduce the brightness temperature observed at 06:01 UT are listed in Table 1. A visual inspection of Figure 3 and Figure 5 indicates that the discrete sources S8-S13 in the latter correspond most likely to the enhanced radio emission in the former. In order to verify this, we plotted the reproduced brightness distribution corresponding to S8-S13 alone (Figure 6) and estimated the difference with Figure 3. The result is shown in Figure 7. There is a 9% difference between the observed and reproduced data. This could give rise to the following errors in the fitted parameters (refer discussion in section 5.3 of chapter 5):



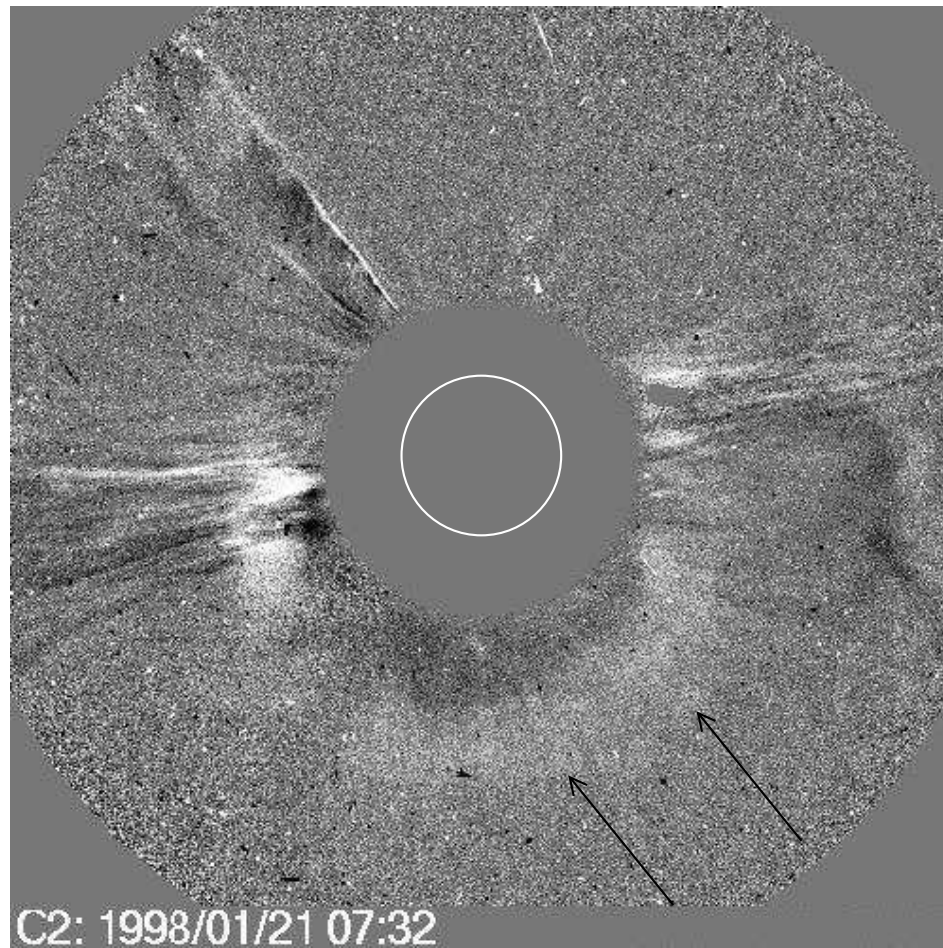


FIG. 4: Difference image (07:32-06:06 UT) of the 'halo' CME event observed with the LASCO C2 coronagraph on January 21, 1998. The inner open circle represents the solar limb. The outer filled circle is the occulting disk of the coronagraph. It extends approximately up to  $2.2 R_{\odot}$  from the center of the Sun. Solar north is straight up and east is to the left. The CME under study can be noticed as a faint ring (indicated by the arrow marks) above the occulter of the coronagraph in the southern quadrant.

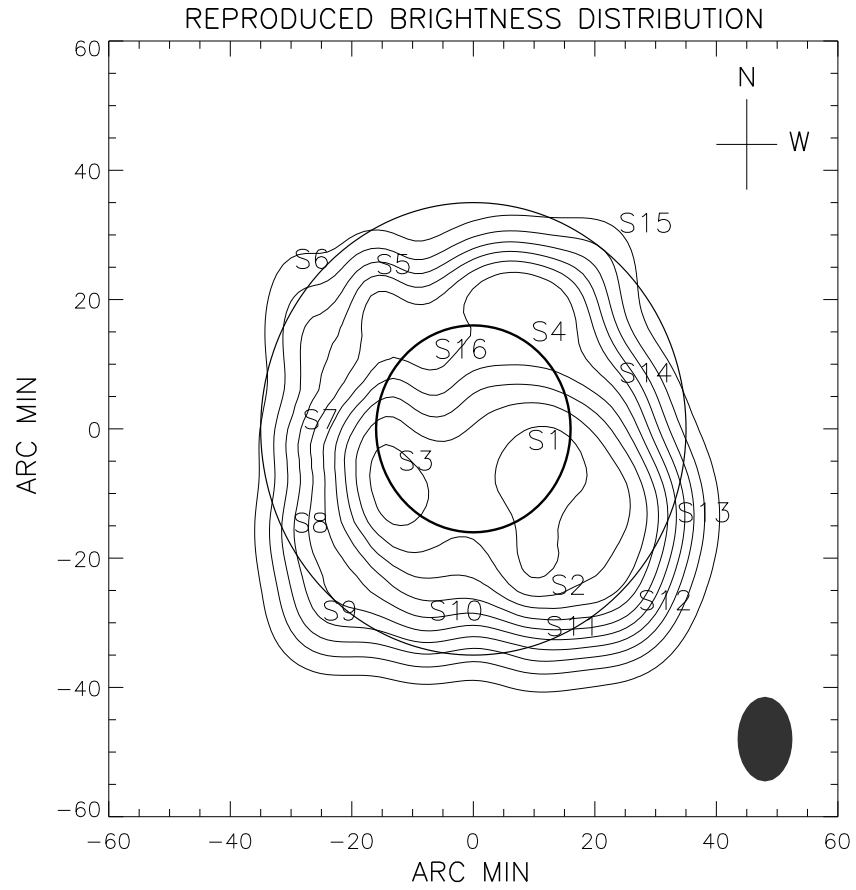


FIG. 5: Radio brightness distribution of the Sun obtained through ray-tracing calculations of the GRH data obtained at 06:01 UT (Figure 2). The numbers S1-S16 indicate the location of the centroid of the discrete sources used to reproduce this image. Refer Table 1 for the values of different parameters used in the simulation.

TABLE 1: Parameters of the discrete sources used in the ray-tracing calculations to reproduce the radioheliogram obtained with the GRH on January 21, 1998 at 06:01 UT.

Source $n$	<sup>1</sup> Position $(x_n, y_n, z_n)$	<sup>2</sup> Distance $R_\odot$	<sup>3</sup> Size $[(\sigma_x)_n, (\sigma_y)_n, (\sigma_z)_n]$	<sup>4</sup> $C_n$	Density $cm^{-3}$
S1	1.72, 0.56, -0.20	1.82	0.32, 0.74, 0.59	34.0	$3.4 \times 10^8$
S2	1.60, 0.80, -1.60	2.40	0.32, 0.47, 0.52	16.0	$4.2 \times 10^7$
S3	1.70, -0.77, -0.40	1.91	0.22, 0.55, 0.71	18.0	$1.4 \times 10^8$
S4	1.10, 0.60, 0.85	1.51	0.22, 0.63, 0.77	18.0	$5.5 \times 10^8$
S5	1.00, -1.00, 1.50	2.06	0.22, 0.22, 0.50	8.0	$4.2 \times 10^7$
S6	0.60, -1.84, 1.55	2.48	0.22, 0.32, 0.77	7.0	$1.6 \times 10^7$
S7	1.10, -1.75, 0.00	2.07	0.22, 0.32, 0.32	7.5	$3.8 \times 10^7$
S8	0.80, -1.85, -1.00	2.25	0.22, 0.32, 0.45	9.0	$3.1 \times 10^7$
S9	1.20, -1.55, -1.85	2.70	0.22, 0.45, 0.45	17.3	$2.9 \times 10^7$
S10	1.60, -0.45, -1.85	2.49	0.22, 0.39, 0.52	12.4	$2.8 \times 10^7$
S11	1.00, 0.75, -2.00	2.36	0.22, 0.45, 0.55	10.0	$2.8 \times 10^7$
S12	1.00, 1.70, -1.75	2.64	0.22, 0.45, 0.50	22.0	$4.0 \times 10^7$
S13	1.40, 2.10, -0.90	2.68	0.22, 0.45, 0.67	22.0	$3.8 \times 10^7$
S14	1.10, 1.50, 0.45	1.91	0.22, 0.45, 0.32	10.0	$7.7 \times 10^7$
S15	0.40, 1.50, 1.90	2.45	0.22, 0.39, 0.45	7.0	$1.7 \times 10^7$
S16	1.70, -0.40, 0.68	1.87	0.22, 0.19, 0.39	-0.3	$2.0 \times 10^6$

- 1 The co-ordinates of the source centroid in units of  $R_\odot$ .
- 2 Radial distance of the source from the center of the Sun in units of  $R_\odot$ .
- 3  $x$ ,  $y$ , &  $z$  size of the source in units of  $R_\odot$ .
- 4 Density factor: Density higher/lower than the background. The assumed electron density and temperature for the background are  $\approx (1.90 \times 10^4) 10^{(4.32/r)} cm^{-3}$  and  $1.0 \times 10^6$  K, respectively.

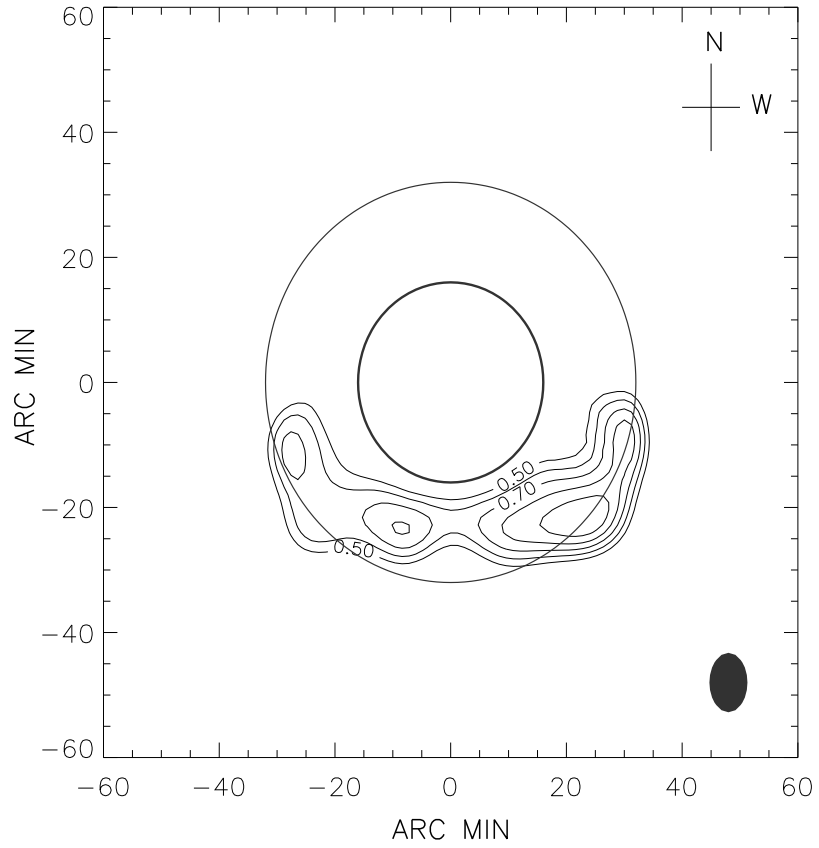


FIG. 6: Reproduced brightness temperature distribution corresponding to the radio sources S8 to S13 alone in Table 1. The brightness temperature of the CME is about  $5.4 \times 10^5$  K.

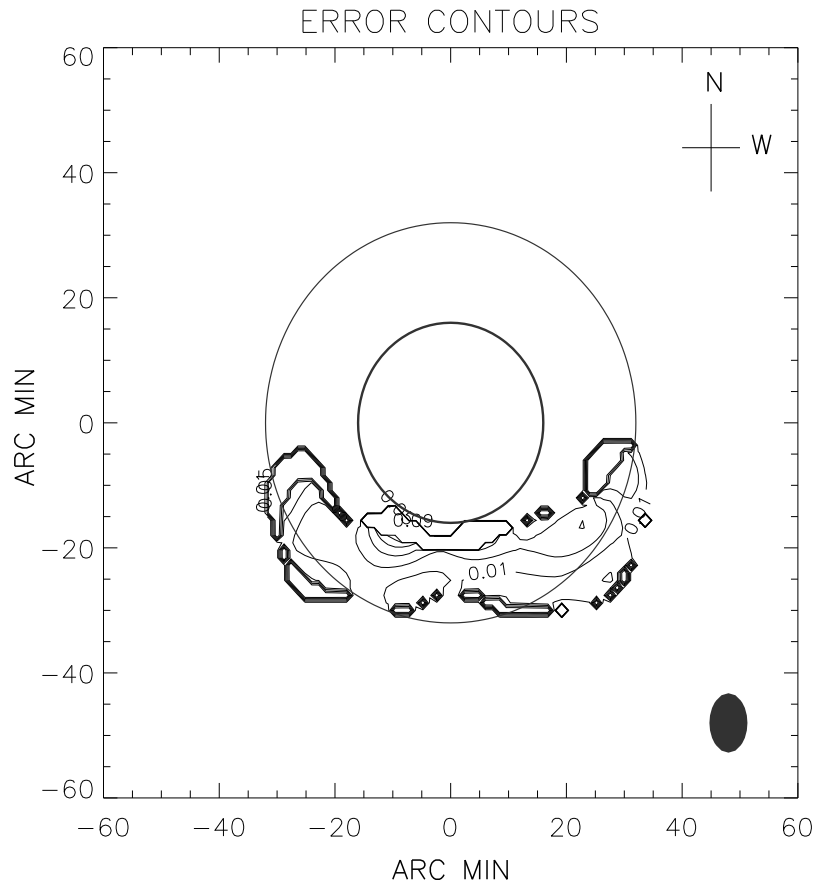


FIG. 7: Contours showing the normalized absolute difference obtained by subtracting Figure 6 from Figure 3. The maximum residual is about 9%. Some portion of the contours appear darker because the successive contours there are closely spaced.

(a) the  $x$ -coordinate.

<u>Source</u>	<u>Position</u> ( $x_n, y_n, z_n$ )
S8	→ $(0.80 \pm 0.08 R_\odot, -1.85 R_\odot, -1.00 R_\odot)$
S9	→ $(1.20 \pm 0.11 R_\odot, -1.55 R_\odot, -1.85 R_\odot)$
S10	→ $(1.60 \pm 0.07 R_\odot, -0.45 R_\odot, -1.85 R_\odot)$
S11	→ $(1.00 \pm 0.08 R_\odot, 0.75 R_\odot, -2.00 R_\odot)$
S12	→ $(1.00 \pm 0.11 R_\odot, 1.70 R_\odot, -1.75 R_\odot)$
S13	→ $(1.40 \pm 0.11 R_\odot, 2.10 R_\odot, -0.90 R_\odot)$

(b) the  $y$ -coordinate (also applicable to  $z$ -coordinate based on the symmetry property).

<u>Source</u>	<u>Position</u> ( $x_n, y_n, z_n$ )
S8	→ $(0.80 R_\odot, -1.85 \pm 0.08 R_\odot, -1.00 R_\odot)$
S9	→ $(1.20 R_\odot, -1.55 \pm 0.08 R_\odot, -1.85 R_\odot)$
S10	→ $(1.60 R_\odot, -0.45 \pm 0.08 R_\odot, -1.85 R_\odot)$
S11	→ $(1.00 R_\odot, 0.75 \pm 0.08 R_\odot, -2.00 R_\odot)$
S12	→ $(1.00 R_\odot, 1.70 \pm 0.08 R_\odot, -1.75 R_\odot)$
S13	→ $(1.40 R_\odot, 2.10 \pm 0.08 R_\odot, -0.90 R_\odot)$

(c) the  $x$ -width.

<u>Source</u>	<u>Width</u> ( $\sigma_x, \sigma_y, \sigma_z$ )
S8	→ $0.22 \pm 0.04 R_\odot, 0.32 R_\odot, 0.45 R_\odot$
S9	→ $0.22 \pm 0.04 R_\odot, 0.45 R_\odot, 0.45 R_\odot$
S10	→ $0.22 \pm 0.04 R_\odot, 0.39 R_\odot, 0.52 R_\odot$
S11	→ $0.22 \pm 0.04 R_\odot, 0.45 R_\odot, 0.55 R_\odot$
S12	→ $0.22 \pm 0.04 R_\odot, 0.45 R_\odot, 0.50 R_\odot$
S13	→ $0.22 \pm 0.04 R_\odot, 0.45 R_\odot, 0.67 R_\odot$

(d) the  $y$ -width (same for  $z$ -width also).

<u>Source</u>	<u>Width (<math>\sigma_x, \sigma_y, \sigma_z</math>)</u>
S8	→ 0.22 $R_\odot$ , 0.32 ± 0.06 $R_\odot$ , 0.45 $R_\odot$
S9	→ 0.22 $R_\odot$ , 0.45 ± 0.06 $R_\odot$ , 0.45 $R_\odot$
S10	→ 0.22 $R_\odot$ , 0.39 ± 0.06 $R_\odot$ , 0.52 $R_\odot$
S11	→ 0.22 $R_\odot$ , 0.45 ± 0.06 $R_\odot$ , 0.55 $R_\odot$
S12	→ 0.22 $R_\odot$ , 0.45 ± 0.06 $R_\odot$ , 0.50 $R_\odot$
S13	→ 0.22 $R_\odot$ , 0.45 ± 0.06 $R_\odot$ , 0.67 $R_\odot$

(e) the density enhancement factor  $C_n$ .

<u>Source</u>	<u>Density factor</u>
S8	→ 9.0 ± 0.8
S9	→ 17.3 ± 0.6
S10	→ 12.4 ± 0.8
S11	→ 10.0 ± 0.8
S12	→ 22.0 ± 0.6
S13	→ 22.0 ± 0.6

(f) the temperature enhancement factor. This deviation will be about  $\pm 0.3 \times 10^6$  K for all the sources.

(g) the background density and temperature could vary by  $\approx \pm 0.1 N_0$  and  $\pm 0.15 \times 10^6$  K, respectively.

### 6.3.1 The density of the radio CME

Since the radio CME is an extended structure, we calculated its density in the following manner.

$$(N_e)_{\text{CME}} = \frac{1}{n} \sum_i (N_e)_i \times C_i \quad ; i = \text{S8}, \dots, \text{S13} \quad (1)$$

where  $n$  is the total number of sources. From our earlier discussion we find that the sources S8-S13 constitute the radio CME. Their densities are

$$\begin{aligned}
(N_e)_{S8} \times C_{S8} &= (4.2 \times 10^4) 10^{\left(\frac{4.32}{R_8}\right)} \times 9.0 \\
&= (4.2 \times 10^4) 10^{\left(\frac{4.32}{2.25}\right)} \times 9.0 = 3.2 \times 10^7 \text{ cm}^{-3} \\
(N_e)_{S9} \times C_{S9} &= (4.2 \times 10^4) 10^{\left(\frac{4.32}{R_9}\right)} \times 17.3 \\
&= (4.2 \times 10^4) 10^{\left(\frac{4.32}{2.70}\right)} \times 17.3 = 2.9 \times 10^7 \text{ cm}^{-3} \\
(N_e)_{S10} \times C_{S10} &= (4.2 \times 10^4) 10^{\left(\frac{4.32}{R_{10}}\right)} \times 12.4 \\
&= (4.2 \times 10^4) 10^{\left(\frac{4.32}{2.49}\right)} \times 12.4 = 2.9 \times 10^7 \text{ cm}^{-3} \\
(N_e)_{S11} \times C_{S11} &= (4.2 \times 10^4) 10^{\left(\frac{4.32}{R_{11}}\right)} \times 10.0 \\
&= (4.2 \times 10^4) 10^{\left(\frac{4.32}{2.36}\right)} \times 10.0 = 2.8 \times 10^7 \text{ cm}^{-3} \\
(N_e)_{S12} \times C_{S12} &= (4.2 \times 10^4) 10^{\left(\frac{4.32}{R_{12}}\right)} \times 22.0 \\
&= (4.2 \times 10^4) 10^{\left(\frac{4.32}{2.64}\right)} \times 22.0 = 4.0 \times 10^7 \text{ cm}^{-3} \\
(N_e)_{S13} \times C_{S13} &= (4.2 \times 10^4) 10^{\left(\frac{4.32}{R_{13}}\right)} \times 22.0 \\
&= (4.2 \times 10^4) 10^{\left(\frac{4.32}{2.68}\right)} \times 22.0 = 3.7 \times 10^7 \text{ cm}^{-3}
\end{aligned}$$

Assuming that the average of the above represents the electron density of the radio CME, we get  $(N_e)_{\text{CME}} \approx 3.25 \times 10^7 \text{ cm}^{-3}$ . Upon including the corresponding errors discussed above, we find that the density of the radio CME should be in the range  $3.0 - 3.5 \times 10^7 \text{ cm}^{-3}$ .

### 6.3.2 The volume of the CME

Following section 6.3, we can calculate the volume of the CME by adding up the corresponding value of the associated discrete sources S8 to S13, i.e.

$$V_{\text{CME}} = V_{S8} + V_{S9} + V_{S10} + V_{S11} + V_{S12} + V_{S13} \quad (2)$$

The volume of the individual radio sources are,

$$\begin{aligned}
V_{S8} &= (\sigma_x)_{S8} \times (\sigma_y)_{S8} \times (\sigma_z)_{S8} \\
&= 0.22 R_\odot \times 0.32 R_\odot \times 0.45 R_\odot \\
&= 1.07 \times 10^{31} \text{ cm}^3 \\
V_{S9} &= (\sigma_x)_{S9} \times (\sigma_y)_{S9} \times (\sigma_z)_{S9} \\
&= 0.22 R_\odot \times 0.45 R_\odot \times 0.45 R_\odot \\
&= 1.50 \times 10^{31} \text{ cm}^3
\end{aligned}$$



$$\begin{aligned}
V_{S10} &= (\sigma_x)_{S10} \times (\sigma_y)_{S10} \times (\sigma_z)_{S10} \\
&= 0.22 R_\odot \times 0.39 R_\odot \times 0.52 R_\odot \\
&= 1.50 \times 10^{31} \text{ cm}^3 \\
V_{S11} &= (\sigma_x)_{S11} \times (\sigma_y)_{S11} \times (\sigma_z)_{S11} \\
&= 0.22 R_\odot \times 0.45 R_\odot \times 0.55 R_\odot \\
&= 1.84 \times 10^{31} \text{ cm}^3 \\
V_{S12} &= (\sigma_x)_{S12} \times (\sigma_y)_{S12} \times (\sigma_z)_{S12} \\
&= 0.22 R_\odot \times 0.45 R_\odot \times 0.50 R_\odot \\
&= 1.67 \times 10^{31} \text{ cm}^3 \\
V_{S13} &= (\sigma_x)_{S13} \times (\sigma_y)_{S13} \times (\sigma_z)_{S13} \\
&= 0.22 R_\odot \times 0.45 R_\odot \times 0.67 R_\odot \\
&= 2.24 \times 10^{31} \text{ cm}^3
\end{aligned}$$

Substituting the values of  $V_{S8}, \dots, V_{S13}$  in equation (2), we get  $V_{CME} \approx 9.82 \times 10^{31} \text{ cm}^3$ . Since there is error in the estimate of size of the above radio sources, the volume of the CME will also have error. Our calculations show that it should be between  $7.9 \times 10^{31} - 1.16 \times 10^{32} \text{ cm}^3$ .

### 6.3.3 The mass of the CME

The total mass of the CME is given by,

$$M_{CME} = m_8 + m_9 + m_{10} + m_{11} + m_{12} + m_{13} \quad (3)$$

where  $m_8, m_9, \dots, m_{13}$  represent the mass of the structure S8, S9, ..., S13, respectively. They were calculated by multiplying the volume of each one of the latter with the electron density at the location of their corresponding centroid, i.e,

$$\begin{aligned}
m_8 &= (N_e)_{S8} \times V_{S8} \times (2 \times 10^{-24}) \text{ g} \\
&= [3.2 \times 10^7 \text{ cm}^{-3}] \times [1.07 \times 10^{31} \text{ cm}^3] \times (2 \times 10^{-24}) \text{ g} = 6.8 \times 10^{14} \text{ g} \\
m_9 &= (N_e)_{S9} \times V_{S9} \times (2 \times 10^{-24}) \text{ g} \\
&= [2.9 \times 10^7 \text{ cm}^{-3}] \times [1.50 \times 10^{31} \text{ cm}^3] \times (2 \times 10^{-24}) \text{ g} = 8.7 \times 10^{14} \text{ g} \\
m_{10} &= (N_e)_{S10} \times V_{S10} \times (2 \times 10^{-24}) \text{ g} \\
&= [2.9 \times 10^7 \text{ cm}^{-3}] \times [1.50 \times 10^{31} \text{ cm}^3] \times (2 \times 10^{-24}) \text{ g} = 8.7 \times 10^{14} \text{ g} \\
m_{11} &= (N_e)_{S11} \times V_{S11} \times (2 \times 10^{-24}) \text{ g} \\
&= [2.8 \times 10^7 \text{ cm}^{-3}] \times [1.84 \times 10^{31} \text{ cm}^3] \times (2 \times 10^{-24}) \text{ g} = 1.0 \times 10^{15} \text{ g} \\
m_{12} &= (N_e)_{S12} \times V_{S12} \times (2 \times 10^{-24}) \text{ g} \\
&= [4.0 \times 10^7 \text{ cm}^{-3}] \times [1.67 \times 10^{31} \text{ cm}^3] \times (2 \times 10^{-24}) \text{ g} = 1.3 \times 10^{15} \text{ g} \\
m_{13} &= (N_e)_{S13} \times V_{S13} \times (2 \times 10^{-24}) \text{ g} \\
&= [3.7 \times 10^7 \text{ cm}^{-3}] \times [2.24 \times 10^{31} \text{ cm}^3] \times (2 \times 10^{-24}) \text{ g} = 1.7 \times 10^{15} \text{ g}
\end{aligned}$$

Substituting the above values in equation (3) and including the error in density and volume, we get  $M_{\text{CME}} \approx 6.42 \pm 1.7 \times 10^{15} \text{ g}$ . Since our main interest is to calculate the space speed of the CME, its position in 3-D space should be known. From section 6.3.1 and 6.3.2, we see that the mass of the CME is not confined to a particular location in 3D space. Therefore, its motion can be understood if we consider it as a system of particles.

#### 6.3.4 The motion of a system of particles in a 3-D space

Consider a group of particles moving in a three-dimensional space under the influence of a driving force ( $\vec{F}$ ). The force on each particle is  $\vec{f}_i$  and the driving force in terms of the latter can be expressed as

$$\vec{F} = \sum_{i=1}^{\xi} \vec{f}_i, \quad (4)$$

where  $\xi$  is the number of particles in the system. Equation (4) can be written explicitly as,

$$M\vec{A} = m_1 \vec{a}_1 + m_2 \vec{a}_2 + \dots + m_{\xi} \vec{a}_{\xi}. \quad (5)$$

The vector  $\vec{A}$  is the net acceleration in the system and  $M$  is its total mass. The vectors  $\vec{a}_1, \vec{a}_2, \dots, \vec{a}_{\xi}$  represent the acceleration of individual particles in the system.

By rewriting equation (5) in the following form

$$M \frac{d^2}{dt^2} \vec{\mathbf{R}}_g = \frac{d^2}{dt^2} \sum_i^{\xi} m_i \vec{\mathbf{r}}_i , \quad (6)$$

we get

$$\vec{\mathbf{R}}_g = \frac{1}{M} \sum_i^{\xi} m_i \vec{\mathbf{r}}_i . \quad (7)$$

where  $\vec{\mathbf{R}}_g$  is the position vector of the center of mass of the system of particles. Equation (7) implies that the motion of a system of particles can be described by the motion of its center of mass.

### 6.3.5 The center of mass of the CME ( $\vec{\mathbf{R}}_{\text{CME}}$ )

The position vector of the ‘radio CME’ can be obtained from the location of its associated radio structures (given in Table 1) in three-dimensional space. If  $\vec{\mathbf{R}}_{\text{CME}}$  indicates the former, then we have

$$\vec{\mathbf{R}}_{\text{CME}} = \frac{1}{M_{\text{CME}}} [m_8 \vec{\mathbf{r}}_8 + m_9 \vec{\mathbf{r}}_9 + m_{10} \vec{\mathbf{r}}_{10} + m_{11} \vec{\mathbf{r}}_{11} + m_{12} \vec{\mathbf{r}}_{12} + m_{13} \vec{\mathbf{r}}_{13}] \quad (8)$$

Here  $\vec{\mathbf{r}}_8, \vec{\mathbf{r}}_9, \dots, \vec{\mathbf{r}}_{13}$  represent the position vector of the radio structures S8, S9, ..., S13, respectively and their values are,

$$\vec{\mathbf{r}}_8 = [0.80 \hat{\mathbf{x}} - 1.85 \hat{\mathbf{y}} - 1.00 \hat{\mathbf{z}}] R_{\odot}$$

$$\vec{\mathbf{r}}_9 = [1.20 \hat{\mathbf{x}} - 1.55 \hat{\mathbf{y}} - 1.85 \hat{\mathbf{z}}] R_{\odot}$$

$$\vec{\mathbf{r}}_{10} = [1.60 \hat{\mathbf{x}} - 0.45 \hat{\mathbf{y}} - 1.85 \hat{\mathbf{z}}] R_{\odot}$$

$$\vec{\mathbf{r}}_{11} = [1.00 \hat{\mathbf{x}} + 0.75 \hat{\mathbf{y}} - 2.00 \hat{\mathbf{z}}] R_{\odot}$$

$$\vec{\mathbf{r}}_{12} = [1.00 \hat{\mathbf{x}} + 1.70 \hat{\mathbf{y}} - 1.75 \hat{\mathbf{z}}] R_{\odot}$$

$$\vec{\mathbf{r}}_{13} = [1.40 \hat{\mathbf{x}} + 2.10 \hat{\mathbf{y}} - 0.90 \hat{\mathbf{z}}] R_{\odot}$$

Using the above numbers in equation (8) along with their corresponding mass, we

get

$$\begin{aligned}
m_8 \vec{\mathbf{r}}_8 &= [6.8 \times 10^{14} \text{ g}] [0.80 \hat{\mathbf{x}} - 1.85 \hat{\mathbf{y}} - 1.00 \hat{\mathbf{z}}] \text{ R}_\odot \\
\Rightarrow \frac{1}{M_{\text{CME}}} \{m_8 \vec{\mathbf{r}}_8\} &= [0.08 \hat{\mathbf{x}} - 0.19 \hat{\mathbf{y}} - 0.11 \hat{\mathbf{z}}] \text{ R}_\odot \\
m_9 \vec{\mathbf{r}}_9 &= [8.7 \times 10^{14} \text{ g}] [1.20 \hat{\mathbf{x}} - 1.55 \hat{\mathbf{y}} - 1.85 \hat{\mathbf{z}}] \text{ R}_\odot \\
\Rightarrow \frac{1}{M_{\text{CME}}} \{m_9 \vec{\mathbf{r}}_9\} &= [0.16 \hat{\mathbf{x}} - 0.21 \hat{\mathbf{y}} - 0.25 \hat{\mathbf{z}}] \text{ R}_\odot \\
m_{10} \vec{\mathbf{r}}_{10} &= [8.7 \times 10^{14} \text{ g}] [1.60 \hat{\mathbf{x}} - 0.45 \hat{\mathbf{y}} - 1.85 \hat{\mathbf{z}}] \text{ R}_\odot \\
\Rightarrow \frac{1}{M_{\text{CME}}} \{m_{10} \vec{\mathbf{r}}_{10}\} &= [0.22 \hat{\mathbf{x}} - 0.06 \hat{\mathbf{y}} - 0.25 \hat{\mathbf{z}}] \text{ R}_\odot \\
m_{11} \vec{\mathbf{r}}_{11} &= [1.0 \times 10^{15} \text{ g}] [1.00 \hat{\mathbf{x}} + 0.75 \hat{\mathbf{y}} - 2.00 \hat{\mathbf{z}}] \text{ R}_\odot \\
\Rightarrow \frac{1}{M_{\text{CME}}} \{m_{11} \vec{\mathbf{r}}_{11}\} &= [0.16 \hat{\mathbf{x}} + 0.12 \hat{\mathbf{y}} - 0.31 \hat{\mathbf{z}}] \text{ R}_\odot \\
m_{12} \vec{\mathbf{r}}_{12} &= [1.3 \times 10^{15} \text{ g}] [1.00 \hat{\mathbf{x}} + 1.70 \hat{\mathbf{y}} - 1.75 \hat{\mathbf{z}}] \text{ R}_\odot \\
\Rightarrow \frac{1}{M_{\text{CME}}} \{m_{12} \vec{\mathbf{r}}_{12}\} &= [0.20 \hat{\mathbf{x}} + 0.34 \hat{\mathbf{y}} - 0.35 \hat{\mathbf{z}}] \text{ R}_\odot \\
m_{13} \vec{\mathbf{r}}_{13} &= [1.7 \times 10^{15} \text{ g}] [1.40 \hat{\mathbf{x}} + 2.10 \hat{\mathbf{y}} - 0.90 \hat{\mathbf{z}}] \text{ R}_\odot \\
\Rightarrow \frac{1}{M_{\text{CME}}} \{m_{13} \vec{\mathbf{r}}_{13}\} &= [0.37 \hat{\mathbf{x}} + 0.56 \hat{\mathbf{y}} - 0.24 \hat{\mathbf{z}}] \text{ R}_\odot
\end{aligned}$$

The vector addition of all the above gives the resultant position vector of the CME, i.e.,  $\vec{\mathbf{R}}_{\text{CME}} = (1.18 \text{ R}_\odot) \hat{\mathbf{x}} + (0.52 \text{ R}_\odot) \hat{\mathbf{y}} - (1.52 \text{ R}_\odot) \hat{\mathbf{z}}$ . But, if we include the error in position coordinates and volume of the CME associated radio structures, this could be anywhere between  $(1.10 \text{ R}_\odot) \hat{\mathbf{x}} + (0.41 \text{ R}_\odot) \hat{\mathbf{y}} - (1.43 \text{ R}_\odot) \hat{\mathbf{z}}$  and  $(1.19 \text{ R}_\odot) \hat{\mathbf{x}} + (0.63 \text{ R}_\odot) \hat{\mathbf{y}} - (1.51 \text{ R}_\odot) \hat{\mathbf{z}}$ .

### 6.3.6 The location of eruption of the CME

As pointed out in Section 6.2, the 'halo' CME of January 21, 1998 was associated with the disappearance of the H $\alpha$  filament from the location (S57 E19) on the solar disk. Assuming the latter to be located on the solar surface, i.e. at a radial distance of  $1 \text{ R}_\odot$  (in three-dimensional space) from the center of the Sun, its position vector can be calculated in the following manner. If  $r$ ,  $\theta$ ,  $\phi$  are the radius, azimuthal angle and the polar angle respectively in the spherical geometry, then

$$x = r \cos \theta \sin \phi \quad (9)$$

$$y = r \sin \theta \sin \phi \quad (10)$$

$$z = r \cos \phi \quad (11)$$

enable co-ordinate transformation from spherical to Cartesian coordinates  $(x, y, z)$ . Any arbitrary point ( $P$ ) on a spherical surface can be represented by the above variables  $\theta$  and  $\phi$ . If the point lies on the surface of the Sun [a sphere of unit radius ( $= 1 R_{\odot}$ )] then the above variables/co-ordinates are its longitude ( $\theta$ ) and latitude ( $90^{\circ} - \phi$ ). Using equations (9)-(11), the Cartesian co-ordinates of the  $H\alpha$  filament on the solar surface were obtained as

$$\begin{aligned} x &= (1 R_{\odot}) \times \cos(-19^{\circ}) \sin[90^{\circ} - (-57^{\circ})] = 0.51 R_{\odot} \\ y &= (1 R_{\odot}) \times \sin(-19^{\circ}) \sin[90^{\circ} - (-57^{\circ})] = -0.18 R_{\odot} \\ z &= (1 R_{\odot}) \times \cos[90^{\circ} - (-57^{\circ})] = -0.84 R_{\odot} \end{aligned}$$

Therefore the position vector of the  $H\alpha$  filament or the eruption location of the CME is,  $\vec{R}_{H\alpha} = (0.51 R_{\odot}) \hat{x} - (0.18 R_{\odot}) \hat{y} - (0.84 R_{\odot}) \hat{z}$ .

### 6.3.7 The space-speed of the CME

According to the LASCO CME catalog<sup>2</sup>, the lift-off time of January 21, 1998 'halo' CME, (projected to  $1 R_{\odot}$ ) is 05:41:17 UT. The above was obtained by employing a linear fit to the LASCO C2/C3 height-time measurements of the leading edge of the white-light CME in the plane of the sky, and is for the case where the CME is considered to travel at a constant speed. Note in the present case the source region of the CME is assumed to be on the solar disk (S57 E19), i.e. the location of the  $H\alpha$  filament. This corresponds to a radial distance of

$$(y^2 + z^2)^{1/2} = [(-0.18 R_{\odot})^2 + (-0.84 R_{\odot})^2]^{0.5} \approx 0.86 R_{\odot}$$

in the plane of the sky. The estimated lift-off time of the CME obtained by back-projecting its height-time curve to the above location is 05:37:26 UT. This implies that the CME had traveled a distance of about (refer section 6.3.5 and 6.3.6)

$$\begin{aligned} |\vec{R}_{CME} - \vec{R}_{H\alpha}| &= |(0.67 R_{\odot}) \hat{x} + (0.70 R_{\odot}) \hat{y} - (0.68 R_{\odot}) \hat{z}| \\ &= [(0.67 R_{\odot})^2 + (0.70 R_{\odot})^2 + (-0.68 R_{\odot})^2]^{0.5} \\ &= 1.18 R_{\odot} \simeq 821280 \text{ km} \end{aligned}$$

in the three-dimensional space between the time at which the CME was observed with the GRH and the the eruption of  $H\alpha$  filament, i.e. 06:01:06 - 05:37:26 UT = 1420 s. This gives an average space speed of  $\approx 578 \text{ km s}^{-1}$  for the radio CME. This value

<sup>2</sup>[http://cdaw.gsfc.nasa.gov/CME\\_list/UNIVERSAL/1998\\_01/univ1998\\_01.html](http://cdaw.gsfc.nasa.gov/CME_list/UNIVERSAL/1998_01/univ1998_01.html)

should be treated with caution since it was assumed that the CME was propagating at a constant speed. Again, the error in  $\vec{\mathbf{R}}_{\text{CME}}$  indicates that the average speed of the CME can vary from 510 to 614 km s<sup>-1</sup>. We could not calculate the speed of the CME independently of its onset time from the solar surface without any assumptions, since we do not have sufficient radio data. The above space-speed can be separated into two components, namely, (i) the speed along the line-of-sight and (ii) in the plane of the sky. The former is the x-component of the space velocity, i.e.,

$$u_x \approx \frac{0.67 R_{\odot}}{1420 \text{ s}} \approx 328 \text{ km s}^{-1}$$

and the latter is the square root of the sum of the squares of y & z components of the space velocity, i.e.,

$$(v_y^2 + v_z^2)^{0.5} \approx \frac{1}{1420} [(0.7 R_{\odot})^2 + (-0.68 R_{\odot})^2]^{0.5} \text{ km s}^{-1} \approx 478 \text{ km s}^{-1}$$

Since we found that the space speed of the CME varies from 510-614 km s<sup>-1</sup>, the speed along the line of sight and in the plane of the sky could lie in the range 289-333 km s<sup>-1</sup> and 410-515 km s<sup>-1</sup> respectively.

## 6.4 CONCLUSION

An independent technique for the estimation of the three-dimensional space speed of a CME in the low corona using meter wavelength radio data is described. It is based on ray-tracing analysis of the thermal radio emission from the free electrons (with respect to the ambient) in the frontal structure of the CME. The method was used to derive the space speed of the radio counterpart of ‘halo’ CME observed on January 21, 1998 with the GRH at 109 MHz, and the value is  $\approx 580^{+34}_{-70}$  km s<sup>-1</sup>. The speed along the line of sight and in the plane of the sky are,  $\approx 328^{+06}_{-38}$  &  $478^{+37}_{-68}$  km s<sup>-1</sup>, respectively. We like to mention here that the speed in the plane of the sky determined by us is higher than that of the LASCO estimate (361 km s<sup>-1</sup>). This is most likely due to error in the fitted parameters and the assumption made in estimating the initiation time of the CME by extrapolating the white light height time curve. Nevertheless, this can be considered as an example to check for the possibility of using radio imaging observations at meter wavelengths to study the inner coronal kinematics of CMEs. But the pre-requisites of the method are: (i) the CME should not be accompanied by any intense non-thermal emission (particularly the long lasting Type-I noise storm continuum) as in the present case, and (ii) it should occur during the observing

period of the particular instrument. The first limitation could be partly overcome by obtaining high dynamic range radio maps (where both large scale thermal emission from the CME as well as the more discrete and localized Type-I source are seen together) through use of good calibration procedures [Subramanian et al. (2005)]. As far as the second drawback is concerned, the only solution is continuous observations of the Sun for a longer time interval. The GRH has been recently equipped with an electronic tracking system that will allow us to carry out observations of the Sun for about 6 hrs ( $\approx$  03:30-09:30 UT) everyday. It is a nice coincidence that observations with Nancay Radioheliograph [NRH; Kerdraon and Delouis (1997)] in France start from around 08:30 UT and continue till  $\approx$  15:00 UT everyday. Though the frequency range of operation of the NRH and the GRH are different, they provide a continuous coverage of the Sun for about 11 to 12 hours in a day. The commissioning of the Frequency Agile Solar Radio telescope [FASR; Bastian (2004)] should increase the above coverage. Therefore, we would like to explore the possibility of estimating the space speed and acceleration of CMEs in the low corona using coordinated radio observations in the future; This could possibly reduce the error in determining the exact initiation time of the CME as described earlier and hence may allow a reliable space speed estimate.

## CHAPTER 7

# DECAMETER WAVELENGTH OBSERVATIONS OF THE CRAB NEBULA AND ITS ANGULAR BROADENING DUE TO A CORONAL MASS EJECTION

### 7.1 INTRODUCTION

The interplanetary scintillation observations of various compact radio sources play a useful role in understanding the evolution of a solar disturbance during its propagation through the heliosphere [Ananthakrishnan (2000); Tokumaru et al. (2000); Manoharan et al. (2001); Jackson and Hick (2004)]. Imaging observations of cosmic radio sources whose radiation traverse the solar corona is another potential and straightforward technique. The radio waves undergo irregular refraction (scattering) due to inhomogeneities in the coronal electron density distribution. This causes a variety of phenomena such as phase scintillation, intensity scintillation, spectral broadening, temporal broadening and angular broadening. Observations of each of these phenomena may be exploited to derive useful information on the scattering medium [Bastian (2000)]. Since we are interested in two-dimensional interferometric imaging observations of the change in the angular extent of sidereal radio sources (point sources for the GRH) when they are occulted by the solar corona, we take up angular broadening for further discussions.

Consider an observer in the  $(x, y)$ -plane of a right handed co-ordinate system at a distance  $L$  along the  $z$ -axis from the origin [ $z = 0$ ; refer Figure 1]. Assume that a plane wave of unit amplitude and wavelength  $\lambda$  propagates from  $z < 0$  to  $z = 0$ . Let us visualize that the scattering medium be a thin ( $\delta z \ll L$ ), two-dimensional screen located at  $z = 0$ . An electromagnetic wave incident on it will be scattered into different directions from the initial direction of propagation. In other words, the observer will receive radiation from many independent scattering blobs present in the medium. Each blob gives rise to an independent phase shift to the incident wave. Therefore, the phase of the latter varies randomly as a function of position. Hence, after passing through the phase-changing screen at  $z = 0$ , the wavefront is said to be ‘corrugated’. For a plane wave, the correlation function of the incident electric field (i.e, the visibility) is given by  $v(s) = \langle E(x)E^*(x + s) \rangle$ , where ‘ $s$ ’ is the base line



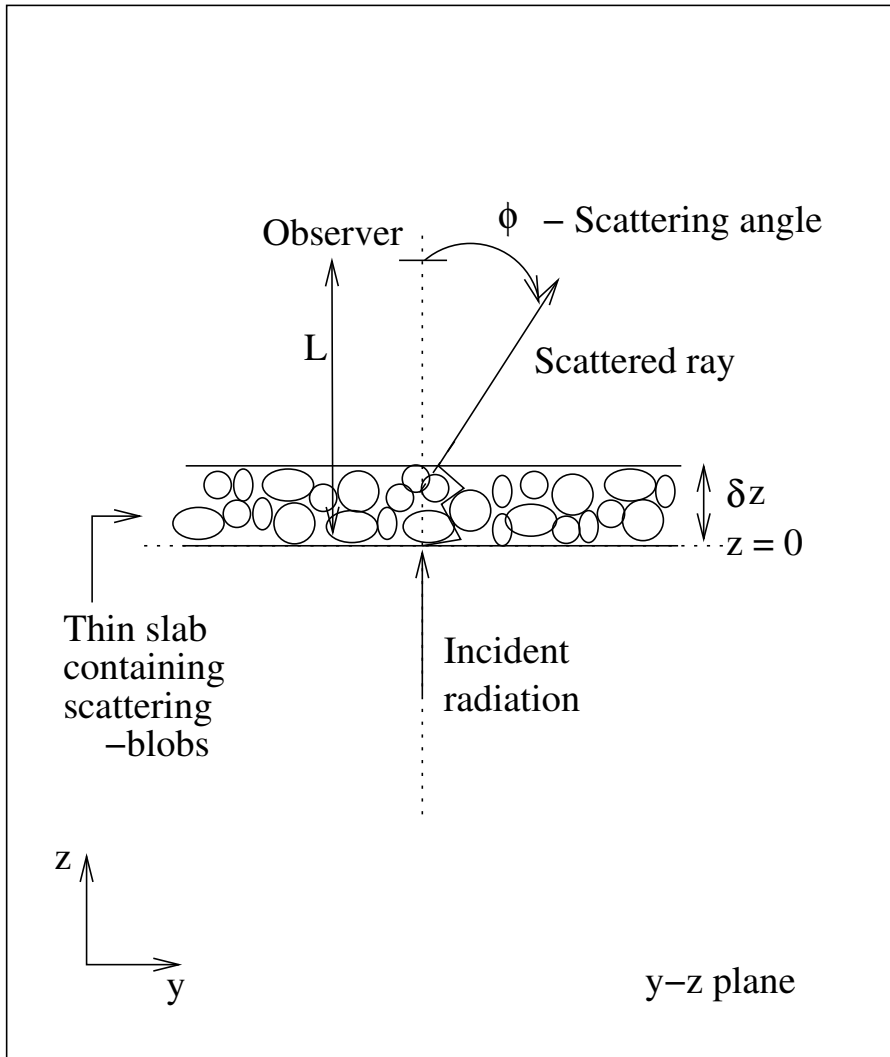


FIG. 1: Schematic showing the scattering of an electro-magnetic wave (traveling from  $z < 0$ ) by density inhomogeneities (or scattering blobs) present in a thin slab (of thickness  $\delta z$ ) located at  $z = 0$ . The observer is at a distance  $L$  from the slab and receives the scattered radiation at an angle  $\phi$  (scattering angle) w.r.t the incident direction. The  $(x, y)$ -plane is perpendicular to the plane of the paper.

length. For a point source  $v(s)$  is a constant independent of  $s$ . But after corrugation, the emergent electric field will have a finite coherence length. According to Van Cittert-Zernike theorem, this is equivalent to stating that the original point source has blurred out to a source of angular extent  $\phi$ . Consequently there is an apparent increase in the observed angular size of the radio source by the above angle and the source is said to be angular/scatter-broadened. Such observations can be used to obtain the coronal electron density at different heights by determining the value of effective radius of occultation (i.e., the location from where one notices the onset of angular broadening of remote radio sources) at various observing frequencies [Machin and Smith (1951)]. The amount of coronal scattering depends to a large extent on the relative location of the Sun and the radio source. For example, the half-width of the angular brightness distribution caused by the multiple small-angle scattering of radiation from a point source observed through the interplanetary medium is given as  $\theta = 50(\lambda^2/r^2)$  [Erickson (1964)], where ' $r$ ' is the distance from the Sun in solar radii,  $\lambda$  is in meters and  $\theta$  is in arcmin. One generally observes a gradual increase/decrease in the angular size of the source during its ingress/egress. According to Rickett & Coles (2000), scattering in the solar wind reduces the visibility on an interferometer baseline by a factor  $v(b) \propto e^{-(b/20f)^2}$  ( $b$  in km and  $f$  in MHz). Bastian (1994) showed that the scattering cross section increases from center to limb of the solar disk at a particular wavelength. But there are instances when transient ( $\sim$  few hours) changes in the observed characteristics of the source have been noticed in addition to the behavior described above, particularly in the case of the Crab nebula, when it is close to the plane of the ecliptic and passes as near as about  $5 R_{\odot}$  from the Sun around June 15 every year [Vitkevich (1955, 1958); Blum and Boischot (1957); Gorgolewski et al. (1962); Sastry and Subramanian (1974)]. This could be due to propagation of streams of charged particles outward from an active area on the Sun's disk [Slee (1959); Vitkevich (1961)]. Since the strength of solar activity varies with sunspot cycle, the magnitude of the aforementioned short term changes vary accordingly [Erickson (1964)]. This indicates that the anisotropy in the coronal electron density distribution should vary with solar cycle. Slee (1966) found that the anisotropy in the solar corona is reduced by a factor of 3 during sunspot minimum. The high level of turbulence in the solar corona observed during solar maximum by Anantharamaiah (1994) confirms this. In this connection we would like to note that the anisotropy in the coronal density structure is scale dependent. Armstrong et al. (1990) found that structures of scale size greater

than 10 km are more anisotropic, comparatively. However, a precise correspondence between an ejection of material from the Sun and a change in the angular dimensions of a radio source at a large distance ( $\sim 41 R_{\odot}$  from the Sun) has not been reported so far. Given the situation, we describe two-dimensional radio imaging observations of the angular broadening of Crab nebula due to its radio radiation passing through a slow coronal mass ejection.

## 7.2 OBSERVATIONS

The radio data presented were obtained with the GRH during the course of our observations on the occultation of the Crab Nebula (a point source for the GRH) by the solar corona in June, 1997. The observing frequency was 50 MHz, and the integration time used was 4.64 s. The angular resolution and the field of view at the above frequency are  $\sim 20' \times 30'$  and  $5^{\circ} \times 12^{\circ}$ , respectively. Figure 2 shows the radio map of the Crab Nebula obtained on June 3, 1997 at 07:37 UT when it was at a distance of  $\sim 45 R_{\odot}$  to the southeast of the Sun. No appreciable angular broadening was noticed on this day. This is consistent with the earlier result that the tangential and radial broadening of Crab Nebula (due to scattering by density irregularities in the solar corona), becomes noticeable only when it is approximately  $15 R_{\odot}$  from the Sun [Harries et al. (1970)]. Figure 3 shows the radio map of the Crab Nebula obtained on June 4, 1997 at 07:33 UT when it was at a distance of  $\sim 41 R_{\odot}$  from the Sun. A comparison with Figure 2 shows a clear broadening of the source in both directions on this day. The observed half-power widths were  $38' \times 35'$ . The measured flux density was  $1852 \pm 200$  Jy. This is less compared with the actual flux density of the Crab Nebula at 50 MHz, which is  $\approx 2287$  Jy. The present observations were calibrated using the radio source Virgo A, whose flux density at 50 MHz is about 2863 Jy [Nelson et al. (1985)]. The radio map of the Crab Nebula obtained on June 5, 1997 when it was at a distance of  $\sim 37 R_{\odot}$  from the Sun is shown in Figure 4. Again, no broadening of the source was observed like in Figure 2. According to the CME catalog<sup>1</sup> for the year 1997, the LASCO C2 coronagraph on board SOHO observed a faint CME on June 2, 1997 at 08:30:05 UT in the southeast quadrant of the Sun at a position angle of  $113^{\circ}$  (Figure 5). The angular width of the event was  $\sim 72^{\circ}$ . Its linear speed was  $\simeq 157$  km s<sup>-1</sup> and no acceleration was reported. The estimated lift-off time of the CME was 05:44:26 UT. The Sun was quiet, and no white-light or

---

<sup>1</sup>[http://cdaw.gsfc.nasa.gov/CME\\_list/UNIVERSAL/1997\\_06/univ1997\\_06.html](http://cdaw.gsfc.nasa.gov/CME_list/UNIVERSAL/1997_06/univ1997_06.html)

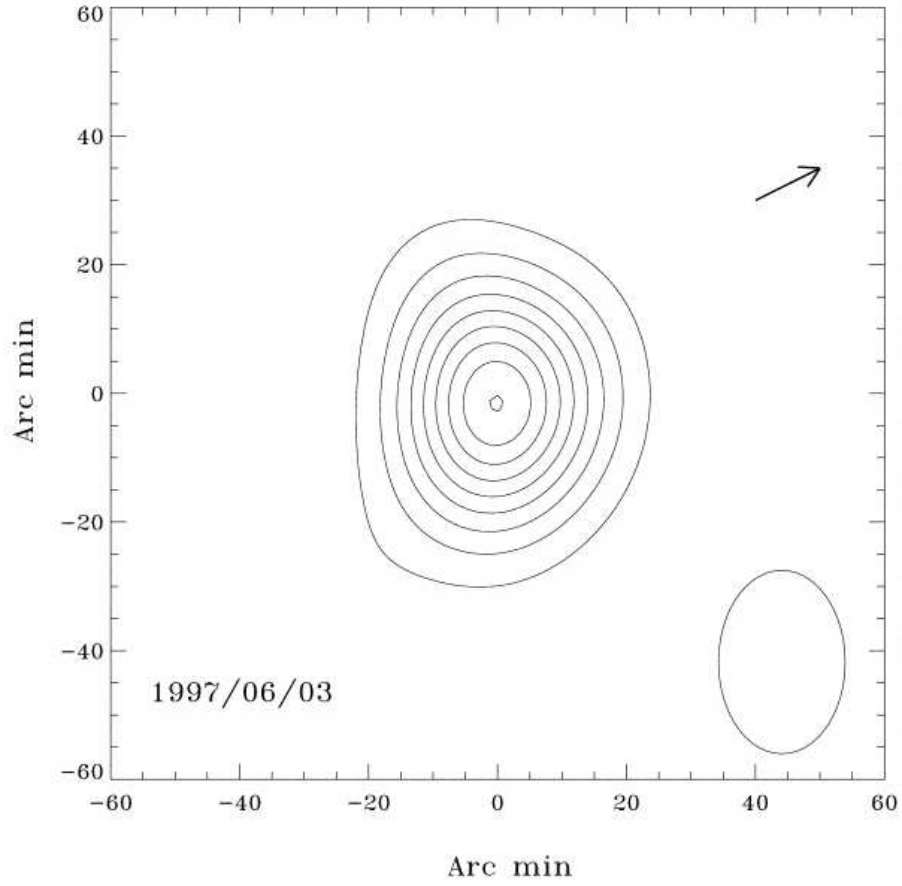


FIG. 2: Radio map of the Crab nebula obtained with the GRH on June 3, 1997 at 50 MHz, when it was at a distance of  $\approx 45 R_{\odot}$  from the center of the Sun (indicated by the arrow mark) The peak flux is  $2287 \pm 200$  Jy, and the contour levels are 0.05, 0.15, 0.25, 0.35, 0.45, 0.55, 0.65, 0.75, and 0.85 times the peak flux. North is straight up, and east is to the left. The GRH beam at 50 MHz is shown in the bottom right-hand corner.

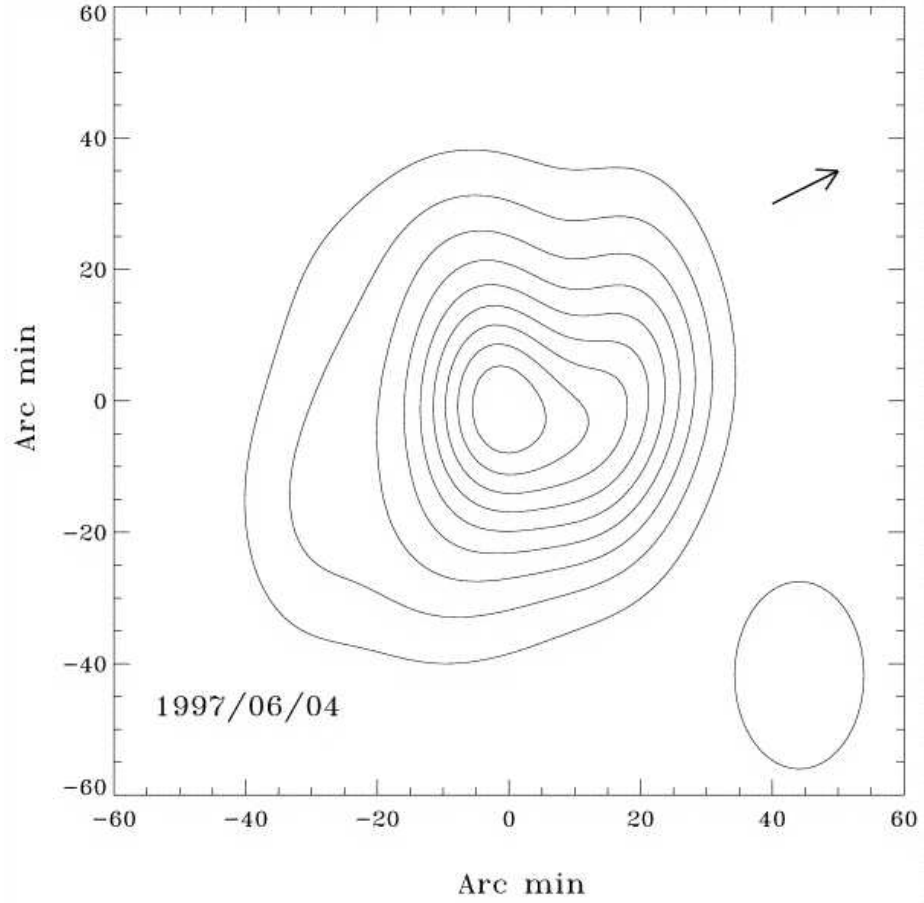


FIG. 3: Same as Figure 2 but obtained on June 4, 1997 with the CME in the foreground at  $41 R_{\odot}$  from the Sun. The peak flux is  $1852 \pm 200$  Jy, and the contour levels are 0.1, 0.2, 0.3, 0.4, 0.5, 0.6, 0.7, 0.8, and 0.9 times the peak flux. One can see a noticeable broadening in the angular size of the Crab nebula both in radial and tangential directions.

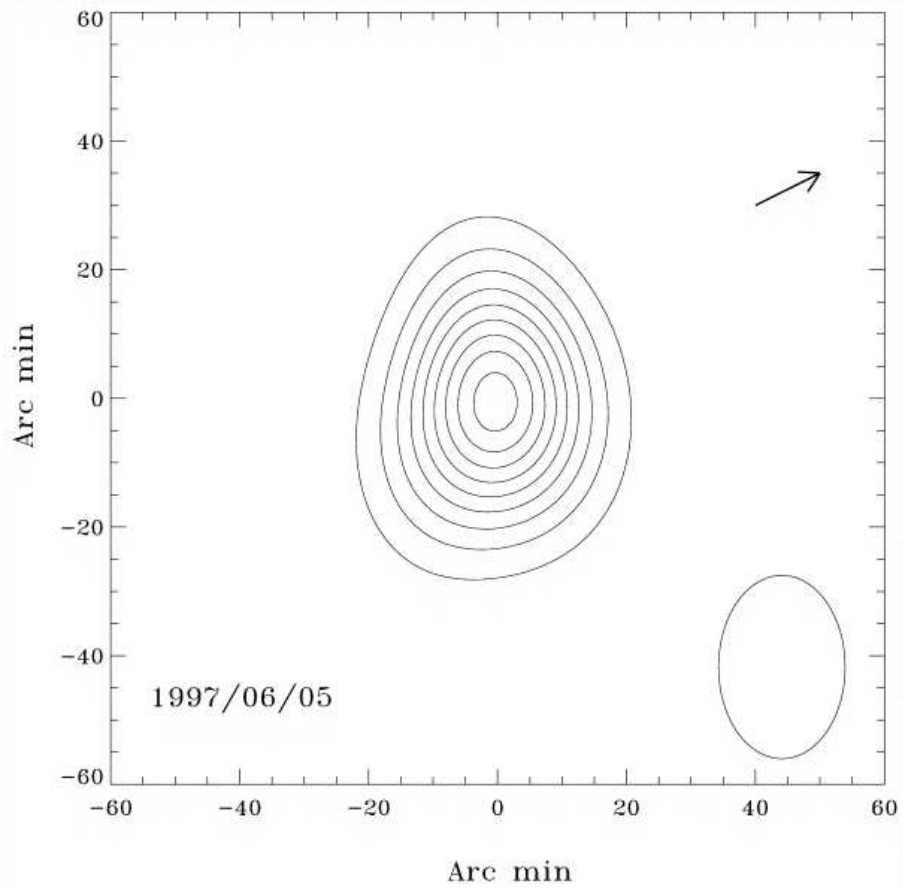


FIG. 4: Same as Figures 2 and 3 but obtained on June 5, 1997, when Crab nebula was at a distance of  $\approx 37 R_{\odot}$  from the center of the Sun. The peak flux is  $2287 \pm 200$  Jy, and the contour levels are 0.05, 0.15, 0.25, 0.35, 0.45, 0.55, 0.65, 0.75, and 0.85 times the peak flux.

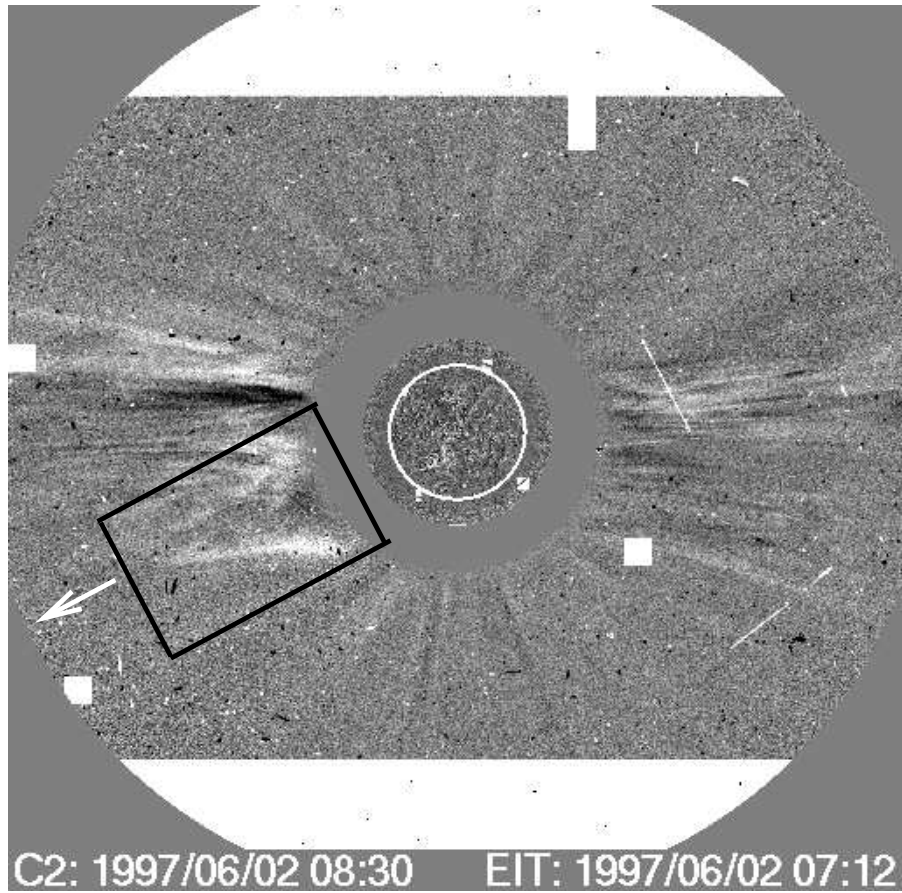


FIG. 5: LASCO C2-EIT running difference image of the CME observed on June 2, 1997. The occulting disk is at a distance of  $2.2 R_{\odot}$  from the center of the Sun. The location of the CME (near the southeast limb) is indicated by the open rectangular box. North is straight up and east is to the left. The direction of the Crab ( $\sim 41 R_{\odot}$  from the center of the Sun) is indicated by the arrow mark.

X-ray flare was observed during the above period. Also, this particular CME event was not accompanied by any non-thermal radio bursts or H $\alpha$  filament disappearance [Sol.-Geophys. Data (1997a,b)]. The final height measurement of the event was in the LASCO C3 image at 20:54:39 UT on June 2, 1997 when the leading edge of the CME was at 13.18 R $_{\odot}$  from the Sun at PA = 113 $^{\circ}$ . Assuming a constant speed and extrapolating the LASCO height-time measurements, we find that the above CME should reach a distance of  $\sim 41$  R $_{\odot}$  from the Sun about 34.5 hr later (i.e. on June 4, 1997 at 07:33 UT). Fortuitously, this is the same as the local meridian transit time of Crab nebula at our observatory on that day. Therefore it is possible that the angular broadened image of Crab Nebula in Figure 3 is most likely due to scattering of its radiation by density inhomogeneities in the foreground CME plasma. We checked the LASCO CME catalog for the possibility of the presence of other CME(s) at a distance of 41 R $_{\odot}$  away from the southeast quadrant of the Sun on June 4, 1997. But, we did not find any.

### 7.3 ANALYSIS

#### 7.3.1 The scattering angle and the electron density associated with the CME

If the observed angular broadening and the subsequent reduction in the flux of the Crab Nebula in the present case is due to scattering effects by the CME in the foreground, then we can calculate the electron density ( $N_e$ ) associated with the latter. The energy distribution ( $Q$ ) of an electromagnetic wave (of wavelength  $\lambda$ ) after it gets scattered by the density irregularities in a medium can be written as [Fejer (1954)],

$$Q = Q_0 \exp(-B), \text{ where} \quad (1)$$

$$B = \left( -\frac{\overline{\Delta\epsilon^2} \pi^{\frac{5}{2}}}{\epsilon^2 \lambda^2} lz \right) . \quad (2)$$

In equation (1),  $Q_0$  is the energy of the wave before scattering. In equation (2)  $\epsilon$  is the dielectric constant,  $l$  is the scale length of the scattering inhomogeneity and  $z$  is the path length of the wave inside the medium. Fejer (1954) also established that the angular spectrum of the scattered energy follows a Gaussian distribution, i.e.

$$P(\phi) \propto \exp\left(-\frac{\pi^2 l^2 \phi^2}{B \lambda^2}\right) . \quad (3)$$



Substituting  $B$  in equation (3), one can see that

$$P(\phi) \propto \exp\left(-\frac{1}{\pi^{1/2}} \frac{l\phi^2\epsilon^2}{z\Delta\epsilon^2}\right) . \quad (4)$$

From equation (4), the 1/e width of the angular broadening is obtained by equating the terms inside the exponential term to 1. That is,

$$\begin{aligned} \frac{l\epsilon^2\phi^2}{\pi^{1/2}z\Delta\epsilon^2} &= 1 \\ \phi^2 &= \pi^{1/2} \frac{z\overline{\Delta\epsilon^2}}{l\epsilon^2} \\ \text{Hence, } \phi &= \pi^{1/4} \left(\frac{z}{l}\right)^{1/2} \left(\frac{\overline{\Delta\epsilon^2}}{\epsilon^2}\right)^{1/2} \end{aligned} \quad (5)$$

At large distances from the corona,  $\epsilon$  can be assumed to be equal to 1, and the square root of the mean square deviation of the dielectric constant will be equal to  $\Delta\epsilon$ . Therefore, equation (5), will become,

$$\phi = \pi^{1/4} \left(\frac{z}{l}\right)^{1/2} \Delta\epsilon. \quad (6)$$

We know that the expression for the dielectric constant of the plasma medium can be written as,

$$\epsilon = \left(\frac{e^2}{m\epsilon_0\omega^2}\right) N_e , \quad (7)$$

where  $e$  and  $m$  are the charge and mass of the electron,  $\epsilon_0$  is the permittivity of free space,  $N_e$  is the electron density of the scattering medium and  $\omega$  is the frequency of observation. Therefore,

$$\Delta\epsilon = \left(\frac{e^2}{m\epsilon_0\omega^2}\right) \Delta N_e . \quad (8)$$

Substituting for the values of the physical constants in equation (8), an expression for the angular width of the scattered source can be obtained as [Hewish (1955)]:

$$\phi = 4.5 \times 10^{-10} \lambda^2 N_e \left(\frac{z}{l}\right)^{1/2} \text{ radian}, \quad (9)$$

where  $\phi$  is the scattering angle,  $\lambda$  is the wavelength of observation,  $z$  is the depth of the scattering region along the line of sight and  $l$  is the scale of the individual irregularities within the scattering region. In applying equation (9) to the present case, the following assumptions were made:

- (a) The radial width of the CME close to the Sun at 05:44:26 UT (the lift-off time) on June 2, 1997 was taken as  $\sim 1 R_{\odot}$ . This was based on the work of Gopalswamy et al. (1999).
- (b) From a statistical study of the characteristics of LASCO CMEs, St. Cyr et al. (2000) found that the CMEs expand radially at a rate of  $5 - 20 R_{\odot}/\text{day}$  as they propagate outward from the Sun. Taking the mean of the above ( $12.5 R_{\odot}/\text{day}$ ) as the typical expansion rate of a CME, we estimated the radial width of the present CME at  $41 R_{\odot}$  (around 07:33 UT on June 4, 1997), and is

$$\begin{aligned}
&\approx 1 R_{\odot} + \frac{12.5 R_{\odot}}{24 \text{ hr}} \times (07 : 33 \text{ UT, June 4} - 05 : 44 : 26 \text{ UT, June 2}) \text{ hr} \\
&= 1 R_{\odot} + \frac{12.5 R_{\odot}}{24 \text{ hr}} \times 50.00 \text{ hr} \\
&= 1 R_{\odot} + 26.0 R_{\odot} = 27.0 R_{\odot} \\
&= 1.8 \times 10^7 \text{ km.}
\end{aligned}$$

- (c) The depth of the CME along the line of sight is the same as its radial width. Therefore,  $z = 1.8 \times 10^7 \text{ km}$
- (d) The scale length ( $l$ ) of the scattering irregularities is  $\sim 1000 \text{ km}$  [Slee (1966)].

Rearranging equation (9), we get

$$N_e = (2.22 \times 10^9) \left( \frac{l}{z} \right)^{1/2} \frac{\phi}{\lambda^2} \text{ cm}^{-3}. \quad (10)$$

In the present case, the scattering angle  $\phi$  was obtained by subtracting the average half-power size of the Crab nebula in the absence of scattering ( $= 25'$ ) from its average scatter-broadened size ( $= 36'$ ). Therefore, substituting  $\phi = 11'$  and the other values in the above equation, we get

$$\begin{aligned}
N_e &= (2.22 \times 10^9) \left( \frac{1 \times 10^6}{1.8 \times 10^{10}} \right)^{1/2} \left[ \frac{11 \times \left( \frac{\pi}{180 \times 60} \right)}{36} \right], \\
&= 1.47 \times 10^3 \text{ cm}^{-3}
\end{aligned}$$

for the CME at a distance of  $41 R_{\odot}$  from the Sun.

### 7.3.2 The approximate volume and mass of the CME at a distance of $41 R_{\odot}$ from the center of the Sun

The observed angular width of the white light CME in the present case is  $\approx 72^{\circ}$ . Since, CMEs do not undergo significant latitudinal expansion during their propagation [Funsten et al. (1999)], the lateral width of the CME at  $41 R_{\odot}$  is

$$\begin{aligned} \frac{\pi}{180} \times 72 \times 41.0 R_{\odot} &= 51.5 R_{\odot} \quad (\text{Since, Arc length} = \text{Angle subtended} \times \text{Radius}) \\ &\approx 3.6 \times 10^7 \text{ km} . \end{aligned}$$

Therefore, the volume of the CME is

$$\begin{aligned} V &= \text{radial width} \times \text{lateral width} \times \text{depth along the line of sight} \\ &= (1.8 \times 10^7 \text{ km}) \times (3.6 \times 10^7 \text{ km}) \times (1.8 \times 10^7 \text{ km}) \\ &= 1.16 \times 10^{37} \text{ cm}^3 . \end{aligned}$$

Since the material comprising a CME is mostly coronal in origin [Hildner et al. (1975)] and the corona consists of fully ionized hydrogen and helium, with the latter being 10% as abundant as the former, one finds that each electron is associated with approximately  $2 \times 10^{-24}$  g of material. Therefore, the mass of the CME is given by

$$M = 2 \times 10^{-24} N_e V \quad \text{g} \quad (11)$$

Substituting for the corresponding values in the above equation, we get

$$\begin{aligned} M &= (2 \times 10^{-24}) \times (1.47 \times 10^3) \times (1.16 \times 10^{37}) \quad \text{g} \\ &\approx 3.4 \times 10^{16} \text{ g} \end{aligned}$$

for the CME at  $41 R_{\odot}$ .

## 7.4 CONCLUSION

We have presented evidence for the angular broadening of the Crab nebula at a distance of  $41 R_{\odot}$  from the Sun due to the passage of its radio radiation through a slow CME in the foreground. The estimated electron density of the CME at the above location is  $\approx 1.47 \times 10^3 \text{ cm}^{-3}$ . The CMEs expand as they move outward from the Sun. Hence, its density decreases. Assuming (i) a typical volume of  $7 \times 10^{32} \text{ cm}^3$  for the CMEs close to their onset (refer chapter 3) and (ii) its mass is a constant ( $3.4 \times 10^{16} \text{ g}$ ), we estimated the electron density of the above CME near the Sun, and is  $\approx 2.4 \times 10^7 \text{ cm}^{-3}$ . This agrees reasonably with the corresponding value used

in CME model calculations [Bastian and Gary (1997)]. According to Leblanc et al. (1998), the density of the solar corona at  $41 R_{\odot}$  is about  $200 \text{ cm}^{-3}$ . This implies that the CME of June 4, 1997 was about 7.4 times denser than the ambient corona at  $41 R_{\odot}$ . But the plasma density corresponding to 50 MHz ( $3.1 \times 10^7 \text{ cm}^{-3}$ ) is much larger than the above value. So, the CME cloud is essentially transparent to radiation from the Crab at the above frequency. This implies that the contribution due to thermal free-free emission from the CME to the observed image in Figure 3 at 50 MHz is very minimal. Assuming an expansion rate of  $12.5 R_{\odot}/\text{day}$  for the present CME, we found that its radial extent at  $41 R_{\odot}$  is  $\approx 1.8 \times 10^7 \text{ km}$ . This is in the range of values ( $1 \times 10^6 - 5 \times 10^7 \text{ km}$ ) reported by Gothoskar & Rao (1999) for the interplanetary magnetic clouds associated with the CMEs. The lateral size of the CME at  $41 R_{\odot}$  was found to be  $\simeq 51.5 R_{\odot}$ . This agrees reasonably with the empirical relation obtained by Manoharan et al. (2000; 2001) that the size of the CME varies as  $r$ , the radial distance from the Sun. We also calculated the mass of the CME and its value is  $\approx 3.4 \times 10^{16} \text{ g}$ . This is close that of the average value ( $5.3 \times 10^{16} \text{ g}$ ) reported in the literature for CMEs at large distances from the Sun [Gothoskar and Rao (1999); Manoharan et al. (2000)]. With the CME rates averaging to more than 5 per day particularly during solar maximum [Gopalswamy et al. (2004)], the interplanetary medium is expected to be highly disturbed. So, high sensitivity observations of even weak radio sources whose line of sight pass close to the Sun will be useful in determining several properties of CMEs at large distances from the Sun in an independent way. The unique measurement of anisotropy provided by angular scattering offers an additional means for distinguishing CMEs from coronal streamers and other structures in the solar wind [Woo (1997)]. Note that the angular scattering is anisotropic and the density structures prefer to orient themselves in the direction of the magnetic field [Armstrong et al. (1990); Grall et al. (1997)]. The linearly polarized radio emission from discrete sources undergo Faraday rotation when they pass through the solar corona. Mancuso and Spangler (2000) used such observations to infer the coronal electron density. It is also possible to use Faraday rotation observations (along with white light data) to get a handle on the magnetic field of a CME since the characteristics of the emergent radiation should be different as compared to the ambient corona [Bird and Edenhofer (1990); Bastian (1999, 2004)].

## CHAPTER 8

### CONCLUSIONS

Coronal mass ejections (CMEs) are large scale magneto plasma structures that erupt from the outer atmosphere of the Sun and enter the interplanetary space with large momentum. The study of this phenomenon is very important in the context of space weather, since it can damage the electronic and communication systems both on the Earth and in space. The discovery and the present understanding of CMEs came from observations made with white light coronagraphs, instruments that can image the corona by occulting the light from the photosphere and chromosphere. The occulter in a coronagraph generally covers a radial extent of  $\approx 2 R_{\odot}$  from the center of the Sun, and therefore it is difficult to predict the behavioral aspects of a CME close to the Sun using them. Hence, non-coronagraphic observations are inevitable in this regard.

Radio imaging observations play a useful role in this connection since they do not have the limitation of an occulter and also one can observe activity at any longitude similar to X-ray and EUV wavelengths. We have reported the observations of the thermal radio emission from a few selected CMEs with the GRH, in this thesis. Note that after the decommissioning of the Clark Lake Radioheliograph and Culgoora Radioheliograph, the Gauribidanur Radioheliograph (GRH) is the only instrument in operation at present to image the solar corona in the frequency range 30-110 MHz. Because of its good declination coverage and the recently implemented tracking facility, the Sun can be observed for about 6 hrs everyday.

The CME event observed with the GRH on November 24, 2000 was used to study its kinematics in the low corona ( $\leq 3.0 R_{\odot}$ ). The radioheliogram obtained during different time interval were used to follow the centroid of the ‘radio’ CME. The average speed of the CME in the plane of the sky was found to be  $1136 \pm 475 \text{ km s}^{-1}$  using running difference radio images. The brightness temperature of the radio enhancements associated with the CME at different epoch were calculated and the average value is  $5.7 \times 10^5 \text{ K}$ . We also determined the electron density of the CME and the mean value is  $2.4 \times 10^7 \text{ cm}^{-3}$  using optically thin approximation (since the  $T_b$  of the CME was less than the coronal electron temperature). The volume of the CME was obtained by assuming that the radial width of the CME is equal

to the depth along the line sight; The radial and lateral widths were measured from the radio difference images. The average volume is  $4.4 \times 10^{32} \text{ cm}^3$ . With the help of the latter and the electron density, the average mass of the CME was calculated as  $2.0 \times 10^{16}$ .

A three-dimensional ray-tracing method - a procedure with which a ray of a known frequency can be sent towards the corona and the value of the total optical depth ( $\tau_{\text{tot}}$ ) accumulated during its propagation can be obtained. The latter is a measure of attenuation suffered by the ray inside the absorptive medium. As it is well known that the corona is a self-emitting and absorbing plasma, its characteristics can be studied using the above ray-tracing procedure. The coefficient of absorption of the plasma depends on the electron density distribution; We used a modified version of the Newkirk density model for the active corona to estimate the optical depth and subsequently the brightness distribution at different locations. The density/temperature enhancement/decrement was incorporated into the calculations through Gaussian distribution.

The process of selecting the background temperature and density using the ray-tracing method was explained for the CME event of June 2, 1998 observed with the GRH. The parameters such as location, size and density of the structures associated with the pre-eruption structure of the above CME in a three-dimensional space were obtained from the reproduction of the observed brightness temperature distribution using the ray-tracing technique. The volume and mass of the CME were estimated from its size (along x, y and z axis) in 3-D space and average density. The corresponding values lie in the range  $3.05 - 4.8 \times 10^{31} \text{ cm}^3$  and  $1.44 - 2.69 \times 10^{15} \text{ g}$ , respectively. The normalized error between the source and reproduced brightness temperature distribution were obtained for different model distributions and the values were plotted as a function of source position.

The difference of the white light coronagraph/radio images obtained as a function of time helps us to understand the characteristics of a CME mainly in the plane of the sky. The estimated speed could be a lower limit to the true speed in a 3-D space especially in the case of an Earth-directed 'halo' CMEs since they lie away from the plane of the sky. Ray-tracing analysis of the thermal radio counterpart of a CME plays a vital role in this connection since the position of the associated density enhancement can be localized in a three-dimensional space. The 'halo' CME event observed with the GRH on January 21, 1998 was chosen for the case study.

The observed radioheliogram were reproduced using the ray-tracing method and the position vector of the radio CME at two different epochs were determined. The speed of the CME along the line of sight and in the plane of the sky were found to be  $328^{+06}_{-38}$  and  $478^{+37}_{-68}$  km s<sup>-1</sup> respectively.

Increase in the size of cosmic radio sources due to scattering of their radiation by the solar corona were reported when their angular distances from the center of the Sun were  $\leq 5 R_{\odot}$ . Such an increase in the angular size of the Crab nebula was observed with the GRH on June 4, 1997, when the latter was at a distance of  $\sim 41 R_{\odot}$  from the center of the Sun. It was found from the LASCO CME catalog that there was a CME in the foreground of the Crab nebula at the above mentioned location and it was confirmed that the above broadening of the Crab nebula was due to the former. Assuming a radial expansion rate of  $12.5 R_{\odot}$  per day for the CME, the depth along the line of sight equal to its radial width, and a scale size of 1000 km for the scattering inhomogeneities, the mass of the CME was calculated as  $3.4 \times 10^{16}$  g.

The various results discussed in this thesis indicate that low frequency (30-110 MHz) radio observations of coronal mass ejections with instruments of good resolution, sensitivity and dynamic range, and their subsequent ray-tracing analysis might play a useful role in understanding the behavior of CMEs close to the Sun.

## BIBLIOGRAPHY

- [1] Akmal, A., Raymond, J. C., Vourlidas, A., Thompson, B., Ciaravella, A., Ko, Y.-K., Uzzo, M., and Wu, R. 2001, *ApJ*, **553**, 922
- [2] Allen, C. W. 1947, *MNRAS*, **107**, 426
- [3] Ananthakrishnan, S. 2000, *J. Astrophys. and Astronomy*, **21**, 439
- [4] Anantharamaiah, K. R., Gothoskar, P. and Cornwell, T. J. 1994, *J. Astrophys. and Astronomy*, **15**, 387
- [5] Armstrong, J. W., Coles, W. A., Rickett, B. J., and Kojima, M. 1990, *ApJ*, **358**, 685
- [6] Aurass, H. 1997, in 'Lecture notes in Physics', 483, *Coronal Physics from radio and space observations*, Eds. G. Trotter (Berlin: Springer), pg: 135
- [7] Aurass, H., Vourlidas, A., Andrews, M. D., Thompson, B. J., Howard, R. H., and Mann. G. 1999, *ApJ*, **511**, 451
- [8] Bastian, T. S. 1994, *ApJ*, **426**, 774
- [9] Bastian, T. S., and Gary, D. E. 1997, *J. Geophys. Res.*, **102**, 14,031
- [10] Bastian, T. S., Benz, A. O., and Gary, D. E. 1998, *Ann. Rev. Astron. and Astrophys.*, **36**, 131
- [11] Bastian, T. S. 1999, in 'Magnetic field and solar processes', *Proceedings of the 9th European meeting on solar physics*, ESA SP-448, pg: 1131
- [12] Bastian, T. S. 2000, in 'Radio Astronomy at long wavelengths', R. G. Stone, K. W. Weiler, M. L. Goldstein and J. L. Bougeret (Eds.), *Geophysical Monograph* 119, AGU, pg: 85
- [13] Bastian, T. S., Pick, M., Kerdraon, A., Maia, D., and Vourildas, A. 2001, *ApJL*, **558**, 65
- [14] Bastian, T. S. 2003, *Adv. Space Res.*, **32**, 2705



- [15] Bastian, T. S. 2004, in Solar and space weather radiophysics - current status and future developments, Eds. Dale E. Gary and Christoph U. Keller Astrophysics and Space Science library (ASSL), **314**, pg: 47
- [16] Baumbach, S. 1937, Astr. Nachr. **263**, 121
- [17] Bird, M. K., and Edenhofer, P. 1990, in 'Physics of the inner Heliosphere I, Eds. R. Schwenn and E. Marsch, Springer-Verlag, pg: 13
- [18] Blum, E. J., and Boischof, A. 1957, The Observatory, **77**, 205
- [19] Born, M., and Wolf, E., Chapter VIII, in 'Principles of optics', Fourth Edition, 1970, Pergamon Press
- [20] Bougeret, J. L. 1985, in 'Collisionless shocks in the Heliosphere. Reviews of current research', Ed. Bruce. T. Tsurutani and Robert. G. Stone, Geophysical Monograph Series-35, AGU, pg: 13
- [21] Bougeret, J.-L. et al. 1995, Space Sci. Rev., **71**, 5
- [22] Brueckner, G. E., et al. 1995, Sol. Phys., **162**, 357
- [23] Burkepile, J. T., and St. Cyr, O. C. 1993, NCAR/TN-369+ST, Boulder
- [24] Burkepile, J. T., Hundhausen, A. J., Stanger, A. L., St. Cyr, O. C., and Seiden, J. A. 2004, J. Geophys. Res. **109**, A03103
- [25] Cornwell, T. J. and Fomalont, E. B, 1989, in 'Synthesis Imaging in Radio Astronomy', Astr. Soc. of the Pacific, Conf. Series, Vol: 6, Eds. R. A. Perley, F. R. Schwab and A. H. Bridle
- [26] Delaboudinière, J. -P., et al. 1995, Sol. Phys., **162**, 291
- [27] Dere, K. P., et al. 1997, Sol. Phys., **175**, 601
- [28] Dere, K. P., Wang, D., and Howard, R. A. 2005, ApJL, **620**, 119
- [29] Dulk, G. A. 1985, Ann. Rev. Astron. Astrophys., **23**, 169
- [30] Dungey, J. W. 1961, Phys. Rev. Lett., **6**, 47
- [31] Erickson, W. C. 1964, ApJ, **139**, 1290

- [32] Eselevich, V. G., and Filippov, M. A. 1991, *Planet. Space Sci.*, **39**, 737
- [33] Fejer, J. A. 1954, *Proc. Roy. Soc. A*, **220**, 455
- [34] Fisher, R. R., Garcia, C. J., and Seagraves, P. 1981, *ApJL*, **246**, 161
- [35] Fleck, B., Domingo, V., and Poland, A. I. (Eds.) 1995, *The SOHO Mission* (Dordrecht: Kluwer)
- [36] Fludra, A., del Zanna, G., Alexander, D., and Bromage, B. J. I. 1999, *J. Geophys. Res.*, **104**, 9709
- [37] Foukal, P. 1990, *Solar Astrophysics*, John Wiley and Sons.
- [38] Funsten, H. O., Gosling, J. T., Riley, P., Cyr, O. C. St., Forsyth, R. J., Howard, R. A., and Schwenn, R. 1999, *J. Geophys. Res.*, **104**, 6679
- [39] Gallagher, P. T., Lawrence, G. R., and Dennis, B. R. 2003, *ApJL*, **588**, 53
- [40] Gary, D. E. 2003, *Journal of the Korean Astronomical Society*, **36**, 143
- [41] Gilbert, H. R., Holzer, T. E., Burkepile, J. T., and Hundhausen A. J. 2000, *ApJ*, **537**, 503
- [42] Gopalswamy, N., and Kundu, M. R. 1992, *ApJL*, **390**, 37
- [43] Gopalswamy, N., Hanaoka, Y., Kundu, M. R., Enome, S., Lemen, J. R., Akioka, M., and Lara, A. 1997, *ApJ*, **475**, 348
- [44] Gopalswamy, N., and Hanaoka, Y. 1998, *ApJL*, **498**, 179
- [45] Gopalswamy, N. 1999, in 'Proc. Nobeyama Symp. 1998 on Solar Physics with Radio Observations', Eds. T. S. Bastian, N. Gopalswamy, and K. Shibasaki (NRO Rep. 479; Nagano: NRO), pg: 141
- [46] Gopalswamy, N., and Thompson, B. J. 2000a, *J. Atmospheric solar terrestrial physics*, **62**, 1457
- [47] Gopalswamy, N., Kaiser, M. L., Thompson, B. J., Burlaga, L. F., Szabo, A., Vourlidis, A., Lara, A., Yoshiro, S., and Bougeret, J.-L. 2000b, *Geophys. Res. Lett.*, **27**(10), 1427

- [48] Gopalswamy, N. 2000c, in 'Radio Astronomy at long wavelengths', R. G. Stone, K. W. Weiler, M. L. Goldstein and J. L. Bougeret (Eds.), Geophysical Monograph 119, AGU, pg: 97
- [49] Gopalswamy, N., Lara, A., Kaiser, M. L., Bougeret, J. -L. 2001a, J. Geophys. Res., **106**, 25261
- [50] Gopalswamy, N., Lara, A., Yashiro, S., Kaiser, M. L., and Howard, R. A. 2001b, J. Geophys. Res., **106**, 29207
- [51] Gopalswamy, N., Yashiro, S., Kaiser, M. L., Howard, R. A., Bougeret, J. -L. 2001c, J. Geophys. Res., **106**, 29219
- [52] Gopalswamy, N. 2004, in Solar and space weather radiophysics - current status and future developments, Eds. Dale E. Gary and Christoph U. Keller Astrophysics and Space Science library (ASSL), **314**, pg: 305
- [53] Gorgolewski, S., Hanasz, J., Iwaniszewski, H., and Turlo, Z. 1962, Acta Astron., **12**, 251
- [54] Gosling, J. T., Hildner, E., MacQueen, R. M., Munro, R. H., Poland, A. I., and Ross, C. L. 1974, J. Geophys. Res., **79**, 4581
- [55] Gosling, J. T., Hildner, E., MacQueen, R. M., Munro, R. H., Poland, A. I., and Ross, C. L. 1975, Sol. Phys., **40**, 439
- [56] Gosling, J. T., Hildner, E., MacQueen, R. M., Munro, R. H., Poland, A. I., and Ross, C. L. 1976, Sol. Phys., **48**, 389
- [57] Gosling, J. T., McComas, D. J., Phillips, J. L., and Bame, S. J. 1991, J. Geophys. Res., **96**, 7831
- [58] Gosling, J. T. 1993, J. Geophys. Res., **98**, 18937
- [59] Gothoskar, P., and Rao, A. P. 1999, Sol. Phys., **185**, 361
- [60] Grall, R. R., Coles, W. A., Spangler, S. R., Sakurai, T., and Harmon, J. K. 1997, J. Geophys. Res., **102**, 263
- [61] Harries, J. R., Blesing, R. G., and Dennison, P. A. 1970, Proc. Astron. Soc. Australia, **1**(7), 319

- [62] Hewish, A. 1955, Proc. R. Soc. London A, **228**, 238
- [63] Hildner, E., Gosling, J. T., Hansen, R. T., and Bohlin, J. D. 1975, Sol. Phy., **45**, 363
- [64] Hildner, E. 1977, in 'Study of Travelling Interplanetary Phenomena', (Eds.) M. A. Shea, D. F. Smart, and S. T. Wu, (D.Reidel, Hingham, MA), pg: 3
- [65] Hildner, E. 1987, in 'Energetic phenomena on the Sun', Eds. M. R. Kundu, B. E. Wood gate, (NASA CP-2439), Greenbelt, MD: NASA
- [66] Hirayama, T. 1974, Sol. Phy., **34**, 323
- [67] Howard, R. A., Michels, D. J., Sheeley, N. R. Jr, and Koomen, M. J. 1982, ApJL, **263**, 101
- [68] Howard, R., Sheeley Jr., N. R., Michels, D. J. and Koomen, M. J. 1984, Adv. Space. Res., **4**, 307
- [69] Howard, R., Sheeley Jr., N. R., Michels, D. J., and Koomen, M. J. 1985, J. Geophys. Res., **90**(A9), 8173
- [70] Howard, R. A., Sheely, N. R., Jr., Koomen, M. J., Michels, D. J. 1986, p. 107, in 'The Sun and the Heliosphere in three dimensions', Eds. R. G. Marsden, pg: 107 (Reidel: Dordrecht)
- [71] Hudson, H. S., Lemen, J. R., St. Cyr, O. C., Sterling, A. C., and Webb, D. F. 1998, Geophys. Res. Lett., **25**, 2481
- [72] Hudson, H. S. et al. 1999, NRO Report, **479**, 159
- [73] Hundhausen, A. J. 1988, in 'Proceedings of the Sixth International Solar Wind Conference', TN306+Proc, edited by V. Pizzo, T. E. Holzer, and D. G. Sime, National center for Atmospheric Research, Boulder, pg: 181
- [74] Hundhausen, A. J. 1993, J. Geophys. Res., **98**, 13177
- [75] Hundhausen, A. J. 1997, in 'The Many Faces of the Sun', edited by K. Strong, J. Saba, and B. Haish, Springer Verlag, New York.
- [76] Illing, R. M. E., and Hundhausen, A. J. 1985, J. Geophys. Res., **90**, 275

- [77] Illing, R. M. E., and Hundhausen, A. J. 1986, *J. Geophys. Res.*, **91**(A10), 10951
- [78] Isbell, D. E. 1960, 'Log Periodic Dipole Arrays' *IRE Trans. Ants. Prop.*, **AP-8**, 260
- [79] Jackson, B. V., and Hick, P. P. 2004, in *Solar and space weather radiophysics - current status and future developments*, Eds. Dale E. Gary and Christoph U. Keller, *Astrophysics and Space Science library (ASSL)*, **314**, pg: 355
- [80] Jennison, R., 1958, *MNRAS*, **118**, 276
- [81] Kahler, S. W. 1977, *ApJ*, **214**, 891
- [82] Kathiravan, C., Ramesh, R., and Subramanian, K. R. 2002, *ApJL*, **567**, 93
- [83] Kathiravan, C., and Ramesh, R. 2004, *ApJ*, **610**, 532
- [84] Kathiravan, C., and Ramesh, R. 2005, *ApJL*, **627**, 77
- [85] Kerdraon, A., Pick, M., Trottet, G., Swayer, C., Illing, R., Wagner, W. and House, L. 1983, *ApJL*, **265**, 19
- [86] Kerdraon, A., and Delouis, J. M., 1997, in 'Coronal Physics from radio and space observations', Edition, G. Trottet (*Lecture notes in Physics, Springer*), **483**, pg: 192
- [87] Ko, Y-K., Raymond, J. C., Lin, J., Lawrence, G., Li, J., and Fludra, A. 2003, *ApJ*, **594**, 1068
- [88] Kopp, R. A., and Pneuman, G. W. 1976, *Sol. Phy.*, **50**, 85
- [89] Koshishi, H. et al. 1994, *Publ. Astron. Soc. Japan*, **46**, L33
- [90] Kraus, J. D. 1966, in 'Radio Astronomy', *Cygnus-Quasar Books*
- [91] Kraus, J. D. 1988, in 'Antennas' (2<sup>nd</sup> edition), pg: 703
- [92] Kundu, M. R., Erickson, W. C., Gergely, T. E., Mahoney, M. J., and Turner, P. J. 1983, *Sol. Phys.*, **83**, 385
- [93] Lanzerotti, L. J. 2004, in *Solar and space weather radiophysics - current status and future developments*, Eds. Dale E. Gary and Christoph U. Keller *Astrophysics and Space Science library (ASSL)*, **314**, pg: 1

- [94] Leblanc, Y., Dulk, G. A., and Bougeret, J.-L. 1998, *Sol. Phys.*, **183**, 165
- [95] Leblanc, Y., Dulk, G. A., Vourlidas, A., Bougeret, J.-L. 2001, *J. Geophys. Res.*, **106**, 25301
- [96] Lin, J., and Forbes, T. G. 2000, *J. Geophys. Res.*, **105**, 2375
- [97] Lin, J. 2004, *Sol. Phys.*, **219**, 169
- [98] Low, B. C., Munro, R. H., and Fisher, R. R. 1982, *ApJ*, **254**, 335
- [99] Low, B. C. 1994, *Phys. Plasmas*, **1**, 1684
- [100] Luhmann, J. G. 1997, in 'Coronal Mass Ejections', Eds. N. Crooker, J. A. Joselyn, and J. Feynman, *AGU Geophys. Mon.* **99**, (AGU: Washington, DC), pg: 291
- [101] Machin, K. E., and Smith, F. G. 1951, *Nature*, **168**, 599
- [102] MacQueen, R. M., Eddy, J. A., Gosling, J. T., Hildner, E., Munro, R. H., Newkirk, G. A., Poland, A. I., and Ross, C. L. 1974, *ApJL*, **187**, 85
- [103] MacQueen, R. M. 1980, *Phil. Trans. R. Soc. London, Ser. A*, **297**, 605
- [104] Maia, D. et al. 1998, *Sol. Phy.*, 181, 121
- [105] Maia, D., Vourlidas, A., Pick, M., Howard, R., Schwenn, R., and Magalhaes, A. 1999, *J. Geophys. Res.*, 104(A6), 12507
- [106] Maia, D., Pick, M., Vourlidas, A., and Howard, R. A. 2000, *ApJL*, **528**, 49
- [107] Mancuso, S., and Spangler, S. R. 2000, *ApJ*, **539**, 480
- [108] Mann, G. 1995, in 'Coronal magnetic energy releases', Ed. A. O. Benz, and A. Kruger, Springer-Berlin, pg: 183
- [109] Manoharan, P. K., Kojima, M., Gopalswamy, N., Kondo, T., and Smith, Z. 2000, *ApJ*, **530**, 1061
- [110] Manoharan, P. K., Tokumaru, M., Pick, M., Subramanian, P., Ipavich, F. M., Schenk, K., Kaiser, M. L., Lepping, R. P., and Vourlidas, A. 2001, *ApJ*, **559**, 1180

- [111] Manoharan, P. K., Gopalswamy, N., Yashiro, S., Lara, A., Michelk, G. and Howard, R. A. 2004, *J. Geophys. Res.*, **109**, A06109
- [112] Martyn, D. F. 1946, *Nature*, **158**, 632
- [113] Martyn, D. F. 1948, *Proc. Roy. Soc. A*, **193**, 44
- [114] McAllister, A. H., Dryer, M., McIntosh, P., Singer, H., and Weiss, L. 1996, *J. Geophys. Res.*, **101**, 13497
- [115] McMullin, J. M., and Helfer, H. L. 1977, *Sol. Phys.*, **53**, 471
- [116] Michalek, G., Gopalswamy, N., and Yashiro, S. 2003, *ApJ*, **584**, 472
- [117] Michels, D. J., Howard, R. A., Koomen, M. J., Sheely, N. R., Jr. 1980, in 'Radio Physics of the Sun', IAU 86, Eds. M. R. Kundu and T. Gergely (Hingman: D. Reidel), pg: 439
- [118] Moon, Y.-J., Cho, K.-S., Dryer, M., Kim, Y.-H, Bong, Su-chan, Chae, J., and Park, Y. D. 2005, *ApJ*, **624**, 414
- [119] Moran, T.G, and Davila, J. M. 2004, *Science*, **305**, 66
- [120] Munro, R. H., Gosling, J. T., Hildner, E., MacQueen, R. M., Poland, A. I., and Ross, C. L. 1979, *Sol. Phy.*, **61**, 201
- [121] Munro, R. H. and Sime, D. G. 1984, NCAR Technical note NCAR/TN-233+STR, Boulder
- [122] Nakajima, H. 1994, *Proc. IEEE*, **82**, 5
- [123] Nelson, G. J., Sheridan, K. V., and Suzuki, S. 1985, in *Solar Radiophysics*, ed. D. J. McLean and N. R. Labrum (Cambridge: Cambridge Univ. Press), pg: 132
- [124] Newkirk, G. 1959, in 'Paris Symposium on Radio Astronomy', ed. R. N. Bracewell, IAUS, **9**, pg: 149
- [125] Newkirk, G. Jr. 1961, *ApJ*, **133**, 983
- [126] Noordam, J. E., and de Bruyn, B. D. 1982, *Nature*, **299**, 597
- [127] Pawsey, J. L., and Yabsley, D. E. 1949, *Aust. J. Sci. Res., Ser. A*, **2**, 198

- [128] Perley, R. A., 1989, in 'Synthesis Imaging in Radio Astronomy' Astr. Soc. of the Pacific, Conf. Series Vol:6, Eds. R. A. Perley, F. R. Schwab and A. H. Bridle
- [129] Pick, M. 1998a, in 'Solar Physics with Radio observations', Proceedings of Nobeyama Symposium 1998, NRO Report No: **479**, pg: 187
- [130] Pick, M. et al. 1998b, Sol. Phys., 181, 455
- [131] Pick, M. 2004, in Solar and space weather radiophysics - current status and future developments, Eds. Dale E. Gary and Christoph U. Keller Astrophysics and Space Science library (ASSL), **314**, pg: 17
- [132] Plunkett, S. P., Thompson, B. J., Howard, R. A., Michels, D. J., St. Cyr, O. C., Tappin, S. J., Schwenn, R., and Lamy, P. L. 1998, Geophys. Res. Lett., **25**(14), 2477
- [133] Plunkett, S. P., Vourlidas, A., Simberova, S., Karlicky, M., Kotrc, P., Heinzel, P., Kupryakov, Yu. A., Guo, W. P., and Wu. S. T. 2000, Sol. Phys., **194**, 371
- [134] Pohjolainen, S., Maia, D., Pick, M., Vilmer, N., Khan, J. I., Otruba, W., Warmuth, A., Benz, A., Alissandrakis, C., Thompson, B. J. 2001, ApJ, **556**, 421
- [135] Poland, A. I., MacQueen, R. M., Munro, R. H., Gosling, J. T. 1977, ApOpt., **16**, 926
- [136] Ramesh, R., Subramanian, K. R., Sundararajan, M. S., and Sastry, Ch. V. 1998, Sol. Phys., **181**, 439
- [137] Ramesh, R. 1998b, in 'Multi-frequency observations of the outer solar corona with the Gauribidanur Radioheliograph', Ph.D thesis
- [138] Ramesh, R., Subramanian, K. R., Sastry, Ch. V. 1999, Astron. Astrophys. Suppl. Ser., **139**, 179
- [139] Ramesh, R., Sastry, Ch. V. 2000a, Astron. Astrophys., **358**, 749
- [140] Ramesh, R. 2000b, Sol. Phys., **196**, 213
- [141] Ramesh, R., Kathiravan, C., and Sastry, Ch. V. 2001a, ApJL, **548**, 229
- [142] Ramesh, R., and Sundaram, G. A. Shanmugha. 2001b, Sol. Phys., **202**, 355



- [143] Ramesh, R., and Ebenezer, E. 2001c, ApJL, **558**, 141
- [144] Ramesh, R., Kathiravan, C., and Sastry, Ch. V. 2003, ApJL, **591**, 163
- [145] Ramesh, R. 2004, Proc. of the IAU symposium 226 on 'Coronal and Stellar mass ejections', (in press)
- [146] Ramesh, R., Sundara Rajan, M. S., and Sastry, Ch. V. 2005, in preparation
- [147] Raymond, J. C. 2004, Science, **305**, 49
- [148] Reames, D. V. 1999, Space Sci. Rev., **90**, 413
- [149] Reiner, M. J., Vourlidas, A., St. Cyr, O. C., Burkepile, J. T., Howard, R. A., Kaiser, M. L., Prestage, N. P., and Bougeret, J.-L. 2003, ApJ, **590**, 533
- [150] Rickett, B. J., and Coles, W. A. 2000, in 'Radio Astronomy at long wavelengths', R. G. Stone, K. W. Weiler, M. L. Goldstein and J. L. Bougeret (Eds.), Geophysical Monograph 119, AGU, pg: 97
- [151] Rogers, A. E. E., Hinteregger, H. F., Whitney, A. R., Counselman, C. C., Shapiro, I. I., Wittels, J. J., Klemperer, W. K., Warnock, W. W., Clark, T. A., and Hutton, L. K. 1974, ApJ, **193**, 293
- [152] Roussev, I. I., Sokolov, I. V., Forbes, T. G., Gombosi, T. I., Lee, M. A., and Sakai, J. I. 2004, ApJL, **605**, 73
- [153] Rust, D. M. 1983, Space Sci. Rev., **34**, 21
- [154] Saito, K., Poland, A. I., and Munro, R. H. 1977, Sol. Phys., **55**, 121
- [155] Sastry, Ch. V., Subramanian, K. R. 1974, Indian J. Radio Space Phys., **3**, 196
- [156] Sastry, Ch. V., Dwarakanath, K. S., Shevgaonkar, R. K., and krishan, V. 1981, Sol. Phys., **73**, 363
- [157] Sastry, Ch. V., Shevgaonkar, R. K., and Ramanuja, M. N. 1983, Sol. Phys., **87**, 391
- [158] Schmahl, E. J., Gopalswamy, N., and Kundu, M. R. 1994, Sol. Phys., **150**, 325

- [159] Sheeley N. R. Jr., Bohlin, J. D., Brueckner, G. E., Purcell, J. D., Scherrer, V. E., Tousey, R., Smith, J. B. Jr., Speich, D. M., Tandberg-Hanssen, E., and Wilson, R. M. 1975, *Sol. Phy.*, **45**, 377
- [160] Sheeley N. R. Jr., Howard, R. A., Koomen, M. J., Michels, D. J., Harvey, J. W., and Harvey, K. L. 1982, *Space. Sci. Rev.*, **33**, 219
- [161] Sheeley N. R. Jr., Walters, J. H., Wang, Y.-M., and Howard, R. A. 1999, *J. Geophys. Res.*, **104**, 24739
- [162] Sheridan, K. V., Jackson, B. V., McLearn, D. J., and Dulk, G. A. 1978, *Proc. Astron. Soc. Australia*, **3**, 249
- [163] Shevgaonkar, R. K., 1984, in 'Low frequency radio astronomy', *Proc. of workshop held at NRAO*, Eds. W. E. Erickson, and H. V. Cane, pg: 62
- [164] Slee, O. B. 1959, *Australian J. Phys.*, **12**, 134
- [165] Slee, O. B. 1966, *Planet. Space Sci.*, **14**, 255
- [166] Smerd, S. F. and Westfold, K. C. 1949, *Phil. mag. Ser. 7*, **40**, 831
- [167] Smerd, S. F. 1950, *Australian J. Sci. Res., Ser. A*, **3**, 34
- [168] *Sol.-Geophys. Data August-1997a*, **636**, Part I (Boulder NGDC)
- [169] *Sol.-Geophys. Data December-1997b*, **640**, Part II (Boulder NGDC)
- [170] *Sol.-Geophys. Data March-1998a*, **643**, Part I (Boulder NGDC)
- [171] *Sol.-Geophys. Data June-1998b*, **646**, Part I (Boulder NGDC)
- [172] *Sol.-Geophys. Data January-2001*, **677**, Part I (Boulder NGDC)
- [173] St. Cyr, O. C., Burkepile, J. T., Hundhausen, A. J., and Lecinski, A. R. 1999, *J. Geophys. Res.*, **104**, 12493
- [174] St. Cyr, O. C., et al. 2000, *J. Geophys. Res.*, **105**, 8169
- [175] Steinolfson, R. S. 1985, in 'Collisonless shocks in the Heliosphere. Reviews of current research', Ed. Bruce. T. Tsurutani and Robert. G. Stone, *Geophysical Monograph Series-35*, AGU, pg: 1

- [176] Sterling, A. C., and Hudson, H. S. 1997, ApJL, **491**, 55
- [177] Subramanian, K. R., and Sastry Ch. V. 1988, J. Astron. Astrophys., **9**, 225
- [178] Subramanian, P. et al. 2005, astro-ph/0508676
- [179] Svestka, Z., Farnik, F., Hudson, H. S., Uhida, Y., Hick, P., and Lemen, J. R. 1995, Sol. Phys., **161**, 331
- [180] Thejappa, G., and Kundu, M. R. 1992, Sol. Phys., **140**, 19
- [181] Thompson, B. J., Plunkett, S. P., Gurman, J. B., Newmark, J. S., St. Cyr, O. C., and Michels, D. J. 1998, Geophys. Res. Lett., **25**, 2465
- [182] Thompson, B. J., Gurman, J. B., Neupert, W. M., Newmark, J. S., Delaboudinière, J.-P., St. Cyr, O. C., Stezelberger, S., Dere, K. P., Howard, R. A., and Michels, D. J. 1999, ApJL, **517**, 151
- [183] Tokumaru, M., Kojima, M., Fujiki, K., and Yokobe, A. 2000, J. Geophys. Res., **105**(A5), 10435
- [184] Tousey, R. 1973, in 'Space Research XIII', Eds. M. J. Rycroft, and S. K. Run-corn, (Berlin: Academic-Verlag), pg: 173
- [185] Tsuneta, S., Acton, L., Bruner, M., Lemen, J., Brown, W., Carvalho, R., Catura, R., Freeland, S., Jurcevich, B., and Owens, J. 1991, Sol. Phys., **136**, 37
- [186] Tylka, A. J. 2001, J. Geophys. Res., **106**, 25333
- [187] Vitkevich, V. V. 1955, Dokl. Akad. Nauk SSSR, **101**(3), 42
- [188] Vitkevich, V. V. 1958, Soviet Astron.-AJ, **4**, 897
- [189] Vitkevich, V. V. 1961, Soviet Astron.-AJ, **2**, 45
- [190] Vourlidas, A., Subramanian, P., Dere, K. P., and Howard, R. A. 2000, ApJ, **534**, 456
- [191] Vourlidas, A. 2004, in Solar and space weather radiophysics - current status and future developments, Eds. Dale E. Gary and Christoph U. Keller Astrophysics and Space Science library (ASSL), **314**, pg: 223

- [192] Wagner, W. J. 1984, *Ann. Rev. Astron. Astrophys.*, **22**, 267
- [193] Warmuth, A., and Mann, G., 2005, *Astron. and Astrophys.*, **435**, 1123
- [194] Webb, D. F., Krieger, A. S., and Rust, D. M. 1976, *Sol. Phys.*, **48**, 159
- [195] Wieringa, M. H., 1991, Ph.D Thesis, University of Leiden
- [196] Wild, J. P., Smerd, S. F., and Weiss, A. A. 1963, *Ann. Rev. Astron. Astrophys.*, **1**, 291
- [197] Wild, J. P. et al. 1967(Sep.), *proc. I.R.E.E. Australia*, 277
- [198] Wild, J. P. and Smerd, S. F. 1972, *Ann. Rev. Astron. Astrophys.*, **10**, 159
- [199] Woo, R. 1997, in 'Coronal Mass Ejections', Eds. N. Crooker, J. A. Joselyn, and J. Feynman, *AGU Geophys. Mon. 99*, (AGU: Washington, DC), pg: 235
- [200] Zhao, X. P., Plunkett, S. P., and Liu, W. 2002, *J. Geophys. Res.*, **107**, SSH 13-1
- [201] Zhang, J., Dere, K. P., Howard, R. A., Kundu, M. R., and White, S. M. 2001, *ApJ*, **559**, 452
- [202] Zhang, J., Dere, K. P., Howard, R. A., and Vourlidas, A. 2004, *ApJ*, **604**, 420
- [203] Zhou, G., Wang, J., and Cao, Z. 2003, *Astronomy and Astrophys.*, **397**, 1057

# APPENDIX A

## THE RAY-TRACING PROGRAM

The following FORTRAN code computes the two-dimensional brightness temperature distribution of the solar corona using the density model given by Newkirk (1961) and an electron temperature of  $1 \times 10^6$  K for the background corona. A Gaussian model was assumed for the electron density and temperature associated with the coronal large-scale structures.

As a first step, the program calculates the density gradients (DGs)  $dn_x$ ,  $dn_y$  and  $dn_z$  (along the x, y and z axes respectively) at an initial point  $P_i(x_0 = 4.0 R_\odot, y_0 = -4.0 R_\odot, z_0 = -4.0 R_\odot)$ . The value of density at any point in the corona is obtained by calling a function 'den(x,y,z)'. The electron density for the background corona as well as for the enhancements/decrements associated with the radio structures are included in the above function. Using the values of DGs, the program obtains the direction cosines (al,bl,cl) of the normal vector at  $P_i$ . The emergent ray direction is decided by the direction of incidence and the local refractive index of the medium (at  $P_i$ ). The direction cosines ( $dc^s$ ) of the incident ray are assigned as  $a1 (= -1.0)$ ,  $b1 (= 0.0)$ ,  $c1 (= 0.0)$ . Since the refractive indices are determined by the local electron density the function 'den(x,y,z)' is used again. The Snell's law in vectorial form is used to obtain the  $dc^s$  of the refracted ray. Finally the absorption coefficient is calculated at  $P_i$ . The multiplication of the latter with the small incremental path length ( $dels = 0.01 R_\odot$ ) gives the value of the infinitesimal optical depth of the ray over a distance range from  $(x_0+dels, y_0+dels, z_0+dels)$  to  $(x_0-dels, y_0-dels, z_0-dels)$ ; Note that,  $dels = 0.01 R_\odot$ . The next point of the ray after it gets refracted or reflected, is calculated from its previous point using the increment formula. The ray is stopped after it reaches a distance of  $10 R_\odot$  from the center of the sun by the limiting variable (rlim). The brightness temperature is obtained from the value of optical depth using the equation of transfer. The function 'heat(x,y,z)' is used to incorporate the temperature enhancement/decrement associated with the radio structures. All the above steps are repeated 10609 times ( $103 \times 103$ ) to obtain the two-dimensional radio map of the corona. The outer 'do loop' takes care of the variation along z-axis (Latitude) while the inner loop generates the y-axis (Longitude). The values obtained for the optical depth and the temperature are stored in arrays 'out1'

and 'out' respectively. The corresponding output data files 'tau.dat' (103×103) and 'temp.dat' (103×103) are generated from the latter. Note that the variable s1 in the function procedure represent the radio source that was used to enhance the density/temperature at the location (1.4,-1.1,-0.06) [in units of  $R_{\odot}$ ]. Its size along  $x$ ,  $y$  and  $z$  axis are 0.70, 0.74 and 0.53  $R_{\odot}$ , respectively.

```

c-----
c-----
      Program RayTracing
c-----
c      Variable Declaration                < Definition >
c
      real x,y,z,x0,y0,z0,x1,y1,z1,zi    < Position variables    |
      real a1,b1,c1,a2,b2,c2,a1,b1,c1    < Direction Cosines      |
      real freq,freq2                    < Frequency variables    |
      real den,dn,len,den1,den2          < Density var & function|
      real dnx,dnx1,dnx2                 < Den. Grad along x-axis|
      real dny,dny1,dny2                 < Den. Grad along y-axis|
      real dnz,dnz1,dnz2                 < Den. Grad along z-axis|
      real d,ad,dad                      < Direction variables    |
      real s11,s112                      < Determinants          |
      real sden1,sden2,amu1,amu2         < Den. square & Ref.indx|
      real mu12,mu22,mu212,mu122,diff    < Ref. indx square      |
      real k                              < Coeff. normal vector  |
      real rlim                           < Limiting Radius       |
      real abco,abco1,abco2              < Absorption coeffs     |
      real tau,tau1                       < Optical depth variable|
      real temp,heat,heat1,heat2,heata   < Temperature variables |
      real out(500,500),out1(500,500)    < O/p arrays-Temp&tau   |
c-----
c      Open files for output data
c
      open(1,file='temp.dat')             < Temperature values    |
      open(2,file='tau.dat')             < Optical Depth values  |
c

```

```

c-----
c      Input Part
c
c      write(*,*)' input frequency : ' < Enter Frequency in MHz |
c      read(*,*)freq
c
c      freq2 = freq**2
c-----
c      Do loops for generating the (103 X 103) array for storing
c      the output values of optical depth and brightness
c      temperature
c
c      do 1 i = 1,103
c          zi = 0.075*float(i-51)          < Z - axis 103 rows      |
c      do 11 j = 1,103
c          x0 = 4.0
c          y0 = 0.075*float(j-51)        < Y - axis 103 columns   |
c          z0 = zi
c          a1 = -1.0                      < Incident ray - Direction
c          b1 = 0.0                        Cosines - Moving toward
c          c1 = 0.0                        the corona                >
c          tau = 0.0                      < Initialize Optic depth |
c          temp = 0.0                     < Initialize Temperature |
c-----
c      Density gradient along x - axis
c
c      10      del = 0.01
c              dnx1 = den(x0-del,y0,z0)    < Change in density along
c              dnx2 = den(x0+del,y0,z0)    x-axis encounter by the
c              dnx = dnx1 - dnx2           ray when it moves from
c                                          x0+0.01 to x0-0.01      >
c
c      Density gradient along y - axis
c

```

```

    dny1 = den(x0,y0-del,z0)      < Change in density along
    dny2 = den(x0,y0+del,z0)     y-axis encounter by the
    dny = dny1 - dny2            ray when it moves from
c                                 y0+0.01 to y0-0.01      >
c

```

```

c      Density gradient along z - axis
c

```

```

    dnz1 = den(x0,y0,z0-del)     < Change in density along
    dnz2 = den(x0,y0,z0+del)     z-axis encounter by the
    dnz = dnz1 - dnz2            ray when it moves from
c                                 z0+0.01 to z0-0.01      >
c

```

```

    dn = sqrt(dnx**2+dny**2+dnz**2) < Change in density
    d = (dnx*a1)+(dny*b1)+(dnz*c1)  the ray encounters
    if (d .eq. 0.0) then             when it moves from
        d = 10e-10                   (x0+0.01,y0+0.01,
    endif                             z0+0.01) to (x0-0.01
    ad = abs(d)                       y0-0.01,z0-0.01)  >
    dad= d/ad                          < Direction parameter>
c-----

```

```

c      Direction cosines of the normal vector
c

```

```

    a1 = -(dnx*dad)/dn             < x-component |
    b1 = -(dny*dad)/dn             < y-component |
    c1 = -(dnz*dad)/dn             < z-component |
c-----

```

```

c      Refractive indices
c

```

```

    x = x0-del*a1                  < Refractive index
    y = y0-del*b1                  at (x0-0.01,y0-0.01,
    z = z0-del*c1                  z0-0.01)      >
    mu12 = 1.0-((81.0e-6)*den(x,y,z))/freq2
c

```

```

    x = x0+del*a1                  < Refractive index

```



```

y = y0+del*b1          at (x0+0.01,y0+0.01,
z = z0+del*c1          z0+0.01)      >
mu22 = 1.0-((81.0e-6)*den(x,y,z))/freq2

```

c-----

```

c      Determination of the coefficient 'k' of the
c      Ray equation (Vector form of Snell's law)

```

```

c
c      mu212 = mu22/mu12
c      diff = 1-mu212
c      mu122 = mu12/mu22

```

```

c
c      s11 = (a1*a1)+(b1*b1)+(c1*c1)
c      s112 = s11**2

```

```

c
c      if (s112 .gt. diff) then
c          mu12 = sqrt(mu122)      < Refraction Condition |
c          k = mu12*s11+sqrt((mu122*s112)-mu122+1.0)
c      else
c          k = 2*s11                < Reflection Condition |
c      endif

```

c-----

```

c      Direction cosines of the Emergent ray

```

```

c
c      a2 = mu12*a1-k*a1          < x-component |
c      b2 = mu12*b1-k*b1          < y-component |
c      c2 = mu12*c1-k*c1          < z-component |

```

c-----

```

c      Density and temperature estimation along the ray
c      path at a specified location

```

```

c
c      den1 = den(x0,y0,z0)
c
c      heat1 = heat(x0,y0,z0)

```

c

```

    amu1 = 1.0-(81.0e-6*den1/freq2)
c
    dels = 0.01
40  x1 = x0+dels*a2          < Initial pt. & Final pt. >
    y1 = y0+dels*b2
    z1 = z0+dels*c2
    if (amu1 .lt. 0.0 ) then < Conditional statement to
        dels = dels - 0.005    avoid incorrect
    goto 40                    propagation of the ray
    endif                       inside the plasma of
c                               negative refractive indx >
    den2 = den(x1,y1,z1)
c
    heat2 = heat(x1,y1,z1)
c
    amu2 = 1.0-(81.0e-6*den2/freq2)
c-----
c    Determination of the absorption coefficient
c
    if ( amu1 .lt. 0.0 ) then
        amu1 = 0.00001
    else
        amu1 = sqrt(amu1)
    endif
c
    if ( amu2 .lt. 0.0 ) then
        amu2 = 0.00001
    else
        amu2 = sqrt(amu2)
    endif
c
    sden1 = den1**2
    sden2 = den2**2
c

```

```

      abco1 = (0.16*0.069*sden1)/(freq2*amu1*(heat1**1.5))
      abco2 = (0.16*0.069*sden2)/(freq2*amu2*(heat2**1.5))
      abco  = (abco1+abco2)/2.0    < Average abs. coeff >
c
c-----
c      Determination of Optical Depth
c
c      len  = (sqrt((x1-x0)**2+(y1-y0)**2+(z1-z0)**2))
c      tau1 = abco*len            < Abs. coeff multiplied
c                                by incremental length >
c      if (tau1 .gt. 5.0) tau1 = 5.0
c      tau  = tau + tau1
c      if (tau .gt. 5.0) tau = 5.0
c      heata = (heat1+heat2)/2.0
c      temp  = temp + ((heata)/exp(tau))*(1.0-1.0/exp(tau1))
c
c                                < The above If statements are
c                                used to stop the addition of
c                                tau and tau1 more than 5,
c                                since the effect of it can
c                                not increase the temperature
c                                much                                >
c-----
c      Ready to go for next step in determining the abs. coeff and
c      temperature until the ray reaches rlim = 10.0 (in units of
c      solar radius)
c
c      a1 = a2    < Assigning the new DCs to the old ones |
c      b1 = b2
c      c1 = c2
c
c      x0 = x1    < Changing the coordinates from old to
c      y0 = y1    new values                                >
c      z0 = z1

```

```

c
c-----
      rlim = sqrt(x0**2+y0**2+z0**2) < limiting radius |
      if ( rlim .lt. 10.0) then
          goto 10
      else
          goto 100
      endif

c
100      out(i,j) = temp    < Storing the values of temperature
          out1(i,j) = tau   and optical depth in different
          write(*,*)i,j     two dimensional arrays           >

c
11      continue
1      continue
c
      do i = 1,103
          write(1,5)(out(i,j),j=1,103) < Writing the arrays
          write(2,6)(out2(i,j),j=1,103) into different files>
      enddo
5      format(103(e12.7,1x))           < Format for writing
6      format(103(f5.2,1x))           the real values      >
      stop
      end

c-----
c-----

c      Function: Density Enhancement
c
c      This function is called by the main program where the
c      electron density values are required.
c      The input variables (x,y,z) are supplied by the function
c      calls and the output will be written at the relevant
c      locations. The variable s1,.. represent the location of
c      density enhancement. The factor of enhancement/decrement

```

```

c      should be multiplied with the Gaussian function
c      at the location defined by the aforementioned variables.
c
c      real function den(x,y,z)
c      real rad,x,y,z
c      real s1
c
c      rad = sqrt(x**2+y**2+z**2)
c
c      s1 = ((x-1.40)**2/1.20)+((y+1.10)**2/1.20)+((z+0.06)**2/0.90)
c
c      .....
c
c      .....
c      den = 42000*(10**(4.32/rad))*(1.0+20.00*exp(-s1)+...)
c
c      return
c      end
c-----
c-----
c      Function: Temperature enhancement
c
c      This is the function procedure that calculates the
c      brightness temperature values at the desired locations.
c      Here also (x,y,z) are the input parameters and the
c      properties of temperature structures are controlled by the
c      variables (s1,...).
c
c      real function heat(x,y,z)
c      real rad,x,y,z
c      real s1
c
c      rad = sqrt(x**2+y**2+z**2)
c      s1 = ((x-1.40)**2/1.20)+((y+1.10)**2/1.20)+((z+0.06)**2/0.90)

```

c

.....

c

.....

heat = 1.0e+6\*(1.0+02.00\*exp(-s1)+.....)

c

return

end

c-----

c-----

# VITA

## C.KATHIRAVAN

Indian Institute of Astrophysics  
Koramangala, Bangalore - 560034  
e-mail: kathir@iiap.res.in

Date of Birth: 01 July 1976

B.Sc. June 1996, Madurai Kamaraj University

M.Sc. June 1998, Madurai Kamaraj University

### List of Publications

1. A new low frequency antenna system for observations of polarized radio emission from the solar corona  
Ramesh, R., Kathiravan, C., Sundararajan, M. S., Subramanian, K. R., and Sastry, Ch. V., Sol. Phys. (in press)
2. A seismology of the solar corona through metric radio observations of Type IV burst emission  
Ramesh, R., Kathiravan, C., and Satya Narayanan, A., Asian J. Phys. (in press)
3. Estimation of the plasma parameters in the solar corona using quasi-periodic metric Type III radio burst emission  
Ramesh, R., Kathiravan, C., Sastry, Ch. V., and Udaya Sankar, N., Astron. and Astrophys. (in press)
4. Estimation of the three dimensional space speed of a coronal mass ejection using metric radio data  
Kathiravan, C., Ramesh. R. 2004, ApJ, **610**, 532
5. Metric radio observations of the evolution of a 'Halo' coronal mass ejection close to the Sun  
Ramesh, R., Kathiravan, C., and Sastry, Ch. V. 2003, ApJL, **591**, 163
6. Metric observations of transient, quasi-periodic radio emission from the solar corona in association with a 'Halo' CME and an 'EIT Wave' event

Ramesh, R., Kathiravan, C., Satya Narayanan, A., and Ebenezer, E. 2003, Astron. and Astrophys., **400**, 753

7. Metric radio observations and ray-tracing analysis of the onset phase of a solar eruptive event

Kathiravan, C., Ramesh, R., and Subramanian, K. R. 2002, ApJL, **567**, 93

8. Low-frequency radio observations of the angular broadening of the Crab nebula due to a coronal mass ejection

Ramesh, R., Kathiravan, C., and Sastry, Ch. V. 2001, ApJL, **548**, 229